192p.

CODE-1
CR-56005

A STUDY OF SPACE RADIATION SHIELDING PROBLEMS FOR MANNED VEHICLES

(NASA CR 56005)

Work performed for
National Aeronautics and Space Administration
under the technical direction of
George C. Marshall Space Flight Center
Huntsville, Alabama

NUCLEAR AEROSPACE RESEARCH FACILITY

GENERAL DYNAMICS FORT WORTH

FZK-144

GIIIIIID

NUCLEAR AEROSPACE RESEARCH FACILITY

8 JUNE 1962

A STUDY OF SPACE RADIATION SHIELDING PROBLEMS FOR MANNED VEHICLES

R. K. WILSON
R. A. MILLER
R. L. KLOSTER

(NASA   CONTRACT NO. NAS5-1093)

GENERAL DYNAMICS | FORT WORTH

ABSTRACT

The resolution of the problem of protecting space vehicle crews from charged particles of either solar-flare or trapped-radiation origin will probably depend upon some sort of shielding. The basic problem is concerned with determining quantitatively the attenuation requirement of the incident radiation and selecting an appropriate material to provide this shielding. The discussion given includes the hazards of space radiation, the methods of dose calculation, the development of a proton penetration procedure, a summary of cross section data, and the results of shielding calculations – with particular emphasis on contributions to the dose from secondary radiation.

ACKNOWLEDGEMENT

TABLE OF CONTENTS

TABLE OF CONTENTS (Cont'd.)

NOTE: The following pages were deliberately left blank:
       2, 8, 14, 16, 20, 72, 158, 180, 184, 192, and 200.

LIST OF FIGURES

9

LIST OF FIGURES (Cont'd.)

11

LIST OF FIGURES (Cont'd.)

LIST OF FIGURES (Cont'd.)

LIST OF TABLES

I. INTRODUCTION

A major goal of the space program is the exploration of the planets of the solar system. In particular, efforts are being concentrated toward early exploration of the moon, the nearest and most promising celestial body for manned missions. The discovery and subsequent investigation of ionizing radiations surrounding the earth have emphasized the existence of a hazard which must be assessed prior to the preparation of vehicle designs for manned space flight. From balloon, satellite, and space probes, the radiation data indicate that the fluxes of ionizing particles are of sufficient magnitude to create a radiation hazard. Detailed investigations are necessary to determine the nature, energy distribution, and spatial distribution of this radiation in space so that adequate radiation protection may be provided for space vehicle crews.

The resolution of the complex problem of protecting space vehicle crews from charged particles of either solar-flare or trapped-radiation origin may well depend upon some sort of shielding. The basic problem is concerned with determining quantitatively the attenuation requirement of the incident radiation and selecting an appropriate material to provide this attenuation. In effect, the shielding problem is involved in determining the radiation field inside a specified compartment as a function of shield thickness.

The problem described in this report is concerned with one phase of determining the requirements for the protection of man from the hazards of space radiation.

The work reported here extends the original investigation by GD/FW, which is reported in Reference 1. The present report describes briefly the space radiations, discusses methods of dose calculations, outlines a proton attenuation procedure (PAP), evaluates the input data, summarizes cross-section data, and gives results of some shielding calculations, with particular emphasis on contributions to the dose from secondary radiation. Some general unsolved shielding problems and data requirements are discussed along with recommendations for a definitive study. An appendix includes a brief discussion of PAP, with flow diagrams and range-energy relations.

This report is primarily concerned with the description of the proton hazards from Van Allen radiation and major solar flares. The Van Allen electron component is not treated since it seems rather certain that, at least with our present knowledge of the particle intensities in the radiation belt, shielding thicknesses necessary for reduction of the proton hazard to an acceptable dose rate would reduce the bremsstrahlung component to a negligible level. The "possible" hazards from galactic cosmic rays (protons and heavy particles) are not analyzed for several reasons. The available data on cosmic proton and heavy-particle intensities in space and the

reaction products therefrom are so limited that it is very difficult, if not impossible, to assess their potential hazard at this time. Estimates indicate that dose levels from the low-intensity galactic cosmic radiation are far below those expected from solar flares on lunar flights of about 14 days. For longer voyages of perhaps a year or more, the cosmic radiation dose may possibly be the deciding factor in shielding weight. This area needs considerable investigation before even rough estimates can be made of the hazards.

II.   RADIATION ENVIRONMENT

2.1   The Hazards of Space Missions

A special problem associated with manned space operations is concerned with the protection of personnel against the deleterious effects of ionizing radiation in space. These radiations are separated into four general classifications: primary cosmic radiation, Van Allen radiation, solar-flare radiation, and miscellaneous radiations. The source of radiation which presents the greatest hazard to crews on missions beyond the earth's magnetosphere is the solar flare. It, thus, appears necessary to provide some shielding for such missions if the expected trajectories are not to be restricted severely by schedules dependent on the development of a capability to predict the occurrence of flares. The energy groups of particles are expected to range from those with very low energy, which yield only superficial dose, to those of very high energy, which may contribute substantial whole-body biological dose.

In the absence of definitive knowledge concerning the existence of radiation fields about the distant planets, cislunar and inter-planetary space may be divided into five domains by virtue of the earth's geomagnetic field and the incident solar and cosmic particle radiations. Each of these regions may influence manned space operations and may be briefly described as follows. The first zone, which is restricted to geomagnetic latitudes less than 60° and to

altitudes less than 600 kilometers, has a paucity of trapped particles and is relatively safe for manned flights without shielding. In the second zone, trapped protons with peak intensity occurring near 3600 kilometers in altitude present a major hazard to man and necessitate shielding for missions which require extensive operations in the region. In the third zone, which extends beyond the second zone and varies in size and in the intensity of the trapped particles, the principal hazard arises from electrons of such intensity that a bremsstrahlung problem may be present. In the fourth zone, over the geomagnetic poles, the proton flux from solar flares is of such magnitude that unshielded manned vehicles are unsafe at altitudes above the earth's atmosphere. In the last region, which is the trans-geomagnetic space in which the earth's magnetosphere does not modify the trajectories of charged particles, the principal hazard is from solar-flare protons. In this case, the radiation exposure to primary protons and secondary protons and neutrons produced in the vehicle may exceed acceptable levels without shielding.

2.2 The Van Allen Radiation Belts

Since the discovery of the ionizing radiation by Van Allen, the radiation regions surrounding the earth have been subjected to considerable experimentation and conjecture regarding their origins, spectra, intensities, and temporal and spatial distributions. Among the several theories advanced relative to the origin and nature of the belts, one proposed by Singer (Ref. 2), and partially supported

by experimental data from satellites, advocates that the origin of the inner belt is primarily due to cosmic-ray albedo neutrons. The outer belt was originally considered to be supplied by solar corpuscular radiation, with particle acceleration originating apparently within the earth's magnetic field.

The early conceptual model of spatial distribution of Van Allen radiation consisted of two concentric toroidal regions extending about the earth equatorially. For this model, the inner zone was considered to be between the geomagnetic latitudes of 25°N and 25°S and extending from about 600 kilometers to about 10,000 kilometers in altitude. The outer zone was represented as extending from an altitude of about 15,000 kilometers to about 70,000 kilometers in an equatorial plane. In a meridian plane, the outer zone dipped down to lower altitudes with increasing latitude so that in the geomagnetic latitude interval from 55° to 70°, the outer zone extended over an altitude of from 300 to 1500 kilometers.

Recent data from Explorer XII, Energetic Particles Satellite launched 16 August 1961, indicate that a revision of this concept will be necessary. These data imply there is not a distinct inner and outer belt; on the contrary, there is one large trapping region with particles of different characteristics. The tentative physical picture appears as follows (Ref. 3):

1. At $1\frac{1}{2}$ earth radii (from the earth's center) there is a pattern of high-energy protons in the tens-of-Mev range.

2. At 3 earth radii, there are low-energy protons of a fraction of an Mev, with proton intensities comparable to those of the electrons. These particles constitute the greatest energy density of any energetic particles measured in the outer magnetosphere. The maximum intensity exceeds 10^8 protons/cm^2-sec, with average energy ranging from 100 kev to about 400 kev dependent on the position in the magnetosphere.

3. At 4 earth radii (the older concept of the outer belt), the penetrating particles are protons in the 20-Mev range and/or electrons in the 2-Mev range. It is conjectured that the electrons predominate in this region.

4. At 6 earth radii and out to the outer range of the magnetosphere (which fluctuates daily out to 8-12 earth radii) soft electrons in the energy range of tens of kev are prevalent.

Past satellite and space-probe measurements were interpreted as showing that the intensity of electrons with energies above 40 kev in the heart of the outer zone was about 10^{11} particles/cm^2-sec. Experimental data from Explorer XII reported by O'Brien, et al. (Ref. 4) show that the previous interpretations had been based on invalid assumptions about the electron spectrum and that the intensity is only of the order of 10^8 particles/cm^2-sec. Explorer XII is the first satellite to provide conclusive measurements of the intensity of 50-kev electrons in the heart of the outer zone. In the following sections, since the data from Explorer XII are preliminary in nature, a summary is given for the knowledge of the belts prior to the release of the Explorer XII data. These older data were used as input for shielding calculations performed on PAP and reported in Section V.

2.2.1 The Inner Van Allen Belt

2.2.1.1 Protons. Several measurements have been made of the proton spectrum and particle intensities in the inner Van Allen belt. The inner-belt proton spectrum shown in Figure 2.1 is from the work of Freden and White (Ref. 5). This spectrum, which is a combination of experimental and calculated data, may be represented analytically by relations of the form

$$N(E) = C_1 E^{-0.72} \text{ for 10 Mev} < E < 80 \text{ Mev and}$$
$$N(E) = C_2(E) \exp(-E/170) \text{ for 80 Mev} < E < 700 \text{ Mev.}$$

More recently, Naugle and Kniffen (Ref. 6) have published the results of the measurements of the proton spectrum as a function of position in the inner belt, with an energy range down to 8 Mev. These results show that, at higher latitudes, the slope of the spectrum below 30 Mev steepens considerably (Fig. 2.2).

An analysis of the data received from Explorer VI between 7 August and 20 October 1959 is given by Hoffman, et al. (Ref. 7). A comparison of exponents k to the power-law spectrum

$$N(E) = N_0 E^{-k}$$

for protons in the inner belt, derived from several different sets of data, is given in Table I.

TABLE I

COMPARISON OF PROTON POWER-LAW SPECTRUM EXPONENTS

Experiment	Reference	Alt. (km)	Mag. Lat.	Energy Range (Mev)	k
FW	8	1200	$25°$	75-700	1.84
AH	9	1080	$22°$	80-600	1.80
NK	6	1600	$27\frac{1}{2}°$	40-600	1.7
HAJ	10	1100	$19°$	>23	1.68
HAW	7	2225	$-28.2°$	>23.6	1.65

A literature survey indicates that above about 100 Mev the proton spectrum obtained from emulsions is in good agreement with that expected from neutron albedo decay. Below 80 Mev, the calculated neutron decay spectrum falls off to an exponent of only 0.72. The principal results of the Explorer VI data on protons are summarized, in part, as follows:

1. For an assumed power-law energy spectrum for trapped protons, the spectrum parameters are $N_0 = 1.14 \times 10^4$ and $k = 1.64$ at the maximum intensity at $-28°$ magnetic latitude.

2. The proton spectra through the belt are not in disagreement with either previously published spectra or the spectrum calculated from neutron albedo decays.

3. The radiation becomes slightly softer with increasing range through the belt and with increasing latitude.

4. An upper limit of about 10% is placed on temporal variations of the proton component due to magnetic storms.

The figure shows the inner-belt proton spectrum with:

$$N(E) \sim E^{-0.72}, \quad 10 \text{ Mev} < E < 80 \text{ Mev}$$
$$N(E) \sim e^{-E/170}, \quad 80 \text{ Mev} < E < 700 \text{ Mev}$$

Y-axis: protons/cm²-sec-Mev (from 10^{-1} to 10^2)

X-axis: PROTON ENERGY (Mev) (from 10 to 1000)
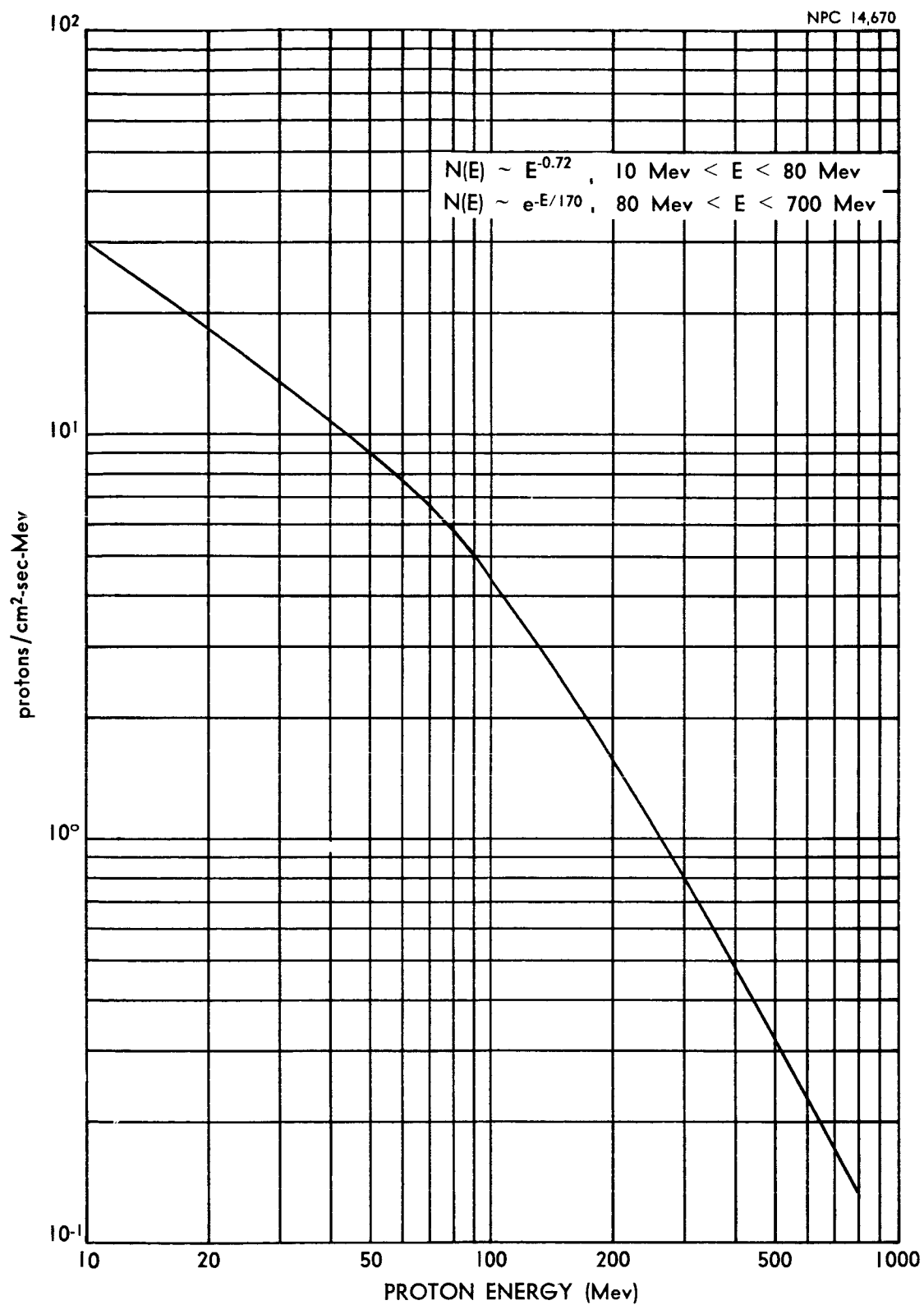
FIGURE 2.1.   INNER-BELT PROTON SPECTRUM
(FREDEN & WHITE)

27

POINT	1	2	3
LATITUDE	28.4°N	25.2°N	21.5°N
LONGITUDE	237.7°W	236.5°W	235.4°W
ALTITUDE	1600 km	1884 km	1600 km
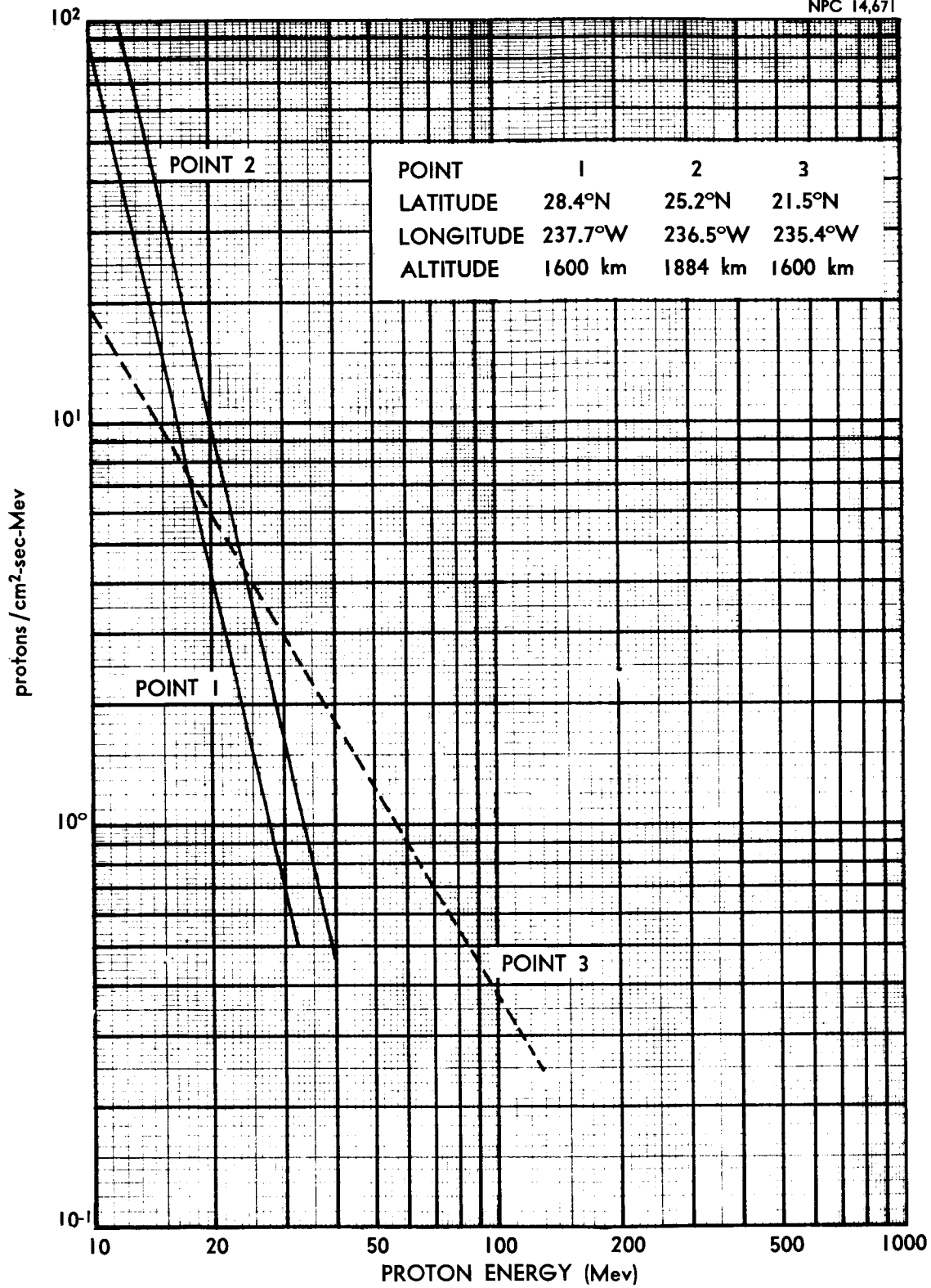
**FIGURE 2.2.   INNER-BELT PROTON SPECTRA
(NAUGLE & KNIFFEN)**

Van Allen (Ref. 11) has estimated that the omnidirectional intensity for protons with energies greater than 40 Mev is on the order of $2x10^4$ protons/cm^2-sec in the heart of the belt.

2.2.1.2 <u>Electrons</u>. Holly, et al. (Ref. 10) have published data of measurements of the inner-belt electron spectrum. The shape of the differential electron spectrum is shown in Figure 2.3. Estimates of the maximum unidirectional intensity for electrons of energy greater than 20 kev are given by Van Allen (Ref. 11) as on the order of $2x10^9$ particles/cm^2-sec-ster. To these estimates are added the Explorer VI measurements (Ref. 6) of electron fluxes at the maximum intensity at -28° magnetic latitude of about $2x10^9$ electrons/cm^2-sec from 200 to 500 kev, and about $1x10^7$ electrons/cm^2-sec greater than 500 kev.

2.2.2 <u>The Outer Van Allen Belt</u>

The energy spectrum of the electrons near the lower edge of the outer zone was measured by Cladis, et al. (Ref. 12). The differential energy spectrum obtained from these measurements can be represented by an expression of the form

$$AE^p \exp(-qE),$$

where $p \approx 1.60$ and $q \approx 0.022$/kev for $E > 50$ kev, and A is a normalization factor. In Figure 2.4, are shown both the differential and integral spectra for the outer belt which have been derived from recent Explorer XII data.
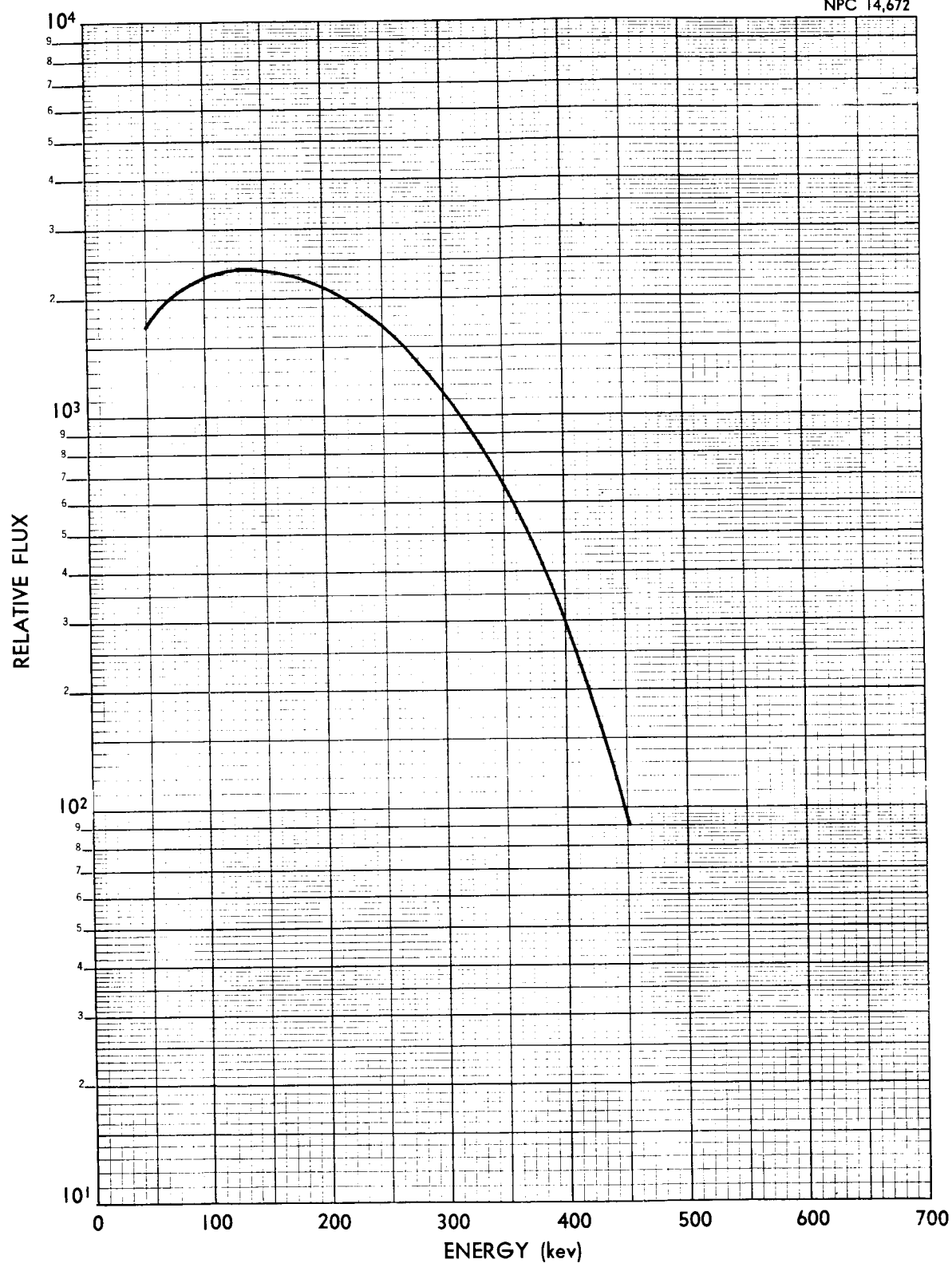
FIGURE 2.3. INNER-BELT DIFFERENTIAL ELECTRON
SPECTRUM (HOLLY, et al.)
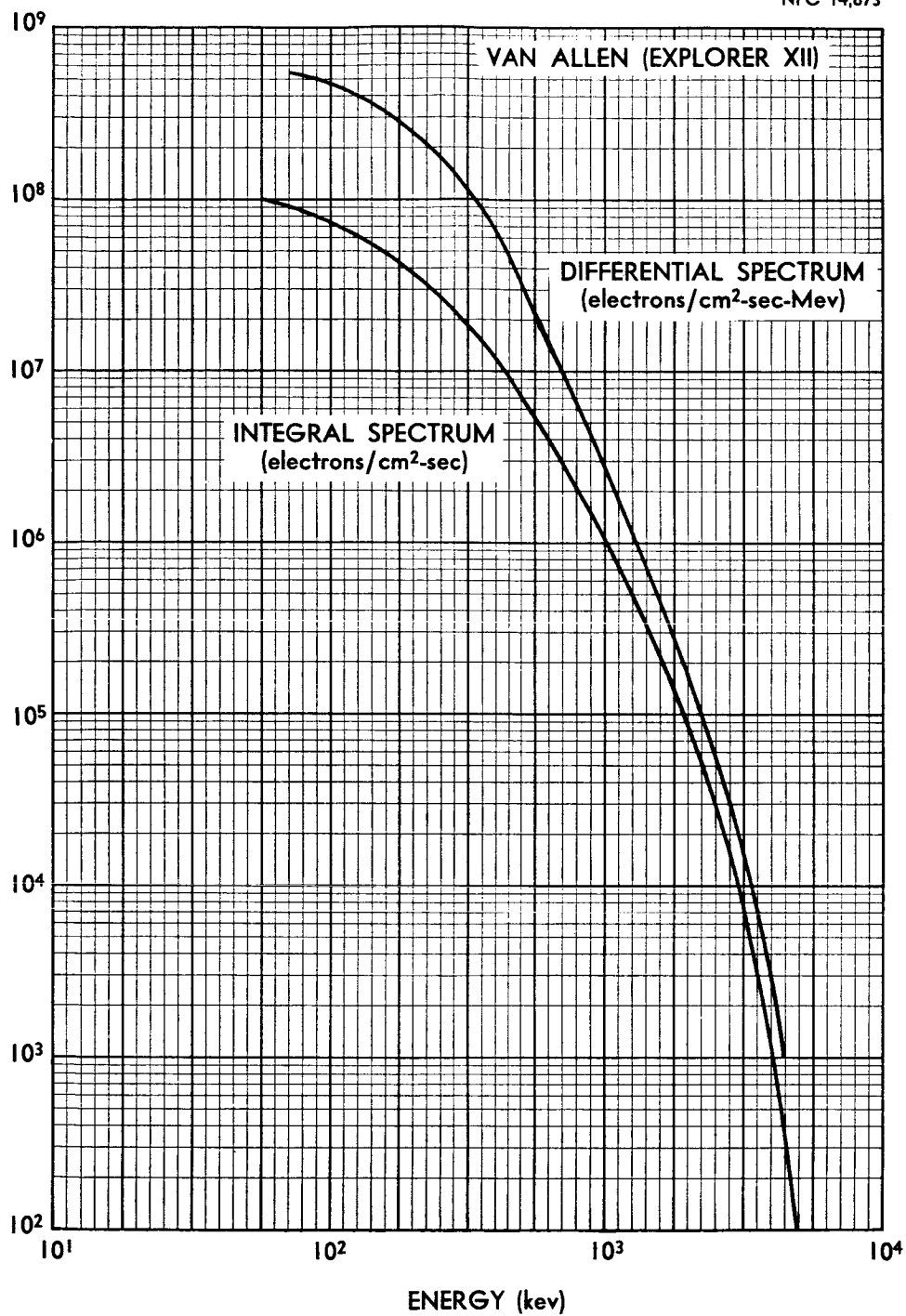
FIGURE 2.4.   TYPICAL-DAY OUTER-BELT ELECTRON SPECTRA

The omnidirectional electron flux in the outer belt has been
the subject of considerable disagreement. The uncertainty stems
from the inherent error involved in measuring electrons unable to
penetrate the shielded instruments. The latest summary of the
electron intensities in the heart of the outer belt (5 Sept. 1961)
from Explorer XII data (Ref. 4) is given in Table II. The omni-
directional intensity of electrons above 40 kev is on the order of
10^8 particles/cm^2-sec.

<div align="center">TABLE II</div>

<div align="center">ELECTRON INTENSITIES IN OUTER BELT</div>

Energy Range (Mev)	Intensity (electrons/cm^2-sec)
$.045 < E < .060$	$\left(9\ ^{+16}_{-6}\right) \times 10^7$
$.080 < E < .110$	$\left(8\ ^{+15}_{-5}\right) \times 10^7$
$.110 < E < 1.60$	$< 10^8$
$1.6 < E < 5.0$	$(2 \pm 1) \times 10^5$
$5.0 < E$	$< 10^3$

In Figure 2.5 are shown flux values for electrons in both
belts for both quiet and excited days.

Freeman (Ref. 13) reports data obtained with a set of CdS-
crystal energy-flux detectors on Injun I in July 1961 that indicate
the presence of an energy flux in excess of 50 ergs/cm^2-sec-ster at
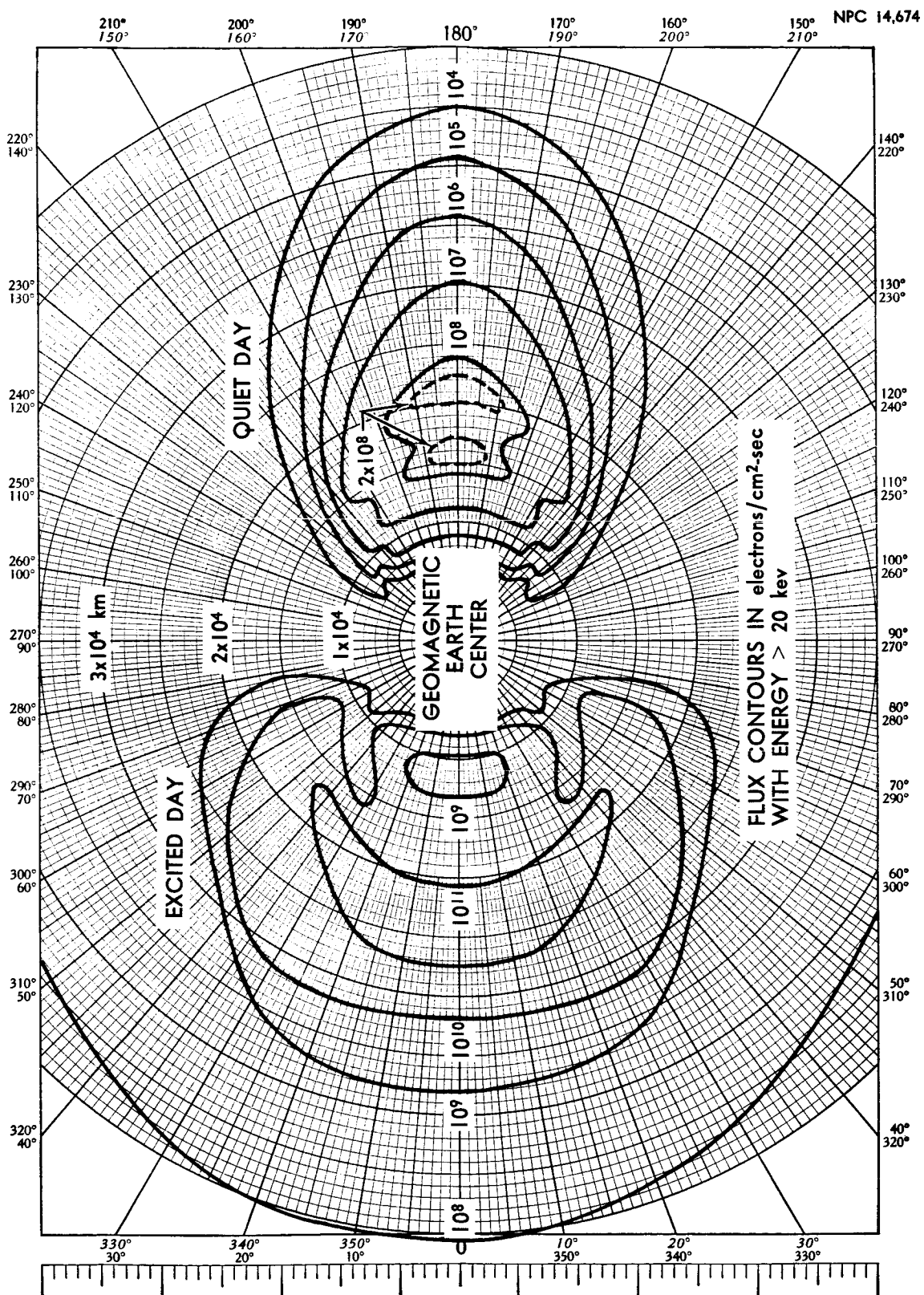
FIGURE 2.5. ELECTRON BELTS (VAN ALLEN AND ALLEN, ET AL.)

approximately 1000 km altitude. The particles are believed to be either protons of energy 0.5 kev $< E < 1$ Mev and/or other heavy ions apparently trapped in the geomagnetic field. Freeman conjectures that the existence of a flux of low-energy trapped protons with more energy than all other particle fluxes at 1000 km implies the existence of an undiscovered source of low-energy protons for the inner zone.

2.3 Solar-Flare Radiations

2.3.1 Frequency and Magnitude of Flares

Solar flares in general have an extreme time variability which may depend to some degree on sunspot activity, since flare occurrence apparently varies roughly with the sunspot number, with a period of approximately 11 years. A plot of the "annual mean sunspot number" showing this cyclic variation over the past century is given in Figure 2.6. Solar flares are associated with sunspot groups and range in size from Class 1, often with a frequency of two per hour, to the Class 3^+, with an average frequency of twelve per year. Flares may be classified according to the characteristics shown in Table III (Ref. 14).

NPC 14,675

POSSIBLE FUTURE MAXIMA

ANNUAL MEANS OF RELATIVE SUNSPOT NUMBERS (W)

YEAR
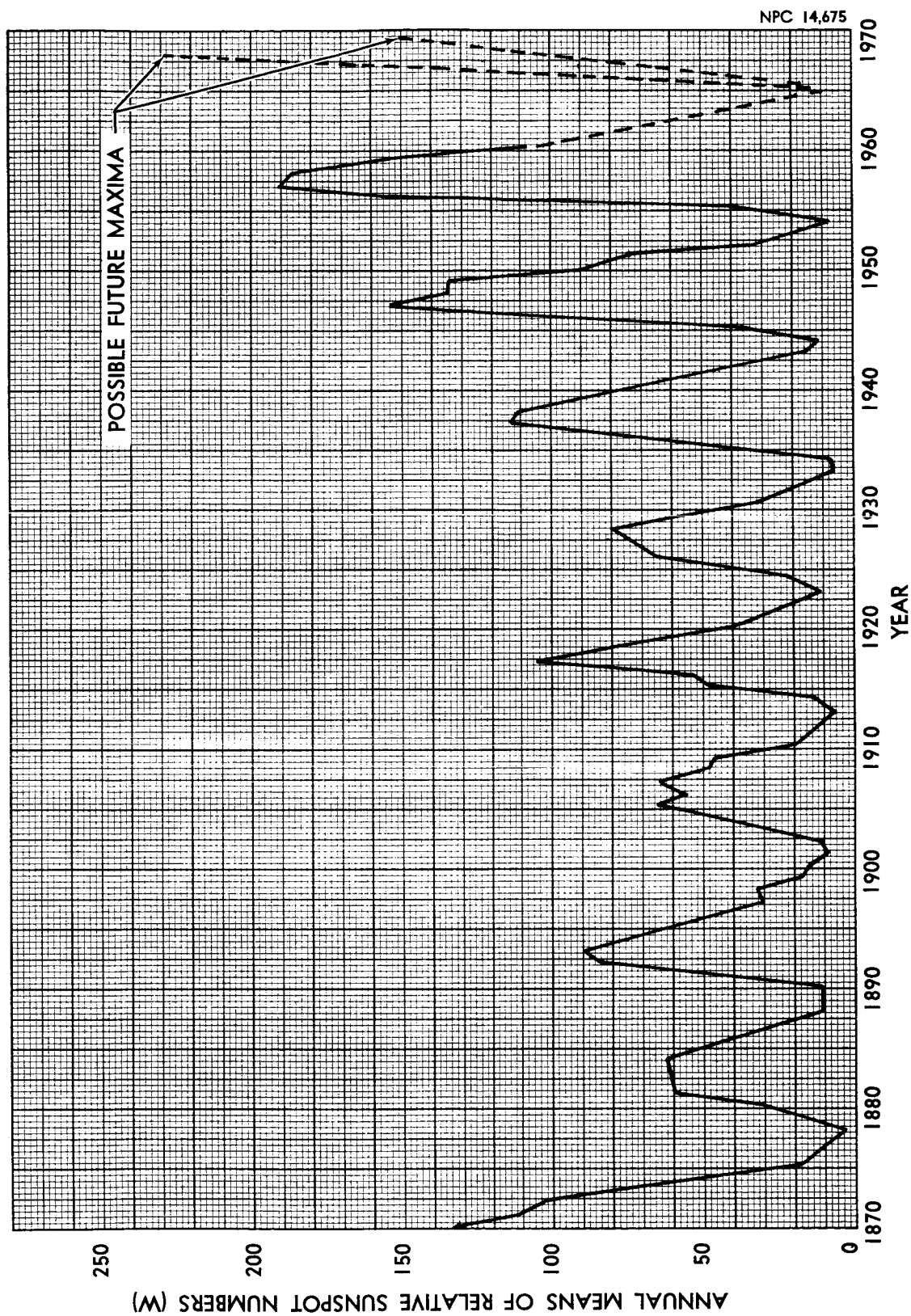
FIGURE 2.6. CYCLICAL VARIATION OF SUNSPOTS

35

TABLE III

SOLAR-FLARE CLASSIFICATION

Class	Duration (min)	Mean Area (10^{-6} visual hemisphere)	Maximum Energy
1-	5-20	25	
1	4-43	100-250	
2	10-90	250-600	
3	20-155	600-1200	10^2 Mev
3$^+$	50-430	>1200	1-40 Bev

A large flare that can generate 10^{33} ergs of energy during its brief lifetime is a distinguishable process occurring at unpredictable times, with characteristic emission of both electromagnetic energy and charged particles. In Figure 2.7 the frequency of solar flares of class greater than 2 is shown with the monthly mean sunspot number since July 1957. During the peak sunspot cycle, Class 3$^+$ flares may average one or more per month; however, during July 1959, three Class 3$^+$ flares were observed within six days.

The Class 3$^+$ flares can be divided into two types: high-energy and low-energy events. During the high-energy events, protons are observed arriving near the earth with relativistic velocities and have been detected with sea-level monitoring instruments. The generation of high-energy radiation by the sun has been detected on seven occasions: 28 February and 7 March 1942; 25 July 1946; 19 November 1949; 23 February 1956; 4 May 1960; and 12 November 1960.

NPC 14,676

FIGURE 2.7. SOLAR-FLARE FREQUENCY AND SUNSPOT NUMBERS

37

An energy spectrum for the great 23 February 1956 flare derived by Winckler (Ref. 15) from balloon data, ionospheric effects, and sea-level monitors is shown in Figure 2.8. This figure shows the estimated prompt spectrum and the observed spectrum after nineteen hours. Also included are the spectrum of a low-energy, high-intensity flare of 10 May 1959, observed thirty-three hours after the flare, and the estimated prompt spectrum for the 14 July 1959 flare.

Low-energy solar-flare events consist primarily of protons in the energy range between 40-500 Mev; thus, the energy is sufficiently low so that the particles are unobservable at sea level because of the magnetic cutoff, and atmospheric attenuation. Most of these events have been detected by a combination of satellites, balloons, and ionospheric techniques, which involve radiation measurements at high altitude.

The principal characteristics of low-energy solar flares have been summarized by Winckler (Ref. 15):

1. Within approximately one hour after the appearance of a major flare, charged particles are detected in the vicinity of the earth.

2. Solar-flare protons are observed (as early as 30 minutes after the flare), incident over the polar region above about 60° geomagnetic latitude.

3. The measured energy spectrum decreases rapidly with increasing energy according to the relation $N(>E) = CE^{-k}$ where k has several empirical values ranging from 4 to 6. The spectral dependence is rather steep, such that few particles of high energy are present in the moderate-intensity events.
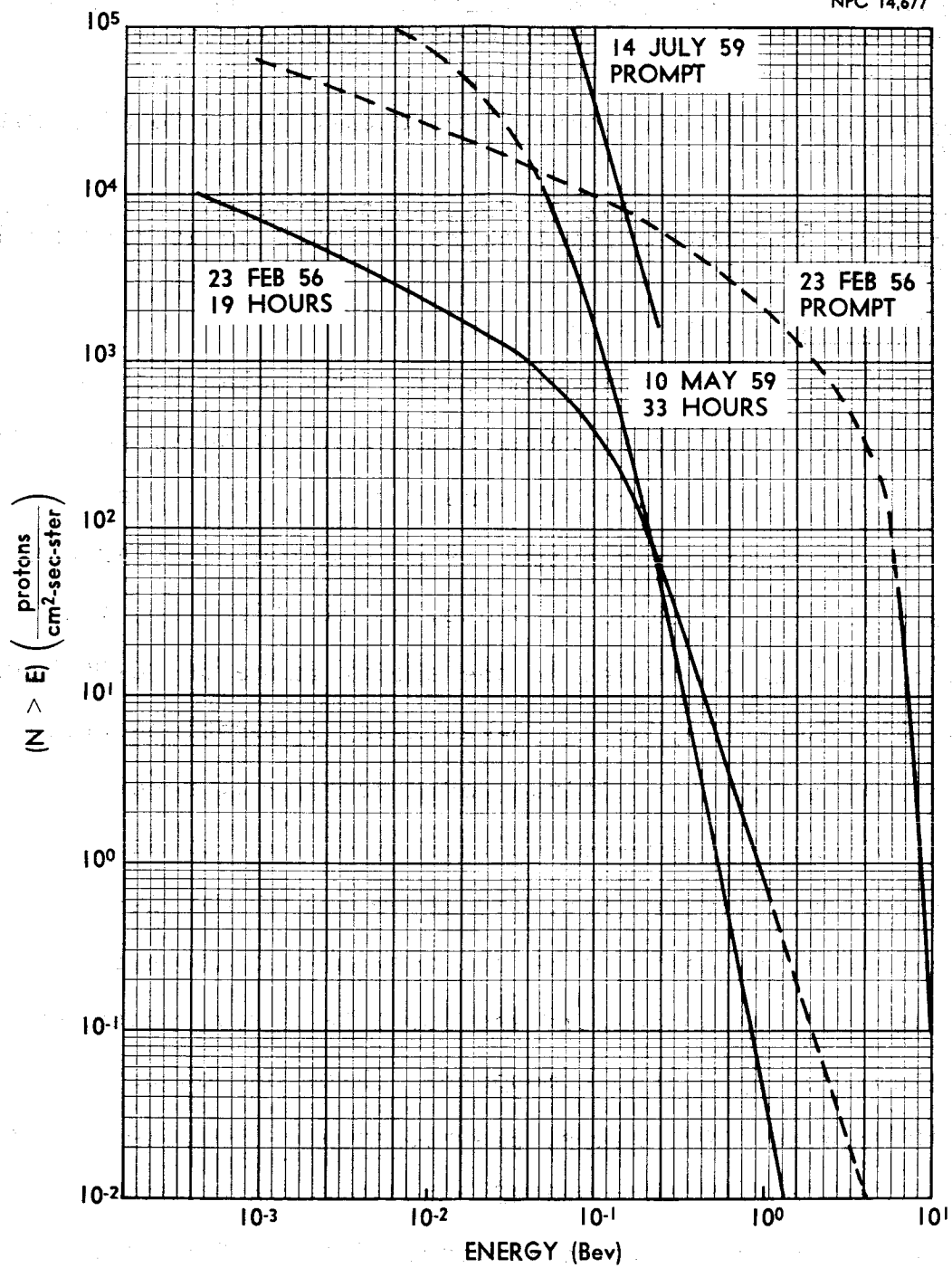
FIGURE 2.8.   SOLAR-FLARE PROTON ENERGY SPECTRA

4. If the solar-flare particles pass near the earth during a geomagnetic storm, the particles may enter the earth's atmosphere at normally forbidden latitudes, below geomagnetic latitudes of $50°$.

5. The intensity of the solar flare decays in conformity with a t^{-2} relation.

6. The total particle flux in free space from solar flares may vary from the cosmic-ray background level to as much as 10^6 particles/cm^2-sec.

2.3.2 Radiation From Flares

Although the major radiation component from solar flares consists of protons, some solar gamma radiation and heavy particles have been detected. Rocket observations have indicated that the variability of the solar x-ray output is a function of solar activity. Solar x-rays have been detected by Chubb, et al. (Ref. 16) with an energy flux of 10^{-5} ergs/cm^2-sec in the energy range of 30-90 kev. Winckler, et al. (Ref. 17), using 30-kev x-ray absorption-coefficient data to extrapolate from the altitude of measurement, report an incident flux of 2×10^7 ev/cm^2-sec on the top of the atmosphere.

Measurements by Bhavsar (Ref. 18) after the 10 May 1959 flare give peak gamma-ray intensity as 54 photons/cm^2-sec and auroral x-ray intensity as 539 photons/cm^2-sec for $E > 22$ kev, measured 10 gm/cm^2 below the top of the atmosphere. From one observation during the 12 November 1960 flare, Biswas, et al. (Ref. 19) gives intensities in the energy interval 42.5 to 90 Mev/nucleon for α-particles and heavier particles as about 12 and 0.2 particles/cm^2-sec-ster, respectively.

2.3.3 Space Distribution and Anisotropy

In the arrival near the earth of charged particles from the sun, it is observed that the high-energy particles arrive ahead of the low-energy particles. Subsequent to the onset of the flare, a directional flux of high-energy particles has been observed to last from ten minutes to nine hours, followed by an isotropic flux of lower-energy particles lasting several hours. After an analysis of the data from the flares of 4 May, 12 November and 15 November 1960, McCracken (Ref. 20) observed that the flux was greatest from a direction west of the sun. During the 4 May flare the flux was maximum from, and symmetrical about, a direction 55° west of the sun and 10° north of the ecliptic for more than nine hours after commencement of the flare. For the 12 November flare the anisotropy persisted for about four hours, with the flux symmetrical about a direction 40° west of the sun and with a magnitude about twice that from the opposite direction. After four hours the radiation was isotropic. For the 15 November 1960 flare, the radiation was highly anisotropic for about 45 minutes after the commencement of the flare; within 90 minutes the radiation was essentially isotropic. During the anisotropic phase of the event, radiation was arriving from a direction to the west of the sun for 30 minutes before there was any significant flux from the opposite direction. From these observations, McCracken formulates a working hypothesis of an interplanetary magnetic field in which magnetic lines of force from a large sunspot near the western limb extend to the vicinity of the earth and in which small-scale irregularities exist in the field lines. These

irregularities violate the conditions for the invariance of the magnetic moments of the cosmic rays. Such numerous small-scale irregularities, which result in small-scale scattering of gyrating particles, explain in general terms the angular distribution of solar cosmic rays of the 4 May flare as well as at other times when the solar protons are generated near the western limb of the sun. Such a model also provides a qualitative explanation of the time dispersions observed during the period of effects produced by flares occurring near the western limb. The experimental data on the flare effect and on the short-lived decrease in the intensity of solar cosmic radiation preceding Forbush decreases are in agreement with either the Gold "Bottle" model (Ref. 21) or the Parker "Blast" model (Ref. 22), provided that the concept of small-scale scattering centers is added to these models (see Fig. 2.9).
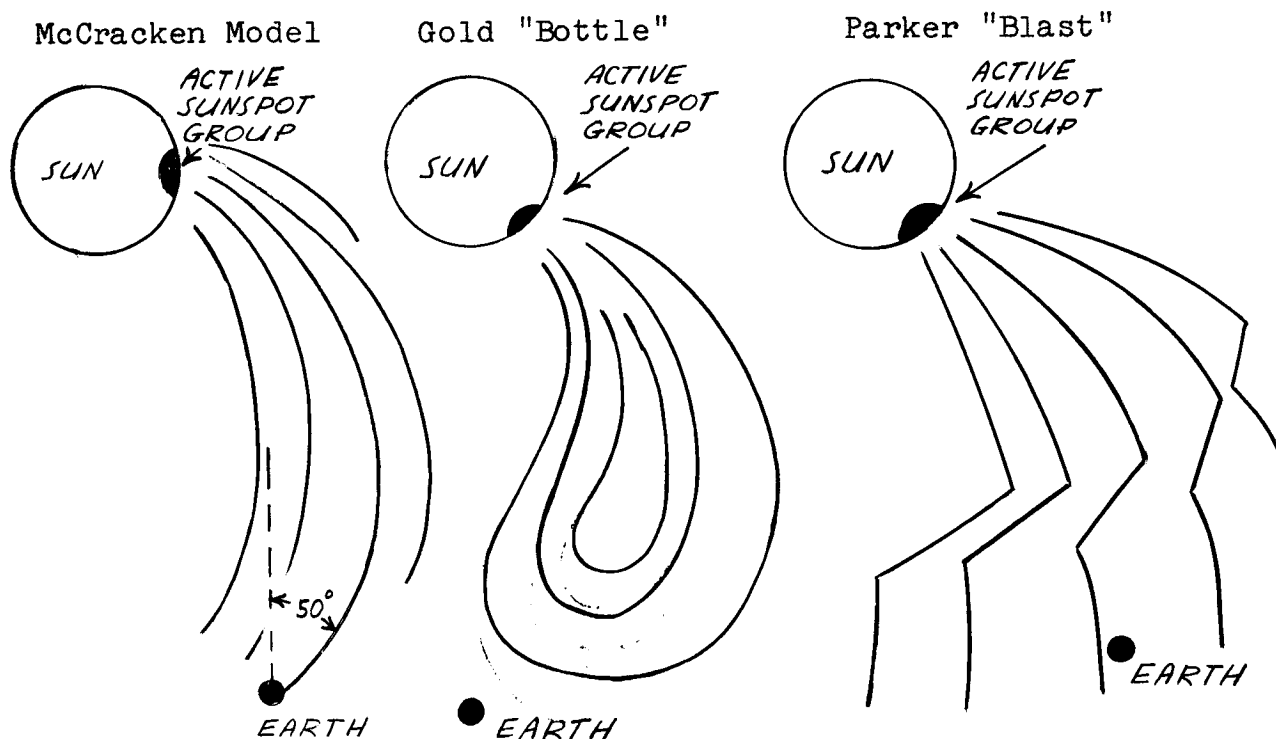
FIGURE 2.9.   MAGNETIC FIELD IN EARTH-SUN REGION

The angular distribution of particles from the solar flare of 28 September 1961 reported by Van Allen (Ref. 23) was markedly anisotropic as measured on Injun I at 1000 km altitude. The isotropy of the greater portion of the solar proton flux is presumably due to the operation of a storage mechanism in interplanetary space.

2.4   Primary Cosmic Radiation

For many years, primary cosmic radiation has been studied from data obtained with balloon, aircraft, and rocket flights to the top of the earth's atmosphere. More recently, the interplanetary cosmic radiation data have been collected through the use of space probes such as the Pioneer series and the Soviet Luniks. An extensive survey of the origin of cosmic radiation, theories of the geomagnetic effects, experimental results of stratospheric flights, shower effects, and meson components is given in Reference 24.

The free-space intensity measurements from the Pioneer V space probe indicate a free-space flux value of 2.5 particles/cm^2-sec, which is in fair agreement with the reported value of 2.3 ± 0.1 particles/cm^2-sec from a Lunik probe (Ref. 25).

Spectral data have been fitted to expressions of the form

$$N(>E) = c_1(c_2 + E)^{-k},$$

where c_1, c_2, and k are constants. For example, Winckler (Ref. 15) finds that the galactic protons may be represented by

$$N(>E) = 0.3(1 + E)^{-1.5} \text{ particles/cm}^2\text{-sec-ster,}$$

where E, in Mev, is valid from $5\text{x}10^2$ to $2\text{x}10^4$ Mev.

III. METHODS FOR CALCULATION OF DOSE

3.1 Basic Shielding Problem

The radiation hazard due to ionizing radiation which may be encountered in cislunar space has been studied with increased interest since the discovery of the radiation belts around the earth. An adequate definition of a representative source term remains the largest problem in evaluating the magnitude of this hazard. Also, questions such as the manner in which the dose should be calculated cause some confusion in the definition of an allowable dose. Studies to date of the radiation hazards to space flight have defined "dose" in two different ways. One method calculates the energy deposited at the surface of a tissue target by the primary and, on occasion, secondary particles (Ref. 26); while the other technique computes the primary-proton depth-dose pattern for a highly idealized body "phantom" (Ref. 27). Under the assumption that the radiation source term is sufficiently well defined, the potential hazard due to primary particles can be determined within acceptable limits. As will be shown in Section V, the secondaries produced in the vehicle structure and shield by primary protons may contribute an appreciable fraction of the total dose received.

The equations which are described in the following sections were developed to investigate the relative importance of the secondary radiation for various composite shield arrangements. The

assumptions made in the calculational methods should give an upper

limit to the secondary-dose contributions, although it is believed

that they are not unduly conservative.

The vehicle structure-shield system in a characteristic solar-

flare or Van Allen belt radiation environment used for this study

is shown in Figure 3.1. The proton radiation source is assumed

isotropic and of a given energy spectrum. The spherical shell chosen
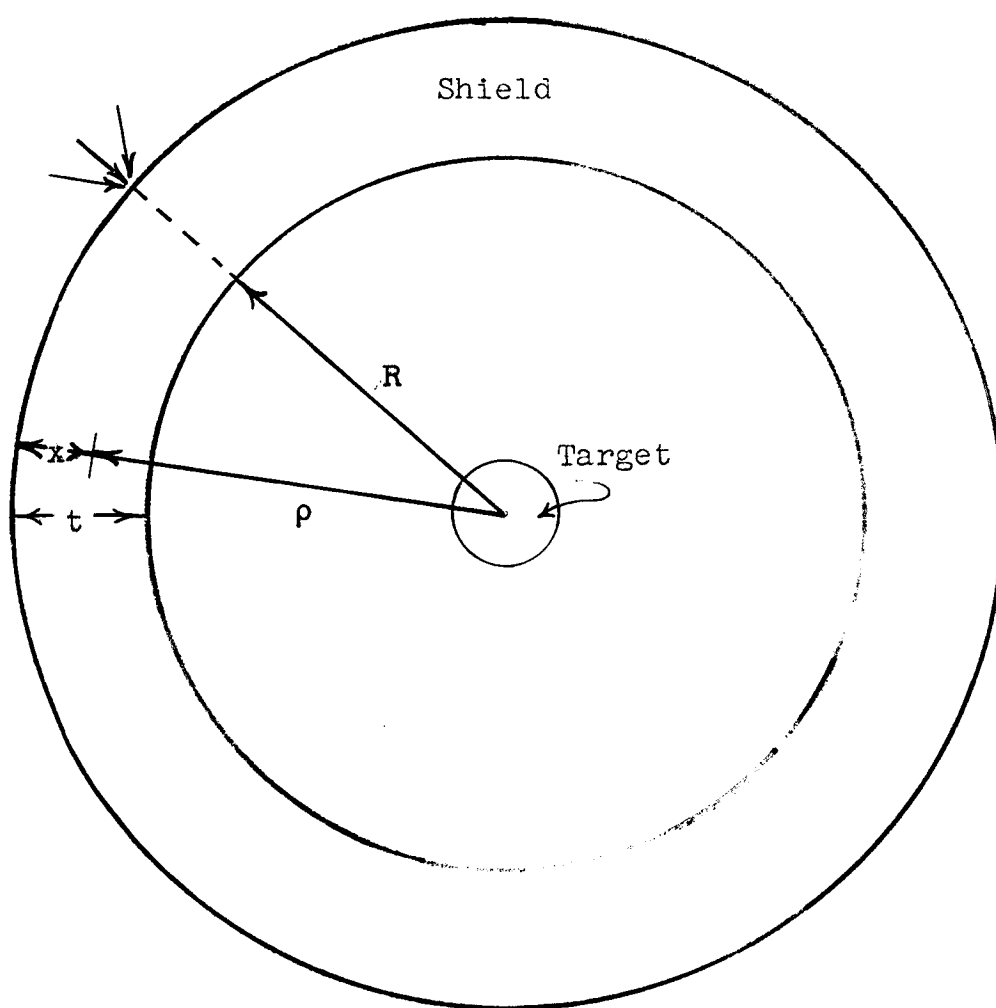
FIG. 3.1 SPHERICAL SHIELD SYSTEM GEOMETRY.

to represent the system is assumed to have a ratio $t/R \ll 1$, where t is the material thickness, R is the radius of the inner surface, and x is a distance from the outer surface measured along the radius vector. The restriction is made that R be large so that the surface of the shield may be treated as a plane. A further restriction is made that t be less than several mean free paths (λ) thick to the incident primary particle whose energy will just permit it to reach the target (Sec. 3.2.1). This limitation in shield size is not too restrictive, since λ is approximately 60 gm/cm^2 in most materials for the energies of interest. The restriction on t will be discussed further in the section on secondary calculations (Sec. 3.2.2).

It is assumed that the shield is in the field of an omni-directional proton flux $\oint_p(E)$, protons/cm^2-sec-Mev. With such an omnidirectional source term it is relatively easy to formulate an equation in terms of the incident energy which gives the dose at the surface of the target volume shown in Figure 3.1. A method is outlined in Section 3.3 by which dose values calculated for the geometry of Figure 3.1 can be used to determine dose levels inside a realistic space-vehicle geometry.

The equations for calculating the primary and secondary dose are described in the next several sections, but, before the methods of calculation are discussed, certain salient features in the calculation of dose will be emphasized. For this study, the dose

due to primary and secondary radiation is calculated for a differential depth, dx, at the surface of the target. It appears that the whole-body dose described in Reference 29 seems to have little meaning in the case of ionizing radiation due to the energies expected in space. As pointed out by Schaefer (Ref. 28), for a particular incident spectrum, the whole-body dose may be at an "acceptable level" while the dose near the surface of the body is excessive. This condition is, of course, due to the self-shielding capacity of the body by which the intensity of the radiation is a decreasing function of depth in the material. The preferable procedure is to look for the point of maximum dose and use this point for determining the permissible design dose level. The depth dose patterns due to primary-proton energy deposition in a body phantom are shown in Figure 3.2 for different prefiltration thicknesses and two different-type incident spectra: Van Allen inner belt and the flare of 10 May 1959 (Ref. 28). Schaefer's review on radiation-dose criteria for space operation (Refs. 27 and 28) are well-known works in this subject area.

Radiation dose values obtained from this study are reported herein in terms of physical (rad) rather than biological (rem) units. In this way one may use his own preferred RBE to convert from physical to biological dose. Use of the RBE factors with a non-differential physical dose, i.e., one in which the energy integral has been performed, is described in Section 4.7. The

WALL OF VEHICLE
OR SHIELD

15 cm RADIUS

PREFILTRATION
(SHIELD)

A: 2 gm/cm²
B: 4 gm/cm²
C: 8 gm/cm²

INNER VAN ALLEN BELT

GIANT FLARE
MAY 1959

TAKEN FROM
REF. 28

REP PER HOUR

DEPTH IN TARGET SPHERE (cm)
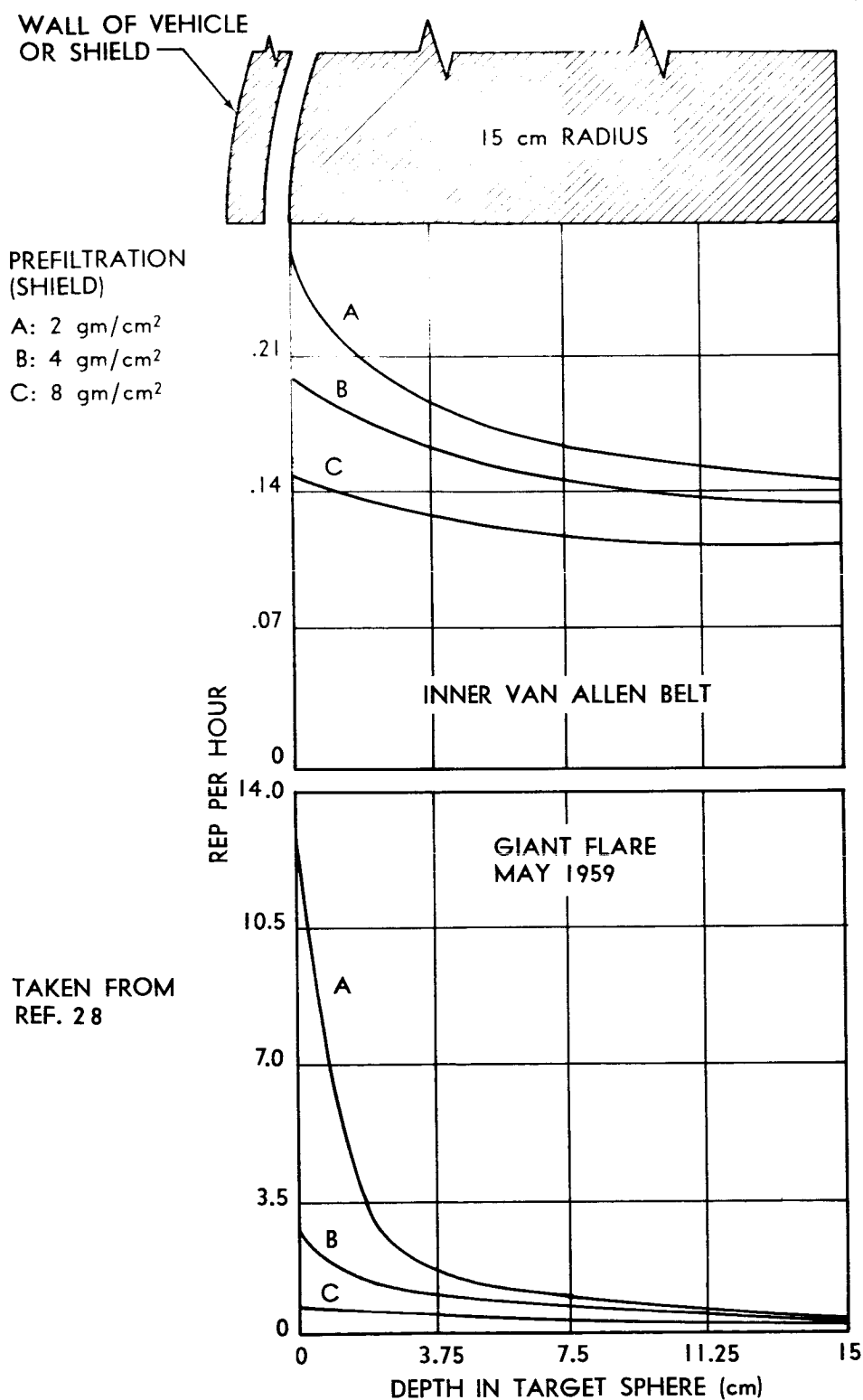
FIGURE 3.2. DEPTH DOSE DISTRIBUTION FOR FLARE-PRODUCED AND VAN ALLEN BELT PROTONS IN SPHERICAL TISSUE PHANTON OF 30 cm DIAMETER BEHIND VARIOUS SHIELD THICKNESSES

basis for calculation of surface dose (differential-surface might be a better name) or, for that matter, depth dose due to protons, is generally taken to be the LET (linear energy transfer) for the particle at the point of interest, i.e., the rate of energy loss in terms of Mev-cm^2/gm which is directly related to the rad dose. The manner of defining the LET for protons and neutrons at the surface of a target is given in Section 4.7 based on calculations by Gibson (Ref. 30). A graph is also given (Fig. 4.45) for the flux-to-dose conversion, using the definition of LET given in that section.

3.2   Calculational Equations

The equations developed in this section are for the calculation of the primary and secondary surface dose received by a target for the system shown in Figure 3.1. The geometry and equations are the result of compromise between a completely realistic structure-shield configuration and a manageable-size computer code. A "Proton Attenuation Procedure" (PAP) was coded in FORTRAN for the IBM-7090 using these equations and is outlined in Appendix B. Use of the results from PAP for design purposes will be described in Section 3.3.

3.2.1   Primary-Proton Component

The model chosen to describe the dose due to primary protons at the skin of the target is relatively simple in form for the geometry used (Fig. 3.1). The model equation is in terms of the

incident energy at the shield rather than at the target because of difficulties in predicting attenuation and exit energies.

The equation for dose, in rads/unit time, as a function of slab thickness for the case of a composite shield is

$$D_{pp}(t) = \int_{E^*(t)}^{E_{max}} dE' \, \oint_p(E') \cdot \exp\left[-\int_0^t dx' \sigma_p(E',x')\right] \cdot S_p(E_t), \qquad (3.1)$$

where

$\oint_p(E')$ is the isotropic flux of protons with energy E' incident at the shield outer surface, units of particles/cm^2-sec-Mev;

$\exp\left[-\int_0^t dx' \sigma_p(E',x')\right]$ is the flux intensity attenuation due to nuclear collisions, where σ_p is equal to

$\sigma_{reaction}(E')$ for a non-hydrogenous shield and

$\sigma_{reaction}(E') + \sigma_{elastic\ hydrogen}(E')$ for a hydrogenous shield;

$S_p(E_t)$ is the surface dose per unit flux at the target, where E_t, the proton energy at the target, is a function of the energy incident on the shield, shell composition, thickness and material ordering (the flux-to-dose relationship for protons is given in Figure 4.45);

$E^*(t)$ is the minimum primary-proton energy necessary for the proton to penetrate the shield (described later in this section); and

E_{max} is the maximum energy of the incident spectrum which will be considered.

The degradation of energy of the protons as they pass through the shield is assumed to be by ionization and excitation of the electrons in the material and not by nuclear collision. It is

51

assumed that elastic collisions are not an important means of energy degradation (except for the case of hydrogen scatter), and scattering with shield nuclei heavier than hydrogen is predominantly straight ahead. A description of the way in which the energy degradation is determined is given in Appendix A for the particular case of a target at the center of the system where the angular distribution of the radiation need not be considered.

Although Equation 3.1 may appear quite simple in form, its solution is particularly subtle due to the rapid variation of the integrand for energies near $E^*(t)$. Plots of the integrand are shown in Figure 3.3 for several different polyethylene slab thicknesses and radiation spectra. A short description is given in Appendix B on the method selected for performing this integration on the computer.
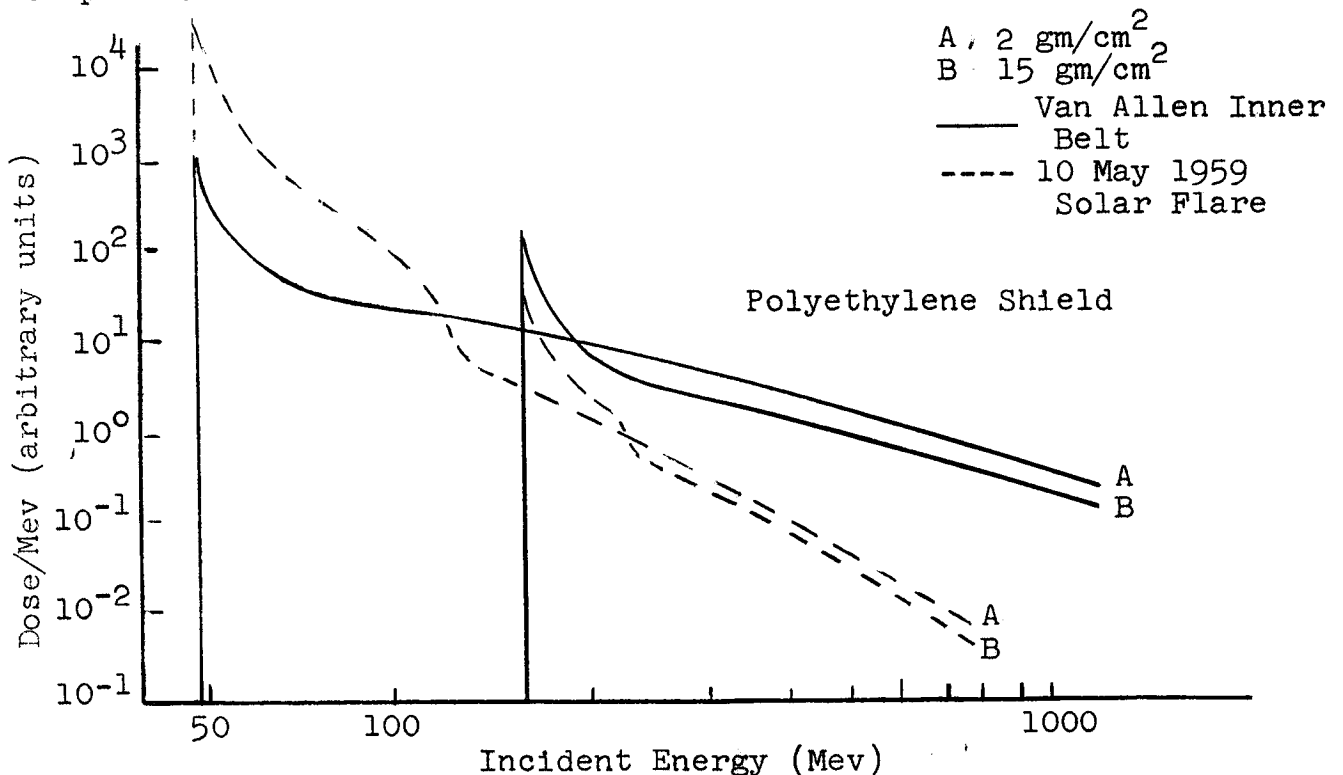
FIGURE 3.3   PRIMARY PROTON INTEGRAND (Eq. 3.1) AS A FUNCTION OF INCIDENT ENERGY

3.2.2 Secondary Components

The high energy of the primary protons in solar-flare and Van Allen spectra make it necessary to consider the secondary component resulting from nuclear collisions in the shield. Much as in neutron reactor shields, where the secondary-particle dose may be as important as that due to the primaries, the secondary component produced in a high-energy proton shield must be analyzed. For energies greater than about 10 Mev, it is certainly possible for secondary particles to cause further reactions (tertiaries) in the slab and, thus, greatly complicate calculations of the total "non-primary" dose. The restriction on the thickness of the shield (several mean free paths to the primaries) is used in the model development in order that the tertiary protons need not be considered and the tertiary neutrons can be handled implicitly through the removal cross sections described in Section 4.6.

The calculation of the secondary-particle dose, $D^S(R_t)$ for an arbitrary geometry (Fig. 3.4) and primary spectrum is given by

$$D^S(\vec{R}_t) = \int d\vec{r} \int d\vec{\Omega} \int dE \ N_S(\vec{r}, E, \vec{\Omega}) \cdot \frac{\tau(|\vec{R}_t - \vec{r}|, \vec{\Omega}, E, E_t)}{|\vec{R}_t - \vec{r}|^2} \ S_S(E_t), \quad (3.2)$$

where

$N_S(\vec{r}, E, \vec{\Omega})$ is the secondary-particle source term which is produced by the primary particle flux $\Phi_p(E', \vec{\Omega}')$;

$\tau(|\vec{R}_t - \vec{r}|, \vec{\Omega}, E, E_t)$ is the transfer function of the secondary particle and/or its tertiaries from the location $\vec{r}$ in the shield to the detector at $\vec{R}_t$;

$S_s(E_t)$ is the flux-to-dose conversion for the secondary-particle energy, E_t, which reaches the target; $E_t = E_t(\vec{R}_t, \vec{r}, E)$;

$d\vec{r}$ is the differential volume element; and

$d\vec{\Omega}$ is a differential element of solid angle measured from the secondary-source location at $\vec{r}$.
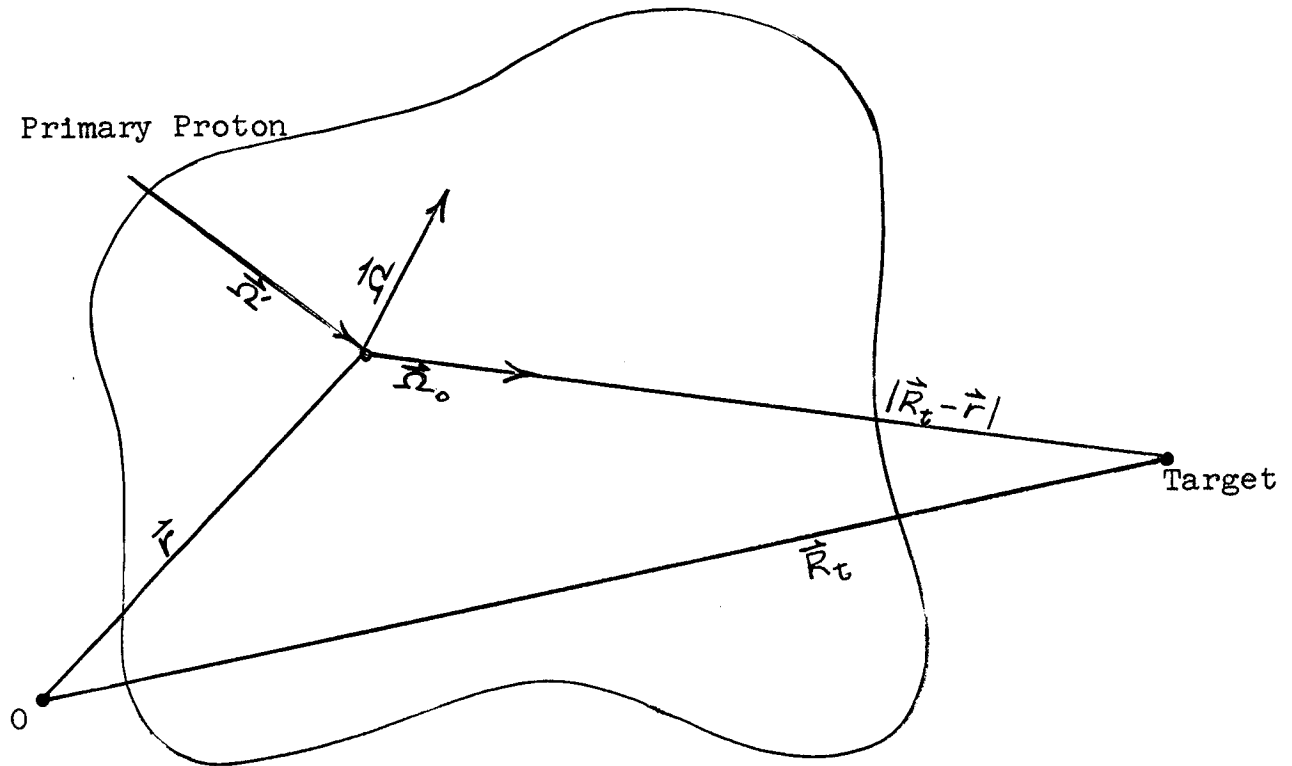
FIGURE 3.4.   SECONDARY-SOURCE COORDINATES
(ARBITRARY GEOMETRY)

For the spherical geometry considered in this study, the volume integral is of a particular tractable form

$$d\vec{r} = \rho^2 \, d\rho \, d\mu_V \, d\phi_V$$

for the origin located at the center. Because of ϕ symmetry, the source term $N_S(\vec{r}, E, \vec{\Omega})$ can be written

$$N_S(x, E, \mu) = \frac{1}{2} \int_{E^*(x)}^{E_{max}} dE' \int_{\mu^*(E',x)}^{1} d\mu' \, \oint_p(E') \cdot$$

$$\exp\left[-\int_0^{x/\mu'} dx' \sigma_p(E', x')\right] \cdot \sigma_S^p(E'', x) f_S(E'', E; \mu', \mu), \tag{3.3}$$

where

$\oint_p(E')$ is the isotropic proton flux of energy E' incident on the shield (proton/Mev-cm^2-unit time);

$\sigma_S^p(E'', x)$ is the production cross section for the particular particle in question at the energy E'', which is the degraded primary-proton energy at the point x in the shield defined to be $\sigma_{reaction}^p(E'')\bar{n}_S(E'')$, where $\bar{n}_S(E'')$ is the average number of particles of type s given off per reaction; and

$f_S(E'', E; \mu', \mu)$ is the secondary energy and angular distribution such that

$$2\pi \int_{-1}^{1} d\mu \int_0^{E''} dE \, f_S(E'', E; \mu', \mu) = 1 \,. \tag{3.4}$$

55

$$\exp\left[-\int_0^{x/\mu'} dx'\sigma_p(E',x')\right]$$ accounts for the primary-particle intensity

attenuation to the secondary-source location due to nuclear colli-

sions, where σ_p was described earlier in Section 3.2.1 in conjunction

with Equation 3.1.

The lower limit on the energy integral in Equation 3.3 is the

minimum energy $E^*(x)$ of a proton incident on the shield which will

reach the point x and cause the resultant reaction product of type

s. The upper limit is the maximum energy of the incident spectrum

which will be considered. The limits on the incident cosine integral,

μ';can best be explained by Figure 3.5.
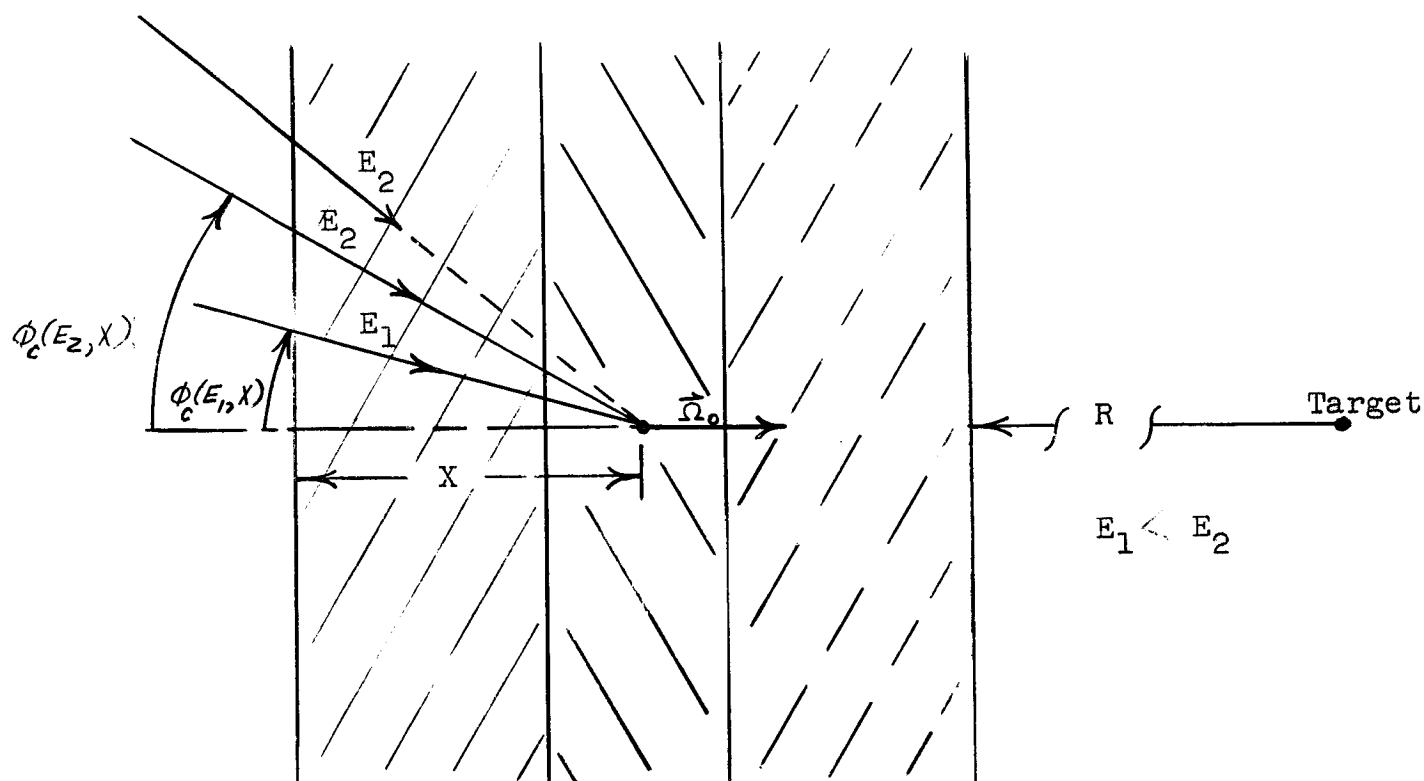
FIGURE 3.5   SECONDARY-SOURCE GEOMETRY

For each proton with energy E'there exists a unique angle, $\phi_c(E',x)$ for which the proton with $\phi > \phi_c$ will not penetrate to the proposed source location, x. The lower limit on the μ' integration is, thus,

$$\mu^*(E',x) = \cos[\phi_c(E',x)],$$

and the upper limit +1 is for normal-incident protons.

It might be pointed out that since the $1/|\vec{R}_t-\vec{r}|^2$ term of Equation 3.2 will cancel with the ρ^2 term in the volume element $d\vec{r}$, neither the ρ^2 nor $|\vec{R}_t-\vec{r}|^{-2}$ terms will appear in the following equations. For the geometry considered (Fig. 3.1) the volume-element differentials, $d\mu_v$ and $d\phi_v$ are replaced by the factor 4π in the following sections.

The integrals over the secondary-particle energy E and μ will be described in detail for the various secondary components in Sections 3.2.2.1 through 3.2.2.3.

The model for calculation of the secondary-dose components must, by necessity, be handled in a highly approximate fashion, unless one wishes to use Monte Carlo or some other sophisticated technique. Previous studies which have considered the secondary components (Refs. 1 and 32) have not made it a point to give the assumptions made in the construction of their model equation. Although the treatment in this report is quite similar to the methods used in the aforementioned references, a description of the models and some of the approximations used will be given in the following sections.

3.2.2.1 Secondary-Proton Component. Secondary protons (reaction products or inelastics) will arise from virtually any nonelastic collision of a primary proton with a shield-material nucleus. The most important charged-particle reaction product which appears to be a hazard is the direct-interaction (cascade) proton. This component will range in energy from the "causing" energy, E'', at the source down to about 10 Mev.

Definition of both the limits of integration and the explicit terms for Equation 3.2 will be used to represent this component of the dose. The secondary-proton dose, $D_p^S(t)$, received by the target for the geometry of Figure 3.1 is

$$
D_p^S(t) = 4\pi \int_0^t dx \int_{E^+(t-x)}^{E''} dE \int d\vec{\Omega}\, N_{sp}(x,E,\mu) \cdot
$$

$$
\tau\left[(t-x),\vec{\Omega},E,E_t\right] \cdot S_p(E_t),
$$

(3.5)

where

$\tau\left[(t-x),\vec{\Omega},E,E_t\right]$ includes both energy degradation and intensity attenuation of the secondary particles of type s from birth place to the inner face of the shield;

$S_p(E_t)$ is the flux-to-dose conversion for a secondary proton of degraded energy E_t; and

$N_{sp}(x,E,\mu)$ is the secondary-proton source term given by the expression

$$N_{sp}(x,E,\mu) = \frac{1}{2}\int_{E^*(t)}^{E_{max}} dE' \int_{\mu^*(E',x)}^{1} d\mu' \oint_p(E') \cdot$$

$$\exp\left[-\int_0^{x/\mu'} dx'\sigma_p(E',x')\right]\sigma_{sp}^p(E'',x)f_{sp}(E'',E;\mu',\mu). \tag{3.6}$$

The lower limit, $E^*(t)$, on the energy integral is the minimum incident energy of a proton that will get through the shield, not the energy required to get to x, the secondary-source location. This selection is made because any secondary proton produced in the shield by a primary proton of energy E'' corresponding to an incident energy less than $E^*(t)$ will not get through the minimum remaining portion $(t-x)$ of the shield.

The lower limit on the secondary-proton energy integral $E^+(t-x)$ is the minimum energy which a secondary proton can have at birth in order to reach the target. The equation is best suited for coding on the computer if the integrals over incident and secondary energy are interchanged to give the resultant equation

$$D_p^S(t) = 4\pi \int_0^t dx \int_{E^*(t)}^{E_{max}} dE' \int_{E^+(t-x)}^{E''} dE \int d\vec{\Omega} \left\{ \frac{1}{2}\int_{\mu^*(E',x)}^{1} d\mu' \oint_p(E') \cdot \right.$$

$$\left. \exp\left[-\int_0^{x/\mu'} dx'\sigma_p(E',x')\right]\sigma_{sp}^p(E'',x)f_{sp}(E'',E;\mu',\mu)\right\} \cdot$$

$$\tau\left[(t-x),\vec{\Omega},E,E_t\right] S_p(E_t). \tag{3.7}$$

A question which immediately arises concerns the assumptions necessary in order to construct an equation which is more tractable than Equation 3.1. The integral over μ can be greatly simplified on the basis of several assumptions enumerated below:

1. $\tau\left[(t-x),\vec{\Omega},E,E_t\right] = \tau(\vec{\Omega}-\vec{\Omega}_o) \Lambda\left[(t-x),E,E_t\right]$, where it is assumed that only those secondary protons that start in the direction of the target contribute an appreciable fraction to this component of the dose(Ω_o in the direction of the line connecting the source and target).

2. Secondaries are predominantly given off in the forward direction, that is to say, with small scattering angle. Under this assumption,

$$\int_{-1}^{1} d\mu \int_{0}^{E''} dE\ f_{sp}(E'',E;\ \mu',\mu) = 1 \qquad (3.8)$$

can be replaced by

$$\int_{\mu_o}^{1} d\mu' \int_{0}^{E''} dE\ f_{sp}(E'',E;\ \mu',1)\approx 1, \qquad (3.9)$$

where $\mu_o<\mu*(E',x)$ is so chosen that in the interval $(\mu_o,\ 1)$,

$E'' = E''(x/\mu',E')$ is essentially constant; thus,
$E''\approx E''(E',x)$.

3. The mean value theorem for integrals can be used to eliminate the integral over μ'.

The angular-dependence factor of Equation 3.7

$$\int_{\mu*(E',x)}^{1} d\mu'\ \exp\left[-\int_{0}^{x/\mu'} dx'\sigma_p(E',x')\right].$$

$$\int_{-1}^{1} d\mu\ f_{sp}(E'',E;\ \mu',\ \mu)\ \tau\left[(t-x),\vec{\Omega},E,E_t\right] \qquad (3.10)$$

can, on the basis of these assumptions, be written in the form

$$\exp\left[-\int_0^{x/\mu'} dx'\,\sigma_p(E',x)\right] \Lambda\left[(t-x),E,E_t\right] \cdot g(E'',E). \qquad (3.11)$$

For Equation 3.10, E'' is the reaction "causing" energy $E''(E'x/\mu')$, and in Equation 3.11, E'' is the like term after the mean value theorem is applied. The function $g(E'',E)$ is used to represent $f_{sp}(E'',E;\mu',\mu)$ after integrating over μ the integral in which the Dirac delta function and f_{sp} appear.

The secondary-proton equation for the dose, $D_p^S(t)$, at the center of the system (Fig. 3.1) is

$$D_p^S(t) = 2\pi \int_0^t dx \int_{E^*(t)}^{E_{max}} dE' \int_{E^+(t-x)}^{E''} dE \left\{ \oint_p(E')\exp\left[-\int_0^x dx'\,\sigma_p(E',x')\right] \cdot \right.$$

$$\left. \sigma_{sp}^p(E'',x)g(E'',E)\right\} \cdot \Lambda\left[(t-x),E,E_t\right]S_p(E_t). \qquad (3.12)$$

Equation 3.12 was solved numerically on the computer to give the secondary-proton dose components reported in Section 5.3 for several shield compositions and thicknesses.

The transfer function $\Lambda\left[(t-x),E,E_t\right]$, considers energy degradation by using the range-energy curves for the materials and intensity attenuation by using the term

$$\exp\left[-\int_x^t dx'\,\sigma_p(E,x')\right],$$

where $\sigma_p(E,x')$ was described in connection with Eq. 3.1.

61

On the basis of the model described above, the secondary proton component can be evaluated if sufficient information is available on the normalized secondary-energy spectra $g(E'',E)$. In order to solve Equation 3.12 it is necessary to evaluate the following integral:

$$\int_{E^+(t-x)}^{E''} dE\, g(E'',E) \cdot \Lambda\left[(t-x),E,E_t\right] \cdot S_p(E_t). \tag{3.13}$$

One method of evaluating the above integral is to determine an average secondary energy $\bar{E}$ (Ref. 33),

$$\bar{E}(E'') = \int_0^{E''} \left\{ Eg(E'',E) \right\} dE \bigg/ \int_0^{E''} g(E'',E)dE, \tag{3.14}$$

and to say this energy is equal to the energy $\widetilde{E}(t-x)$ found by evaluating Equation 3.13 by the mean value theorem. Equation 3.13 is then represented by

$$\Lambda\left[(t-x),\bar{E},\bar{E}_t\right] S_p(\bar{E}_t) \int_{E^+(t-x)}^{E''} dE\, g(E'',E). \tag{3.15}$$

Clearly, this is a very questionable method of treatment, since very possibly $\bar{E}(E'')$ can be less than $E^+(t-x)$, the minimum energy required to get through the remaining portion of the slab from a particular secondary source point. Judicious choice of a "weighted-mean" (and not an average) energy $\widetilde{E}(t-x)$ can be determined by evaluation of

$$\tilde{E}(t-x) = \int_{E^+(t-x)}^{E''} \left\{ E g(E'',E) \right\} \Lambda\left[(t-x),E,E_t \right] S_p(E_t)dE \Bigg/$$

$$\left[\int_{E^+(t-x)}^{E''} g(E'',E) \ \Lambda\left[(t-x),E,E_t \right] S_p(E_t)dE \right]. \qquad (3.16)$$

At best the representation of the secondary-energy integral by the average energy $\bar{E}(E'')$ must be considered usable only when complete data are not available on the secondary-energy spectra and some order-of-magnitude answer is necessary. However, an option is available in the procedure for the handling of this concept.

It was found in the course of analysis of available secondary spectra that a relation of the sort

$$g(E'',E) = k \tan \frac{\pi}{2} \ (1-E/E'') \qquad (3.17)$$

is a good representation for the secondary spectra for energies greater than about 5% of E''. Thus, a subroutine is included in the computer program which uses this approximation to the normalized secondary spectrum $g(E'',E)$.

A subroutine, DURP, is also available in the program, which determines from input tables the spectrum as a function of causing energy E'' and secondary energy E. This option can be used when adequate data are available.

3.2.2.2 <u>Cascade-Neutron Component</u>. High-energy neutron-reaction

products resulting from proton bombardment can be described on the

basis of two models: compound-nucleus formation followed by decay

(evaporation), and the direct-interaction (cascade) model. The

cascade-neutron component is distinguished by its predominantly

forward direction at production and its high energy, ranging from

causing energy E'' down to about 10 Mev. Further description of this

component is given in Section 4.3.2.1.

The development of a model for calculation of the cascade-

neutron component of the dose parallels that of Section 3.2.2.1 for

secondary protons, with the same general assumptions and approxi-

mations. The main differences in the equation are in the limits of

energy integration and the form of the transfer function

$\tau\left[(t-x),\vec{\Omega},E,E_t\right]$. Equation 3.18 gives the cascade neutron component

of the dose deposited in the unit-volume target for the system in

Figure 3.1 on the basis of the secondary-dose equation (Eq. 3.2):

$$D^s_{cn}(t) = 2\pi \int_0^t dx \int_{E^*(x)}^{E_{max}} dE' \int_{E^+}^{E''} dE\left\{\Phi_p(E')\exp\left[-\int_0^x dx'\sigma_p(E',x')\right]\right.$$

$$\left.\sigma^p_{cn}(E'',x)g(E'',E)\right\} \Lambda\left[(t-x),E\right] S_n(E). \qquad (3.18)$$

In the above equation, $E^*(x)$ is the minimum proton energy

necessary to get from the incident face to the point x; E^+, the

lower limit on the secondary-energy integral, is the cutoff energy

64

below which it is assumed the cascade neutrons are not produced. The transfer function $\Lambda\left[(t-x), E\right]$ is given by

$$\Lambda\left[(t-x, E\right] = \exp\left\{-\text{SUM}_{i=n+1}^{N}\left[\Sigma_r^i(E)t_i\right] - \Sigma_r^n(E)\left[\text{SUM}_{i=1}^{n}(t_i)-x\right]\right\}, \qquad (3.19)$$

which represents the relationship between the cascade-neutron dose at its point of origin to that at the target. Through the definition of a removal cross section $\Sigma_r^i(E)$ for each material i, the energy degradation and intensity attenuation of a neutron of energy E can be considered. The method of determining $\Sigma_r^i(E)$ is described in Section 4.6 for the case of a one-material shield. Figure 3.6 shows how Equation 3.19 would be used for a shield composed of 5 segments (N = 5 for this example).

$$\ell_1 = \text{SUM}_{i=1}^{n}(t_i)-x$$

$$\ell_2 = \text{SUM}_{i=n+1}^{N}(t_i)$$

$$t = \text{SUM}_{i=1}^{N}(t_i)$$

$$N = 5$$

$$n = 2$$
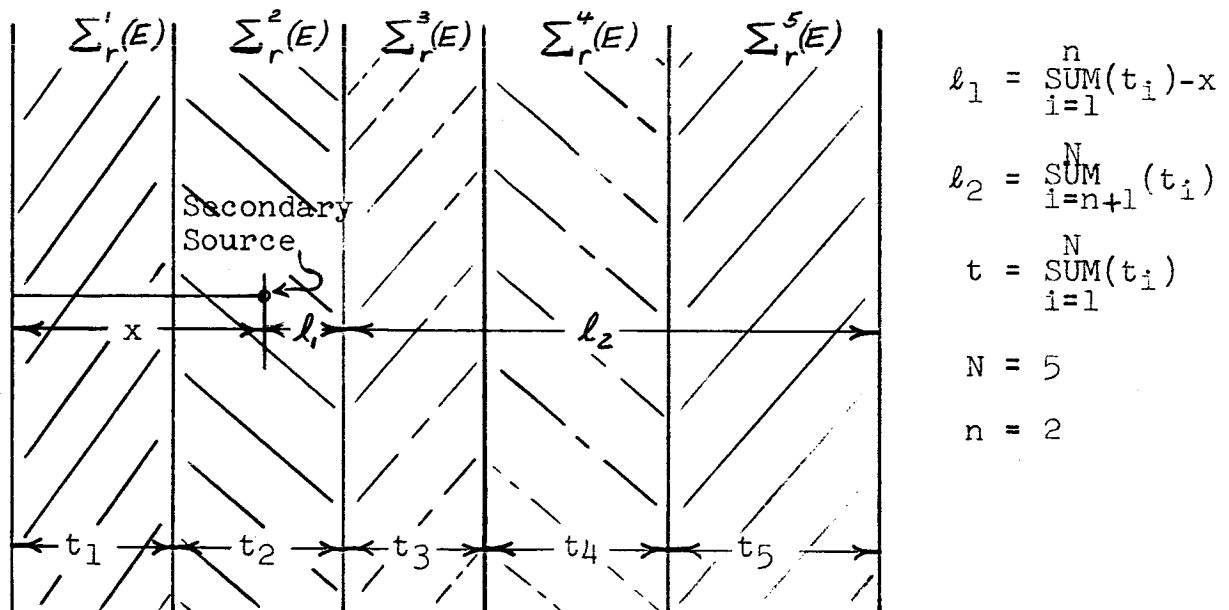
FIGURE 3.6.   REMOVAL-CROSS-SECTION TERMINOLOGY

The flux-to-dose conversion $S_n(E)$ for neutrons is described in Section 4.7 and is shown in Figure 4.45.

The concept of average energy appears to work rather well for cascade neutrons because of the slow variation of the flux-to-dose function $S_n(E)$ and the fixed lower limit $E^\dagger$ on the energy integral.

The same functional form $\tan \frac{\pi}{2}(1-E/E'')$ as used in the secondary-proton-spectrum representation can be used for cascade neutrons. Double interpolation in terms of causing energy $E''(x)$ and secondary energy E can be used as one option for the secondary spectra if sufficient input data are available.

The restriction on shield thicknesses to less than several mean free paths to $E^*(t)$ incident-energy protons was made primarily to hold the tertiary neutron and proton contribution to the total dose to a minimum. However, tertiaries are included implicitly through the removal cross sections.

3.2.2.3 <u>Evaporation-Neutron Component</u>. Evaporation neutrons are the result of any neutron-producing proton reactions considered in this study. They can be produced by the de-excitation of a compound nucleus formed when a proton strikes and reacts with a nucleus in the shield or by de-excitation after the cascade process leaves the resultant nucleus in an excited state.

The energy spectrum of neutrons from this component is quite different from that for cascade particles, with the majority of the neutrons given off having energies less than about 5 Mev. The energy

66

distribution of evaporation neutrons can be described by a statistical model, as outlined in Reference 31, with an assumed and experimentally verified isotropic angular distribution.

The equation for the evaporation-neutron dose received by a target shown in Figure 3.1 is given by

$$D_{en}^{s}(t) = 4\pi \int_{0}^{t} dx \int_{0}^{E_{ex}} dE \int d\vec{\Omega} \quad N_{en}(x,E,\mu) \cdot \tau\left[(t-x),\vec{\Omega},E,E_t\right] S_n(E_t), \quad (3.20)$$

where E_{ex} is the excitation energy of the compound nucleus, minus the binding energy per nucleon, before the evaporation phase begins.

The equation for the evaporation-neutron source term (with no angular dependence) is

$$N_{en}(x,E) = \tfrac{1}{2} \int_{E^*(x)}^{E_{max}} dE' \int_{\mu^*(E',x)}^{1} d\mu' \; \oint_p (E') \cdot$$

$$\exp\left[-\int_{0}^{x/\mu'} dx' \sigma_p(E',x')\right] \; \sigma_{en}^p(E'',x) \; f_{en}(E'',E), \quad (3.21)$$

where the same notation is used as for secondary protons and cascade neutrons. $f_{en}(E'',E)$ is the normalized secondary evaporation-neutron spectrum such that

$$\int_{0}^{E_{ex}} dE \int d\vec{\Omega} \; f_{en}(E'',E) = 1. \quad (3.22)$$

The approximations necessary to eliminate the Ω and μ' integrals are not as straight forward as for the other two components. The tacit assumption will be made that, on the average, the lower limit $\mu^*(E',x)$ is equal to 1/2 for each energy E' and position x in the shield. It will also be assumed that exponential attenuation to the secondary source location can be approximated by $\mu'=1$. The same definition of the transfer function as in the case of cascade neutrons is used, namely,

$$\tau\left[(t-x),\vec{\Omega},E,E_t\right] = \delta(\vec{\Omega}-\vec{\Omega}_0)\,\Lambda\left[(t-x),E\right],$$

where $\vec{\Omega}_0$ is the unit vector parallel to the line connecting the source and target (radius vector). The "straight-ahead" assumption used to consider the angular distribution of the previous two components of the secondary dose cannot be used here, since the assumption of a peaked secondary angular distribution used in Equation 3.9 does not apply for an isotropic secondary source. It will be assumed that

$$\left\{2\pi\int_{\frac{1}{2}}^{1}d\mu'\int_{0}^{E_{ex}}dE\,f_{en}(E',E)\right\} \approx \frac{1}{4}. \qquad (3.23)$$

Thus,

$$D_{en}^S(t) = \frac{\pi}{2} \int\limits_{0}^{t} dx \int\limits_{E^*(x)}^{E_{max}} dE' \int\limits_{0}^{E_{ex}} dE \left\{ \oint_p(E')\exp\left[-\int\limits_{0}^{x} dx'\sigma_p(E',x')\right] \right.$$

$$\left. \sigma_{en}^p(E'',x)f_{en}(E'',E) \right\} \Lambda\left[(t-x),E\ S_n(E)\right] \qquad (3.24)$$

for the evaporation neutron dose at the target shown in Figure 3.1.
Equation 3.24 was coded and solved numerically on the computer to
give the evaporation-neutron dose values reported in Section 5.3.

Analysis of the evaporation dose in relation to the other
components will be given in Section V.

3.2.2.4 Other Secondary Components. Other secondary components
(alpha particles, mesons, heavy spallation products, etc.) were not
considered in this study because of a low estimated contribution to
the total dose. These components of the secondary radiation and
accompanying nuclear de-excitation gammas are all produced by high-
energy protons; however, because of the relative softness (steepness)
of the normal flare spectra, the production of secondary particles
in this group should be low in relation to the components already
considered.

3.3 Practical Design Calculation

The use of the data reported in Section 5.3 on the primary and
secondary dose for various combinations and thicknesses of material

is of immediate interest for evaluating the design of space vehicles.
Because of the "straight-ahead" assumption used in considering the
secondary transport and the idealized geometry (Fig. 3.1), it is
necessary to make several further assumptions in using these data
in practical design.

It will be assumed that the dose received by a target in a
realistic vehicle geometry (Fig. 3.7) due to a particular component
of the radiation of type S is given by the equation

$$D_S = \oint \left[D_S(\vec{r}_t) \, \mu \bigg/ |r|^2 \right] dA,$$

where $D_S(\vec{r}_t)$ is the dose (divided by 4π) due to the radiation
component of type S (Sec. 5.3) for the slant
thickness t at the particular point $\vec{r}_t$;

dA is a differential area element;

μ is the cosine between $\vec{r}_t$ and the normal to the
surface at that point; and

$|\vec{r}_t|$ is the distance from the target to the shield at r_t.

The notation $\oint$ refers to 4π-solid-angle integration.
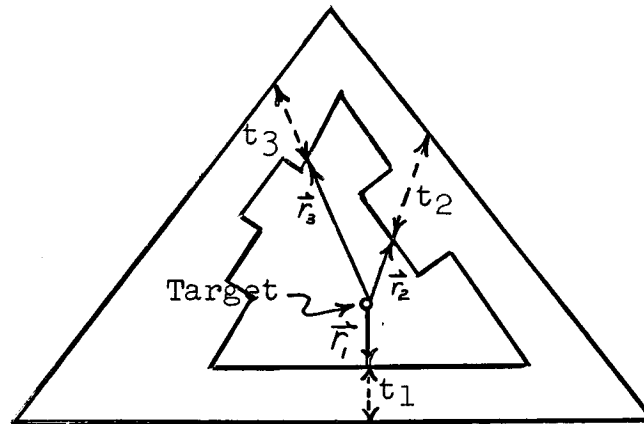
FIGURE 3.7. VEHICLE COORDINATES AND GEOMETRY

70

The obvious need for extensive parametric data is evident if composite shields are to be considered by this method. Refinements to these calculations are suggested in Section 6.3.

IV. EVALUATION OF INPUT DATA

In this section, a brief description is given of the avail-
ability and reliability of some of the data necessary for shield-
ing calculations. These data and topics include the incident
spectra, cross sections, and dose definitions.

4.1 Incident Spectra

The differential energy spectra used in this study were the
Freden and White inner-belt proton spectrum (Fig. 2.1), 10 May 1959
proton solar-flare spectrum (Fig. 4.1) derived by differentiation
of the integral spectrum, and the 23 February 1956 proton solar-
flare prompt spectrum (Fig. 4.1) obtained from Figure 2.8. These
spectra were chosen for several reasons: (1) available data,
(2) representative spectral shape, and (3) assumed intensities
typical of what could be encountered in space.

Complete analysis of the time variation of flare intensities
after onset is not presently adequate for shielding studies;
however, with conservative estimates, as described in Section 5.2,
some conclusions can be drawn as to the importance of these
radiation sources.

4.2 Cross Sections

4.2.1 Terminology

The following terminology will be used for the various cross
sections discussed:

    1. σ_t is the total nuclear cross section: total cross
        section for neutrons; total minus coulomb scattering
        for protons.
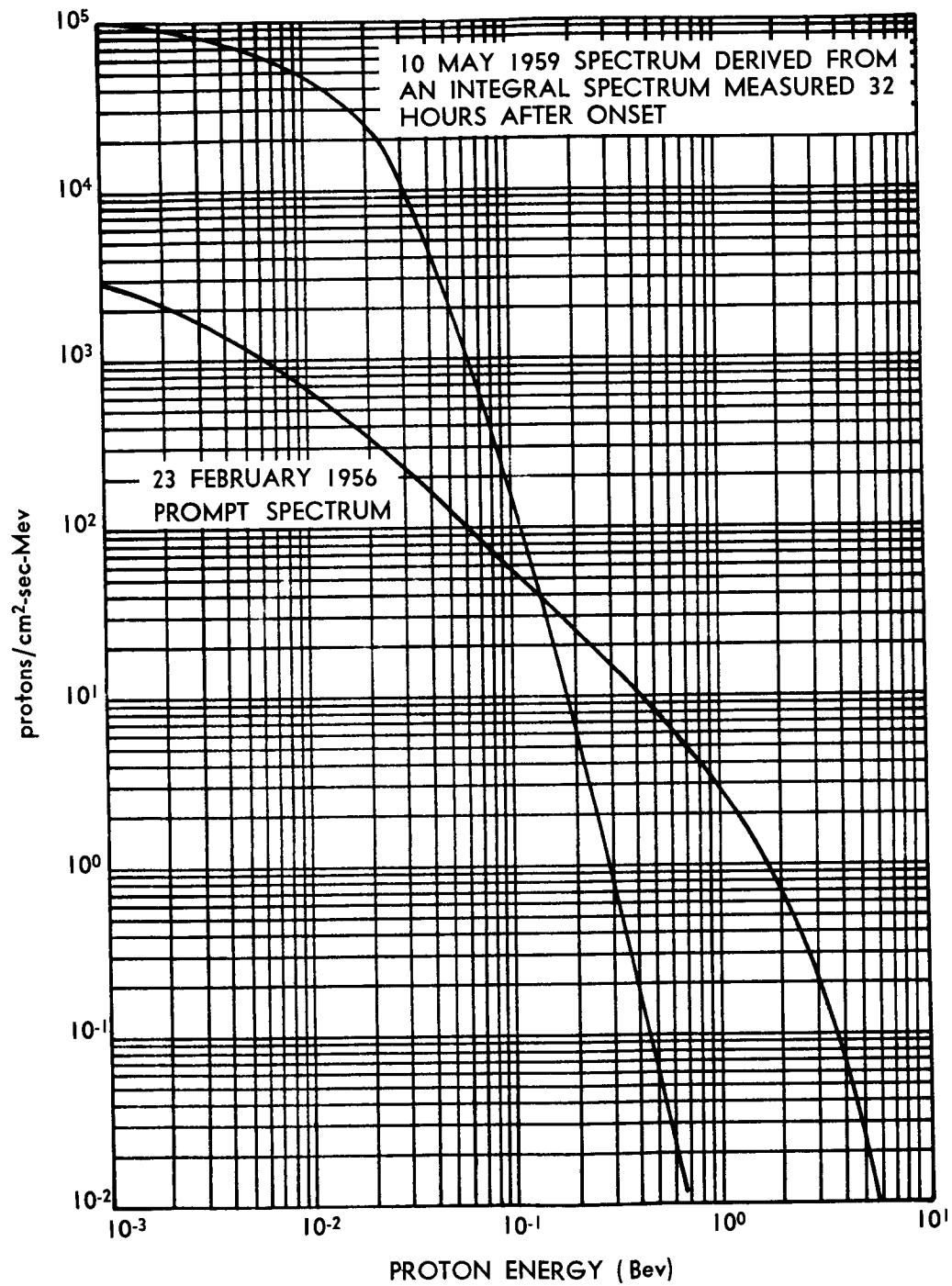
FIGURE 4.1. DIFFERENTIAL SOLAR-FLARE SPECTRA

2. σ_e is the nuclear elastic scattering cross section, or diffraction scattering cross section (neglecting coulomb scattering for protons). It includes all contributions for which the energy of the scattered particle is equal to that of the incident particle in the C. M. system.

3. σ_{ne} is the nonelastic, absorption, inelastic, or reaction cross section. These terms are used synonomously in the literature. $\sigma_{ne} = \sigma_t - \sigma_e$ includes all nonelastic processes.

4.2.2 Total and Nonelastic Cross Sections

The total and nonelastic cross sections obtained from the literature are given in Tables IV and V, respectively, for both neutrons and protons with energies above 25 Mev. Values for neutrons below this energy are given in BNL 325 (Ref. 33) and are not included here. An excellent source of measured total neutron cross sections between 16 and 118 Mev is given in Reference 34, where the values are tabulated for H, C, Al, Cu, Cd, Pb, and U.

Because of the large Rutherford scattering cross section at small angles, total nuclear cross sections for protons are determined by extrapolating the results of "poor" geometry measurements to "good" geometry conditions. Various corrections for coulomb scattering and coulomb-nuclear interference are made in some cases. This method becomes increasingly difficult as the atomic number (Z) of the target nuclide increases. Therefore, measurements of total nuclear proton cross sections do not exist for elements with atomic numbers above 29 (copper).

75

TABLE IV

TOTAL CROSS SECTIONS

σ_t (mb)

Energy (Mev)	Ref.	H*	D	Li	Be	C	N	O	Al
					Neutron				
42	36	203 ± 7	289 ± 13	684 ± 11	853 ± 10	1089 ± 11	1220 ± 25	1358 ± 12	1782 ± 20
96	37			294	431	505 ± 8			1025 ± 17
270	38,39	38 ± 1.5	57 ± 3		229 ± 3	288 ± 3		372 ± 7	555 ± 8
280	38,40	33 ± 3	49 ± 5		225 ±	279 ± 4		380 ± 8	566 ± 18
350	38	35.6+0.7	58.9 ± 1			285.3+1.6		366 ± 3	565 +4.5
380	38	34 ± 2	57 +2.5			286 ± 2		376 ± 6	582 ± 8
400	41	33 ± 1				298 ± 3			
410	38,42	33.7+1.3	62.0+ 4		231 ± 4	297 ± 3		378 ± 5	587 ± 7
500	38					306			
590	38					320			
630	38					340			
765±30	43	34.4+1.6	68.8+2.8	221.2+4.7		342.1+3.7		460.7+6.0	660.2+7.3
					Proton				
134	44				304 ± 5	353 ± 7	411 ± 15	493 ± 10	592 +10
138	44					396 ± 4		395 ± 8	580 +16
208	45,46	36.5+4	61.0+4		247 ± 4	292 ± 6		379 ± 10	201**
315	45,46	32.5+4	56.8+5		229 ± 6	98+**			
340	47								
408	45,48	24.0+1	55.6+2.2	194 ± 8	242 ± 6	285 ± 4		406 ± 3	
860	49,46				316 ± 16	405 ± 23			750 +50
900	50					392 ± 24			823 +30

* See Reference 35 for complete compilation of hydrogen cross sections.

** Total cross section for elastic scattering (value for Ag, σ = 884 mb, not given in Table IV).

76

TABLE IV (Cont'd.)

Energy (Mev)	S	Cl	Fe	Cu	Cd	Sn	Sb	Pb	Th	U
Neutron										
42	1974±30	2110±40	2441±21	2540±19		3251±23		4440±50	5030±70	5120±70
96				2063±26				4666±50		5070±60
270				1145±15		1870±30		2840±30		
280				1190±20		1830±30		2890±30		
350				1138±9		1887±15		2828±14		
380				1170±30		1880±40		2810±50		
400				1190±15	1840±30			2880±40	3230±50	3260±50
410	672±9	742±9	1073±12	1187±14	1848±21			2890±30	3210±40	3230±40
500										
590										
630										
765±30				1310±24			2149±74	3106±45		
Proton										
134	680±20	740±20								
138	686±18	740±20								
208										
315										
340				515**				934**		
408										
860										
900				1530±160						

** Total cross section for elastic scattering.

TABLE V

NONELASTIC CROSS SECTIONS

$$\sigma_{ne}\,(mb)$$

Energy (Mev)	Ref.	Li	Be	C	Al	Ca	Fe	Cu	Ag
Neutron									
55	51			276±25	499±40			1122±14	
81	51			202±21	412±33			840±43	
90	52	155	210	220	440			780	
96±2.5	37			235				815	
105	51			234±8	428±10			773±13	
140	51,53			221±10	418±14			741±13	
300	53,54			203±33	390±23			755±33	
350	53			201±5	395±11			774±18	
1400	53,55			201±13	415±23			674±34	
3600±700	56				430±56			704±140	
Proton									
25±15	57			376±40					995±40
34	58,59			445±35	600±60		902±102		1040±40
54±14	57			355±50					1120±40
61	58,60			200±13			617±40	765±25	1070±40
77	58			220±9	392±25			790±25	
95	58			233±7	445±15			770±30	
113	58			220±6	420±15			780±15	
133	58			224±7	410±15			752±70	
134	46			220±7	426±14				
180	58	149±3	185.5±4.5	212.3±4.8	374±40	524±14	662±19	750±125	
185	58		172±25	204±31	390±10				
230	58		170±17	202±21	410±60			667±75	
240	46,61			199±20	383±35			718±75	
290	46,61		151±15	187±17	416±42			605±50	
305	58			227±12	335±30			850±50	
650	43		170±15	209±22	394			728±17	
860	43			230±20				740±52	
895	43,50				370±29				

TABLE V (Cont'd.)

Energy (Mev)	Cd	In	Sn	Sb	Au	Pb	U
Neutron							
55	1546 ± 17					2337 ± 21	
81	1249 ± 54					1977 ± 30	
90						1790	
96±2.5	1200					1865	2028
105	1198 ± 31					1715 ± 41	
140	1073 ± 19					1704 ± 24	
300						1720 ± 80	
350						1849 ± 42	
1400						1727 ± 45	
3600±700						1930 ± 300	
Proton							
34						1777 ± 155	
61			1930 + 130			1490 ± 77	
77			995 ± 70			1670 ± 60	
95						1740 ± 65	
113						1710 ± 50	
133						1810 ± 85	
134		1165±34				1780 ± 140	
180	1270 ± 100						1880 ± 300
185					1660+50	1550 ± 240	1750 ± 180
230							1820 ± 190
240						1560 ± 170	1110 ± 30
290						1480 ± 150	
305				1153±22		1930 ± 110	
650						1680 ± 40	
860						1660 ± 50	
895							

The nonelastic cross sections for protons are somewhat easier to determine from "poor" geometry measurements at high energies due to the different angular distributions of elastic and nonelastic particles (Ref. 62).

At intermediate energies (a few Mev to about 50 Mev), the angular distributions of elastic and nonelastic particles are not sufficiently distinct to permit the above method of determination, and use is made of the relatively large energy difference between the two types of particles (Ref. 60). However, the ionization losses for these low energies require the use of very thin absorbers, which increases the difficulty of the measurement. Only recently have measurements been reported for energies below 135 Mev. These were at 34 and 61 Mev for C, Al, Fe, Sn, and Pb (Ref. 60), and at 25 ± 15 and 54 ± 14 Mev for C (Ref. 57).

The total and nonelastic cross sections for C, Al and Pb are shown in Figures 4.2 through 4.5. Comparison of these curves reveals that, for corresponding energies and elements, the proton cross sections in the energy range 100-1000 Mev are very nearly equal to those for neutrons. This condition is in agreement with the hypothesis of charge independence. Thus, reasonable estimated values for the total nuclear proton cross sections for high-Z elements may be obtained from the neutron values.

The nonelastic cross sections are very nearly constant in the energy range 100-1000 Mev. The optical model for nuclear cross sections expresses the nonelastic cross sections by the formula of Fernbach, Serber and Taylor (Ref. 68) in the form
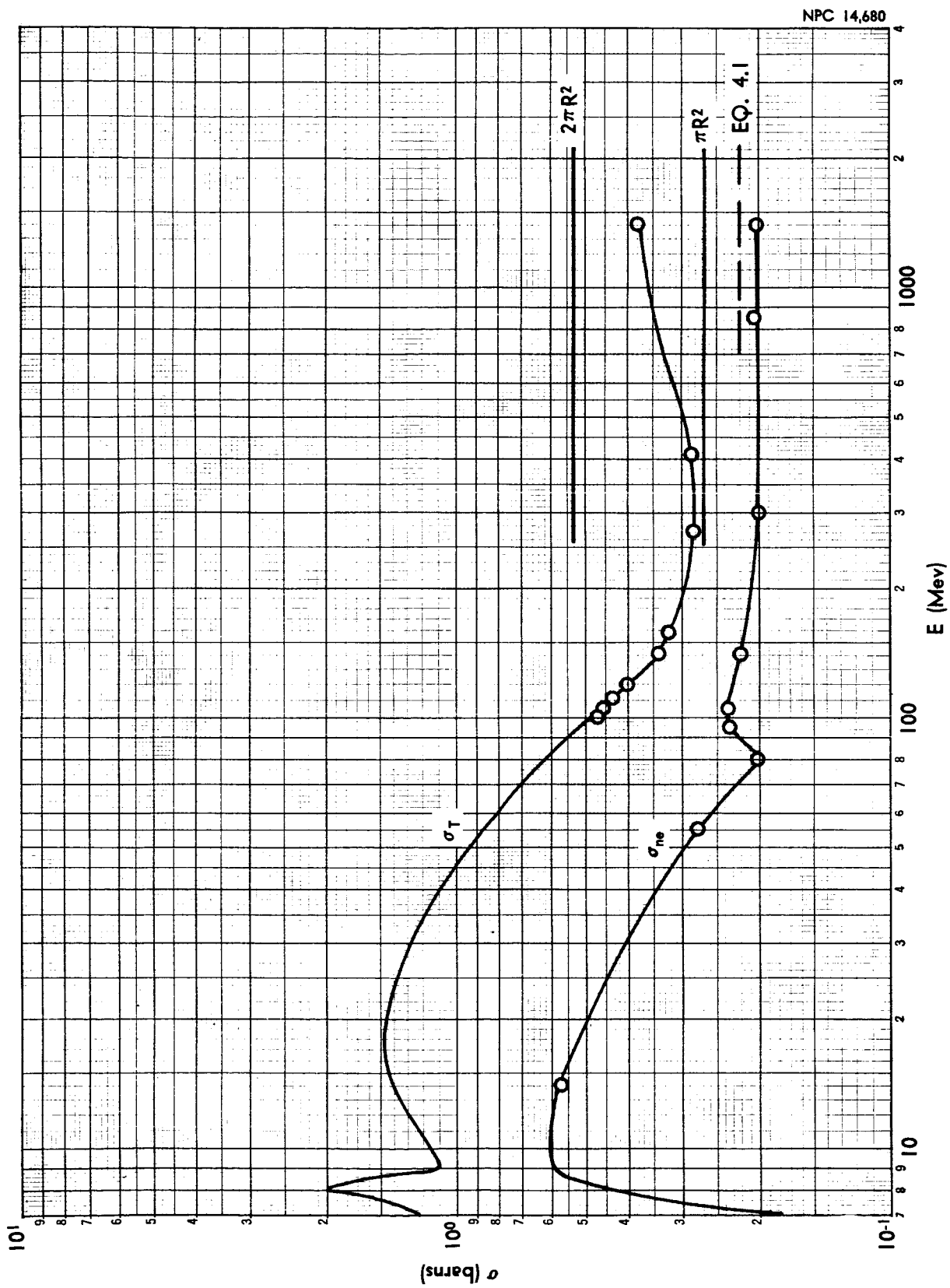
FIGURE 4.2. NEUTRON CROSS SECTIONS FOR CARBON

81
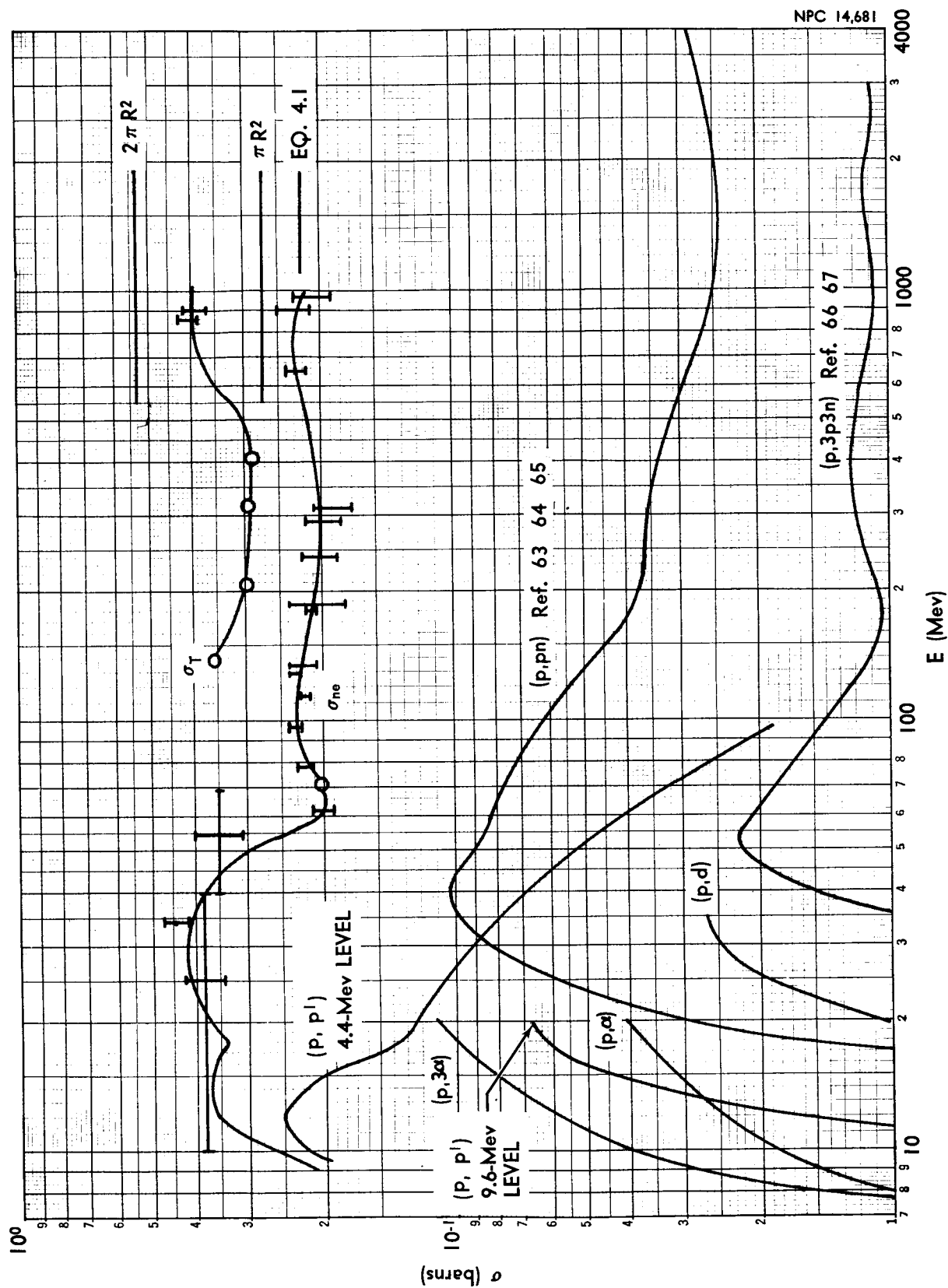
FIGURE 4.3. PROTON CROSS SECTIONS FOR CARBON
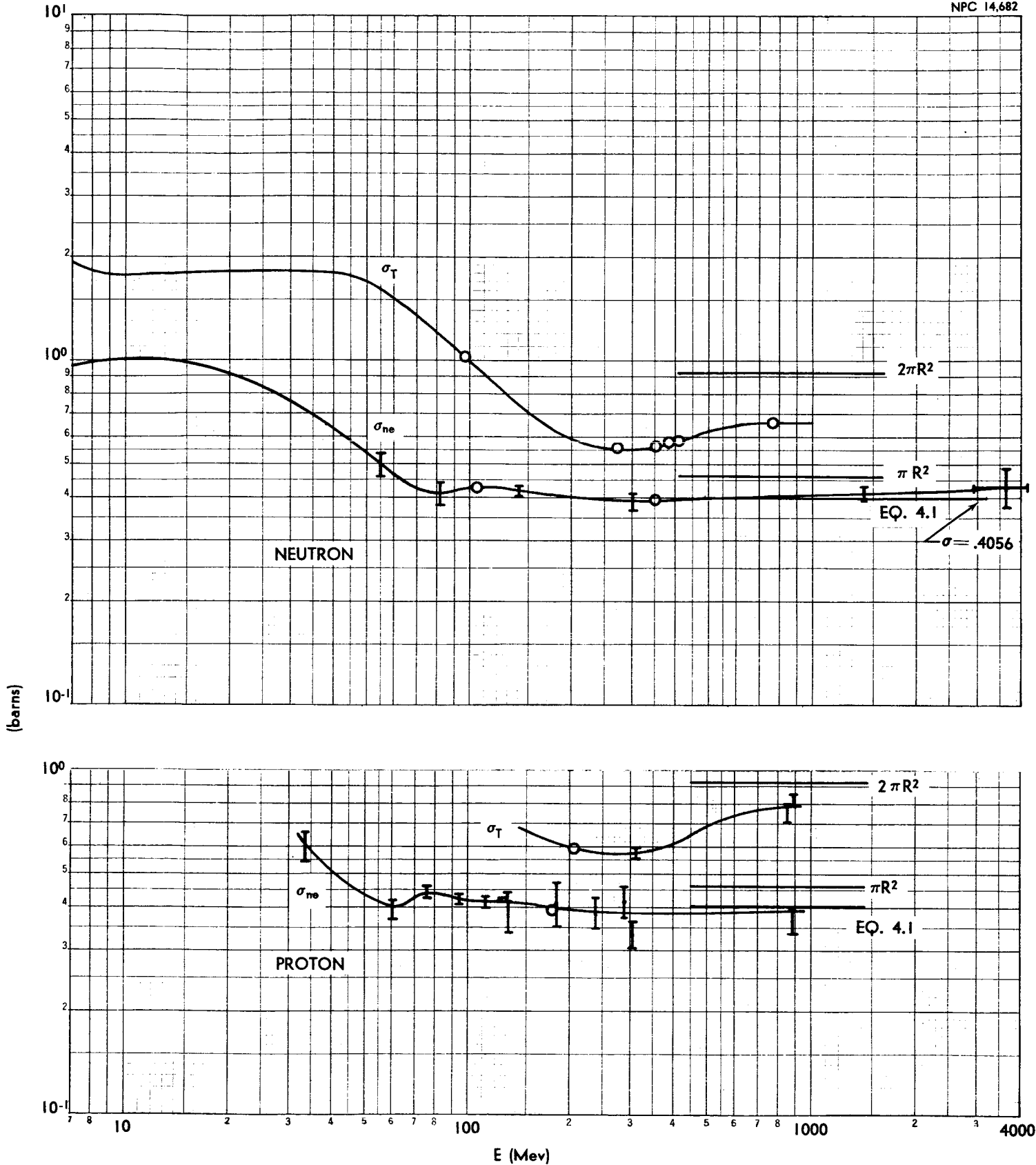
FIGURE 4.4. NEUTRON AND PROTON CROSS SECTIONS FOR ALUMINUM
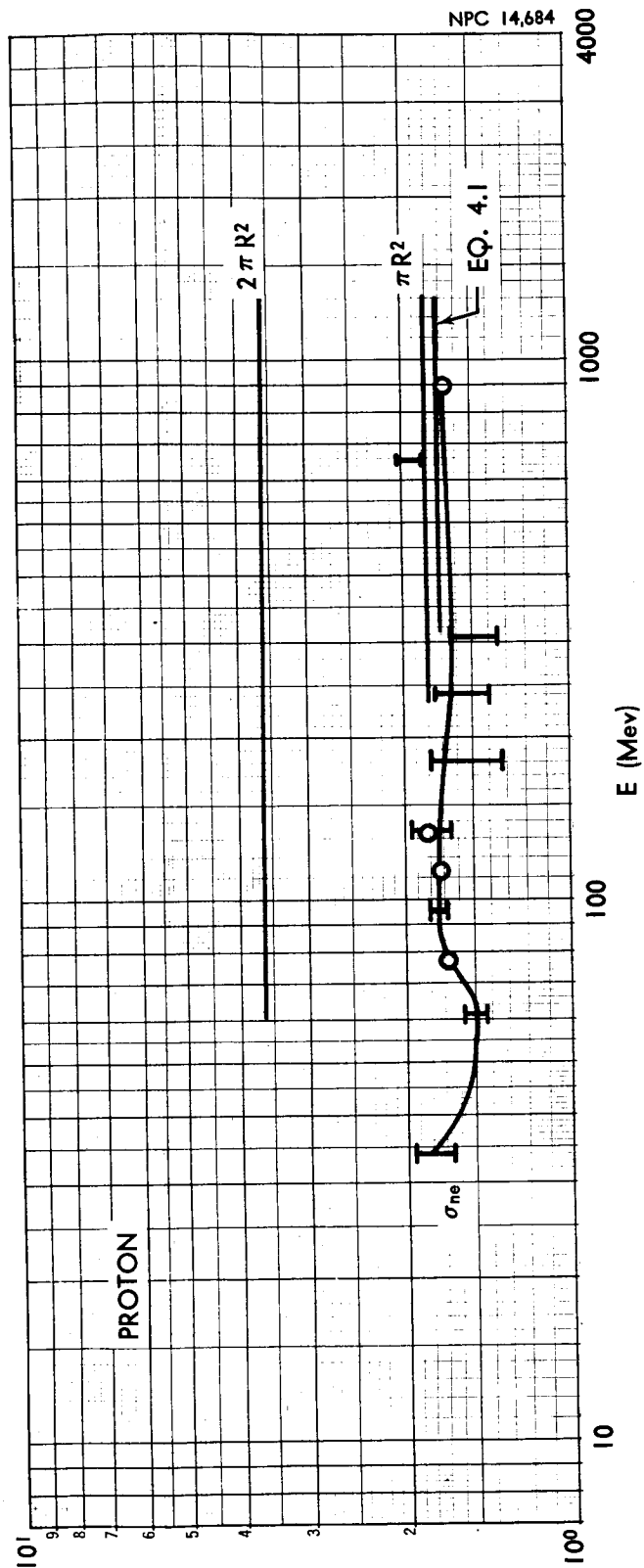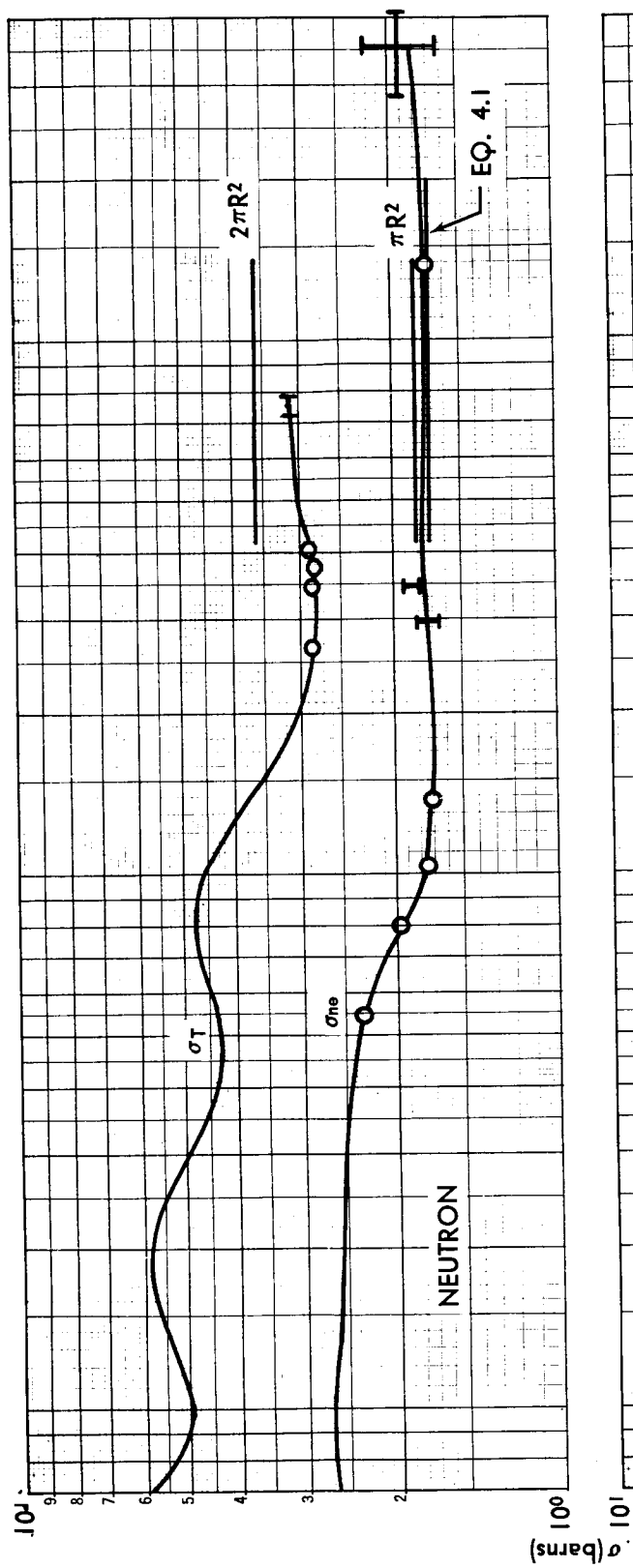
FIGURE 4.5. NEUTRON AND PROTON CROSS SECTIONS FOR LEAD

$$\sigma_{ne} = \pi R^2 \left[1 - \frac{1-(1+2KR)e^{-2KR}}{2K^2R^2} \right], \qquad (4.1)$$

where $R = r_0 A^{1/3}$ is the radius of the target nucleus with mass number A, and K^{-1} is the mean free path in nuclear matter. A very good fit to the average experimental data in the region 200-1000 Mev is obtained for the values $r_0 = 1.28 \times 10^{-13}$ cm and $K = 5 \times 10^{12}$ cm^{-1}. The theoretical and average experimental values are shown in Figure 4.6. A simpler expression which also fits this data reasonably well is given by

$$\sigma_{ne} = 0.034A^{0.737} \text{ (barns)} \qquad (4.2)$$

Theoretically, the total cross section, K, in nuclear matter for a uniform density of particles within the nucleus is given (Ref. 68) by

$$K = \sigma A / \frac{4}{3}\pi R^3, \qquad (4.3)$$

where σ is the average cross section per nucleon within the nucleus and

$$\sigma = A^{-1} \left[Z\bar{\sigma}_{np} + (A-Z)\bar{\sigma}_{nn} \right] \text{ for neutrons}$$

$$\sigma = A^{-1} \left[Z\bar{\sigma}_{pp} + (A-Z)\bar{\sigma}_{pn} \right] \text{ for protons,} \qquad (4.4)$$

where $\bar{\sigma}_{np}$, etc. are the "effective" cross sections within the nucleus. The theory of charge independence predicts $\sigma_{np} = \sigma_{pn}$ and $\sigma_{nn} = \sigma_{pp}$. This equality is supported by experiment (Ref. 35).

σ_{ne} (barns)

MASS NUMBER, A

O MEASURED
X EQUATION 4.1

πR^2
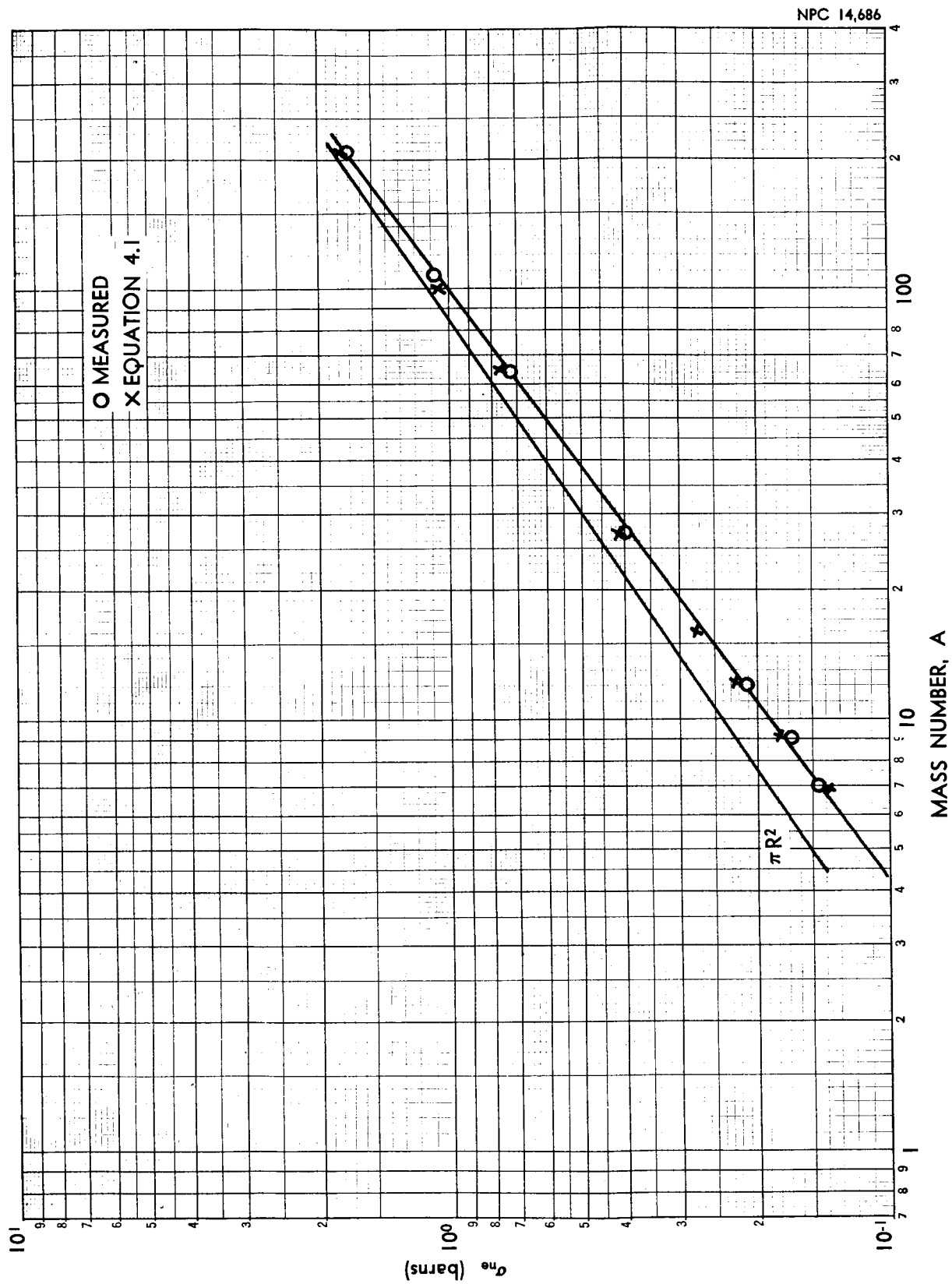
FIGURE 4.6.   VARIATION OF NONELASTIC CROSS SECTIONS WITH MASS NUMBER

The cross sections such as $\overline{\sigma}_{np}$ are not the free nucleon-nucleon cross section, however, because of the effect of the Pauli exclusion principle, which prevents small-momentum transfers, and the momentum distribution of nucleons within the nucleus modifies these cross sections (Ref. 46). A rough estimate of the effective cross sections is given by an expression obtained by Goldberger (Ref. 69):

$$\overline{\sigma}_{xy} = \sigma_{xy(free)} \left[1 - \frac{28}{E} \right] , \quad E > 40 \text{ Mev.} \tag{4.5}$$

Determination of K values from these equations, however, does not always agree with those obtained from measurements using the optical model equation (Eq. 4.1).

The total nuclear cross sections for various elements have very similar energy variation for energies greater than 10 Mev. There is a rapid decrease in the magnitude of the cross sections from 10 to 150 or 200 Mev. This is followed by a region up to about 400 Mev where the cross section remains relatively constant. The cross section then increases slightly to a constant value, as shown by measurements within the range 800-1400 Mev. This increase is assumed to be associated with the threshold for π-meson production in nucleon-nucleon collisions - approximately 300 Mev (Ref. 46). If the struck nucleus can be approximated by a "black disc", quantum mechanics predicts a total cross section at high energies of twice the geometrical cross section ($\sigma_e = \sigma_{ne} = \pi R^2$) (Ref. 31). Using the most widely accepted value for r_o of 1.28 x 10^{-13}cm, $2\pi R^2 = 0.103A^{2/3}$ barns. This value is also shown in Figures 4.2

through 4.5. Since the mean free path in nuclear matter, K^{-1}, is not zero, the nucleus is partially transparent to the incoming nucleon, which is evident from the figures. This transparency decreases with increasing mass number or nuclear radius and is relatively small for lead.

The various components of the nonelastic cross section for protons on carbon are shown in Figure 4.3. The curves labeled $(p,3\alpha)$, (p,α), (p,pn), (p,d), $(p,p'-9.6$ Mev), and $(p,p'-4.4$ Mev) were taken from Reference 57. The dashed portion of the $(p,p' - 4.4$ Mev) curve is an extension of the data of Reference 57 to the value at 96 Mev, obtained from the angular distribution measurements of Strauch and Titus (Ref. 70) extrapolated to 0°.

4.3 Angular Distributions of Scattered and Nonelastic Particles

4.3.1 Elastic Scattering Angular Distributions

The angular distribution of elastically scattered nucleons for high energies is highly peaked at small angles. For this reason there is very little energy loss or change in direction incurred by the scattered nucleons. A fairly good approximation to the angular distribution at high energies is given by the expression

$$\frac{d\sigma}{d\Omega} \propto e^{-\alpha(1-\mu_L)} , \qquad (4.6)$$

where μ_L is the cosine of the scattering angle in the laboratory system and α is an energy-dependent parameter obtained from experimental data. This expression provides a better fit for the

neutron angular distribution than for the proton data which is complicated by coulomb scattering and coulomb-nuclear interference effects at angles of a few degrees. The coulomb scattering at high energies is so highly peaked that it may safely be neglected in shielding calculations. The angular distributions for 180-Mev protons (Refs. 71 and 72) and 155-Mev neutrons (Ref. 73) elastic-ally scattered by carbon (Fig. 4.7) are typical of the measured data. The curves derived from Equation 4.6 do not agree with the experimental data for large scattering angles; however, 96% of the nuclear scattering cross section is included in the angular regions in which results from Equation 4.6 do agree with the measured values.

The energy dependence of the parameter α (Eq. 4.6) is shown in Figure 4.8 for C, Al, and Pb. The rate at which $\frac{d\sigma}{d\Omega}$ decreases with angle, increases rapidly as the mass number of the target nucleus and energy of the incident particle increases. The varia-tion of α with energy may be expressed by

$$\alpha(E) = \beta E^{\gamma}, \quad (E \text{ in Mev}) \tag{4.7}$$

where the values of β and γ for C, Al, and Pb are given in Table VI.

TABLE VI

Angular Distribution Parameters

Parameter	C	Al	Pb
β	1.81	1.53	2.56
γ	0.656	0.788	0.940
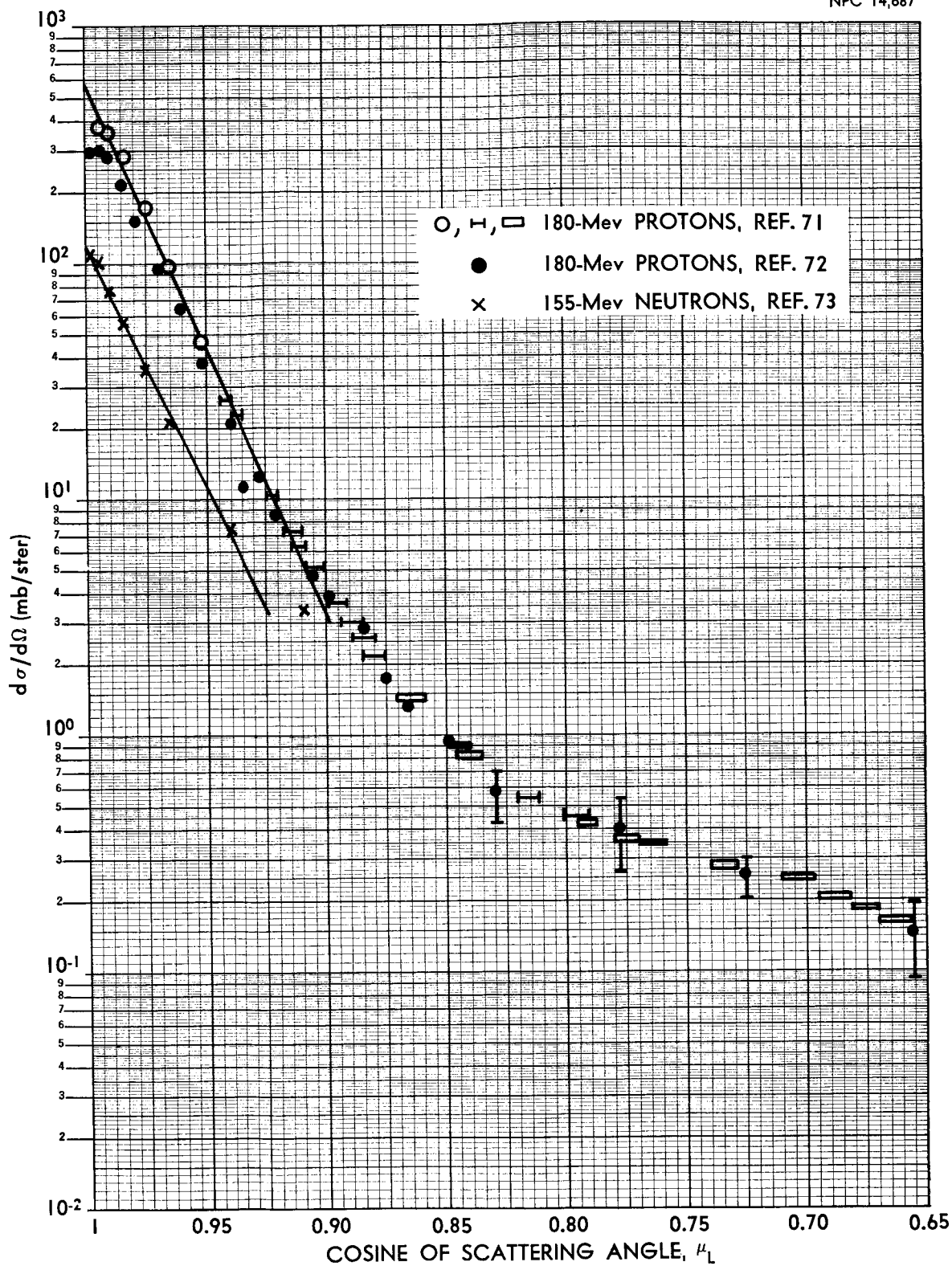
FIGURE 4.7. NEUTRON AND PROTON ELASTIC SCATTERING ANGULAR DISTRIBUTION FOR CARBON
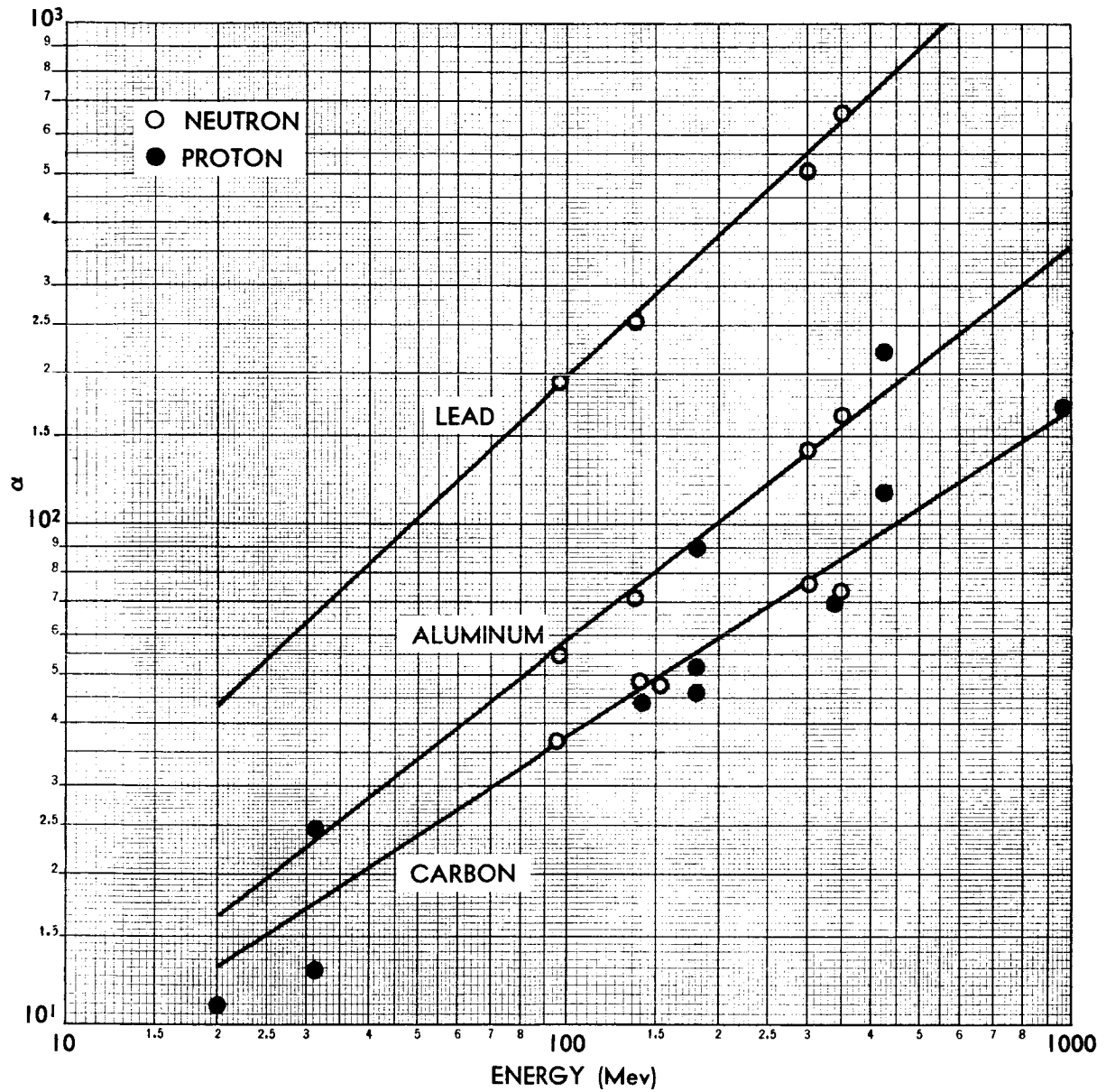
FIGURE 4.8. ENERGY DEPENDENCE OF THE ANGULAR DISTRIBUTION PARAMETER α

91

The approximate nature of these parameters is apparent from Figures 4.7 and 4.8. However, the energy loss from elastic scattering at high energies is negligible and Equation 4.7 should provide a reasonable approximation for the small, but significant, angular deflection.

4.3.2 Nonelastic Angular Distributions

Very little data exist for the angular distribution of non-elastic particles at high energies. At low energies (10 Mev) the theory of compound nucleus formation and subsequent evaporation of particles (Ref. 74) has been very successful. This theory predicts the angular distribution of the emitted particles to be symmetric about 90° in the C. M. system, and that the nature of the particle emissions be independent of the mode of formation.

Experiments designed to measure the angular dependence and energy spectra of nucleons emitted from 30- and 190-Mev proton bombardment have shown that the angular distributions of emitted particles of highest energy were not symmetric about 90° but were strongly peaked forward (Refs. 74, 75, 76, and 77). Also, the type of emitted particle was found to depend on the mode of formation (incident protons resulting in a preferential emission of protons, etc.). The high-energy emission was also found to be greater than predicted (Ref. 76).

Contradictions such as these led to the direct-interaction concept, in which the incident high-energy particle interacts with individual nucleons or groups of nucleons in the target

nucleus which in turn collide with other nucleons (collision cascade). Some of the struck nucleons will acquire sufficient energy to leave the nucleus directly, predominantly in the forward direction.

These particles are called cascade nucleons and their emission leaves the residual nucleus in a highly excited state. The cascade stage takes place in approximately 10^{-22} sec and is followed by the comparatively slower evaporation phase (Ref. 77). Emitted nonelastic particles are therefore designated as either cascade or evaporation.

4.3.2.1 <u>Cascade Nucleons.</u> The angular distributions of protons produced by 90-Mev neutrons bombarding C, Cu, and Pb have been measured (Ref. 52) and are shown in Figures 4.9 through 4.12 along with the angular distribution of neutrons produced by 95-Mev protons incident on C, Al, Cu, and Pb (Ref. 78).

The angular distributions of emitted protons were measured out to only 45°; however, the curves have been extended to 135°, using the measured angular distribution of all emitted charged particles. This extrapolation is justified by the high percentage of protons per-average-emitted charged particle ($\sim 85\%$) and the agreement in the shape of the angular distributions out to 45°.

The measured angular distribution of emitted neutrons from 95-Mev proton bombardment extends only to 28°. However, the angular distribution of emitted cascade neutrons and protons are expected to be very similar at high energies and, in addition, should be independent of the nature of the bombarding particle (neutron or proton).
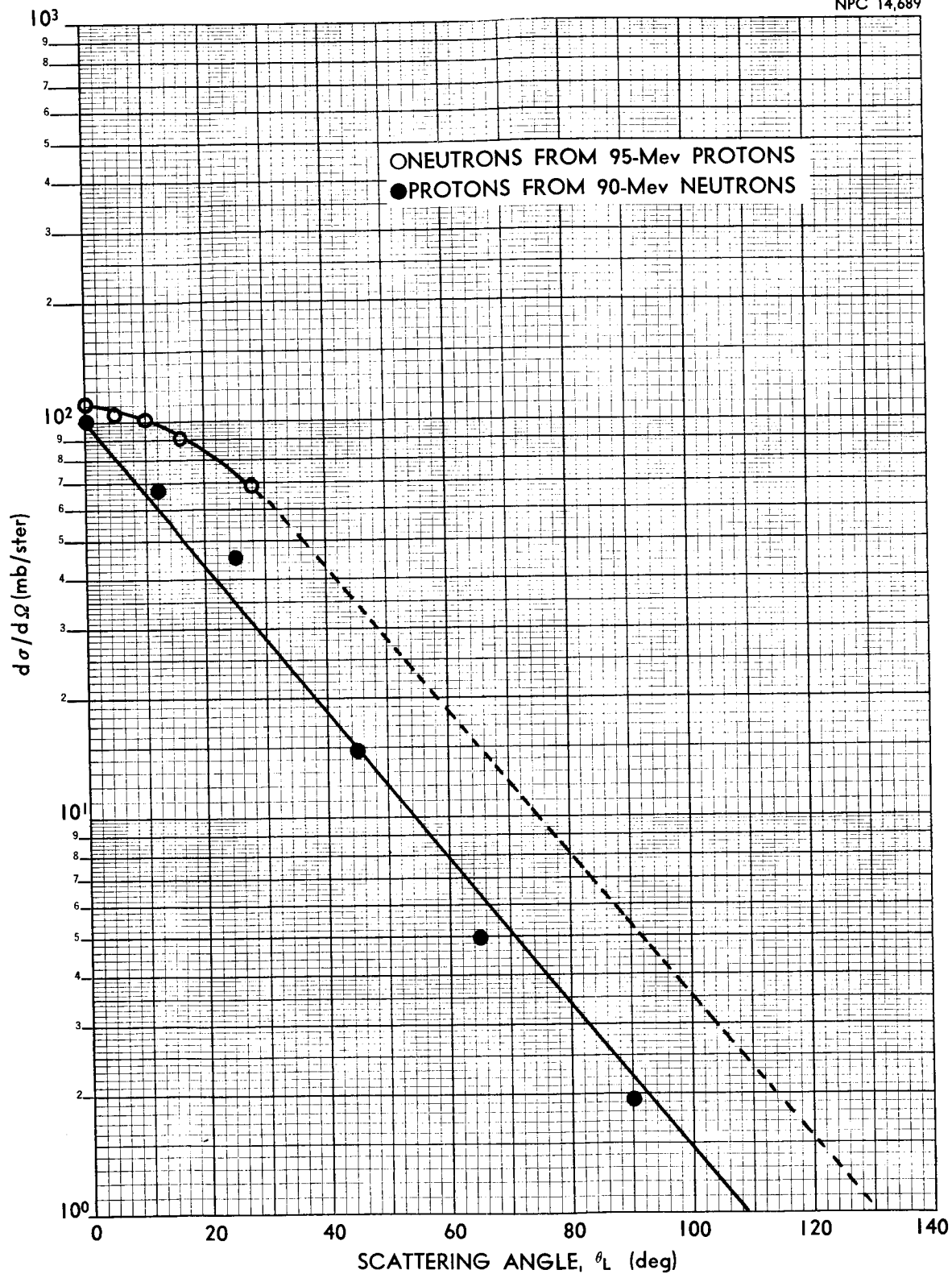
**FIGURE 4.9.   ANGULAR DISTRIBUTIONS FROM 90- AND
95-Mev NEUTRONS INCIDENT ON CARBON**

O NEUTRONS FROM 95-Mev PROTONS
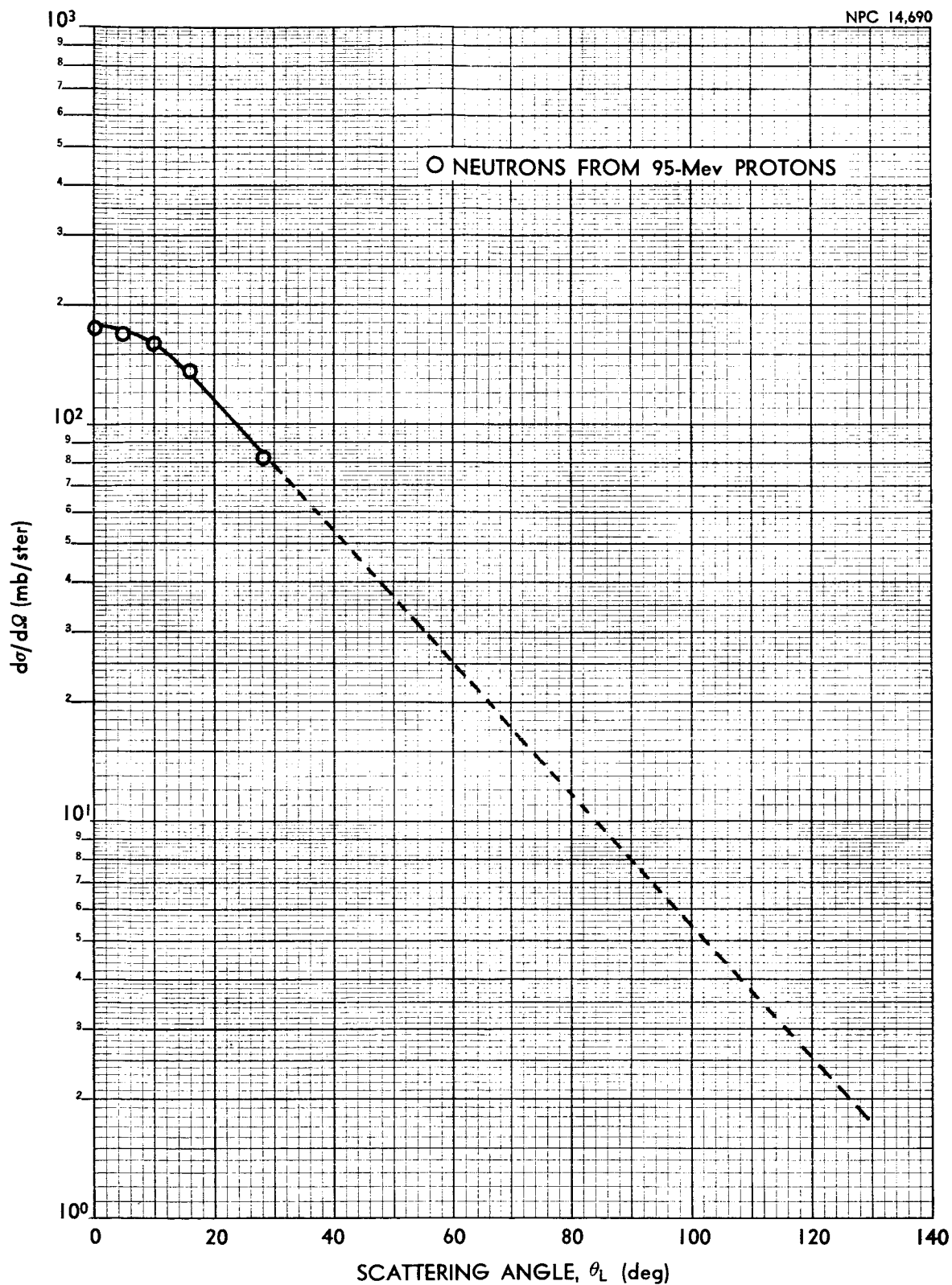
FIGURE 4.10. ANGULAR DISTRIBUTIONS FROM 95-Mev PROTONS INCIDENT ON ALUMINUM
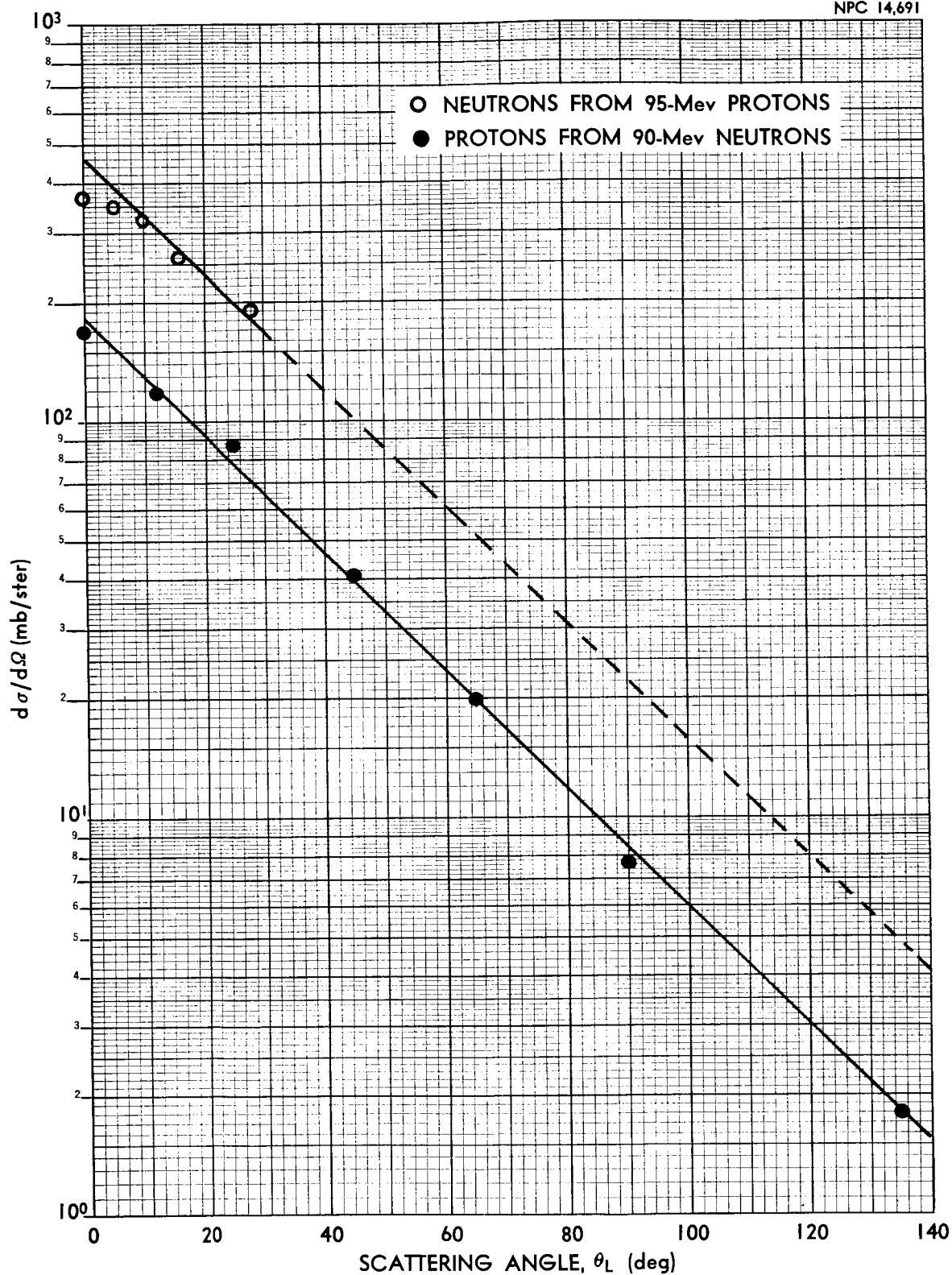
FIGURE 4.11. ANGULAR DISTRIBUTIONS FROM 90- AND 95-Mev NEUTRONS INCIDENT ON COPPER

O NEUTRONS FROM 95-Mev PROTONS
● PROTONS FROM 90-Mev NEUTRONS

SCATTERING ANGLE, θ_L (deg)

$d\sigma/d\Omega$ (mb/ster)
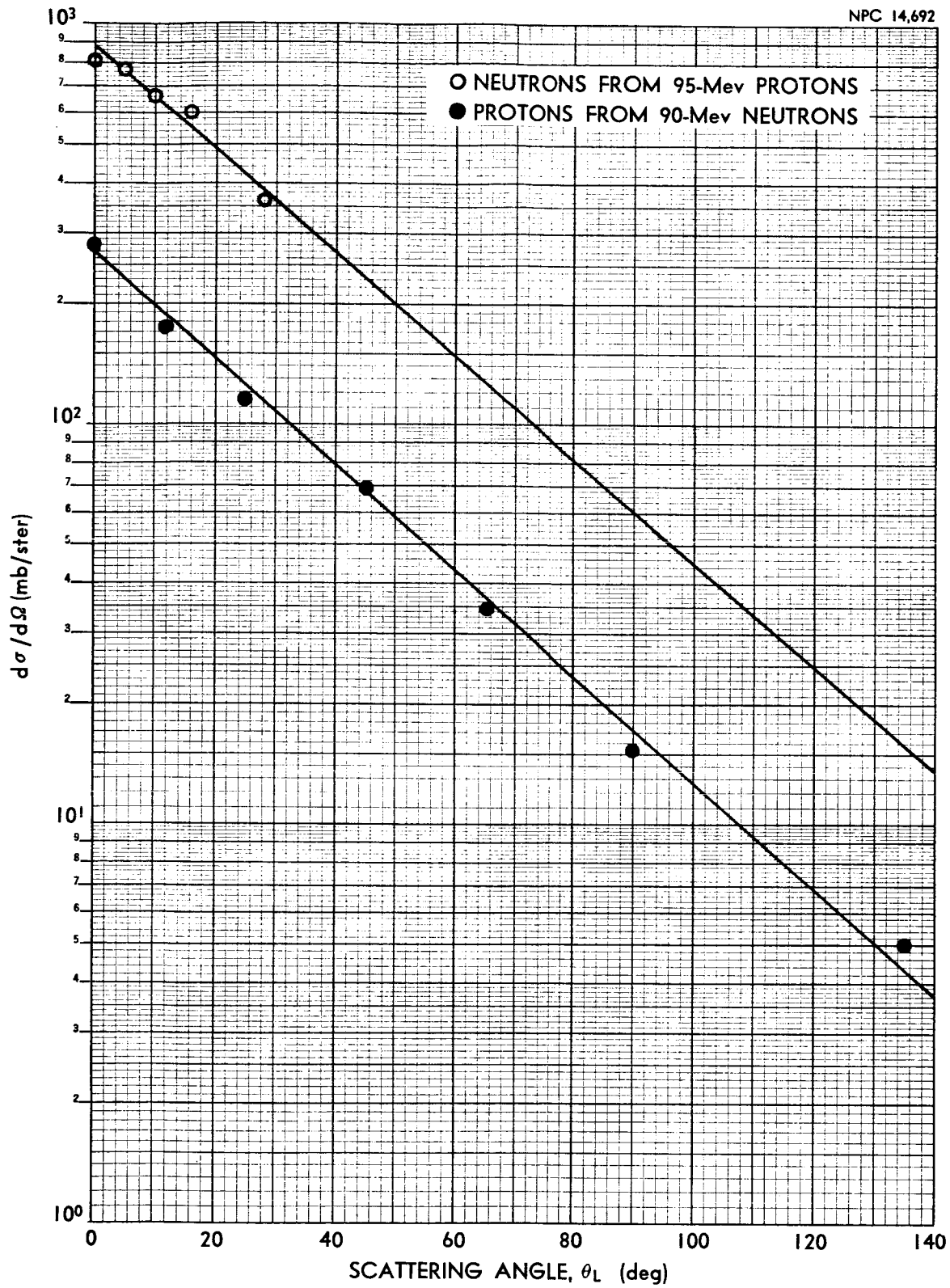
FIGURE 4.12.   ANGULAR DISTRIBUTIONS FROM 90- AND 95-Mev NEUTRONS INCIDENT ON LEAD

The angular distribution of cascade protons emitted from bombardment of Al and U by 460- and 1840-Mev protons are shown in Figure 4.13. These angular distributions were calculated by Metropolis, et al. (Refs. 79 and 80), using a Monte Carlo procedure. The data for Al and U have very nearly the same spectral shape within the energy interval of 30-90 Mev and for E = 90 Mev. Therefore, it appears that the angular distribution of cascade particles is relatively insensitive to mass number at these energies. The experimental data at 95 Mev (Figs. 4.9 through 4.12) show a slightly larger dependence on mass number, with the emitted particles concentrated more at forward angles for the lower mass numbers.

The angular distributions shown in Figure 4.13 indicate a marked dependence on bombarding energy for large angles of emission. However, there is very little difference in shape between the 460- and 1840-Mev results for small angles. Since most of the nucleons are emitted at small angles, the effect of bombarding particle energy is not large, at least above the threshold for meson production ($\sim$300 Mev).

Although mass number and bombarding energy do not effect the angular distributions to a large degree, comparison of the two graphs on Figure 4.13 indicates that the angular distribution is strongly dependent on the energy of emission. The emitted particles with energies near that of the bombarding particle have angular distributions which are highly peaked in the forward direction. For the lower-energy particles (30-90 Mev) the peaking is
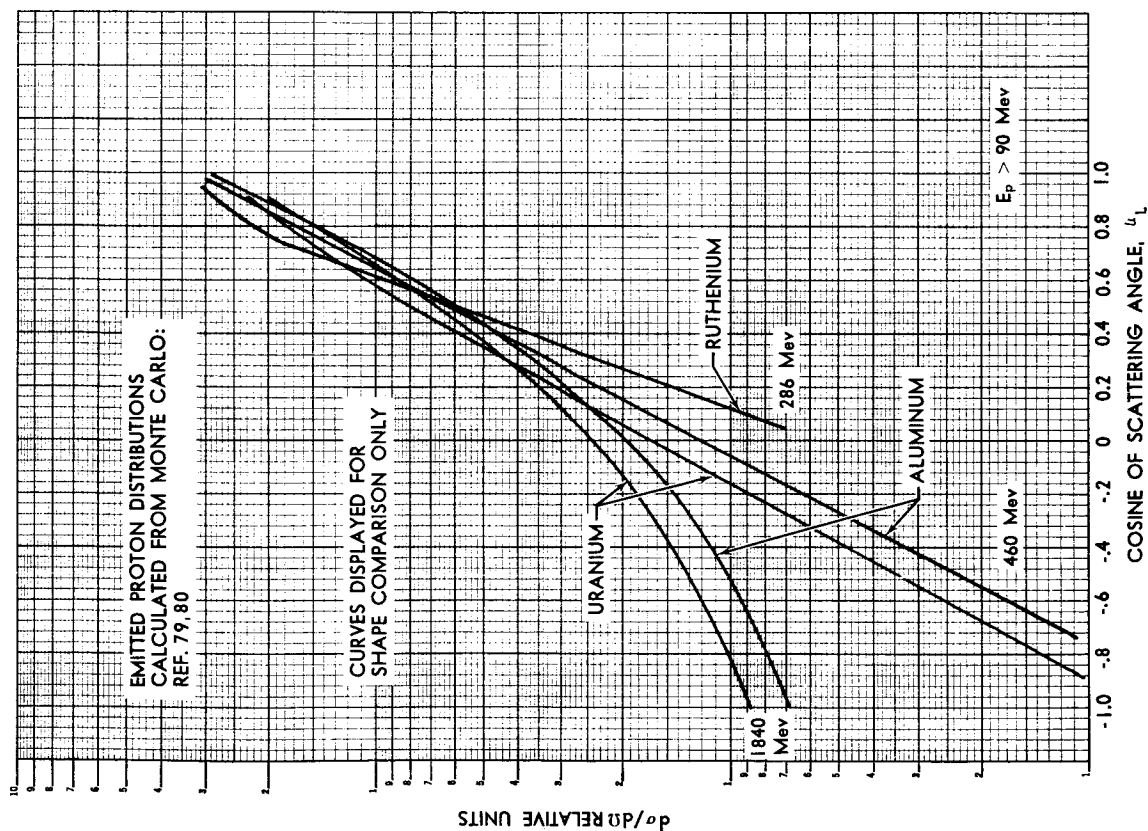
FIGURE 4.13. ANGULAR DISTRIBUTIONS FROM 286-, 460-, and 1840-Mev PROTONS FOR ALUMINUM, RUTHENIUM, AND URANIUM

99
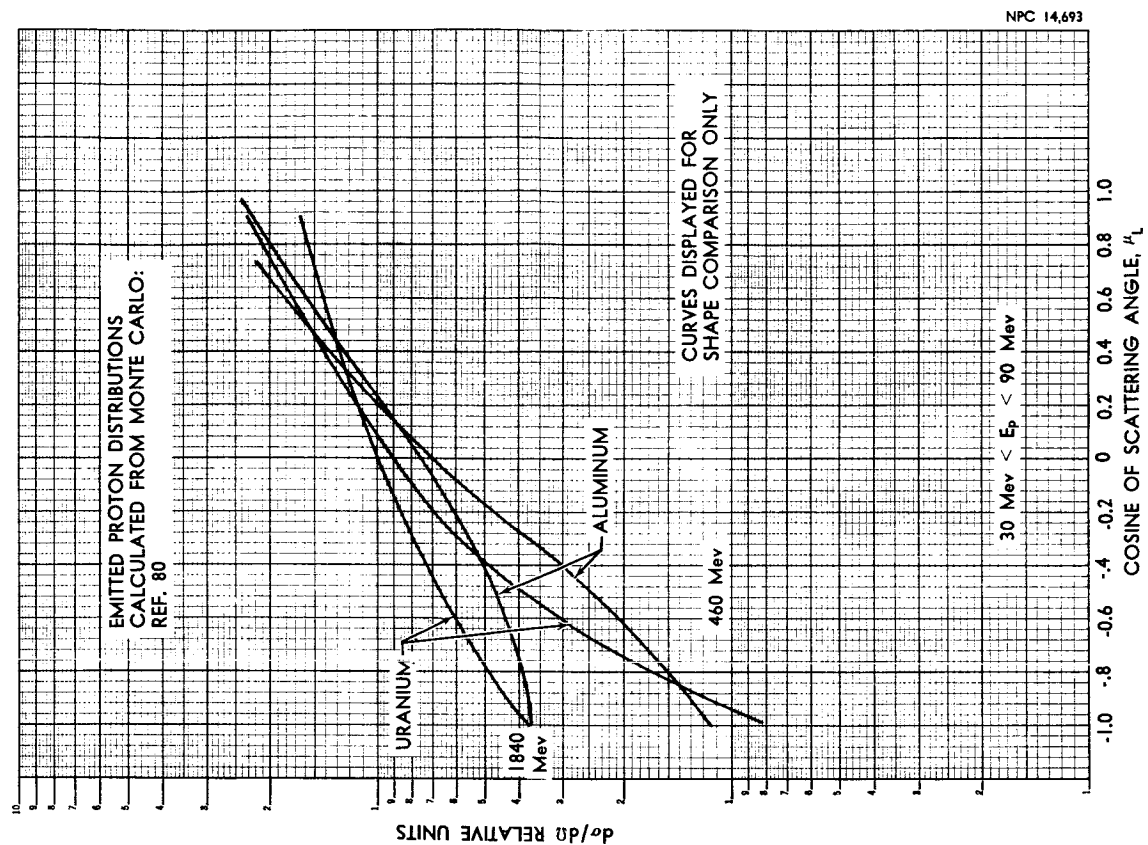
much less pronounced. These results are in qualitative agreement with the measurements for 90-Mev neutrons incident on carbon (Ref. 52), which indicate a steeper angular distribution for emitted protons with energies greater than 35 Mev than that which was found for energies greater than 20 Mev (Fig. 4.14).

The Monte Carlo data giving the angular distribution of cascade protons $(E_p > 90$ Mev) from bombardment of Ru^{100} with 286-Mev protons (Ref. 79) is also shown in Figure 4.13. The angular distribution is slightly more peaked for 286-Mev protons than for the 460- and 1840-Mev bombarding energies (at least from 0° to 90°). The same trend is apparent in Figure 4.14, where the angular distributions (normalized to 1 emitted particle) for all emitted protons with energies greater than approximately 30 Mev are shown for 90-Mev neutrons incident on carbon, and 460- and 1840-Mev protons incident on aluminum. The more rapid decrease with angle of the number of emitted particles for the 90-Mev data is contrary to the direct-interaction concept, since higher-energy particles would be expected to result in more production at the forward angles. However, above approximately 400 Mev, π-meson production in the nuclear collisions becomes important. This production introduces an effective means of energy transfer from the high-energy incident particle to the nucleons within the nucleus (Ref. 80). This increased transfer is a result of the shorter mean free path in nuclear matter for the pion as compared to that of the incident nucleon and the high probability for pion absorption. Actually, several scatterings

100
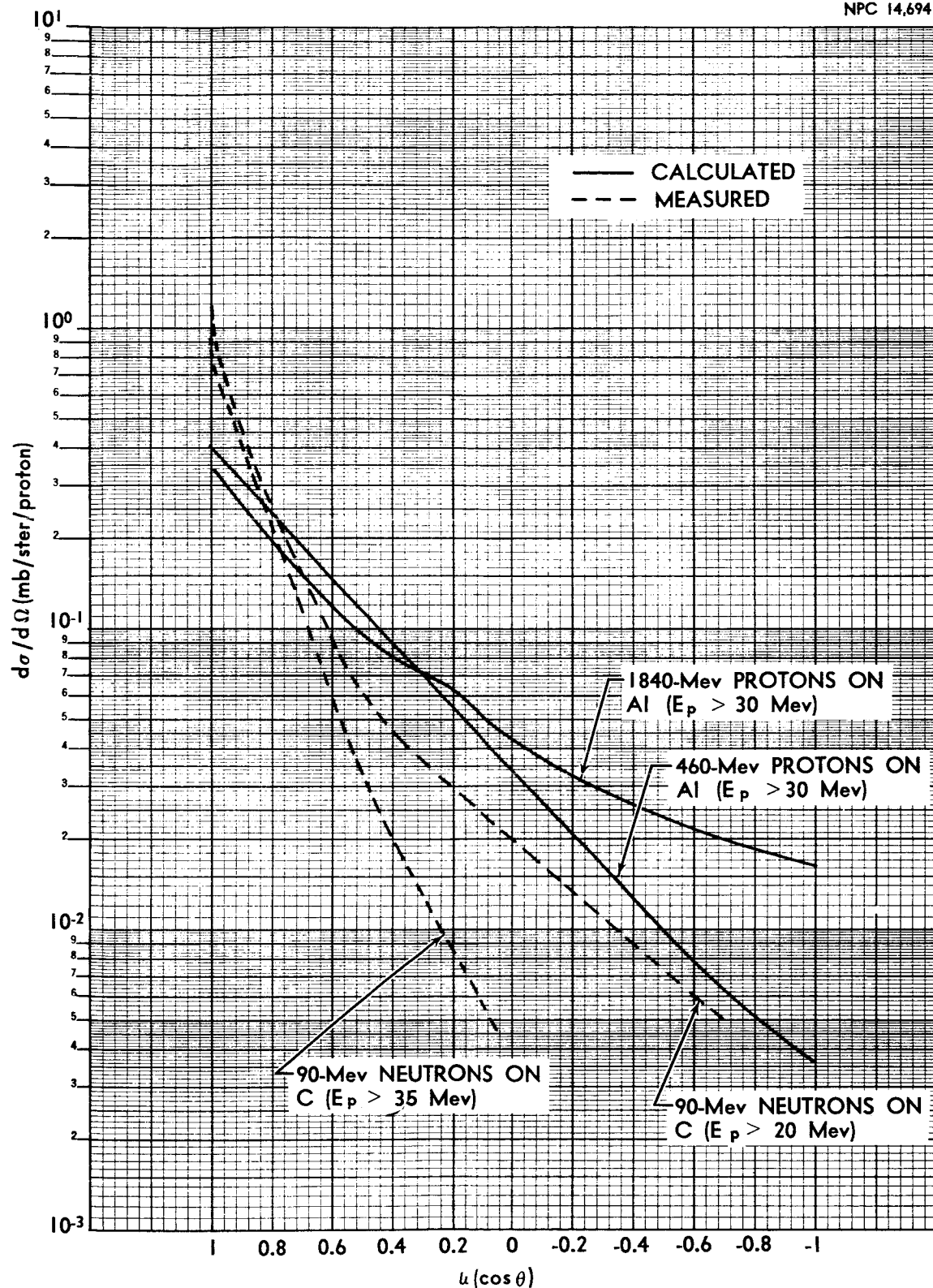
FIGURE 4.14. PROTON ANGULAR DISTRIBUTIONS FROM NEUTRONS AND PROTONS
AT VARIOUS ENERGIES FOR CARBON AND ALUMINUM

may take place before the pion is absorbed, thus increasing the average number of interacting particles (Ref. 80). Because of the larger number of particles and collisions being considered, the angular distribution of the emitted nucleons will be smoothed out somewhat, as can be seen in Figure 4.14.

4.3.2.2 <u>Evaporation Nucleons</u>. The angular distribution of evaporation nucleons has been measured for 190-Mev protons bombarding C, Al, Ni, Ag and Au (Refs. 77, 81). The results were complicated by the appearance of a significant number of cascade particles in the energy range of the evaporation particles that extends up to approximately 20 or 25 Mev. By considering the energy range up to approximately 2 or 3 Mev for neutrons, which includes most of the evaporation particles, the influence of the cascade particles was eliminated and the resultant angular distributions were interpreted as being isotropic in the C.M. system (Ref. 77). A similar conclusion was reached for the evaporation protons (Ref. 81), although the peak in the evaporation energy spectra occurs at higher energies for protons because of the coulomb barrier.

It is necessary to point out here that the C.M. system referred to in the preceding paragraph is not that of the bombarding particle and struck nucleus. The system referred to is that of the residual excited nucleus remaining after the cascade process. Since the cascade particles are emitted in the forward direction preferentially, the average velocity of this "center-of-mass system" in the laboratory system will be much lower than

that of the bombarding particle and struck nucleus. For targets with large mass numbers (e.g., Au, Ag) the angular distributions were approximately isotropic in the laboratory system.

The results of the 31.5-Mev proton bombardment of Be, N, Al, Co, and Ni (Refs. 75, 76) did not indicate an isotropic angular distribution for the emitted particles (neutrons). However, the use of a bubble chamber as a detector prevented measurements from being made for emitted neutron energies below 5 Mev. Thus, most of the evaporation particles were not detected and the angular distributions measured were interpreted as being mostly due to cascade neutrons.

4.4 Average Numbers of Emitted Particles Per Nonelastic Collision

4.4.1 Cascade Nucleons

The bulk of data reported here for the average number of cascade nucleons per nonelastic collision was obtained from the results of the Monte Carlo calculations of Metropolis, et al. (Ref. 79 and 80) and their supplementary data as reported by Lockheed (Ref. 26). Unfortunately, the range of mass numbers investigated begins at 27 (aluminum) and, therefore, does not include carbon, which is of great interest in shielding of space vehicles. However, data for carbon has been obtained by extrapolation and appears to be in reasonable agreement with the few existing experimental values.

The results for C, Al, and Pb are given in Figures 4.15, 4.16, and 4.17, respectively, along with the experimental data. The experimental values were obtained from measured production
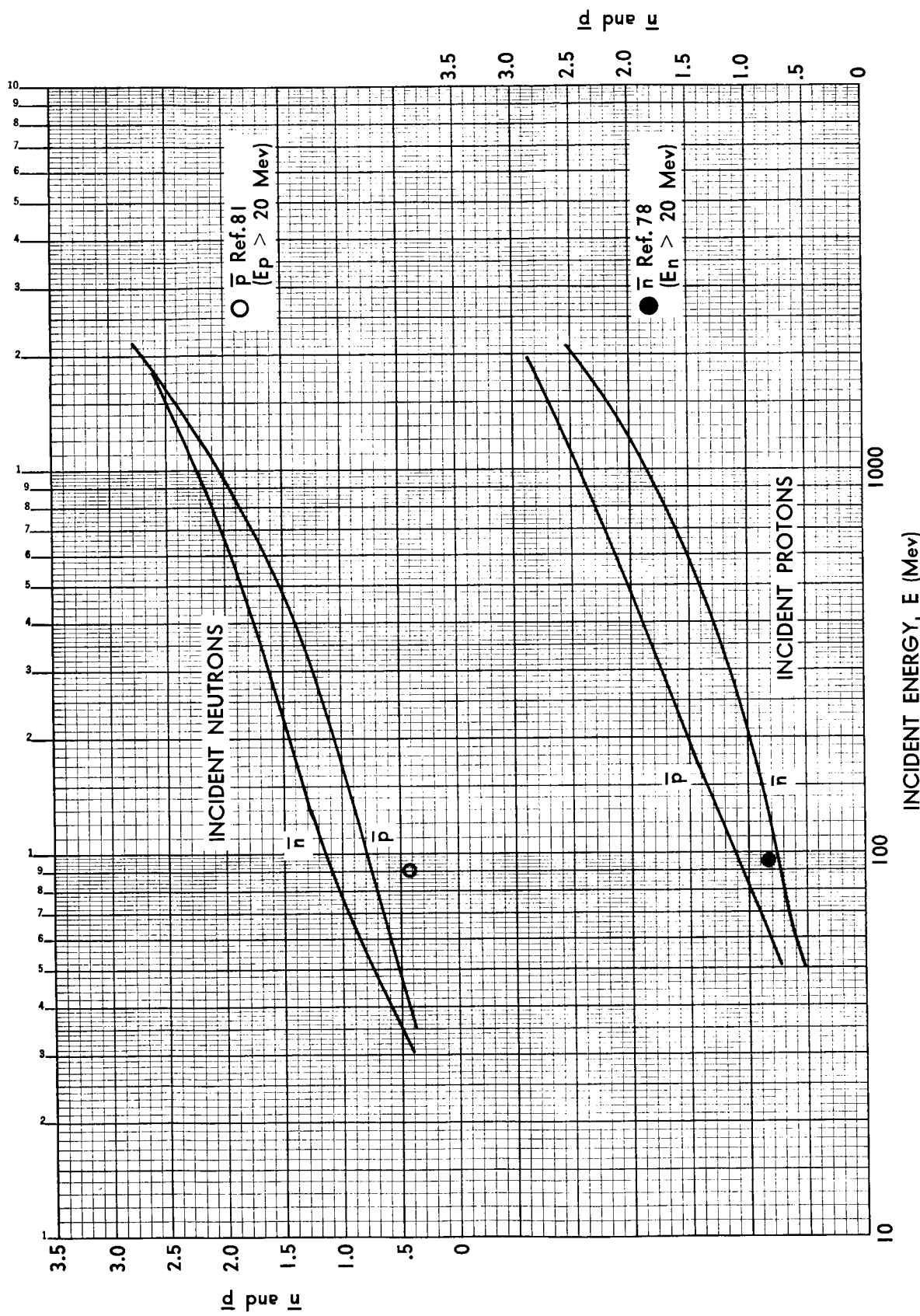
FIGURE 4.15. AVERAGE NUMBER OF CASCADE NEUTRONS AND PROTONS PER NONELASTIC COLLISION IN CARBON
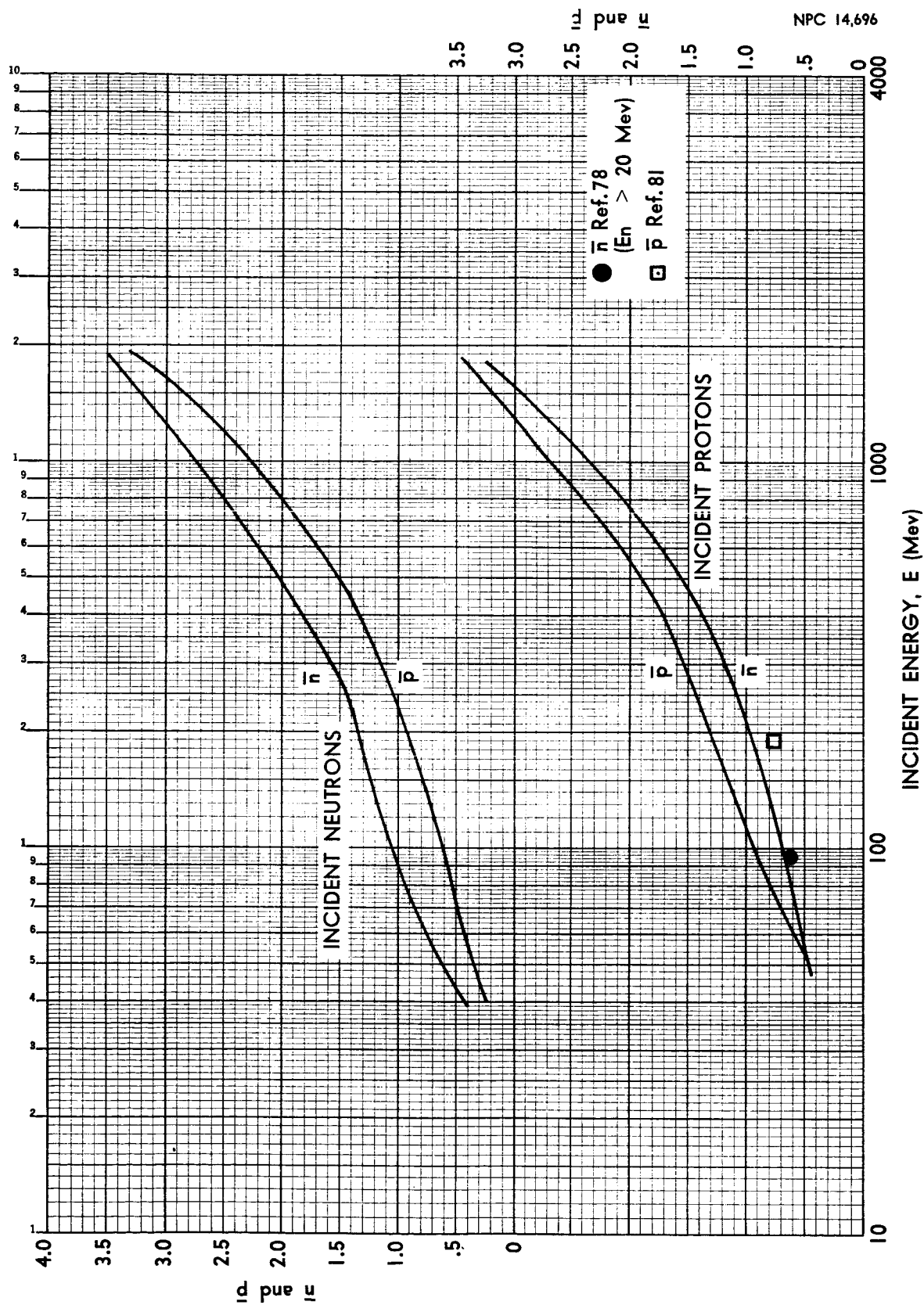
FIGURE 4.16. AVERAGE NUMBER OF CASCADE NEUTRONS AND PROTONS PER NONELASTIC COLLISION IN ALUMINUM

NPC 14,696

105
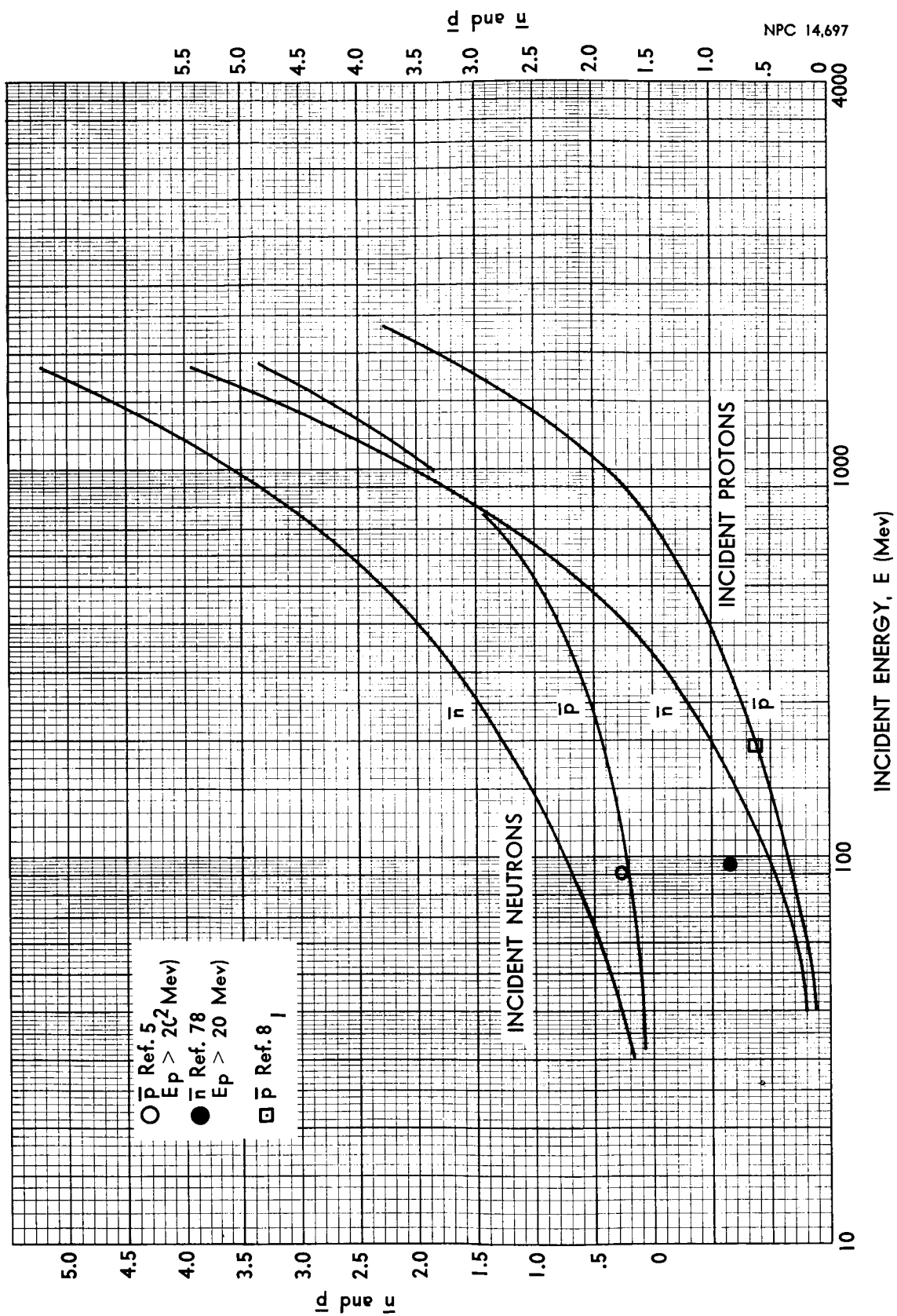
FIGURE 4.17. AVERAGE NUMBER OF CASCADE NEUTRONS AND PROTONS PER NONELASTIC COLLISION IN LEAD

NPC 14,697

INCIDENT ENERGY, E (Mev)

106

cross sections (σ_{prod}) by means of the relation

$$\bar{n} = \frac{\sigma_{prod-n}}{\sigma_{ne}} \, , \tag{4.8}$$

where $\bar{n}$ $(\bar{p},\bar{\alpha},$ etc.) is the average number of neutrons (protons, alpha particles) emitted per nonelastic collision.

The experimental data are given in Tables VII through IX. The average number of cascade protons produced by 190-Mev proton bombardment were obtained from Bailey's data (Ref. 81) by subtracting the production cross sections for evaporation protons from the total production cross sections for emitted protons. The average number of protons per nonelastic collision produced by 90-Mev neutrons was obtained by extending the angular distribution data of Handley and York (Ref. 52) from 45° to 180°, as described in Section 4.5. This same angular distribution at large angles was used in extending the data of Hofmann and Strauch for 95-Mev protons (Ref. 78) from 28° to 180°. Integration of the differential cross sections (Figs. 4.9 through 4.12) resulted in production cross sections from which the average number of particles per nonelastic collision were obtained using Equation 4.8.

The Monte Carlo data was obtained mainly for incident protons, although approximately 1/3 as many neutron problems were run. It was found that the ratio of emitted protons to emitted neutrons was highly dependent on the nature of the incident particle (proton or neutron), particularly for low-mass nuclides.

TABLE VII

CASCADE CHARGED-PARTICLE PRODUCTION BY 90-MEV NEUTRONS

Element	Ref.	σ_{ne} (mb)	$\sigma_{prod} - p$ (mb)	$\bar{p}$	$\sigma_{prod} - d$ (mb)	$\bar{d}$
C	82	220	85.3±9.2	.388±.042	26.1±3.4	.119±.016
C	52	220	93±3	.41±.01	23±3	.10±.01
Cu	52	780	251±10	.32±.01	42±10	.055±.013
Pb	52	1790	439±15	.24±.01	60±15	.034±.008

TABLE VIII

CASCADE NEUTRON PRODUCTION BY 95-MEV PROTONS

Element	σ_{ne} (mb)	σ_{prod} (mb)	$\bar{n}$	Ref.
C	233 ± 7	192	.822	78
Al	420 ± 15	265	.63	78
Cu	790 ± 25	654	.83	78
Pb	1740 ± 65	1460	.84	78

TABLE IX

CASCADE PROTON PRODUCTION BY 190-MEV PROTONS

Element	σ_{ne} (mb)	σ_{prod} (mb)	$\bar{p}$	Ref.
C	230	178	.774	81
Al	410	313	.763	81
Ni	710	415	.585	81
Ag	1100	590	.536	81
Au	1700	1068	.628	81

However, the total number of emitted cascade particles was found
to be almost independent of the nature of the bombarding particle,
especially for the higher bombarding energies. Figures 4.18,
4.19, and 4.20 show the average number of emitted cascade nucleons
as a function of bombarding energy for both incident protons and
neutrons. Additional points for the curves of Figures, 4.15,
4.16, and 4.17 were obtained by plotting the percent of neutrons
and protons emitted as a function of energy for both types of
incident particles (Fig. 4.21) and applying these values to the
curves of Figures 4.18, 4.19, and 4.20. The carbon data have
been extrapolated in all cases.

4.4.2 Evaporation Nucleons

The data reported in this section have been obtained from
the Monte Carlo calculations of Dostrovsky, Rabinowitz, and Bevins
(Ref. 83) and from experimental data. The relationships between
average excitation energy and bombarding energy from Reference 79
were used in the presentation of the results (see Fig. 4.26).
The calculations begin with mass number 64 (copper), therefore
requiring a larger extrapolation than in the case of cascade
emission in order to obtain data for carbon and aluminum. In
addition, the use of average excitation energies instead of a
distribution of excitation energies may introduce significant
errors. However, the results are again in reasonable agreement
with the existing experimental data. The results for C, Al and
Pb are plotted in Figures 4.22, 4.23, and 4.24, as a function
of bombarding energy. The experimental data are also shown in
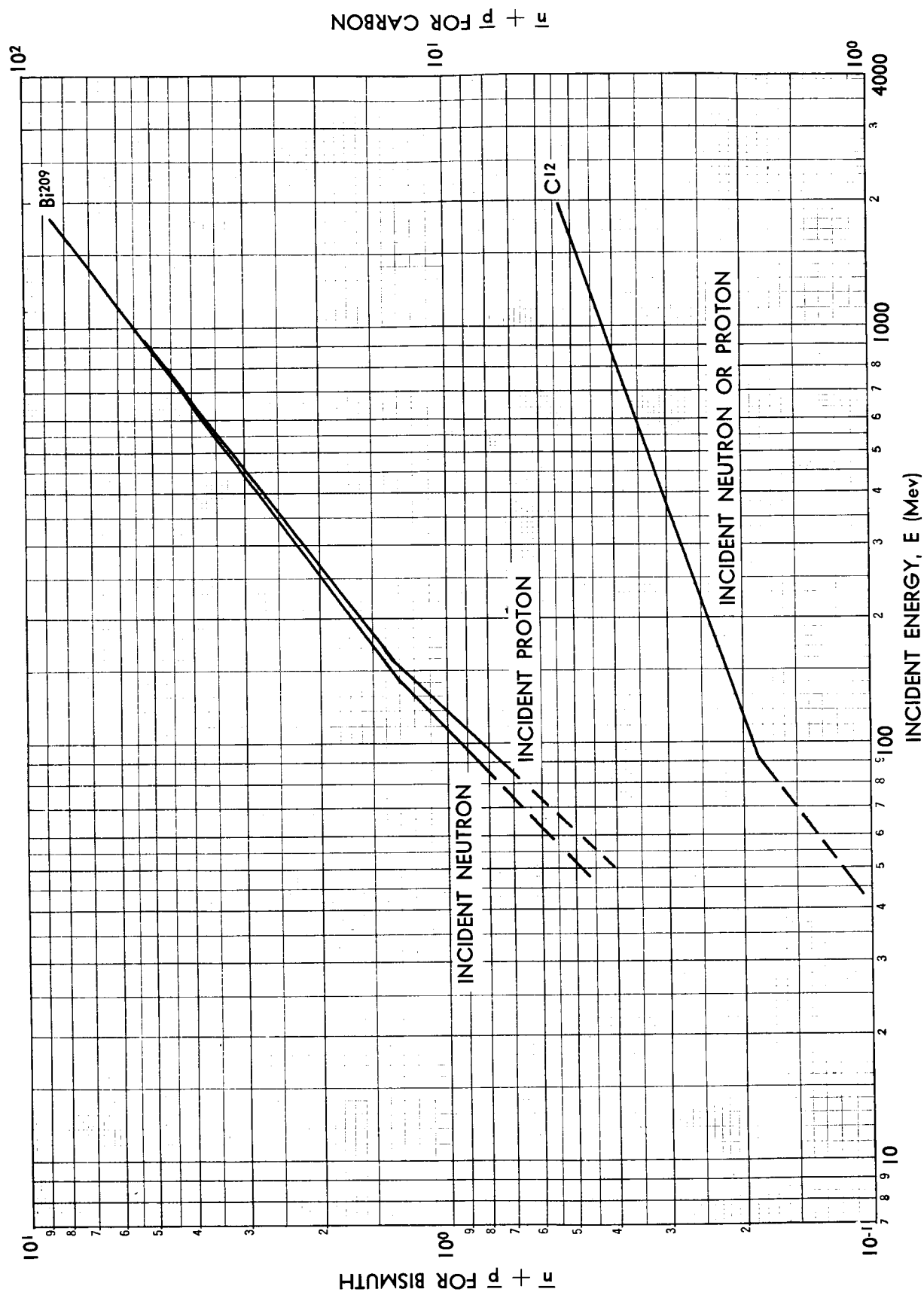
FIGURE 4.18. AVERAGE NUMBER OF CASCADE NUCLEONS PER NONELASTIC COLLISION IN CARBON AND BISMUTH

110
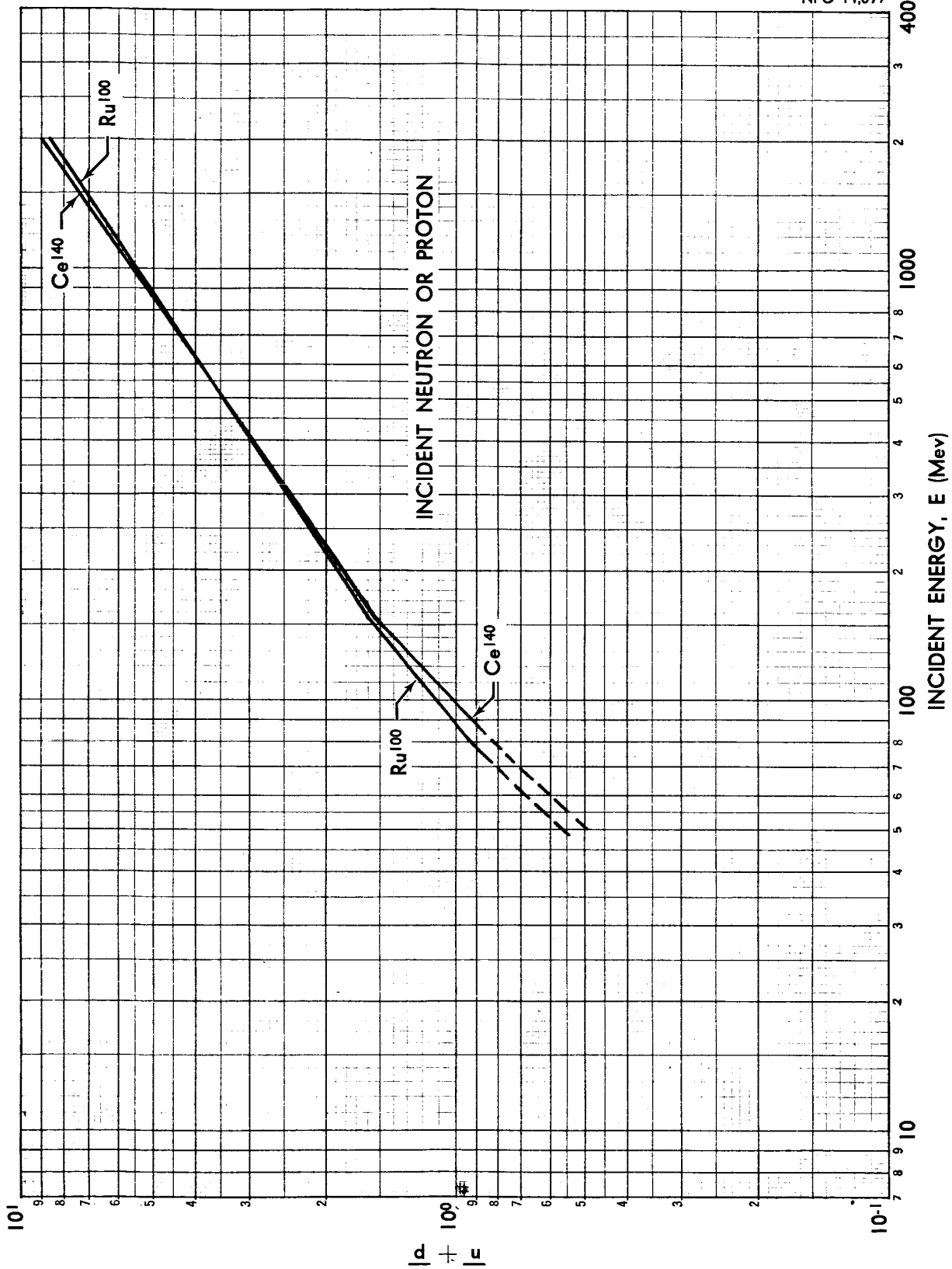
FIGURE 4.19. AVERAGE NUMBER OF CASCADE NUCLEONS PER NONELASTIC COLLISION IN RUTHENIUM AND CESIUM
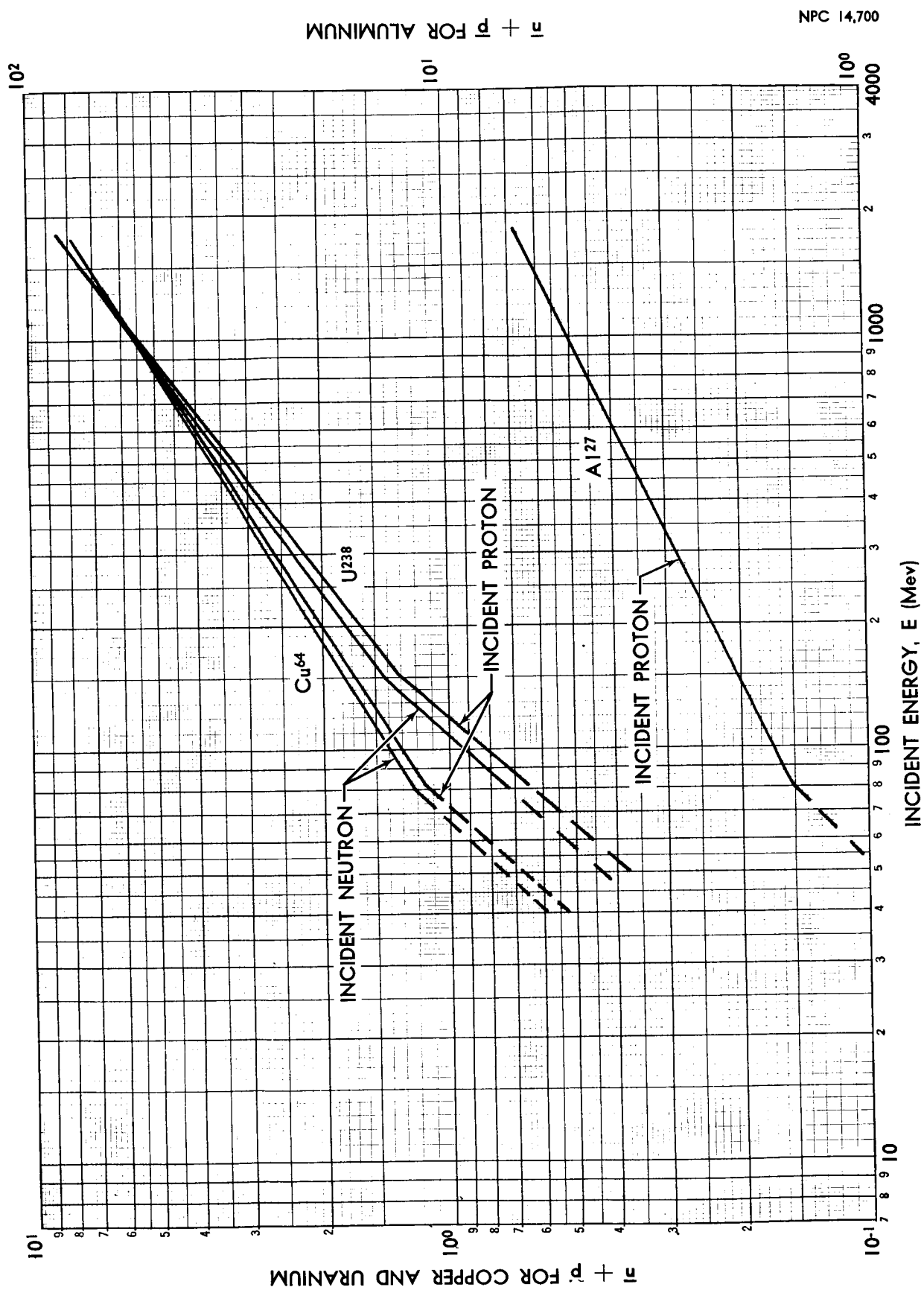
FIGURE 4.20. AVERAGE NUMBER OF CASCADE NUCLEONS PER NONELASTIC COLLISION IN ALUMINUM, COPPER, AND URANIUM

NPC 14,701

INCIDENT NEUTRONS

U238
Bi209
Ru100
Cu64
Al27
C12

$(\underline{d} + \underline{u})/\underline{u}$

0.80
0.70
0.60

INCIDENT PROTONS

C12
Al27
Cu64
Ru100
Ce140
Bi209
U238

$(\underline{d} + \underline{u})/\underline{d}$

0.6
0.5
0.4
0.3

10   100   1000   10000

INCIDENT ENERGY. F (Mev)
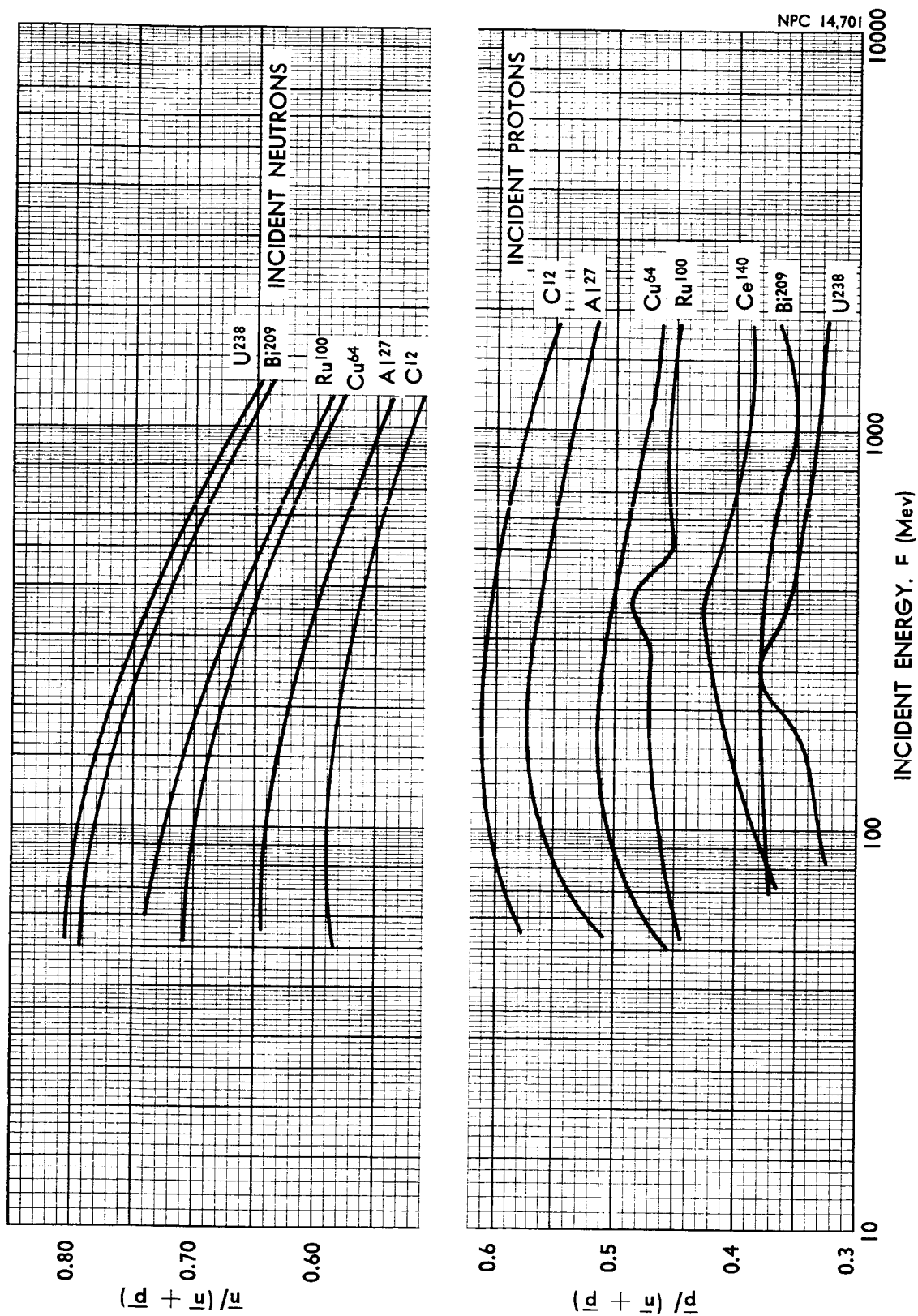
FIGURE 4.21. EMITTED NUCLEON FRACTIONS

113

these figures and are plotted as a function of mass number of the target nucleus in Figure 4.25.

The data (with temperature correction for the coulomb barrier) obtained from the tables and curves of Reference 83 for Cu^{64}, Ag^{109}, Ta^{181}, and At^{219} are given in Table X as a function of initial excitation energy. These consist of the average number of α particles, deuterons, protons, tritons, He^3 particles, neutrons, and total number of charged particles evaporated from the various nuclei.

The data are used in two separate ways to obtain the average number of emitted neutrons. The calculations have shown that the total change in mass number caused by evaporation is proportional to the mass number of the starting nuclide for a given nuclear temperature (τ) defined as

$$\tau = \left(\frac{E_{ex}}{a}\right)^{1/2} , \qquad (4.9)$$

where E_{ex} is the initial excitation energy of the nucleus and $\underline{a}$ is the level-density parameter. The effect of changing the level-density parameter from $a = A/10$ to $a = A/20$ increased the number of neutrons emitted by as much as 60% for Cu (depending on excitation energy) and decreased the number of neutrons emitted by 30% for Ag and by as much as 25% for Ta. The effect on protons and other charged secondaries was even larger. However, the average excitation energies of interest in this report are usually less than 200 Mev, except for the highest mass nuclides

NPC 14,702
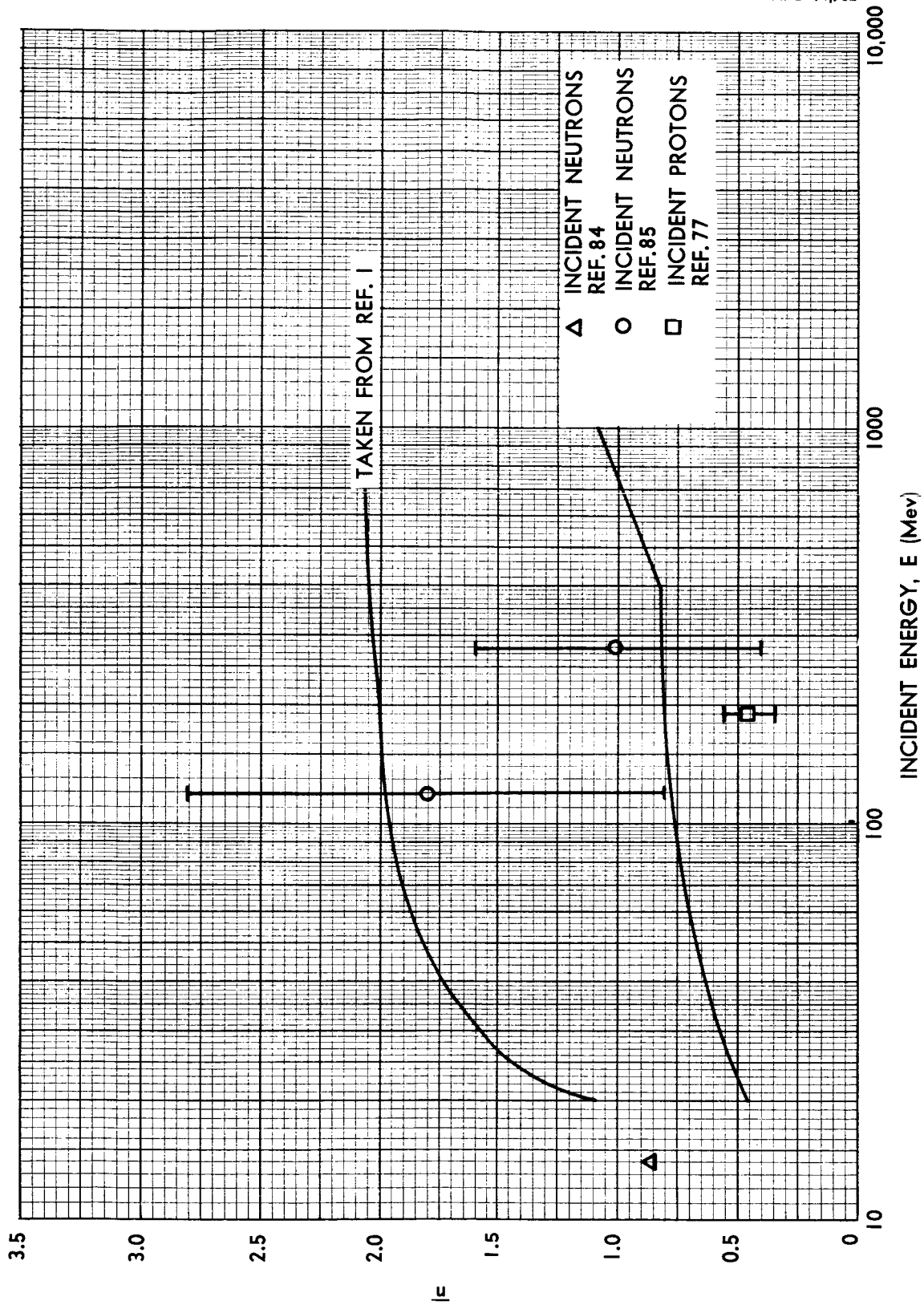
FIGURE 4.22. AVERAGE NUMBER OF EVAPORATION NEUTRONS FOR CARBON

NPC 14,703

TAKEN FROM REF. I

INCIDENT ENERGY, E (Mev)

O INCIDENT NEUTRONS
  REF. 84

△ INCIDENT NEUTRONS
  REF. 85

□ INCIDENT PROTONS
  REF. 77
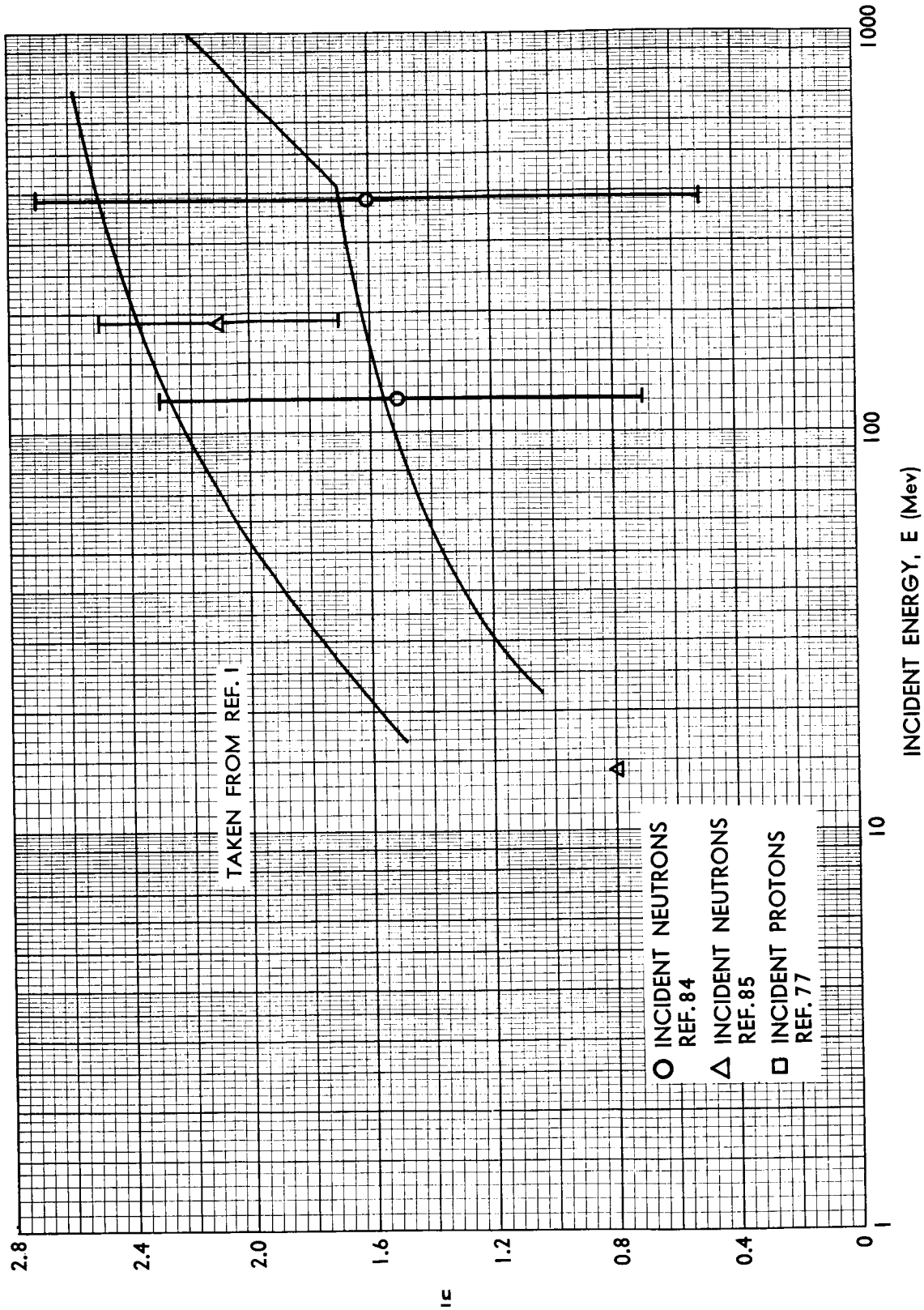
FIGURE 4.23.   AVERAGE NUMBER OF EVAPORATION NEUTRONS FOR ALUMINUM

NPC 14,704
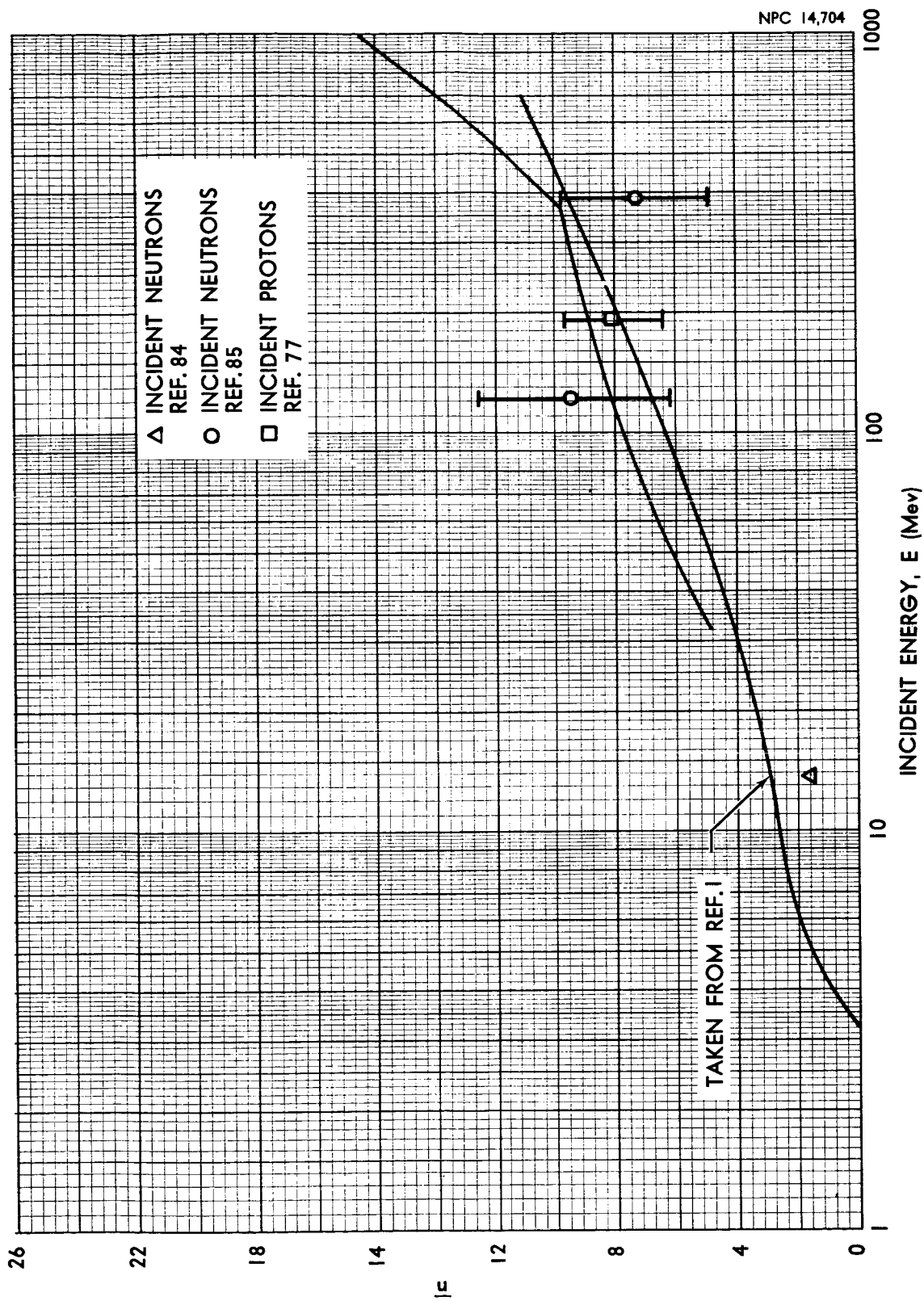
FIGURE 4.24. AVERAGE NUMBER OF EVAPORATION NEUTRONS FOR LEAD

117

NPC 14,705
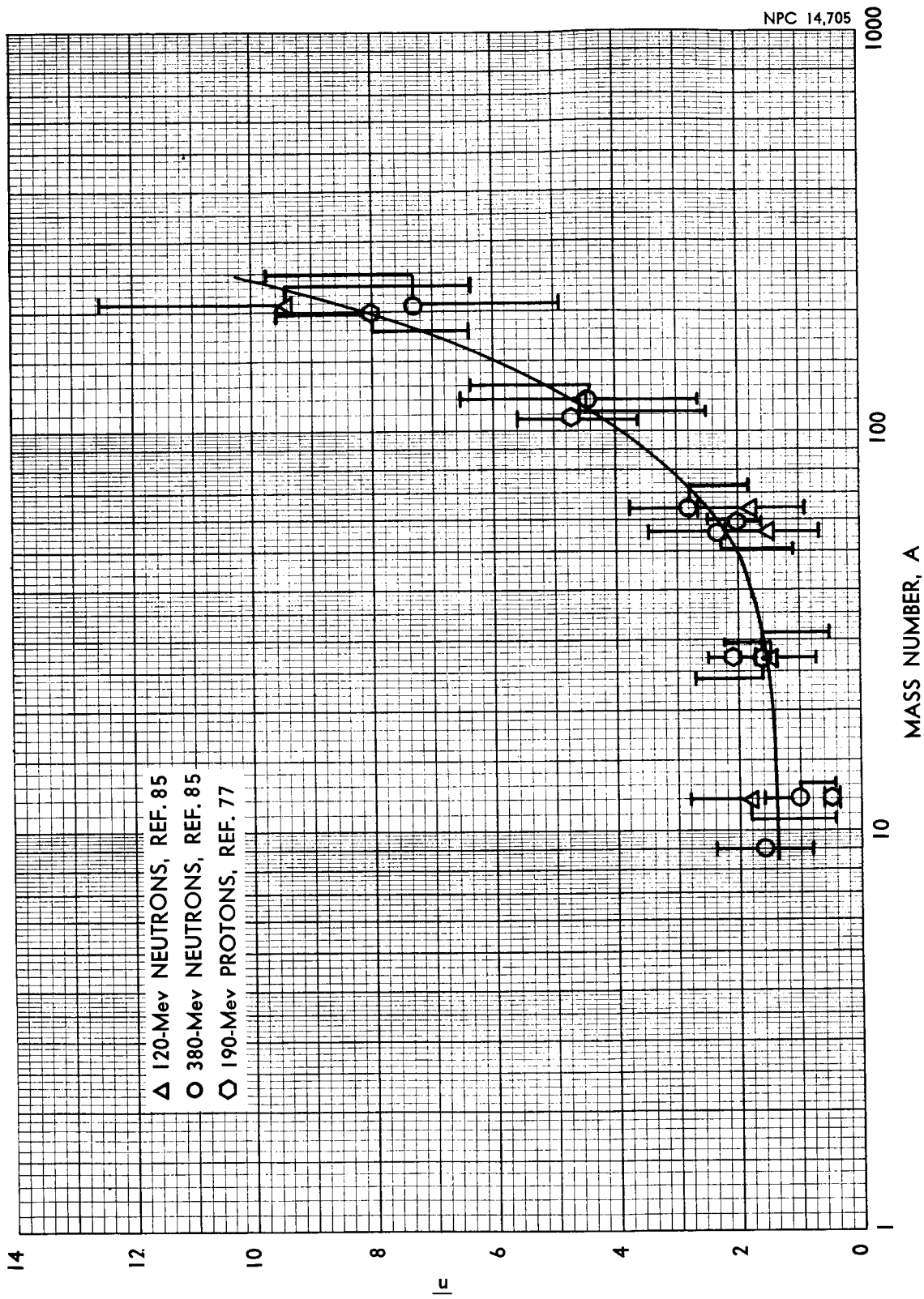
FIGURE 4.25. VARIATION OF AVERAGE NUMBER OF EVAPORATION NEUTRONS WITH MASS NUMBER

△ 120-Mev NEUTRONS, REF. 85

○ 380-Mev NEUTRONS, REF. 85

◇ 190-Mev PROTONS, REF. 77

MASS NUMBER, A

TABLE X

EVAPORATION PARTICLE PRODUCTION FROM MONTE CARLO CALCULATION

Temperature τ (Mev)	Excitation Energy (Mev)	$\bar{n}$	$\bar{p}$	$\bar{d}$	$\overline{H^3}$	$\overline{He^3}$	$\bar{\alpha}$
Cu^{64}							
2.80	50	2.5	0.225	0.15	0	0	0.15
3.95	100	4.0	1.4	0.35	0	0	0.35
4.00	102	4.13	1.6	0.35	-	-	0.35
5.60	200	5.7	3.0	0.90	0.25	0	0.75
6.00	230	5.2	3.2	0.60	-	-	-
7.90	400	8.3	4.7	2.1	.70	0.40	1.45
9.67	600	10.5	6.0	3.6	1.00	0.90	1.6
Ag^{109}							
2.14	50	3.8	0.40	0	0	0	0.20
3.03	100	5.9	1.00	0	0.20	0	0.40
4.00	174	8.15	2.0	0.40	-	0	0.57
4.28	200	8.4	2.00	0.45	0.20	-	0.90
6.00	392	12.0	4.8	1.80	-	-	1.2
6.05	400	11.7	5.0	1.6	0.70	0.35	1.75
7.40	600	14.4	6.6	3.3	1.10	0.65	2.25
Ta^{181}							
1.66	50	4.8	0.20	0	0	0	0
2.36	100	8.0	0.50	0	0	0	0.2
3.32	200	12.7	1.20	0.30	0.30	0	0.6
4.00	290	16	2.3	0.46	-	-	0.69
4.70	400	18.5	3.4	1.15	0.50	0.15	1.6
5.75	600	22.3	5.7	2.4	1.20	0.35	1.7
6.00	651	24.0	6.4	2.3	-	-	2.25
At^{219}							
4	350	19.7	2.5	0.65	-	-	1.1
6	790	29	6.5	2.5	-	-	2.0

(Pb) and highest bombarding energies of about 1000 Mev (see Sec. 4.5.1). For these relatively lower excitation energies the variation with $\underline{a}$ is much smaller. Since most of the data is reported for a = A/10, this expression for the level-density parameter will be assumed correct.

In the first method of extrapolating this data, the total change in mass (ΔA) was plotted as a function of nuclear temperature (τ), using Equation 4.9. Points for various nuclear temperatures of interest (4-6 Mev) were then replotted as a function of mass number, and interpolation for carbon and aluminum was accomplished assuming the curves extrapolate to $\Delta A = 0$ at A = 0.

Similarly, $\bar{n}/\Delta A$, the fraction of neutrons emitted per unit ΔA (determined from Table X), was plotted as a function of τ and was found to vary slowly with nuclear temperature. Again, the values for several nuclear temperatures of interest were replotted versus mass number and were found to vary slowly with A, thus permitting extrapolating to A = 12 and to A = 27.

Combining the results for ΔA and $\bar{n}/\Delta A$, the values of $\bar{n}$ for the temperatures (or excitation energies) and mass numbers of interest were found.

In the second method for determining the average number of evaporation neutrons, the values of $\bar{n}$ obtained directly from Table X were plotted as a function of nuclear temperature. The values for various temperatures were replotted as a function of mass number and interpolations for carbon and aluminum obtained,

again assuming $\bar{n} = 0$ for A = 0. Using the relationships between τ and excitation energy, as well as between average excitation energy and bombarding energy (Fig. 4.26), the curves in Figures 4.22, 4.23, and 4.24 were drawn.

As stated previously, the distribution of excitation energies after cascade should be considered in determining the average number of emitted particles. In addition, the distribution of residual nuclides after cascade (or starting nuclides for the evaporation) should be considered; however, data giving the correlation between excitation-energy distribution and distribution of residual nuclei exist for only one target material (copper) and two bombarding energies, 460 and 1890 Mev (Ref. 80). Furthermore, the uncertainty in the relationship between excitation energy and nuclear temperature, as well as the necessity of extrapolation for C and Al, does not justify such detailed analysis at this time. Therefore, average excitation energies are used and the mass of the residual nuclei is taken to be that of the target nucleus. From the data of Table X, it may be seen that the variation of the number of evaporation neutrons with mass number is not very large and, therefore, the use of the target mass number instead of an average residual nucleus is reasonable.

Tables XI and XII give the production cross sections and average numbers of emitted particles from evaporation measured in various experiments (Refs. 77, 81, and 85).

TABLE XI

EVAPORATION NEUTRON, PROTON AND ALPHA-PARTICLE PRODUCTION BY 190-MEV PROTONS
(Refs. 77,81)

Element	σ_{ne} (mb)	$\bar{n}$	$\bar{E}_n$ (Mev)	$\bar{p}$	$\bar{E}_p$ (Mev)	$\bar{\alpha}$	$\bar{E}_\alpha$ (Mev)	$\bar{E}_{ex}$ (Mev)
C	230	0.45 ± 0.11	3.4	0.43 ± 0.1	4.4	0.55 ± 0.11	7.1	27 ± 5
Al	410	2.1 ± 0.4	3.0	0.80 ± 0.16	6.1	0.42 ± 0.09	7.0	50 ± 8
Ni	710	2.0 ± 0.4	2.7	1.10 ± 0.22	7.45	0.20 ± 0.04	12.0	57 ± 9
Ag	1100	4.7 ± 0.9	2.5	0.56 ± 0.11	9.8	0.18 ± 0.04	17.4	69 ± 12
Au	1700	8.0 ± 1.6	2.4	0	—	0.10 ± 0.02	25.2	83 ± 17

122

TABLE XII

EVAPORATION NEUTRON PRODUCTION BY 120- AND 380-MEV NEUTRONS
(Ref. 85)

Element	$\overline{n}$	$\overline{E}$ (Mev)	Neutron Binding Energy (Mev)	Evaporation Excitation Energy (Mev)
			120-Mev Neutrons	
C	1.8 ± 1	4	25	30 ± 17
Al	1.5 ± 0.8	3	17	20 ± 10
Fe	1.5 ± 0.8	3	12	15 ± 8
Cu	1.8 ± 0.9	4	15	20 ± 10
Sn	4.5 ± 2	9	35	45 ± 20
Pb	9 ± 3	20	65	85 ± 28
Pb*	9.9 ± 3.3	-	-	-
			380-Mev Neutrons	
Be	1.6 ± 0.8	3	12	15 ± 7
C	1 ± 0.6	2	18	20 ± 12
Al	1.6 ± 1.1	3	15	18 ± 12
Fe	2.3 ± 1.2	5	20	25 ± 13
Cu	2.8 ± 1	6	24	30 ± 11
Sn	4.4 ± 1.8	10	35	45 ± 20
Pb	6.5 ± 2.4	15	50	65 ± 24
Pb*	7.4 ± 2.5	-	-	-
Pb*	7.1 ± 2.4	-	-	-
Pb*	7.7 ± 2.6	-	-	-
Pb*	7.8 ± 2.6	-	-	-

* Various sample thicknesses.

4.5 Energy Distributions of Nonelastic Particles

4.5.1 Average Excitation Energies

The average excitation energies of residual nuclei following cascade shown in Figure 4.26 were obtained from the Monte Carlo calculations (Ref. 79 and 80). The measured values of excitation energy given in Table XI for 190-Mev protons (Ref. 77) are compared with the calculated data in Figure 4.27. The agreement is within experimental error.

4.5.2 Average Energy of Emitted Nucleons

4.5.2.1 Cascade Nucleons. A rough estimate of the average energy of emitted cascade nucleons may be obtained as follows. The average total energy available in the form of kinetic energy of the cascade particles E_{av} is given by

$$E_{av} = E - \overline{E}_{ex} + \left[M + m_p - \overline{M}' - \overline{n}m_n - \overline{p}m_p \right] c^2 - \overline{E}_{M'}, \qquad (4.10)$$

where

E is the bombarding energy,

$\overline{E}_{ex}$ is the average excitation energy,

M is the mass of the target nuclide,

$\overline{M}'$ is the average mass of the residual nuclides,

m_p, m_n and $\overline{p}, \overline{n}$ are the masses and average numbers of the emitted protons and neutrons, respectively, and

$\overline{E}_{M'}$ is the average kinetic energy of the residual nuclides.

$\overline{E}_{M'}$ will be assumed negligible. An upper limit to the effect of the terms in parenthesis should be given by the expression $(\overline{n} + \overline{p})B$, where $\overline{B}$ is the average binding energy per nucleon (~ 10 Mev). With these assumptions, the effect of this term on E_{av} is shown in Table XIII for several representative cases.
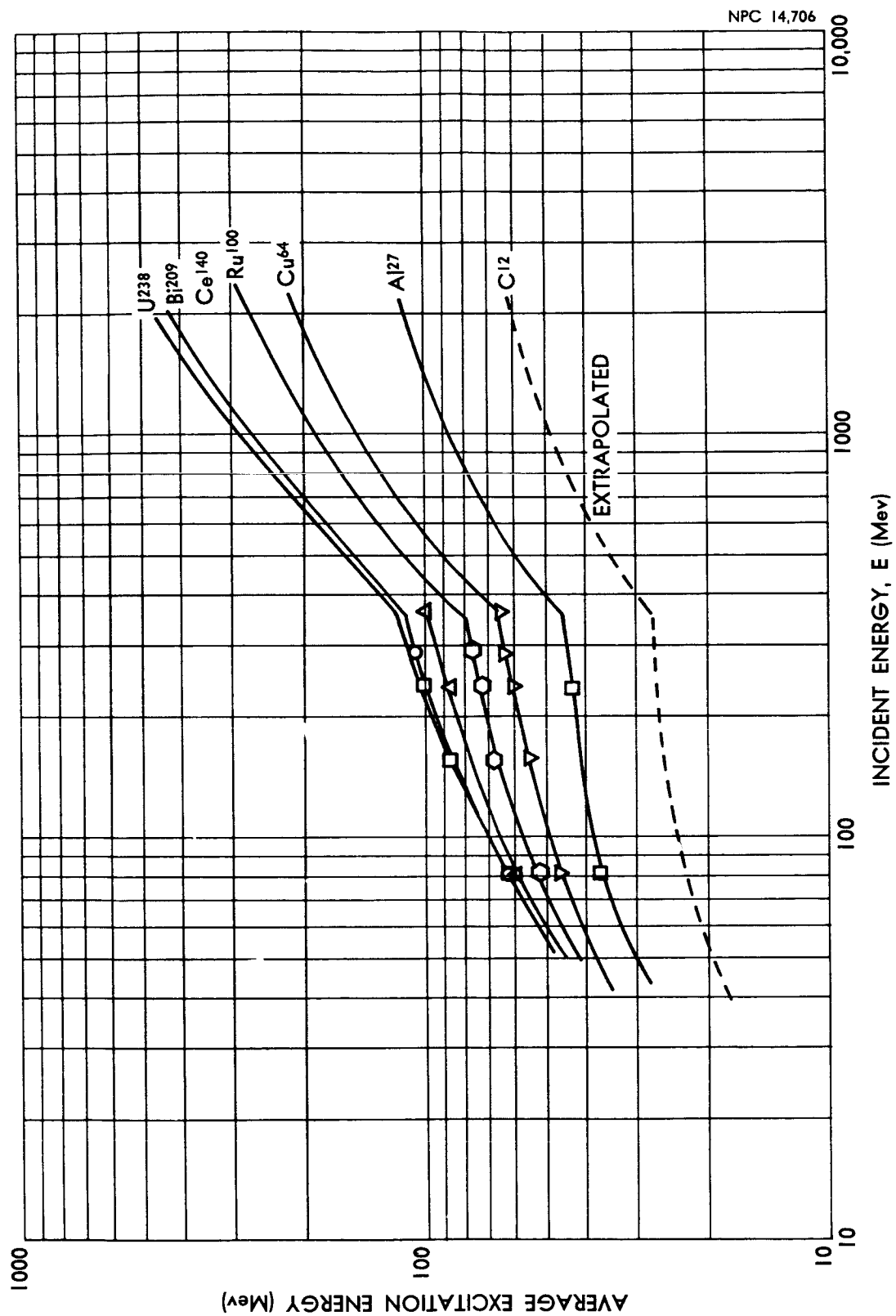
NPC 14,706

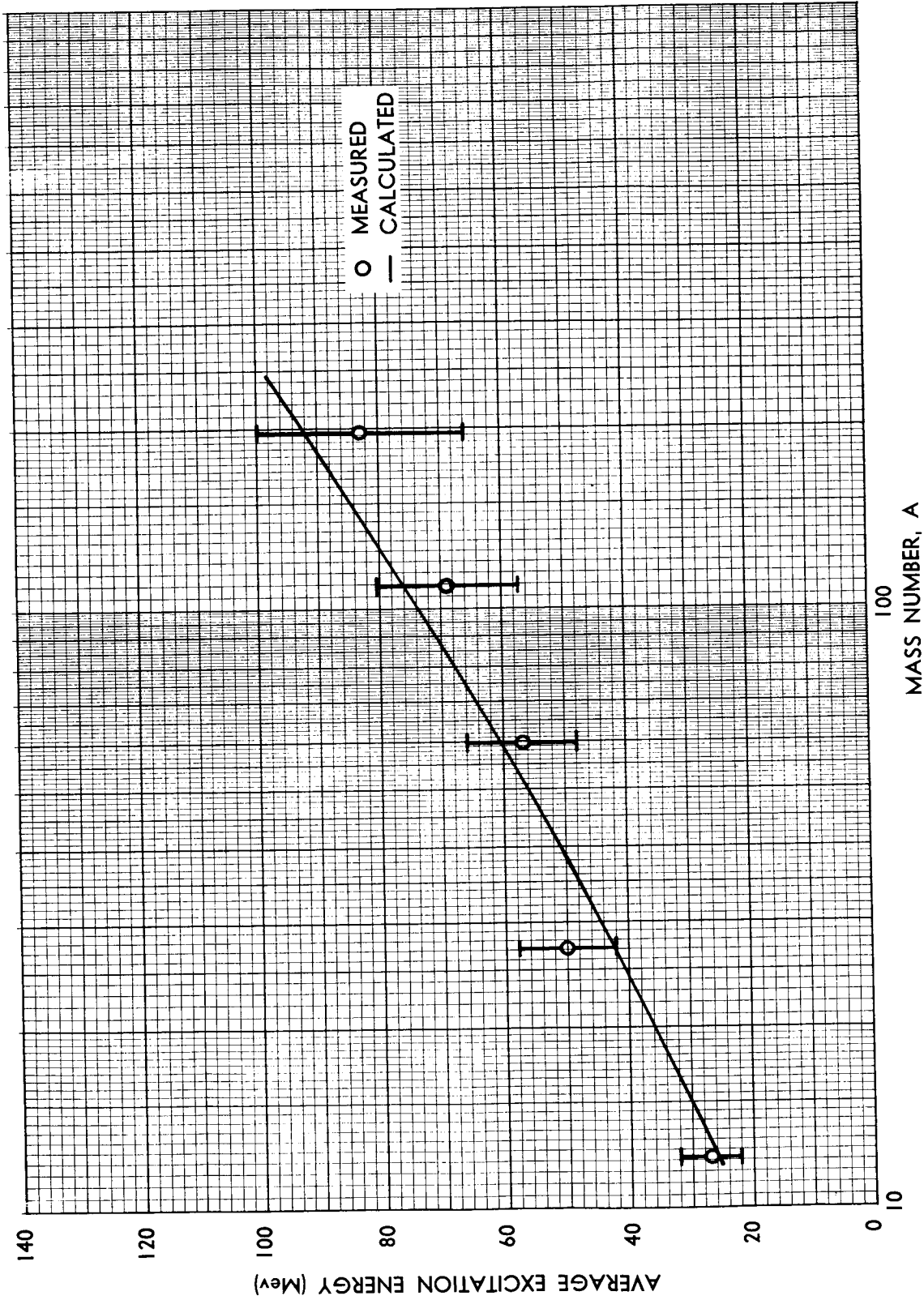FIGURE 4.26. AVERAGE EXCITATION ENERGIES FOR VARIOUS INCIDENT ENERGIES

125

FIGURE 4.27.   COMPARISON OF MEASURED AND CALCULATED AVERAGE EXCITATION ENERGIES

TABLE XIII

ERROR IN CALCULATION OF AVERAGE ENERGY

E_p (Mev)	A	E_{ex} (Mev)	$(\bar{n} + \bar{p})$	E_{av} (Mev)	% Error
1840	12	59	5.2	1781 ± 52	3
1840	238	450	8.6	1390 ± 86	6
500	12	34	3.4	466 ± 34	7
500	238	160	3.3	340 ± 33	10
80	12	22	1.66	58 ± 17	30
80	238	70	0.66	10 ± 6.6	66

The effect is seen to be small at high energies, but becomes increasingly important for low bombarding energies and high mass numbers (A). The uncertainty in $\bar{E}_{ex}$ is also important in this range. Therefore, the average energy of emitted nucleons $\bar{E}$ determined by this method may be considerably in error for energies below 100 Mev. The equation used was

$$\bar{E} = \frac{E - \bar{E}_{ex}}{\bar{n} + \bar{p}} . \qquad (4.11)$$

The results are shown in Figures 4.28, 4.29, and 4.30 for C, Al, and Pb, respectively.

The average energy of emission of the cascade nucleons may be obtained from the measured and calculated spectra discussed in Section 4.5.3.1. The average energies of emitted cascade protons from 460- and 1340-Mev protons bombarding Al and U are compared
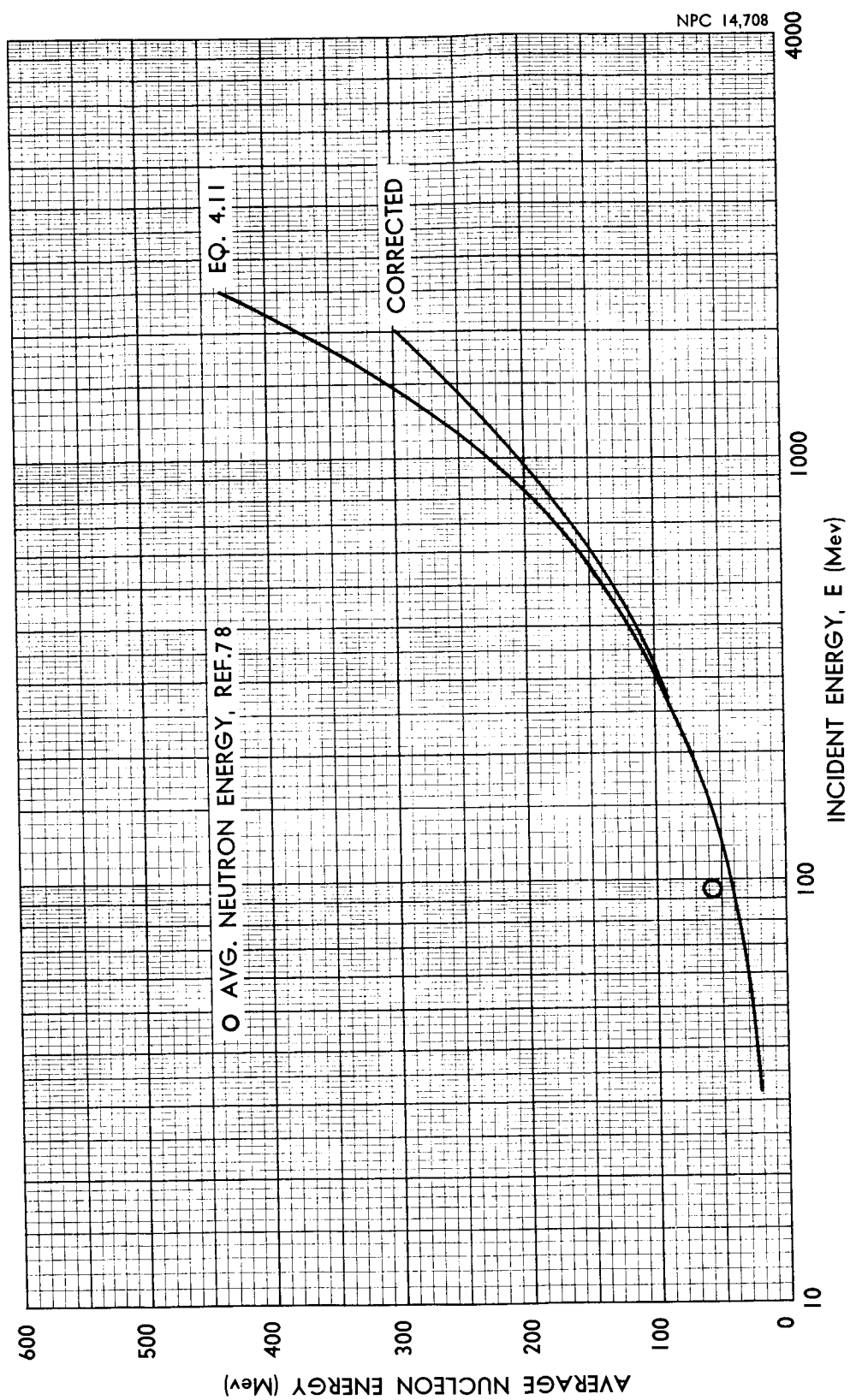
127

NPC 14,708

FIGURE 4.28. AVERAGE ENERGIES OF CASCADE NUCLEONS FOR CARBON
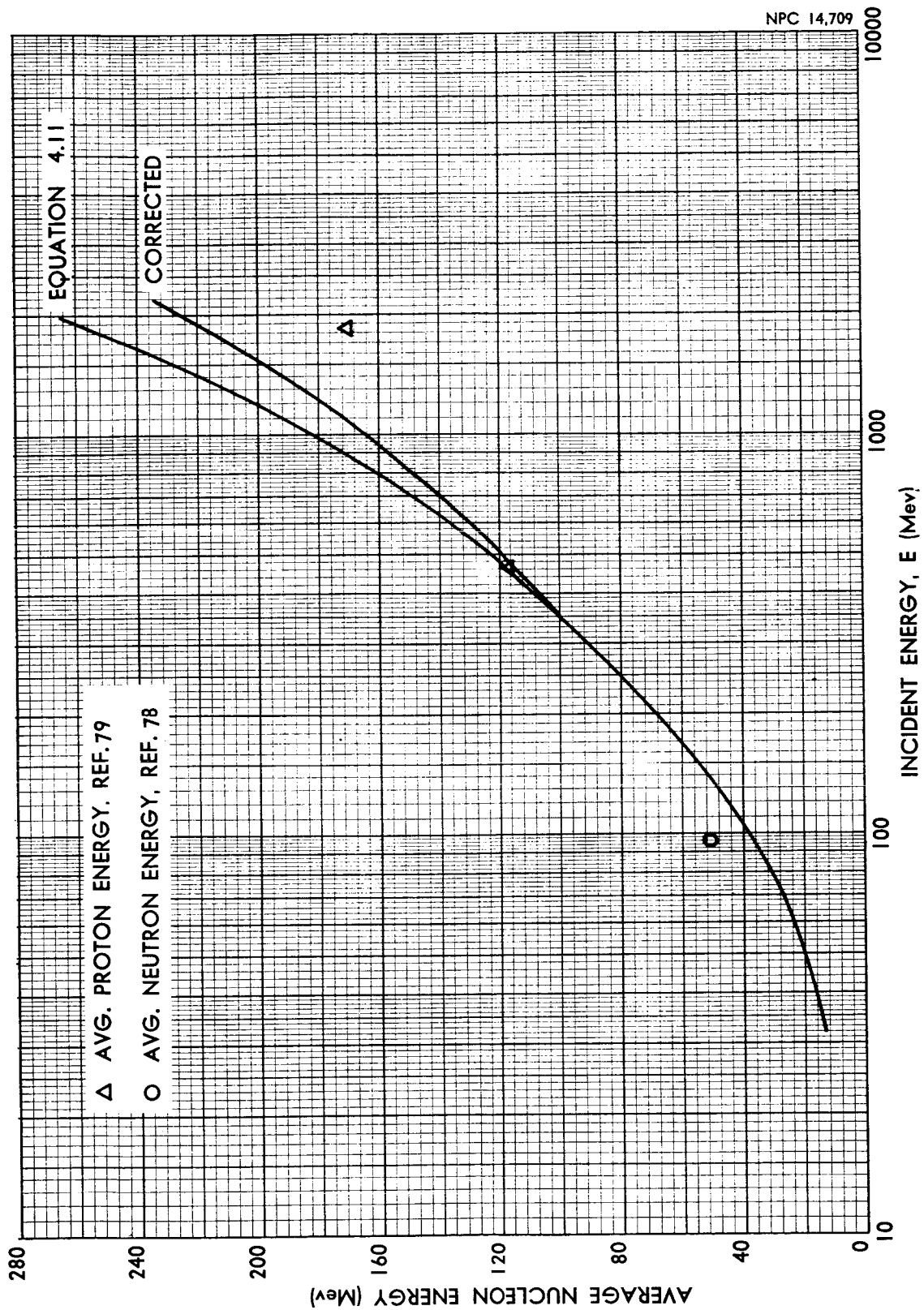
FIGURE 4.29. AVERAGE ENERGIES OF CASCADE
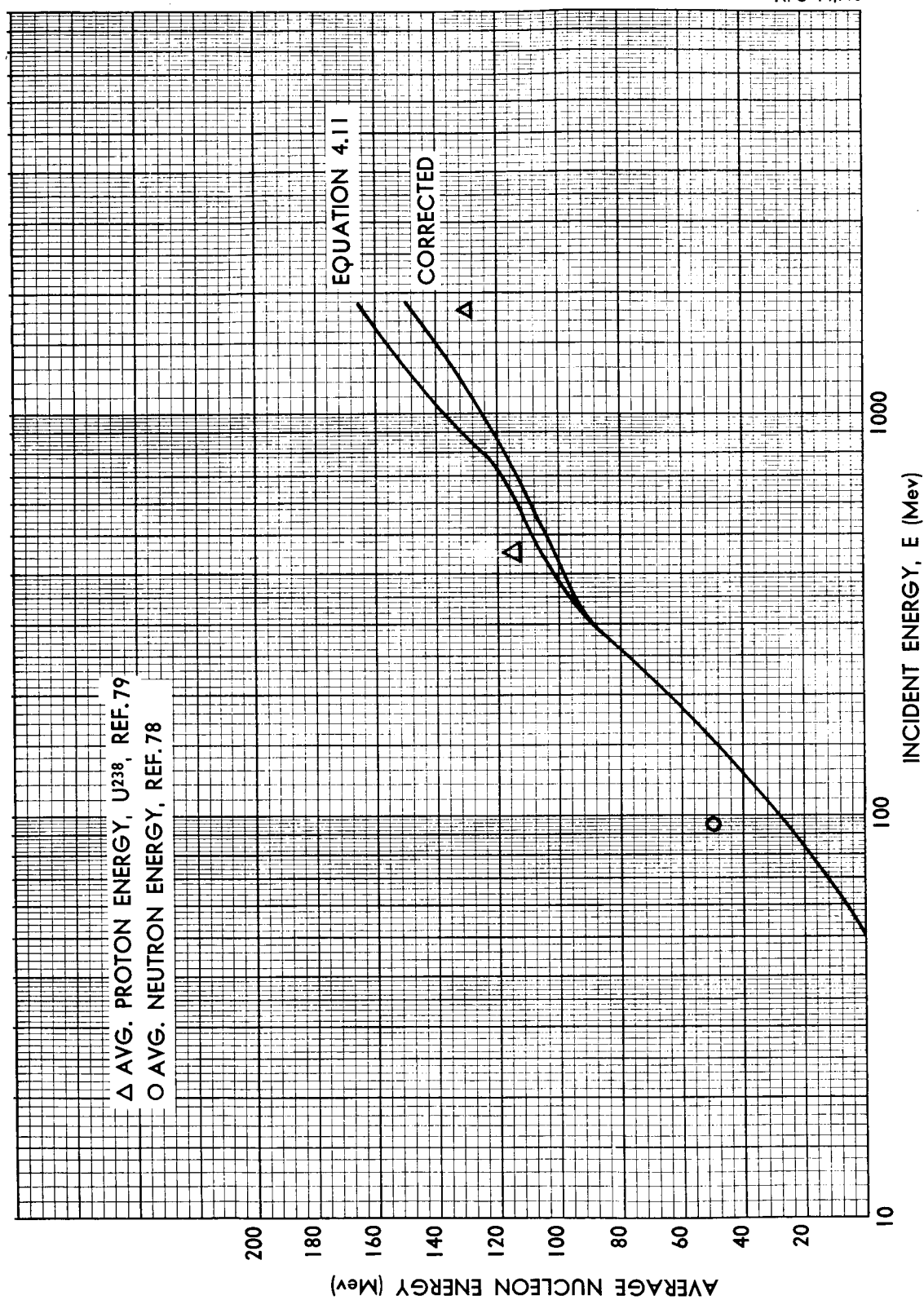NUCLEONS FOR ALUMINUM

129

FIGURE 4.30. AVERAGE ENERGIES OF CASCADE NUCLEONS
FOR LEAD

in Figures 4.29 and 4.30 to the values obtained from Equation 4.11 for Al and Pb, respectively. Since the average energies do not change rapidly with mass number, particularly for large mass numbers, the difference between the values for Pb and U should be negligible. The values obtained from the spectra are slightly higher, but agree fairly well with those of Equation 4.11 at 460 Mev. However, at 1840 Mev the values from Equation 4.11 are very much larger than those obtained from the spectra. A major source of error in Equation 4.11 is the neglect of pion production above 300 Mev. The average number of pions emitted per nonelastic interaction was calculated by Metropolis, et al. (Ref. 80) and was found to depend only slightly on mass number. The values were approximately 1.1 at 1840 Mev, 0.5 at 940 Mev, 0.3 at 690 Mev, and 0.12 at 460 Mev. If the assumption is made that the average energy of the emitted pions is equal to that for nucleons, the average number of pions produced may be added to the denominator in Equation 4.11. This procedure results in a significant decrease in the average energy of the nucleons at high bombarding energies, although there is still considerable disagreement with the values obtained from the spectrum, part of which is due to the assumption that $\overline{E}_{M'}$ is negligible. The assumption of equality for the average energies of pions and nucleons is supported by measurements of proton and pion energy spectra from Be bombarded by 2.2-Bev protons (Ref. 86). The average energy is roughly 400 Mev, which agrees with the values calculated from Equation 4.11 for Be, including the average number of pions in the denominator.

The average energies for the spectra from 95-Mev protons (Ref. 78) were found to decrease very slowly with angle out to 28°. The average energies for C, Al, and Pb were all approximately 50 Mev. These values are significantly higher than those obtained from Equation 4.11 of 40 Mev for C, 36 Mev for Al, and 30 Mev for Pb. This discrepancy is probably due to the small angular interval considered in Reference 78, since the forward angles contribute the highest energies.

4.5.2.2 <u>Evaporation Nucleons</u>. The average energies of emitted evaporation neutrons from bombardment by 190-Mev protons shown in Figure 4.31 were obtained from the measurements of Gross (Ref. 77). The average energy changes by only 1 Mev as the target nuclide varies from carbon to gold. Also, the average energies were found to change slowly with bombarding energy (or excitation energy), since the energy interval containing the evaporation particles and the spectral shape change very little with bombarding energy (Ref. 77). The average energies of evaporation protons obtained from the spectra of Reference 81 are also shown in Figure 4.31.

4.5.3 <u>Energy Spectra</u>

4.5.3.1 <u>Cascade Nucleons</u>. The energy spectra of cascade neutrons produced by 95-Mev protons bombarding D, Li, Be, C, Al, Cu, and Pb have been measured for angles of 0°, 5°, 10°, 16°, and 28° by Hoffmann and Strauch (Ref. 78). Their results for C, Al, Cu, and Pb are shown in Figures 4.32, 4.33, 4.34, and 4.35, respectively. Handley and York (Ref. 52) have measured the energy

spectra of protons produced by 90-Mev neutrons incident on C, Cu, and Pb. Comparison of their results (not shown) with those of Handley and York shows very little difference between the energy spectra for the various angles - in conformity with the theory of charge independence.

The energy spectrum of cascade protons ejected in the bombardment of Ru^{100} by 366-Mev protons was calculated by Monte Carlo (Ref. 79) and is shown in Figure 4.36. The spectrum is seen to fall rather rapidly from 30 to 90 Mev. It then falls more slowly out to about 160 Mev, after which it remains fairly constant. The rapid fall in the low-energy region is apparently related to the high probability for the incident particle to share its energy with many nucleons for targets with large mass numbers. This effect was somewhat apparent in the change in spectral shape with mass number for 90-Mev neutrons (Figs. 4.32 through 4.35).

The energy spectra of cascade protons produced by 460- and 1840-Mev protons bombarding Al and U were also calculated by Metropolis, et al. (Ref. 80) and are shown in Figures 4.37 and 4.38. Comparison of these spectra reveals that the shapes do not depend strongly on the mass of the nuclides being struck, although uranium does have a slightly higher percentage of low-energy particles in agreement with the results at lower energies. The spectra at 90 Mev were similarly not very sensitive to mass number.

There is also very little difference between the spectra at 460- and 1840-Mev in that very few particles with energies greater than 500 Mev were found in the 1840-Mev calculations. This effect
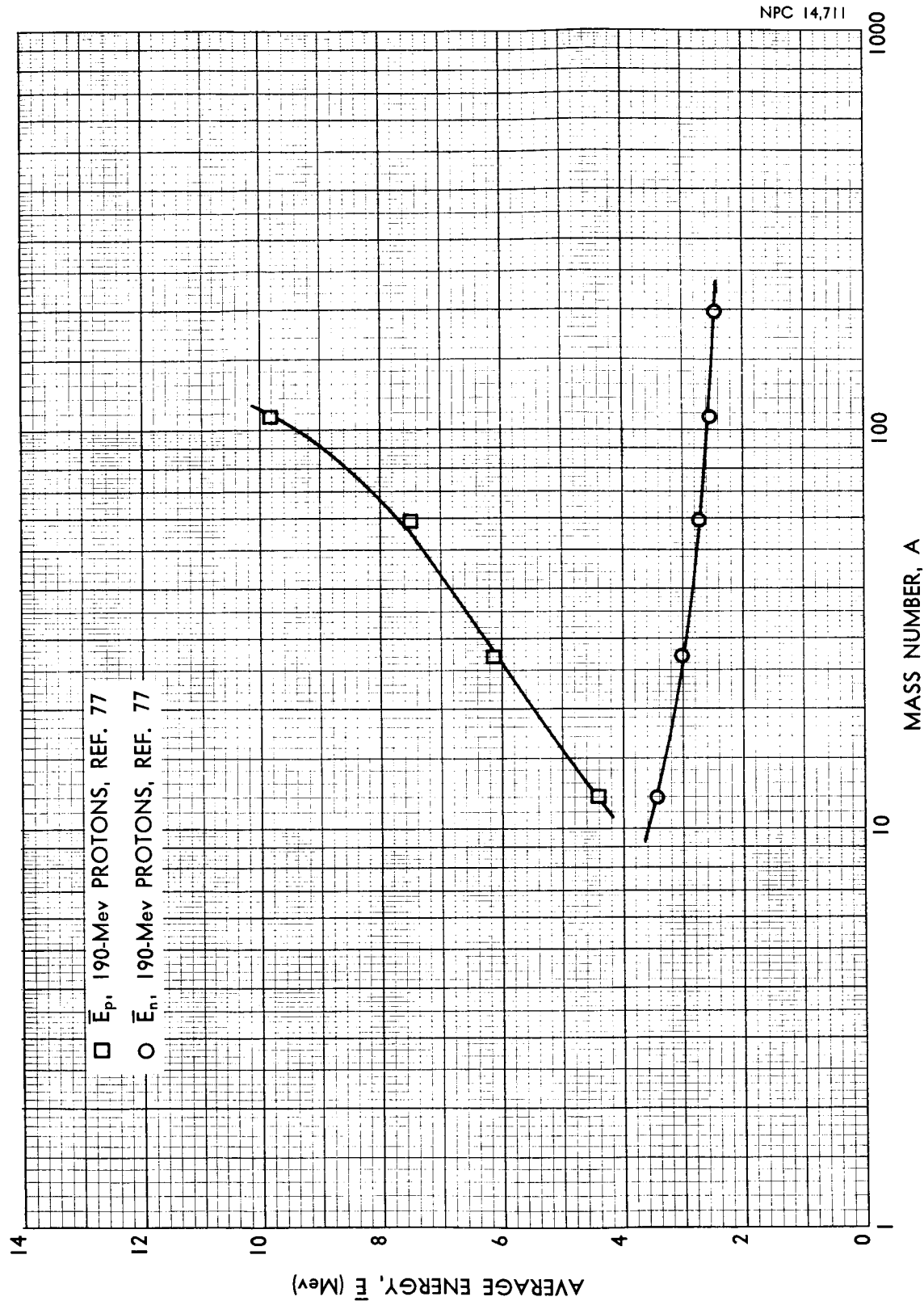
FIGURE 4.31.   VARIATION OF AVERAGE ENERGIES OF EVAPORATION
NUCLEONS WITH MASS NUMBER
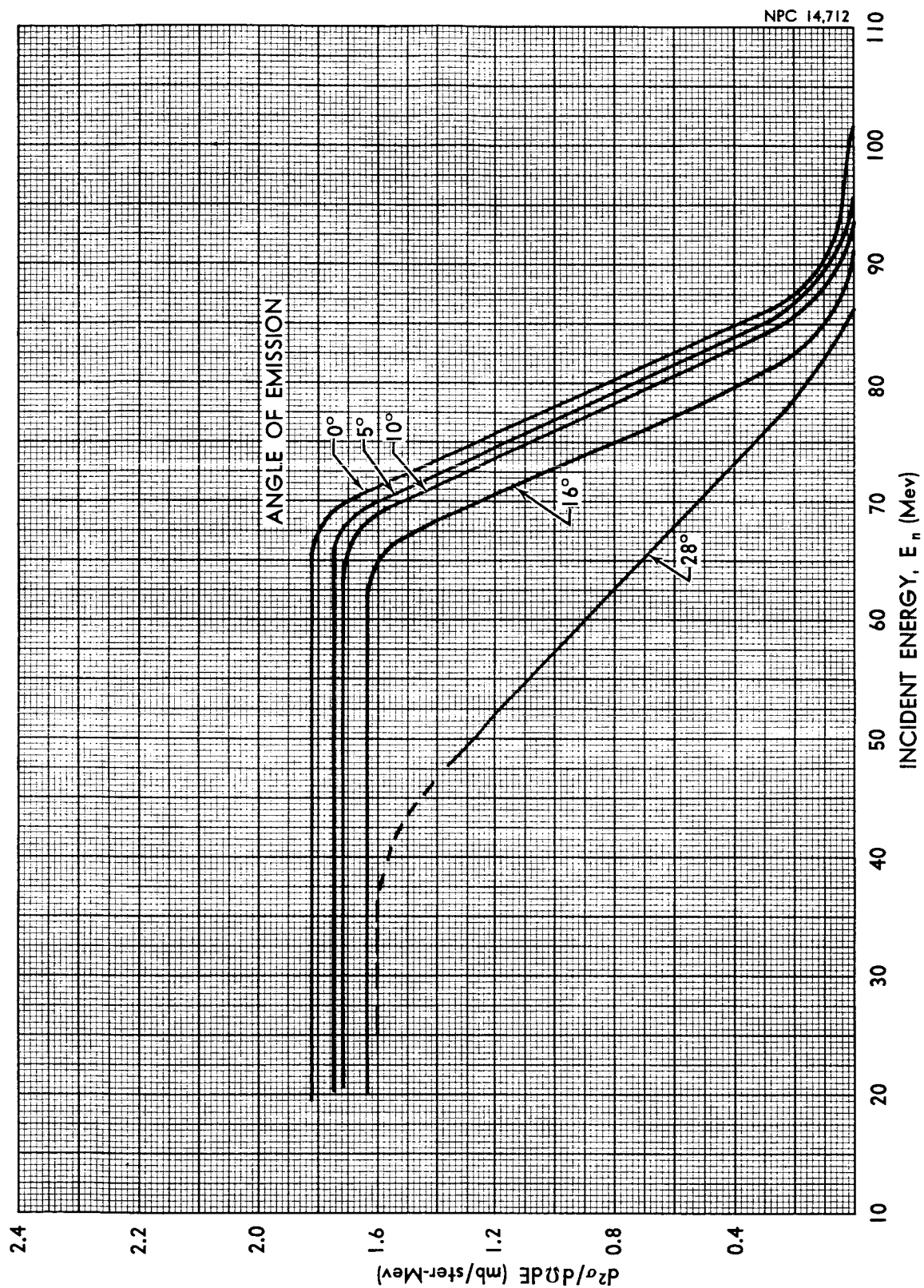
FIGURE 4.32. MEASURED CASCADE NEUTRON SPECTRA FROM
95-Mev PROTONS INCIDENT ON CARBON

135
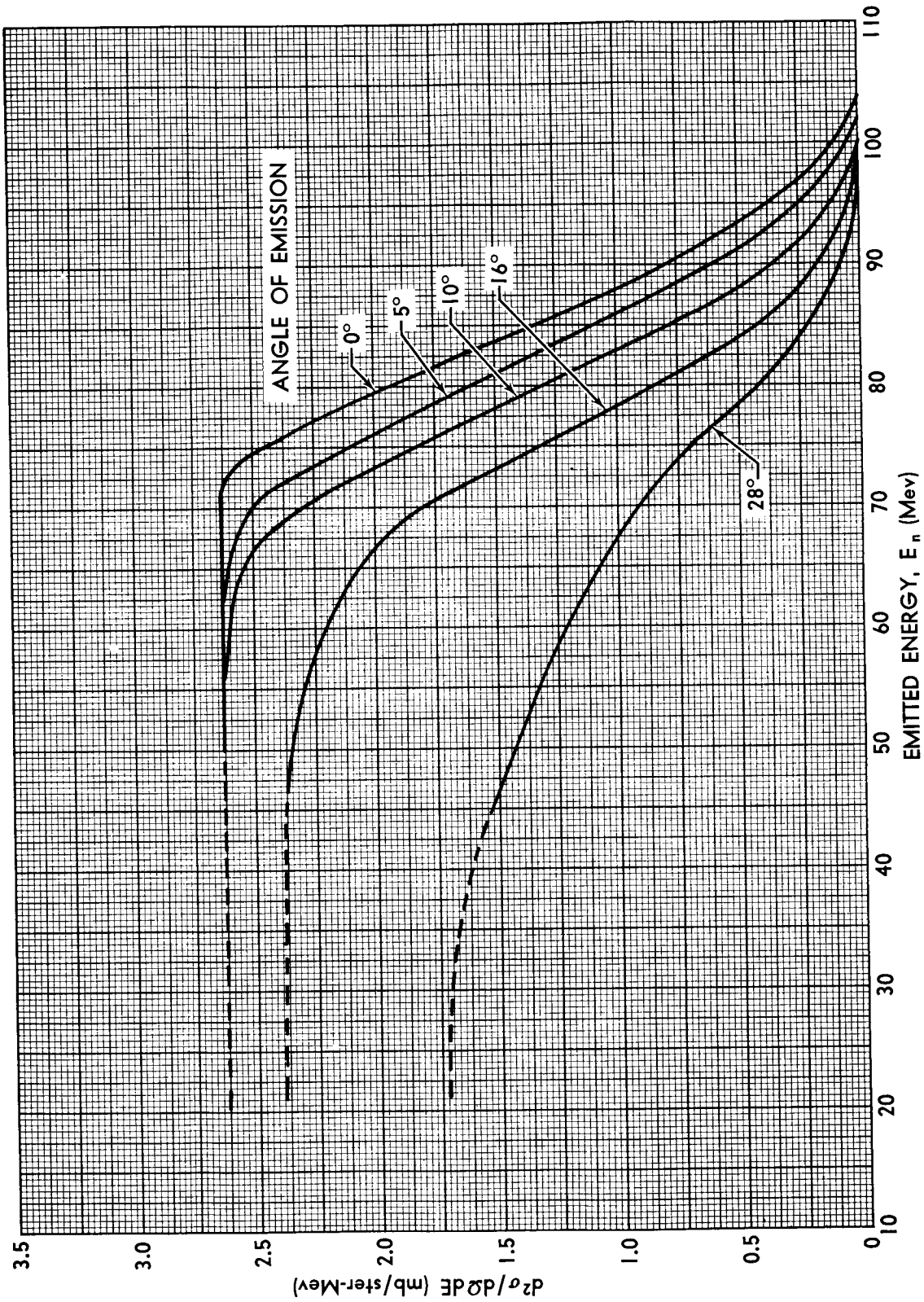
FIGURE 4.33.   MEASURED CASCADE NEUTRON SPECTRA FROM 90-Mev PROTONS INCIDENT ON ALUMINUM
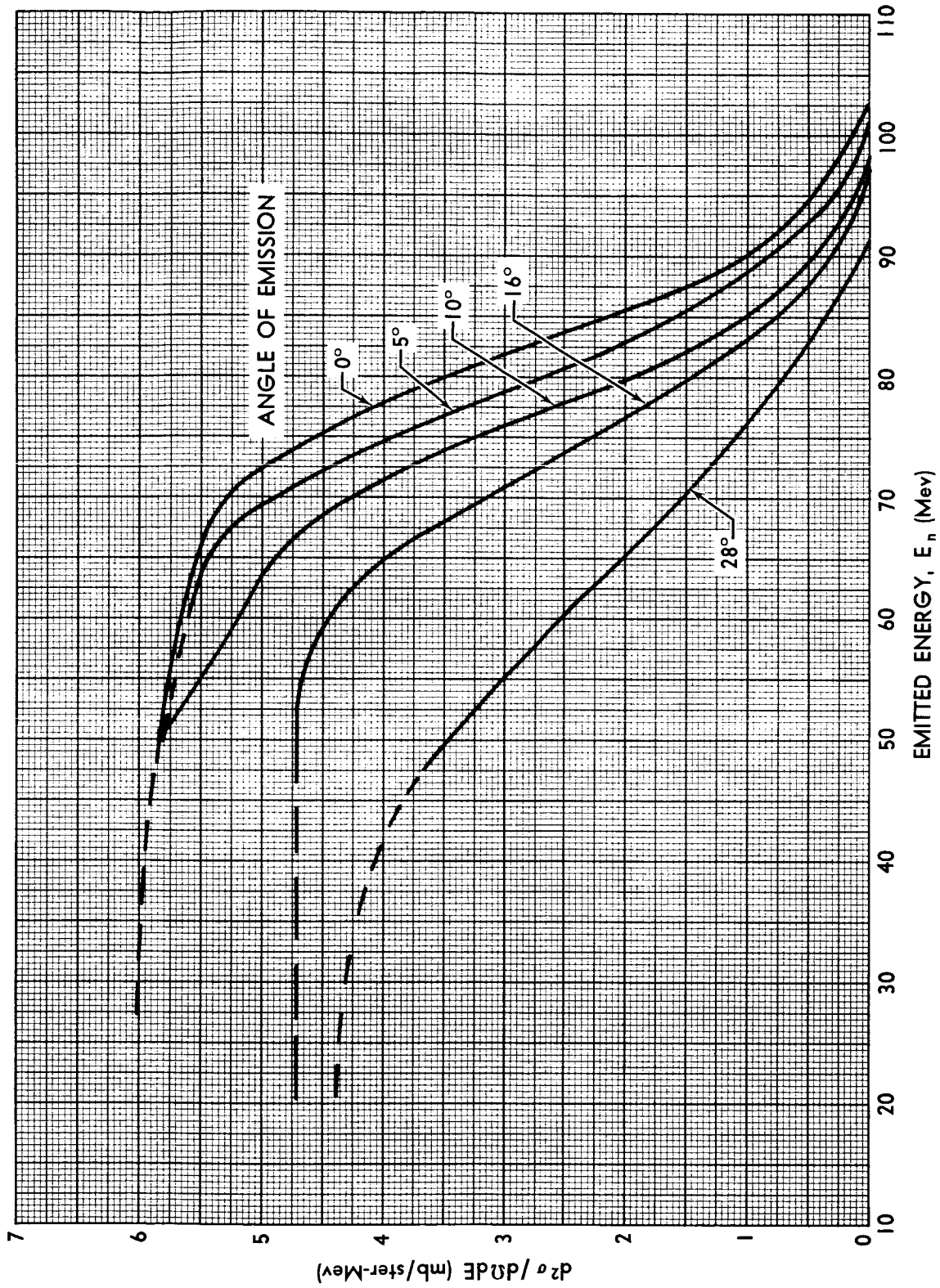
FIGURE 4.34. MEASURED CASCADE NEUTRON SPECTRA FROM
95-Mev PROTONS INCIDENT ON COPPER
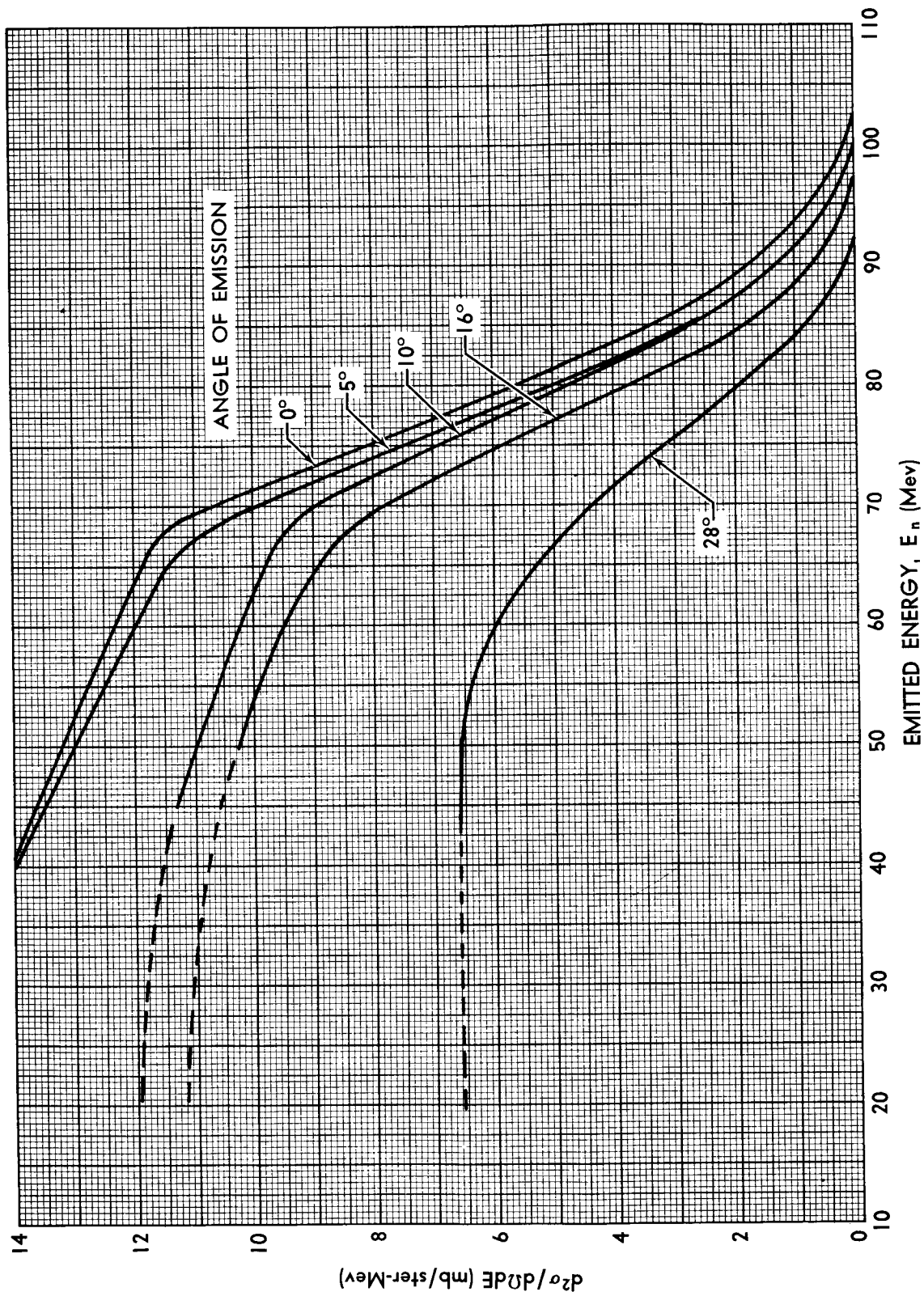
**FIGURE 4.35.   MEASURED CASCADE NEUTRON SPECTRA FROM
95-Mev PROTONS INCIDENT ON LEAD**

FIGURE 4.36. CASCADE PROTON SPECTRUM FROM 366-Mev PROTONS INCIDENT ON RUTHENIUM

139
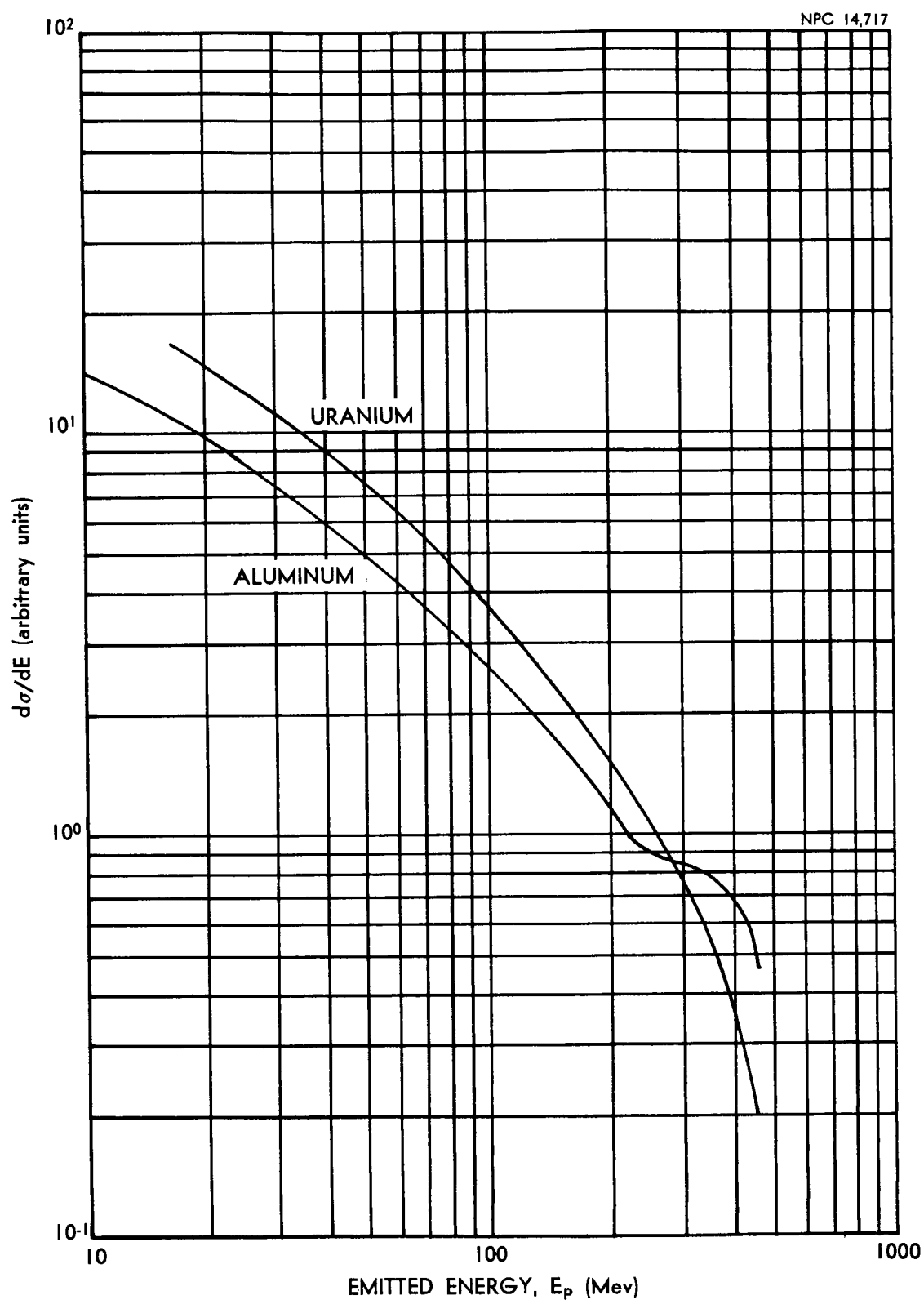
FIGURE 4.37. CASCADE PROTON SPECTRUM FROM 460-Mev PROTONS INCIDENT ON ALUMINUM AND URANIUM
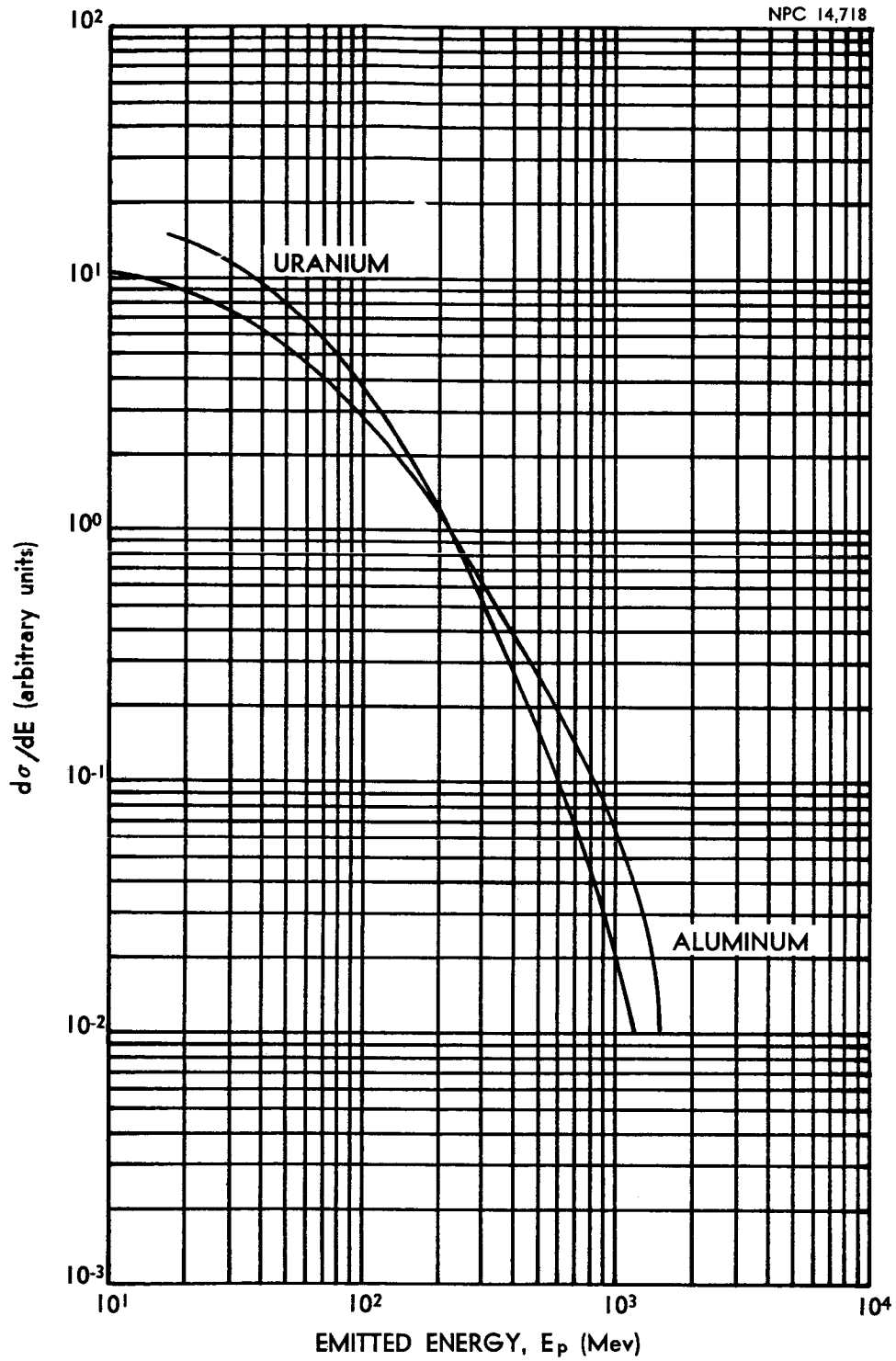
FIGURE 4.38. CASCADE PROTON SPECTRUM FROM 1840-Mev PROTONS INCIDENT ON ALUMINUM AND URANIUM

141

was attributed to pion production beginning with bombarding energies of around 300 Mev. The pions produced in the nucleon-nucleon collisions are a very efficient mechanism for energy transfer and their production reduces the probability of high-energy nucleons escaping the nucleus.
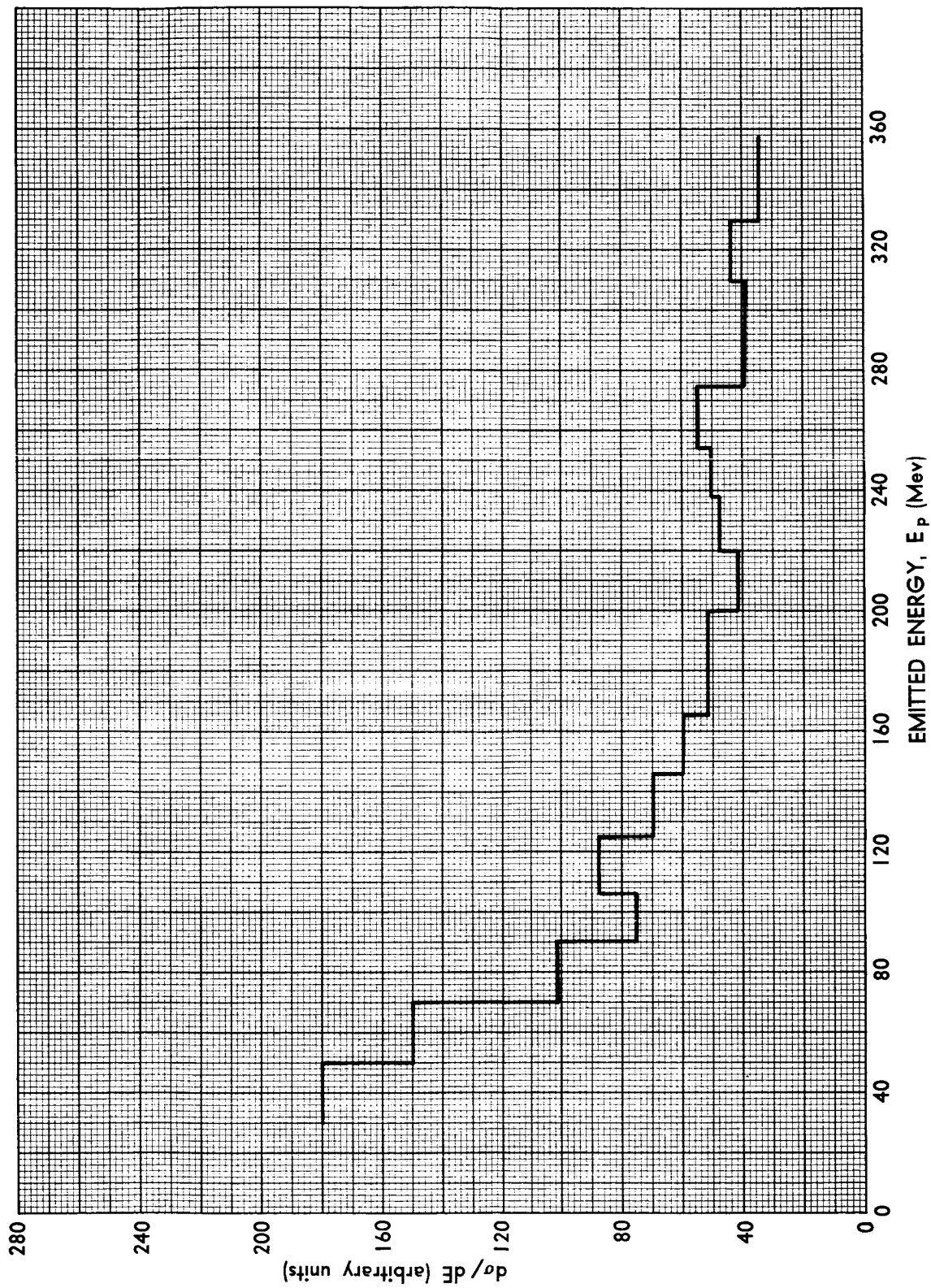
4.5.3.2 Evaporation Nucleons. The energy spectra of evaporation particles were found to change very little with bombarding energy (Ref. 77). Typical spectra are shown in Figures 4.39, 4.40, and 4.41 for 190-Mev proton bombardment (Refs. 77 and 81). A simplified theoretical expression for spectral shape obtained by Weisskopf (Ref. 87) may be written (Ref. 77) as

$$N(E) \propto \sigma_c(E)E \, e^{-E/\tau}. \tag{4.12}$$

Here, $\sigma_c(E)$ is the cross section for formation of the compound nucleus by the inverse process given by Blatt and Weisskopf (Ref. 31), and τ is the "temperature" of the nucleus <u>after the</u> <u>evaporation</u> of a nucleon and is given by

$$\tau^{-1} = \frac{d \log \omega(E_{ex})}{dE_{ex}} \Bigg|_{E_{ex} = E_{max}} \tag{4.13}$$

or by

$$\tau^{-1} = \left(\frac{E_{ex}}{a}\right)^{1/2} \Bigg|_{E_{ex} = E_{max}}, \tag{4.14}$$

where $\omega(E_{ex})$ is the level density as a function of excitation energy E_{ex}, and E_{max} is the maximum energy of the evaporation particles. The temperatures for emitted neutrons, protons, and α particles were found to be approximately equal for 190-Mev proton

142

FIGURE 4.39. MEASURED EVAPORATION NEUTRON SPECTRA FROM
190-Mev PROTONS INCIDENT ON CARBON,
ALUMINUM AND NICKEL

143
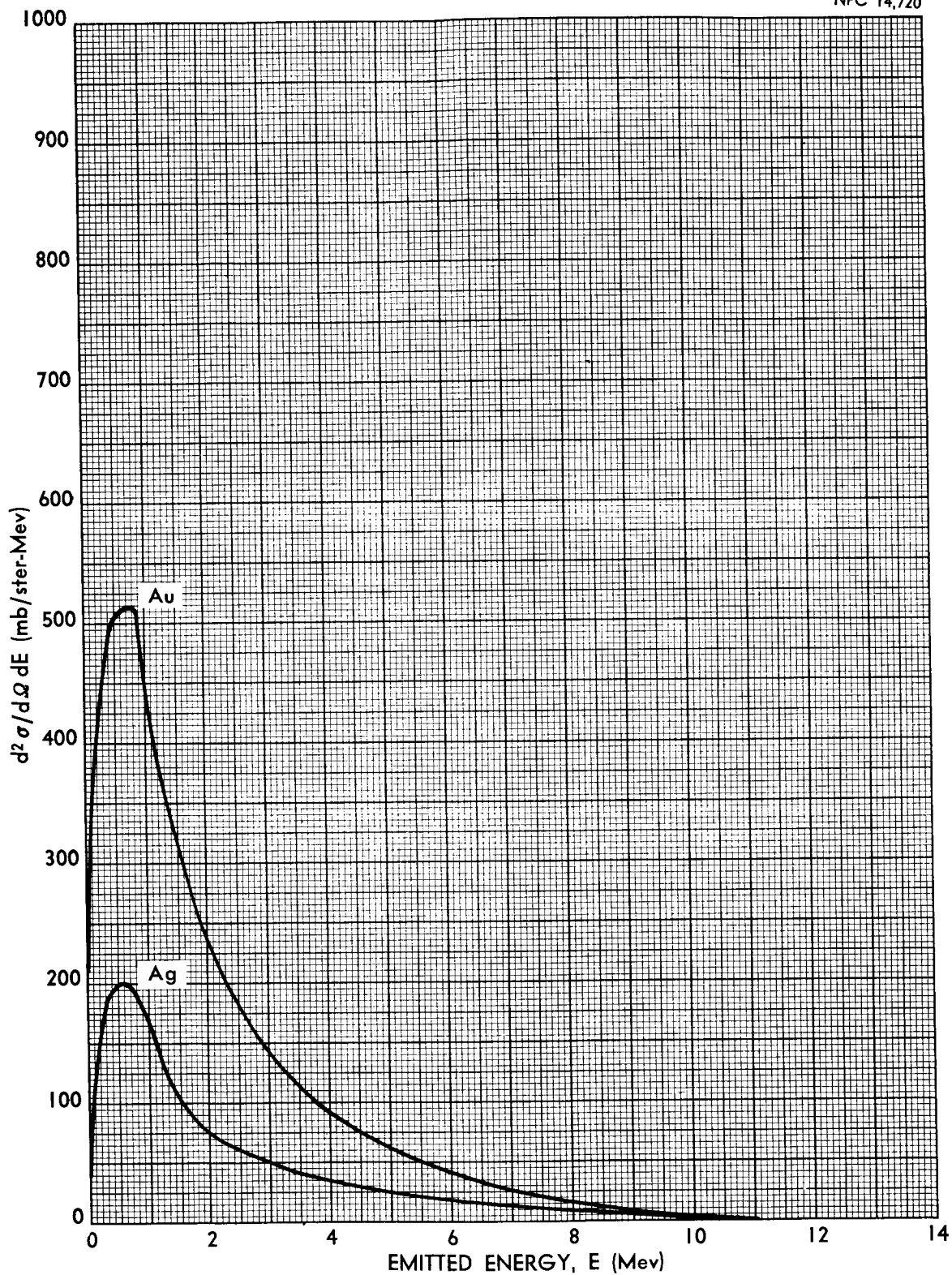
FIGURE 4.40. MEASURED EVAPORATION NEUTRON SPECTRA FROM 190-Mev
PROTONS INCIDENT ON SILVER AND GOLD

144
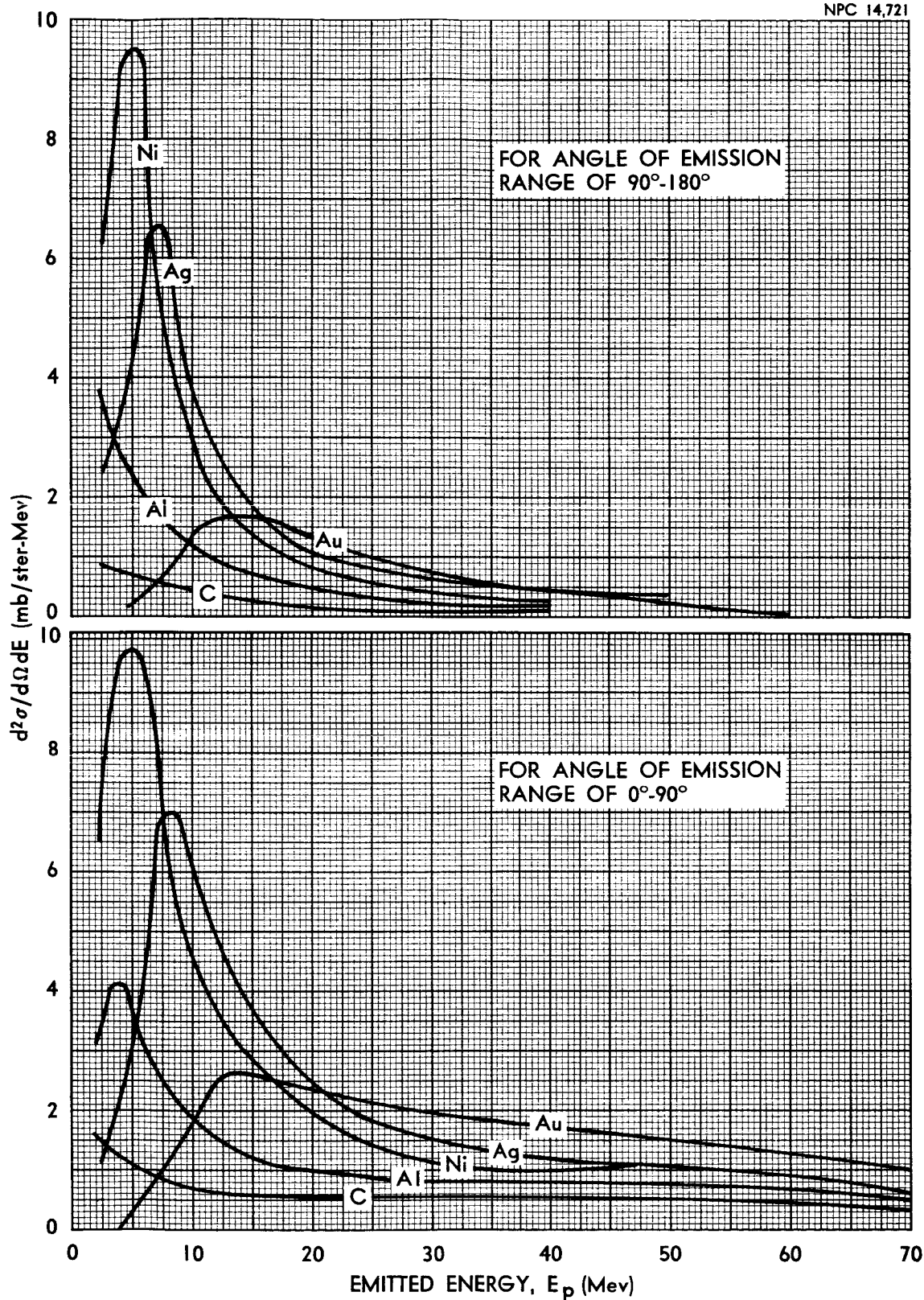
FIGURE 4.41.   MEASURED EVAPORATION PROTON SPECTRA FROM
190-Mev PROTONS FOR VARIOUS ELEMENTS

145

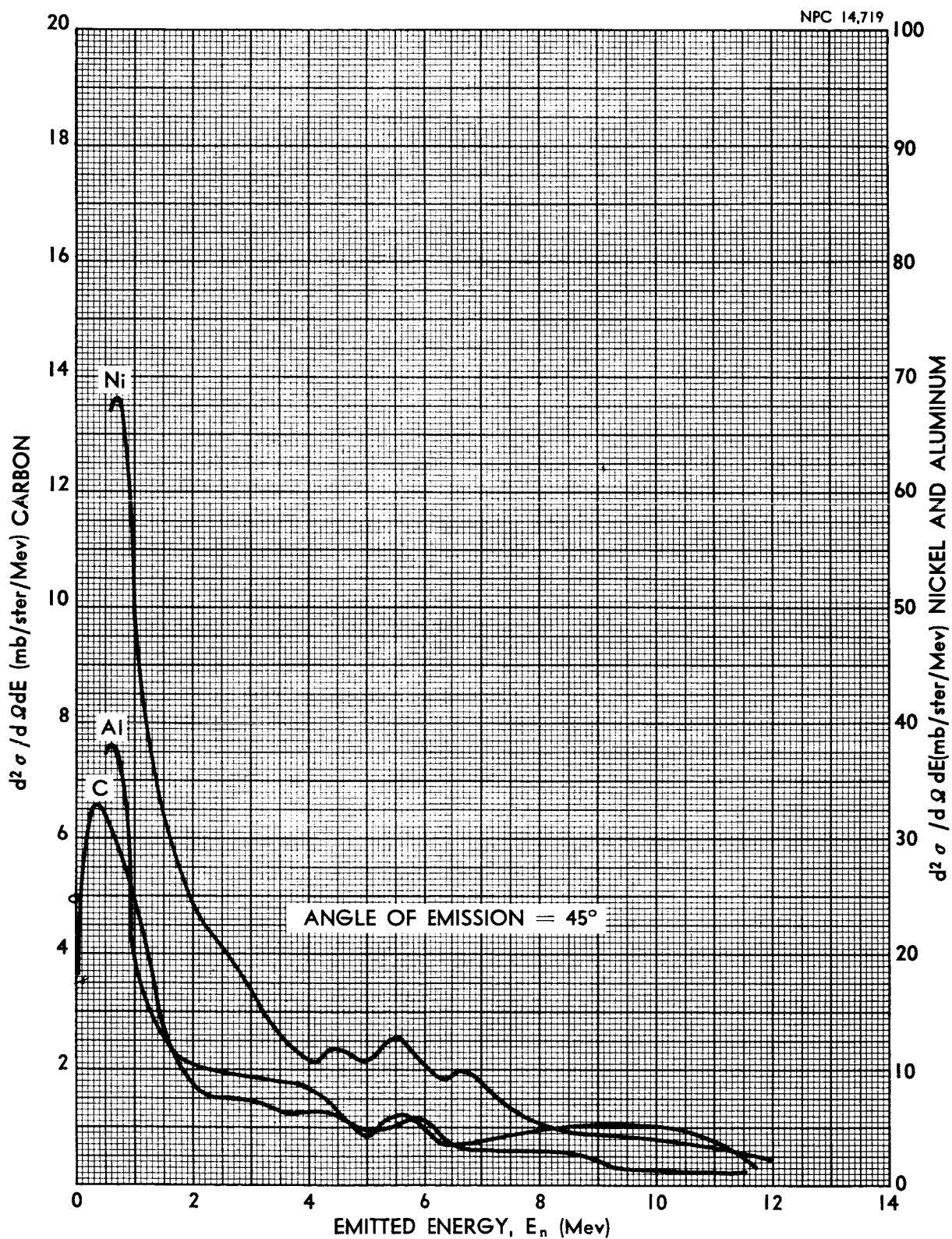bombardment (Ref. 81); however, the temperature decreased with increasing energy of emission. Since more than one particle may be emitted from the same evaporating nucleus, there is a nuclear "cooling", resulting in different values of τ.

The effect of the coulomb barrier on emitted protons is such that the evaporation peaks are broader and shifted to higher energies than in the case of neutron emission. The neutron spectra are relatively independent of the mass number of the bombarded nucleus. The spectra all peak at approximately 0.7 Mev and decrease rapidly for larger energies. For protons, the effective coulomb-barrier height increases with increasing mass number, causing the peak to increase from the 0.5-1-Mev range for carbon to approximately 17 Mev for gold. Therefore, the average energy of emitted neutrons should be fairly independent of mass number, decreasing slightly as seen in Figure 4.31. The average energies of evaporation protons show a fairly rapid increase with mass number.

4.6 Secondary Neutron Penetration - Effective Removal Cross Sections

A problem encountered in the treatment of secondary neutrons produced by proton bombardment is the determination of a suitable method for attenuation of these neutrons through the remainder of the shield. Since these neutrons may possess energies up to the incident energy, their subsequent interactions must be considered. In addition, it is desirable to investigate the effect of using average energy of emission for secondary particles, i.e., the effect of a change in spectrum during penetration.

The quantity of ultimate interest is the dose rate contributed by the secondary neutrons at the detector position. Therefore, the possibility of using an effective removal cross section for dose-rate attenuation was investigated. This approach, introduced in Section 3.2.2.2 (Eq. 3.19), requires adequate flux-to-dose conversion factors. Very little data exist for flux-to-dose conversion factors at high energies. Gibson (Ref. 30) calculated the energy removed from the neutron beam by assuming that the neutron lost 50% of its energy in a collision with a hydrogen nucleus and all of its energy in a nonelastic interaction with a heavy nucleus. Since much of the energy lost in a nonelastic interaction at high energies is transferred to secondary nucleons and is not all imparted to matter at the point of collision, this assumption is certainly an overestimate, providing, therefore, an upper limit to the flux-to-dose conversion factor $\frac{\text{rads/neutron}}{\text{hr/cm}^2\text{sec}}$.

The only additional data available are given by the measurements of absorbed energy in tissue obtained by Shal'nov (Ref. 88) and are shown in Figure 4.42 along with the energy removal calculation. The measurements were obtained up to an energy of 300 Mev and the results were extrapolated out to 1 Bev.

Two Monte Carlo procedures were used for the penetration calculations in carbon. In the first, the flux spectra and dose rates were calculated for monoenergetic point isotropic sources of 60-, 200-, 400-, and 1000-Mev neutrons in infinite media. An additional calculation, using the second procedure, with an

147
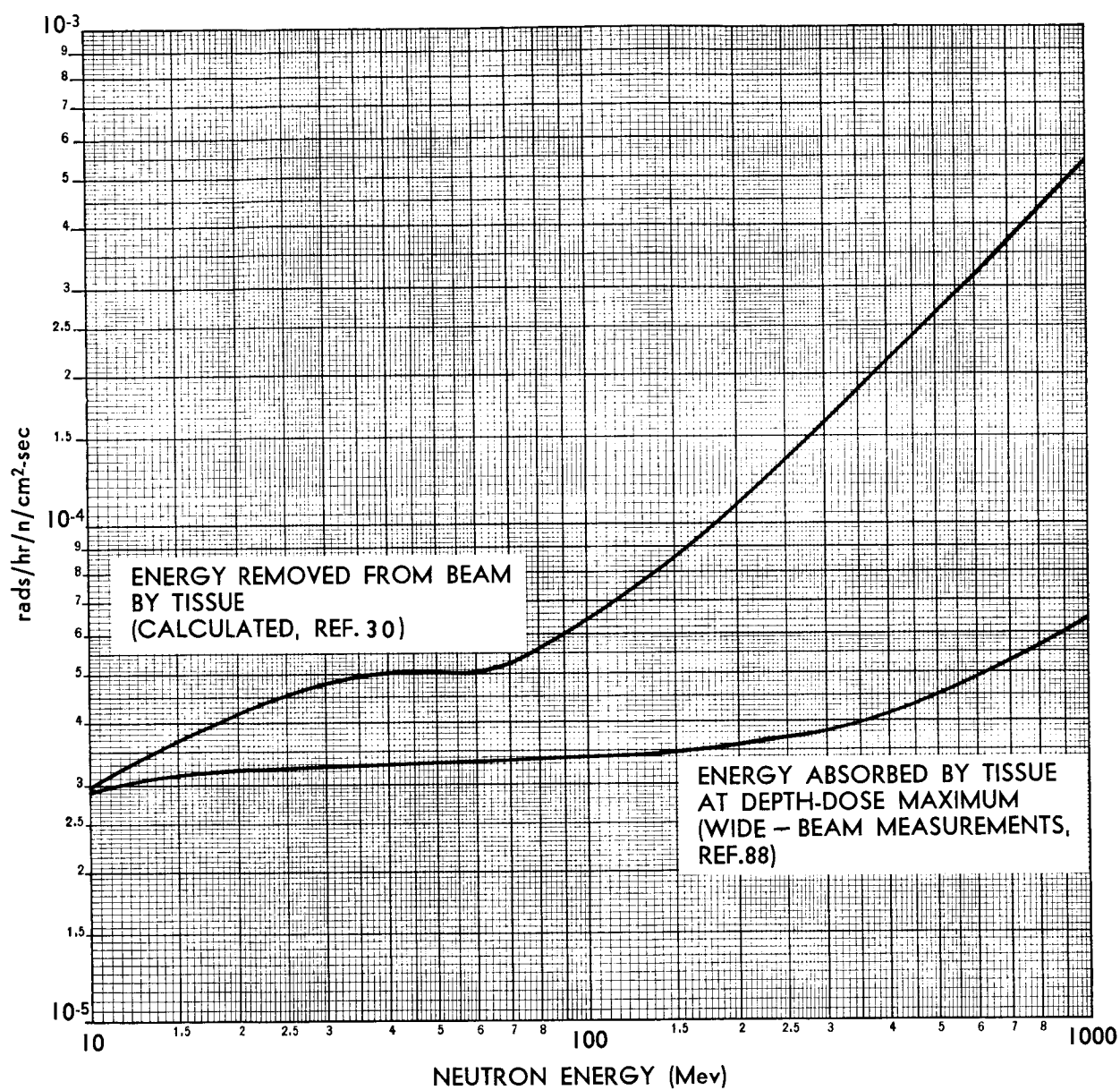
FIGURE 4.42. NEUTRON FLUX-TO-DOSE CONVERSION FACTORS

infinite plane monoenergetic source of 1000-Mev neutrons was obtained in order to determine the effects of different source angular distributions.

At each collision the energy spectra and angular distribution of elastic scattered and nonelastic secondary neutrons, as well as the average number of secondary neutrons produced, were considered, using the data for carbon presented in the previous sections. The energy spectra for aluminum at 460 and 1840 Mev were assumed to apply to carbon.

The results of the calculations using Shal'nov's conversion factors are shown in Figure 4.43, where $4\pi R^2$ times the dose rate from a point isotropic source is presented and compared, in the 1000-Mev case, to the dose rate from an infinite plane source. The geometrical attenuation has therefore been removed from the point-isotropic results for this comparison. The results for the point isotropic and infinite plane source show the same general trends, although the shapes are somewhat different. The dose rates are seen to increase initially with penetration distance and then fall slowly for increasing thicknesses. This lack of attenuation is, of course, a result of the relatively large production of secondary neutrons from nonelastic collisions at high energies. The initial dose-rate buildup is, in fact, probably higher than indicated by these results, since the Monte Carlo penetration programs did not permit consideration of secondary protons or pions, which could add considerably to the dose rate. The curve for 4-Mev neutrons calculated from the NDA moments method data (Ref. 89) is also shown.
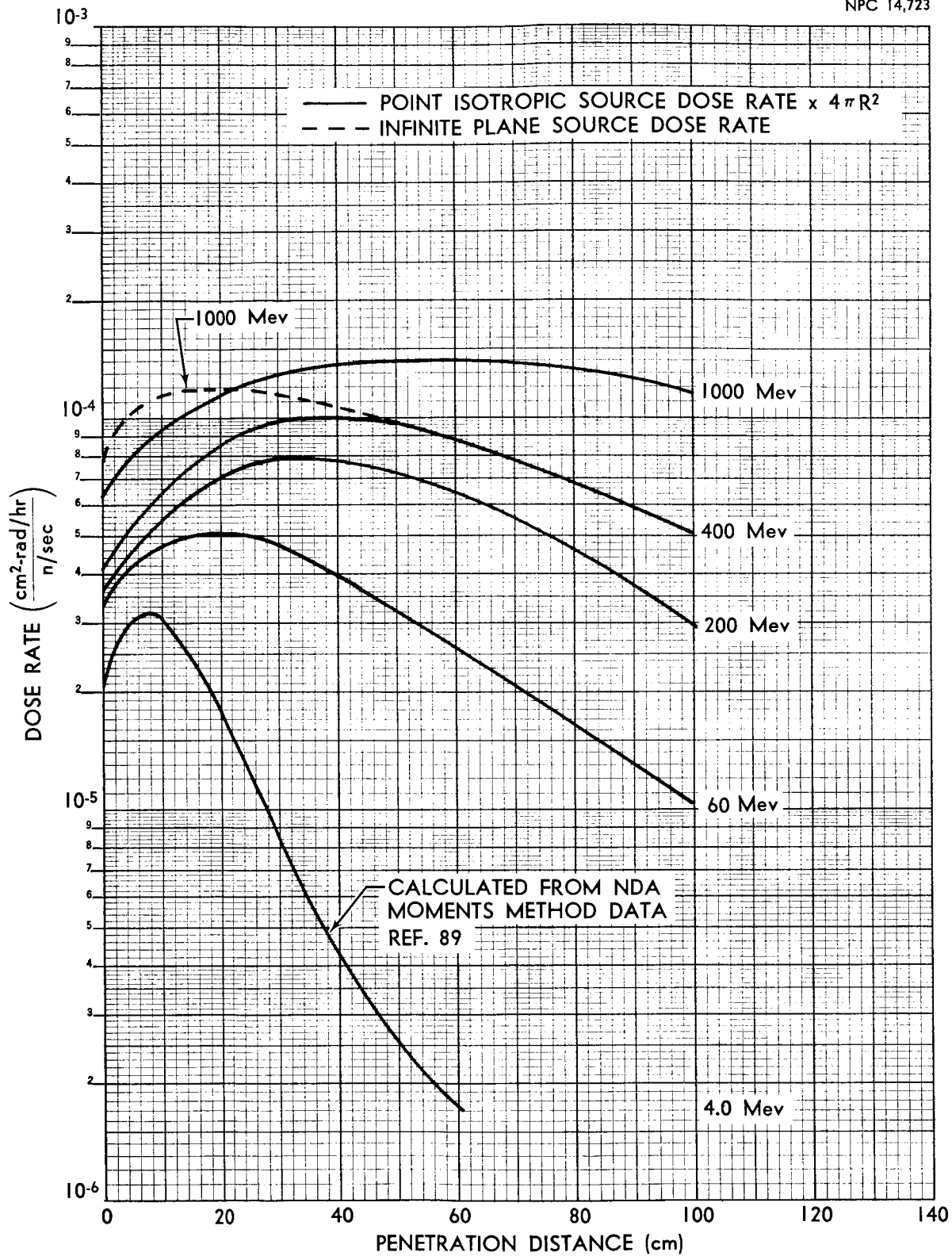
**FIGURE 4.43.   NEUTRON DOSE RATE IN CARBON USING
MEASURED CONVERSION FACTORS**

If the calculated flux-to-dose conversion factors of Figure 4.42 are used, the dose rate is much higher but shows considerably less buildup with penetration distances because of the rapid increase in flux-to-dose conversion factor. These results, shown in Figure 4.44, were used in the proton penetration procedure (PAP) in conformity with the upper-limit philosophy of Section III.

The effective removal cross sections $\Sigma_r(E)$ as a function of secondary neutron energy are defined by

$$\Lambda(t,E) = \frac{4\pi R^2 D}{D_o} = e^{-\Sigma_r t}, \qquad (4.15)$$

where D_o is the source strength multiplied by the flux-to-dose conversion factor at the initial energy E, t is the penetration distance, D is the dose rate from a point isotropic source of neutrons, and $\Lambda(t,E)$ is the transfer function of Equation 3.19. The form of this equation certainly does not agree with the results of Figures 4.43 or 4.44 (the fit for Fig. 4.44 is much better at the higher energies, at least) and Σ_r is found to depend on thickness. However, over a limited range of approximately 30 cm an average of Σ_r may be used as a first approximation.

To obtain some idea of the error introduced by the use of average energy of emission in place of an energy spectrum for secondary-neutron calculations, the following problem was considered. The secondary-neutron spectrum from 1840-Mev protons incident on Al given in Figure 4.38 was assumed to be applicable

151
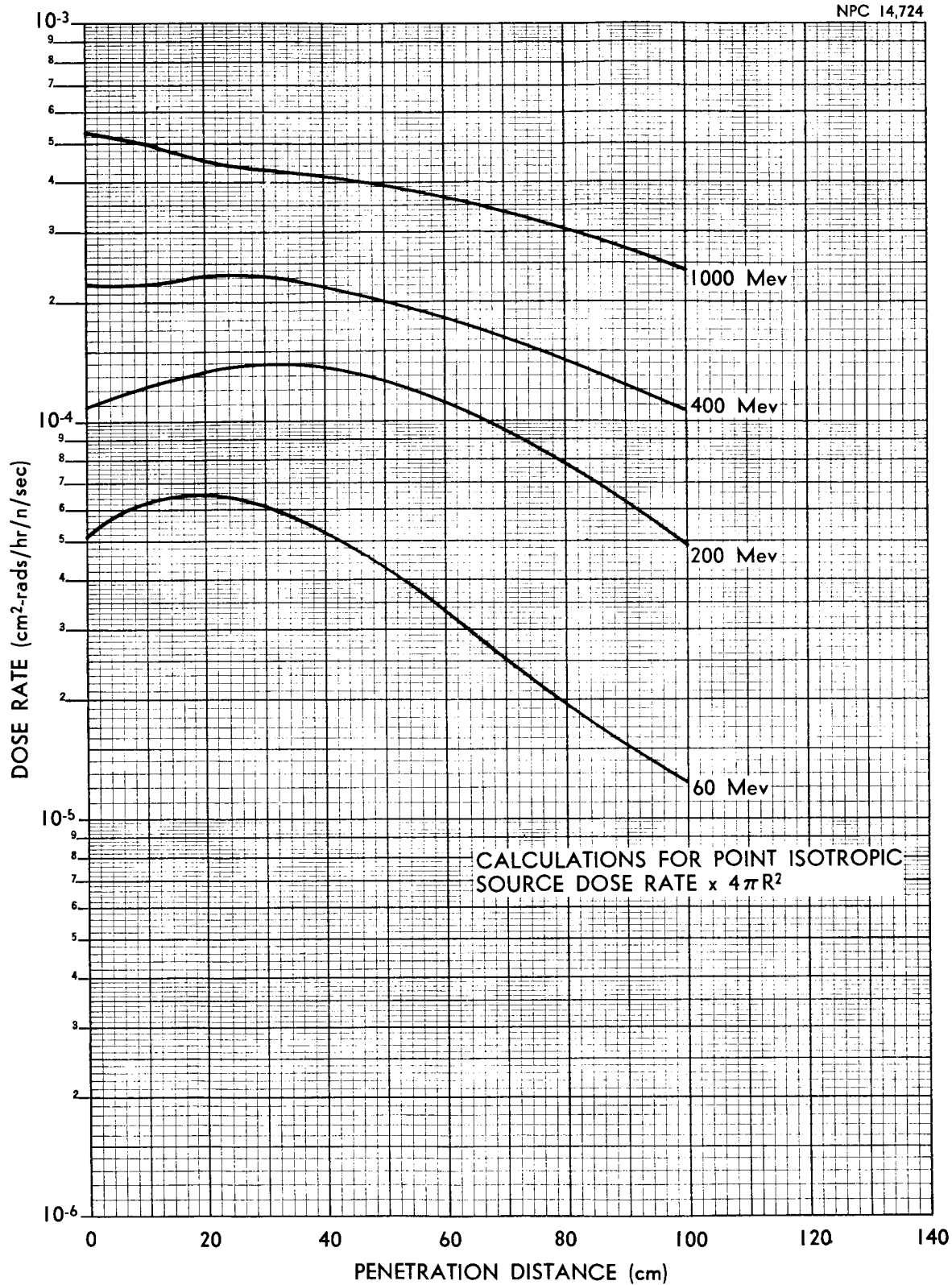
**FIGURE 4.44.   NEUTRON DOSE RATE IN CARBON USING
CALCULATED CONVERSION FACTORS**

152

to a carbon medium. This spectrum was used to determine the dose rate for penetration of 30 cm of carbon, using the results of Figure 4.43 at 30 cm, to determine the dose-rate contribution as a function of secondary-neutron energy.

The dose rate obtained using an average energy of emission (170 Mev for this spectrum) and the data from Figure 4.43 was 33% higher than the dose rate obtained using the energy spectrum. The effective energy was found to be 90 Mev for this thickness of carbon, considerably lower than the average energy of emission.

Similar calculations for the spectrum resulting from 460-Mev protons (Fig. 4.41) gave a dose rate using average energy of emission which was 19% higher than that obtained using the energy spectrum. The effective energy in this case was 75 Mev - much closer to the average energy of emission, 115 Mev, than in the previous case.

These results show that considerable care is necessary in calculating secondary-neutron penetration. It was found that, (1) use of an average energy for secondary neutrons is not too well justified for high-energy primaries, and (2) tertiary and higher-order reactions are of considerable importance for high-energy neutron penetration. Better methods of applying these results in secondary-neutron penetration are needed. One improvement would be the addition of a buildup factor in Equation 4.15.

4.7   Dose-Rate Definitions in PAP

Determination of the energy transfer to tissue by ionizing radiation is generally based on the LET (linear energy transfer),

i.e., the energy loss, dE/dx, of the particle due to ionization and excitation of electrons in the tissue. This term is evaluated at the surface of, or as a function of depth in, the body, and then can be integrated to find the total body dose. The manner of energy deposition for neutrons in tissue is considered to be by collision with hydrogen atoms which, after being torn from their molecule with very little energy loss, are assumed to lose energy by the typical process described above. These processes of energy transfer for neutrons and protons will be called soft collisions, or non-nuclear reactions.

The definition of the flux-to-dose conversions for neutrons and protons used in PAP is based on the premise that not only soft collisions but also hard (nuclear inelastic) collisions contribute to the transfer of a particle's energy to the tissue. When both hard and soft collisions are included in the definition of the LET for a nucleon, the mechanics of energy deposition of secondaries resulting from the hard collisions must be considered. Because of the obvious problems in considering the energy-loss history of each type of secondary produced by the inelastic collision of a nucleon and a heavy nucleus in the tissue ($C_7 H_{70} O_{32} N_2$), it will be assumed that all the incident-particle energy is given up at the point of reaction. This consideration certainly results in an overestimate of true flux-to-dose conversion; however, until Monte Carlo studies suggested by Gibson at ORNL (Ref. 30) are used to investigate the volume distribution

of energy deposition in the body, it is a better estimate than the simple soft-collision approach. The LET for a nucleon in tissue, using the combined soft- and hard-collision definition, is given by the equation

$$(dE/dx)_{H+S} = (dE/dx)_H + (dE/dx)_S ,$$

where $(dE/dx)_S$ for ionizing particles is the simple ionization and excitation energy loss of the particle per unit path length for the energy incident at the surface of the tissue target;

$(dE/dx)_S$ for neutrons is $\Sigma_{n-p}(E) \cdot E/2$, with $\Sigma_{n-p}(E)$ equal to the macroscopic neutron-proton cross section at the neutron energy E (under the assumption that half the energy of the neutron is given to the recoil hydrogen nucleus per collision);

$(dE/dx)_H$ for a nucleon is $[\Sigma_O(E) + \Sigma_N(E) + \Sigma_C(E)] \cdot E$, with $\Sigma_O(E)$, $\Sigma_N(E)$, and $\Sigma_C(E)$ equal to the macroscopic nuclear absorption cross sections at the incident target energy, E, for oxygen, nitrogen and carbon, respectively.

The flux-to-dose conversions $(dE/dx)_{H+S}$ for neutrons and protons using the above assumptions are shown in Figure 4.45. In conclusion, the definition of "skin dose" is based on the selection of a differential depth, dx, below the body surface, over which the energy of an incident particle does not change appreciably except by nuclear collisions.

The biological dose, $D_B^S(E)$, due to the various components is given by the equation

$$D_B^S(E) = \int_0^E dE_x \; \bar{\phi}_S (E_x) \; dE_x/dx \; F_S(E_x) ,$$

155
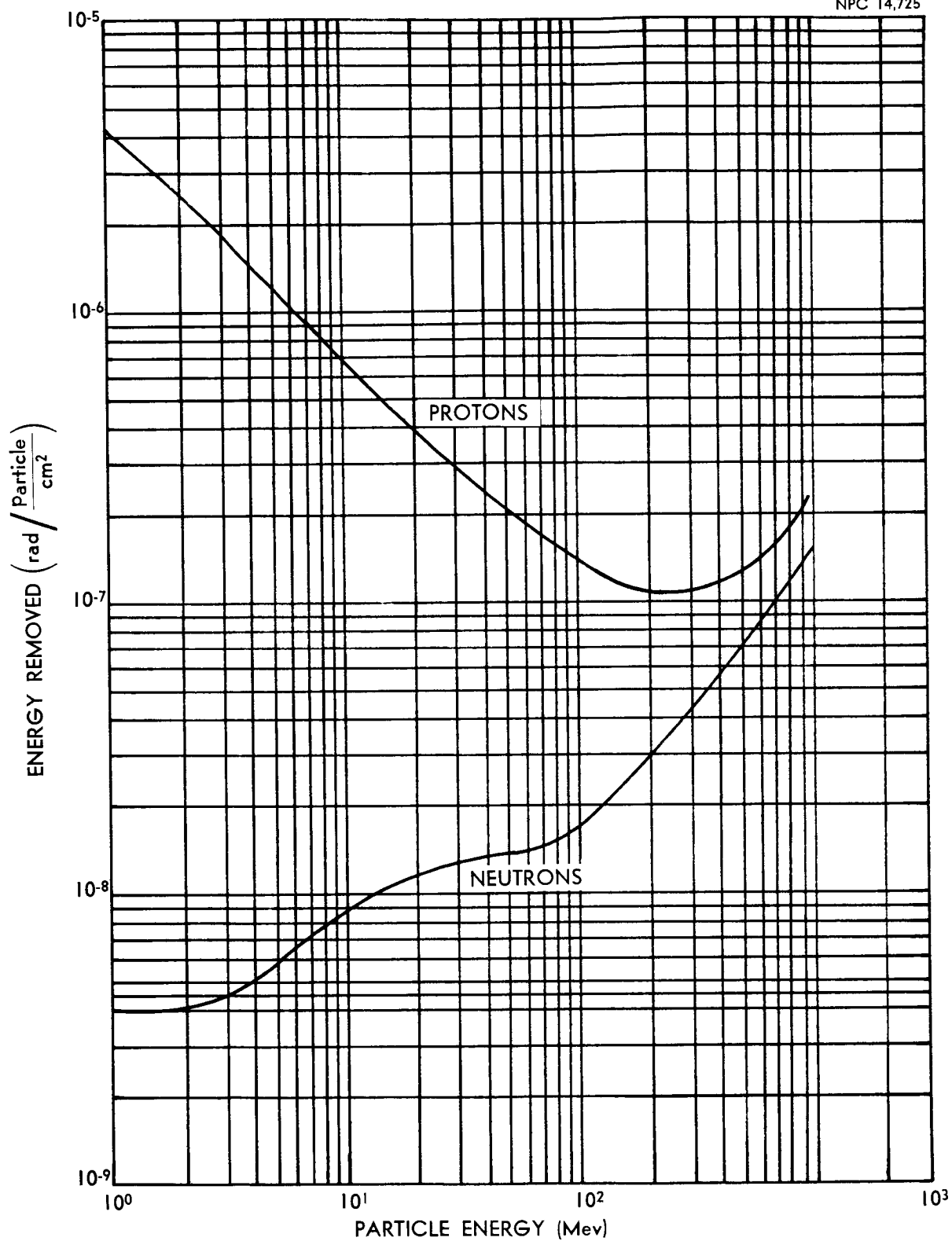
FIGURE 4.45. ENERGY DEPOSITION IN TISSUE FOR PROTONS AND NEUTRONS

where $\phi_S(E_x)$ is the differential energy spectrum for particles of type S at the target as a function of energy E_x at the target;

dE_x/dx is the LET of the particles, determined at the surface of the target, for both hard and soft collisions;

$F_S(E_x)$ is the RBE for the S-type component as a function of energy.

The physical dose $D_P^S(E)$ reported in Section V is obtained by letting $F_S(E_x) = 1$ and integrating the above equation. Thus, in order to determine the biological dose due to the various components of radiation on the basis of data in Section V, an average RBE, $\overline{F}_S$, must be defined such that

$$D_B^S = D_P^S \overline{F}_S$$

It is believed that, commensurate with the approximations necessary to define the physical dose, the following average RBE's can be used:

TABLE XIV

Representative Average RBE Values

Component	RBE
Primary protons	2
Secondary protons	5
Cascade neutrons	1
Evaporation neutrons	5

A very good review of this subject is given by Schaefer (Ref. 28) and the NBS Handbook (Ref. 29).

V.   RESULTS OF SHIELDING CALCULATIONS

5.1   General Remarks About the Calculations

A computer program for solution of the equations developed
in Section III was used to calculate the physical dose (energy
deposited/unit length) as a function of shield thickness for
several shield combinations and proton spectra. The primary
objective in the generation of these data was to evaluate the
possible biological hazards arising from the secondary radiation
produced in the shield. It was conjectured that the primary
component would be all important for thin shields,and only in
the case of thick shields would the contribution from secondaries
outweigh that from primaries. This condition was certainly not
the case in all the shield arrangements and spectra investigated.

The three proton spectra used in the calculations were:
Van Allen inner belt (Fig. 2.1), 23 February 1956 solar flare
(Fig. 4.1), and 10 May 1959 major solar flare (Fig. 4.1). The
most important flare type presenting a radiation hazard for the
short-duration cislunar flights proposed for the immediate future
is the 10 May 1959 low-energy-high-intensity flare. As a con-
sequence, the majority of the data reported herein is for this
flare. For low-thrust departure from the earth, the data for
Freden and White inner Van Allen proton spectra were needed for
an evaluation of the dangers inherent in passing through the
radiation belts. The possibility of the encounter of a giant
flare of the 23 February 1956 type is so remote for a short-

duration cislunar flight that only one graph (Fig. 5.7) is included for comparison purposes with the data on the other two spectra.

The material arrangements chosen were intended to simulate the integration of the structure, proton shield, and equipment for a space vehicle, i.e., the effect on the dose when the structure and material inside the shield are considered as a part of the effective shield. One case (Fig. 5.15) of a structure-proton-gamma shield was considered to look at the possibility of a prohibitively high evaporation neutron component coming from the gamma shield. No appreciable effect was observed.

5.2 Time Variation of the Intensity

In order to place confidence limits on the magnitude of the total time-integrated dose for a flare, it is necessary to know the time variation of the particle intensity in the vicinity of the earth. On the basis of data available on various effects in the atmosphere and on the earth following the 10 May 1959 solar flare (Refs. 90 and 91), the ad hoc assumption will be made that the time variation of the proton intensity in cislunar space was as shown in Figure 5.1.

The total time-integrated intensity (and dose) is an order of magnitude higher than that suggested by Foelsche (Ref. 32); however, it is not as difficult to reconcile as the multiplicative factor necessary if one handles the intensity variation as suggested by Winckler (Ref. 92) for the 14 July 1959 flare, i.e., continuous intensity decay by $t^{-2.56}$ from one hour after the flare started.

Some typical intensity variations for solar flares are
shown in Figure 5.2 (Ref. 93). For the case of the solar flare
of 4 May 1960, the total flare intensity is 222 times that measured
at the 33-hour point. Thus, if the 10 May 1959 solar flare had a
similar intensity time variation, rather than that given in
Figure 5.1, a substantially lower total flare dose would be
received.

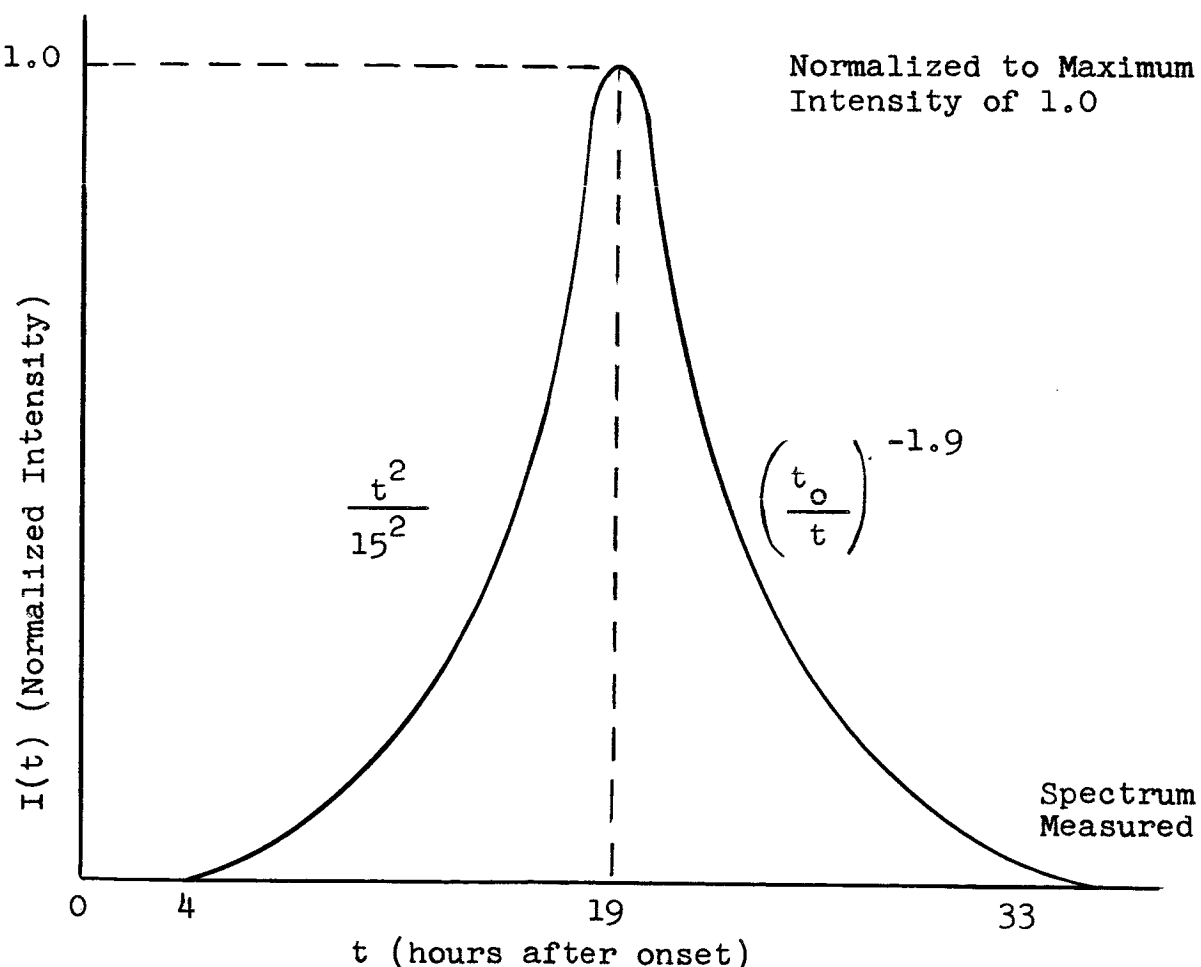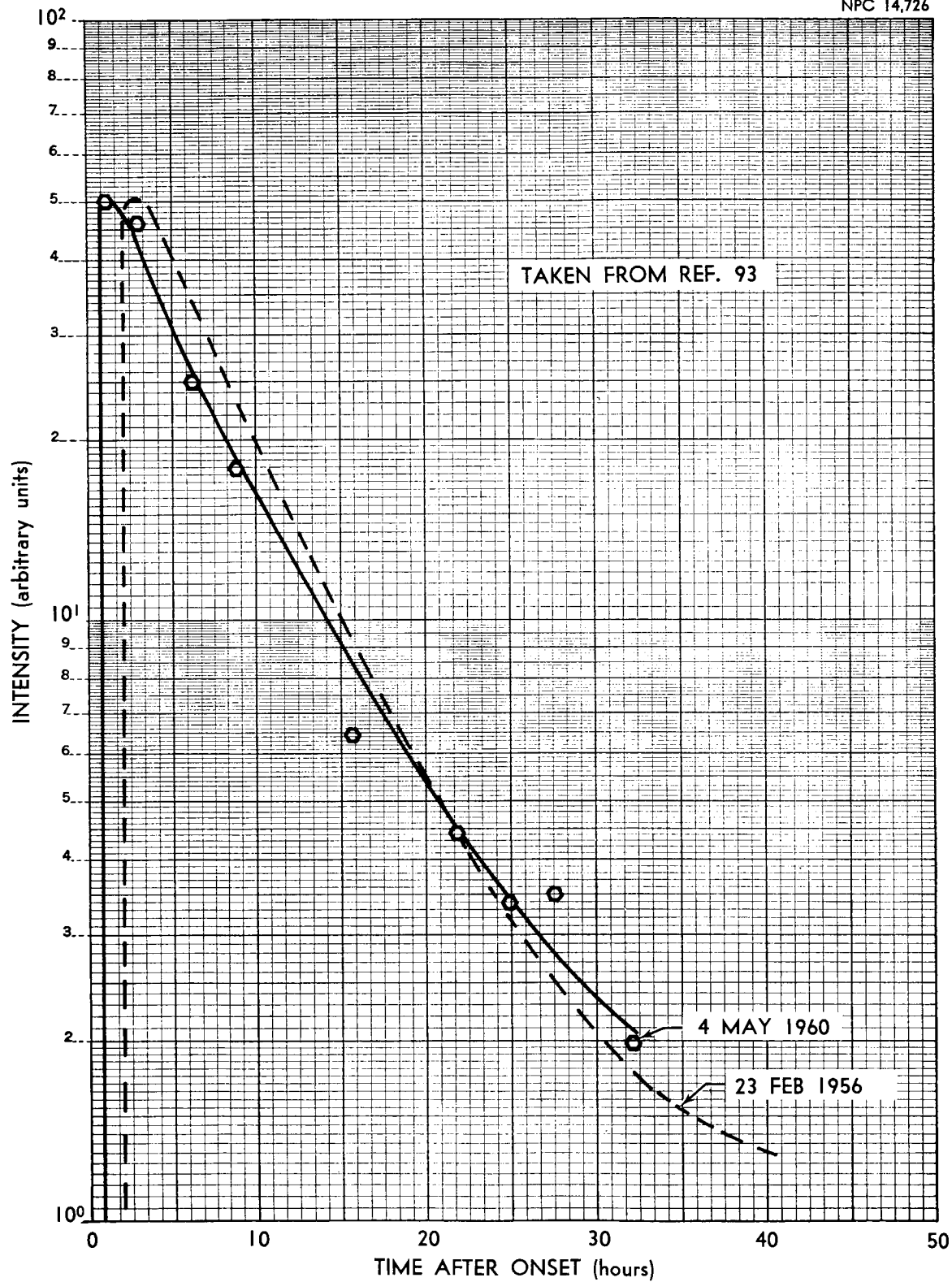Figure 5.1   Assumed Time Variation of Intensity for
the 10 May 1959 Solar Flare

TAKEN FROM REF. 93

4 MAY 1960

23 FEB 1956

INTENSITY (arbitrary units)

TIME AFTER ONSET (hours)

FIGURE 5.2. SOLAR-FLARE PROTON TIME VARIATION OF INTENSITY
IN THE EARTH'S STRATOSPHERE

162

5.3   Components of the Radiation

In the following, each component of the dose will be considered separately in relation to the particular incident spectrum used. Calculational results are shown in Figures 5.7 to 5.15.

5.3.1   Primary Protons

The dose due to primary protons was found to be the dominant component for small shield thicknesses (less than about 20 gm/cm^2) for all three spectra. The cascade-neutron and secondary-proton components generally were found to be more important for the larger thicknesses.

A most interesting feature of the primary dose is exhibited by determining the incident energies which contribute to the majority of the dose. From Equation 3.1 it is found that the primary dose is the integral of the product of three functions: two generally rapidly varying functions - incident spectrum and $S_p(E)$, the flux-to-dose conversion (Fig. 4.45) - and an attenuation function. It was found that the majority of the primary dose originated from protons with energies just above E*(t), the minimum energy to get through the shield. In Figure 5.3 is a plot of integral dose (dose due to incident protons of energy greater than a particular energy E) versus the percent of the effective spectrum, $\left[(E-E_{min})/(E_{max}-E_{min})\right]$, for a 15-gm/cm^2 shield of polyethylene and the 10 May 1959 spectrum. It should be noted that over 80% of the dose comes from the first 10% of the effective spectrum. This same general relation between percent of incident spectrum and integral dose holds

163

$$I(E) = \int_{E_{min}}^{E} dE\, D(E) \Big/ E_{max} \int_{E_{min}} dE\, D(E)$$

INTEGRAL DOSE, I(E)

PERCENT OF INCIDENT ENERGY INTERVAL $\left\{ (E - E_{min}) \Big/ (E_{max} - E_{min}) \right\}$
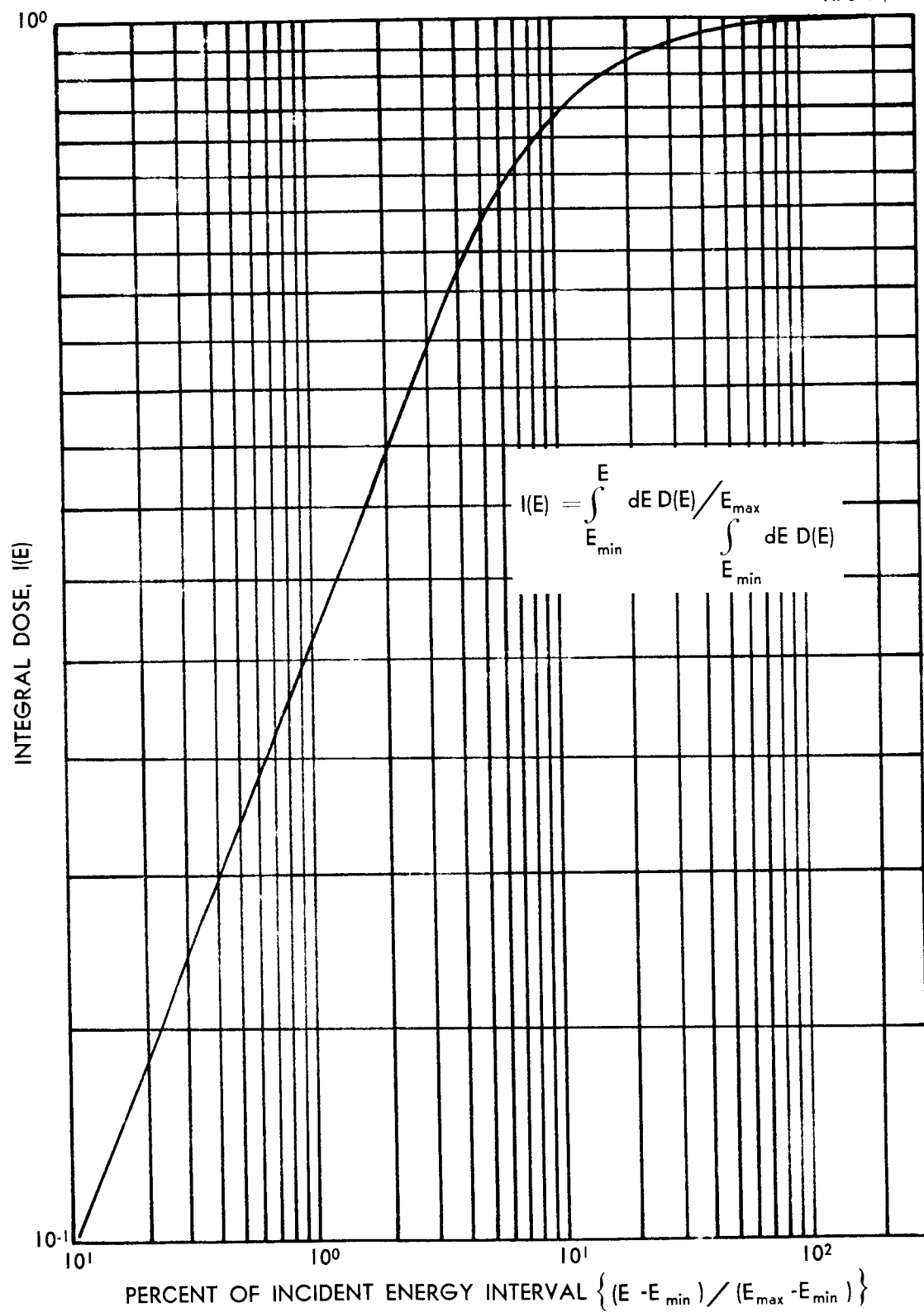
FIGURE 5.3. INTEGRAL DOSE ABOVE E_{min} FOR 15 gm/cm^2 OF POLYETHYLENE

for all the materials and spectra studied. Figure 5.4 (scale is meant only for shape comparison) shows the generally constant ratio between spectra at cutoff [intensity of incident spectra at $E*(t)$] and the dose as a function of the shield thickness, t. Thus, it would appear that Equation 3.1 could be approximated by an equation of the form

$$\int_{E*(t)}^{E_{max}} dE' \phi_p(E') S_p(E',t) \tau(E',t) \approx \phi_p[E*(t)] \int_{E*(t)}^{E_1} dE' S_p(E',t) \tau(E',t), \quad (5.1)$$

where $E*(t) < E_1 \ll E_{max}$ and the interval $[E_{max}, E*(t)]$ is large.

5.3.2 Secondary Protons

The secondary-proton component of the dose, like the primary component, is largely dependent on the shape of the incident spectrum (Figs. 5.7, 5.8, and 5.9). This statement is valid to the extent that the component may or may not be the major contribution to the total dose.

In order to understand the reasons why this component of the dose can be so important in the case of a hard spectrum like that of Freden and White, it is necessary to restate, briefly, the model used in the calculation. For each energy selected to represent the incident spectrum, that part of the incident proton flux which reacts in an interval Δx in the shield produces secondary protons of energies ranging from zero to $E(x)$, the average energy of the primary protons across that spatial interval. Some of the
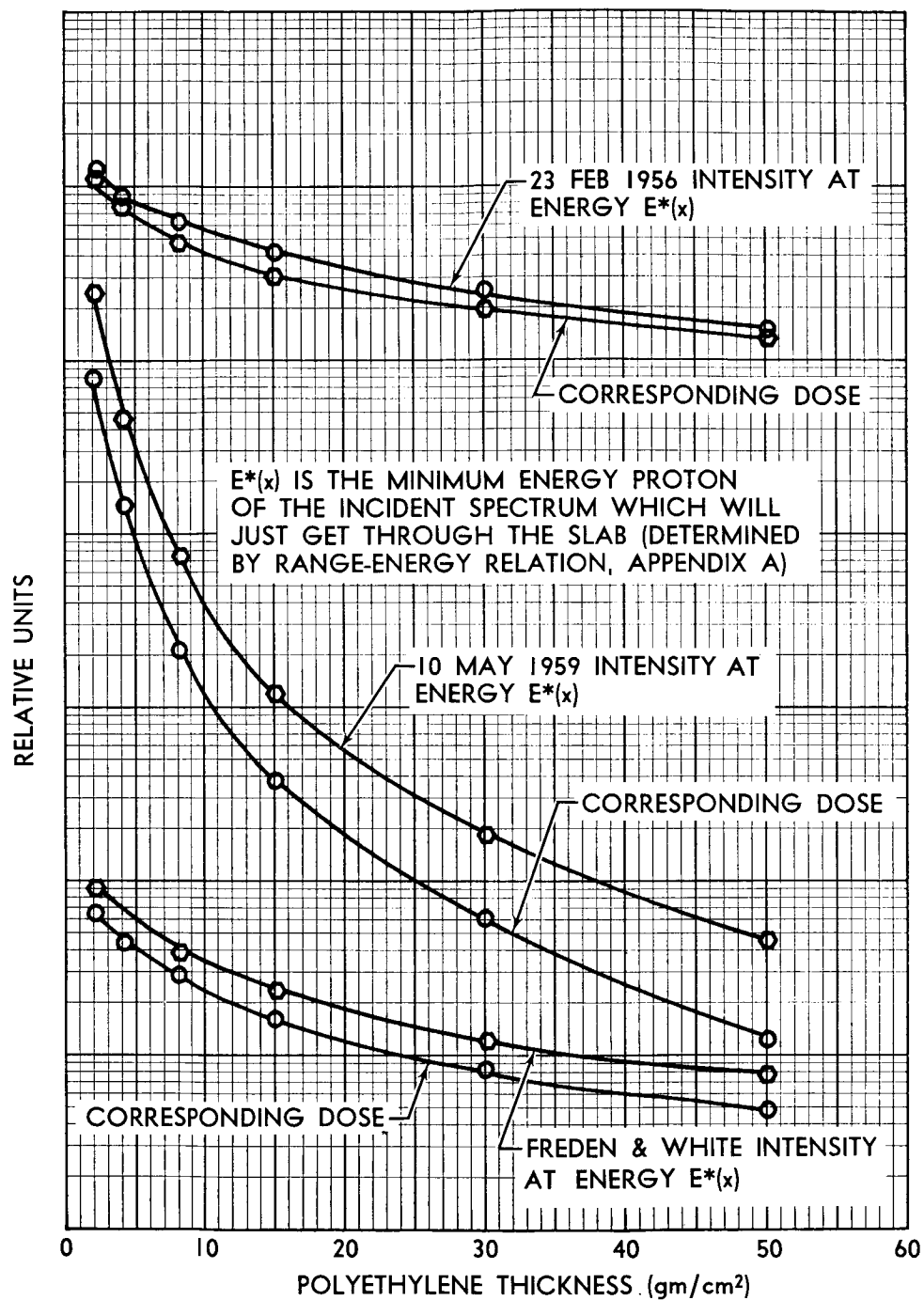
FIGURE 5.4. RELATION OF DOSE AND INCIDENT SPECTRUM INTENSITY AT E*(x) AS A FUNCTION OF POLYETHYLENE THICKNESS

166

protons born in this interval do not reach the target because
of their low energy; however, for each incident proton with energy
greater than E*(t) at the incident face, some of the secondary
protons produced get to the target, some with the maximum energy
loss occurring at the target surface. It was pointed out in
Section 5.3.1 that those protons with incident energy much greater
than E*(t) do not contribute much to the primary-proton
component of the dose. However, in the case of the secondary-
proton dose these are just the primary energies which produce
most of the high-dose secondaries. Figure 5.5 shows the spatial
distribution of the secondary-dose sources for each of the
secondary components for the Freden and White spectrum and
30 gm/cm^2 of aluminum.

5.3.3 Cascade Neutrons

This component of the secondary radiation is particularly
unique, since after its birth in the shield it experiences very
little energy degradation before reaching the target. For each
nuclear collision in the material, the neutron has an approxi-
mately equal probability of experiencing a reaction which would
lead to either tertiaries or elastic collision resulting in low-
energy loss. Thus, although the cascade neutron may not reach
the target, the tertiaries resulting from its reaction in the
shield may arrive there. This possibility is considered for
the case of tertiary neutrons through the removal cross section
and is included in the results as part of the cascade component.
The cross section for hydrogen collision in the energy range of

cascades is too low to contribute much to energy degradation, since little energy loss is experienced by the neutrons by this mechanism. Spatial distribution of cascade-neutron sources for an aluminum shield and the Freden and White spectrum is given in Figure 5.5.

5.3.4 Evaporation Neutrons

This component of the radiation is greatly influenced by the material between its source and the target. The low energy of the majority of the evaporation spectrum (Fig. 4.39) means that collision with hydrogen in the material can greatly reduce the contribution of this component. This is dramatically shown by a comparison of the evaporation-neutron dose behind an aluminum (Fig. 5.11) and a polyethylene shield (Fig. 5.9). For the case of the aluminum shield, little attenuation to the evaporation neutrons is afforded by the shield and it functions primarily as a source. In the case of the polyethylene, the evaporation neutrons are largely eliminated from consideration by high-energy-loss collisions with the hydrogen.

Spatial distribution of the evaporation-neutron dose sources is shown in Figure 5.5 for aluminum and the Freden and White spectrum and in Figures 5.6 and 5.7 for different spectra and materials.
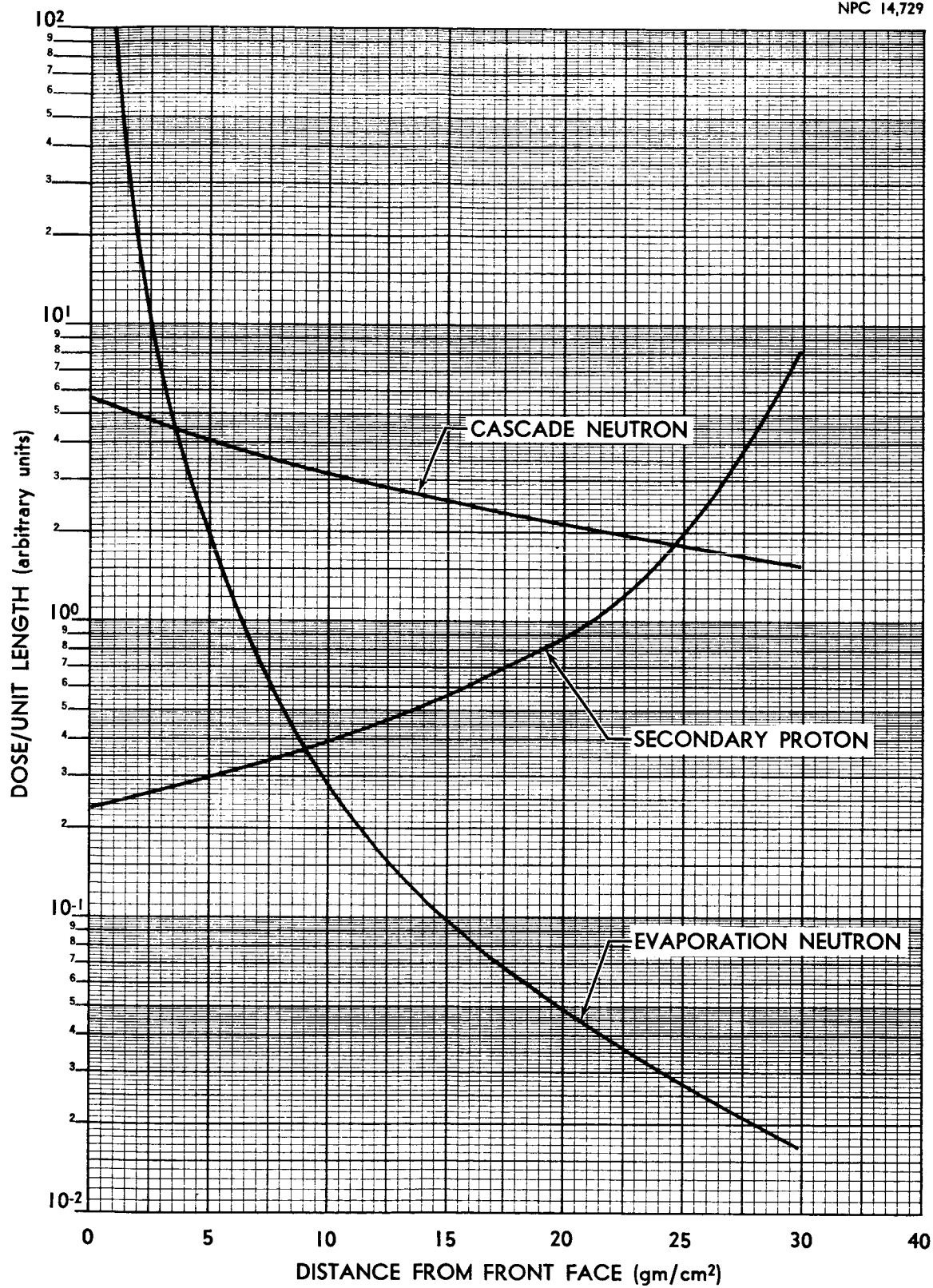
FIGURE 5.5. RELATIVE SPATIAL VARIATION OF SECONDARY DOSE SOURCES FOR ALUMINUM, FREDEN & WHITE SPECTRUM
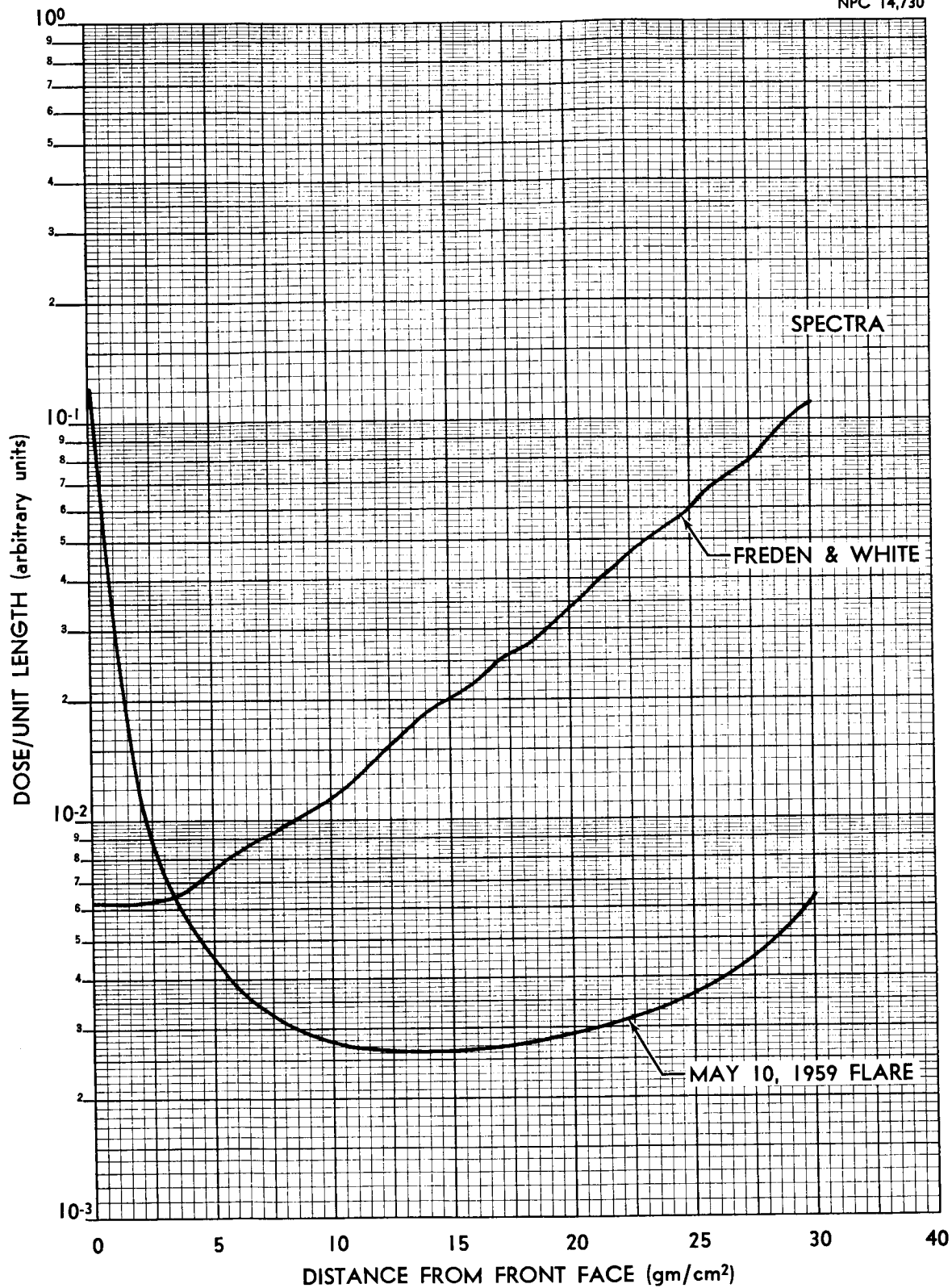
FIGURE 5.6. SPATIAL DEPENDENCE OF EVAPORATION NEUTRON DOSE SOURCES FOR 30 gm/cm² OF POLYETHYLENE

SPECTRUM: 23 FEB 1956 GIANT SOLAR FLARE, PROMPT
TOTAL DOSE CONVERSION: MULTIPLY BY 2 HOURS
MATERIAL ARRANGEMENT: THICKNESS IN TERMS OF gm/cm^2
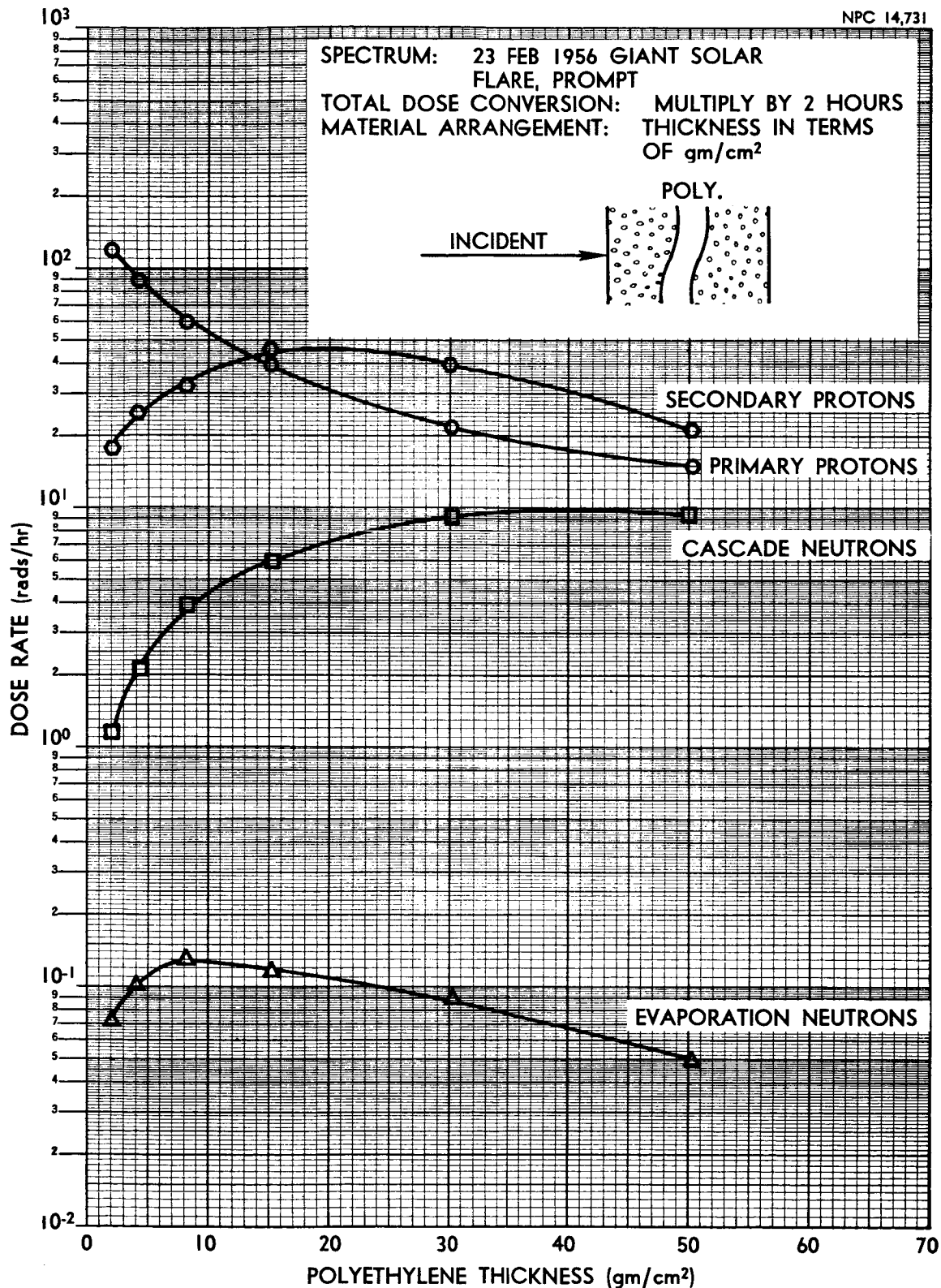
FIGURE 5.7. SINGLE-COMPONENT SHIELD (POLYETHYLENE) DOSE RATE AS A FUNCTION OF POLYETHYLENE THICKNESS, 23 FEBRUARY 1956 SPECTRUM

171

SPECTRUM: PROTON, BY FREDEN & WHITE FOR
THE LOWER RADIATION BELT
TOTAL DOSE CONVERSION: MULTIPLY BY TIME
IN THE BELT
MATERIAL ARRANGEMENT: THICKNESS IN TERMS
OF gm/cm²

POLY.

INCIDENT

SECONDARY PROTONS

PRIMARY PROTONS

CASCADE NEUTRONS

EVAPORATION NEUTRONS

DOSE RATE (rads/hr)

POLYETHYLENE THICKNESS (gm/cm²)
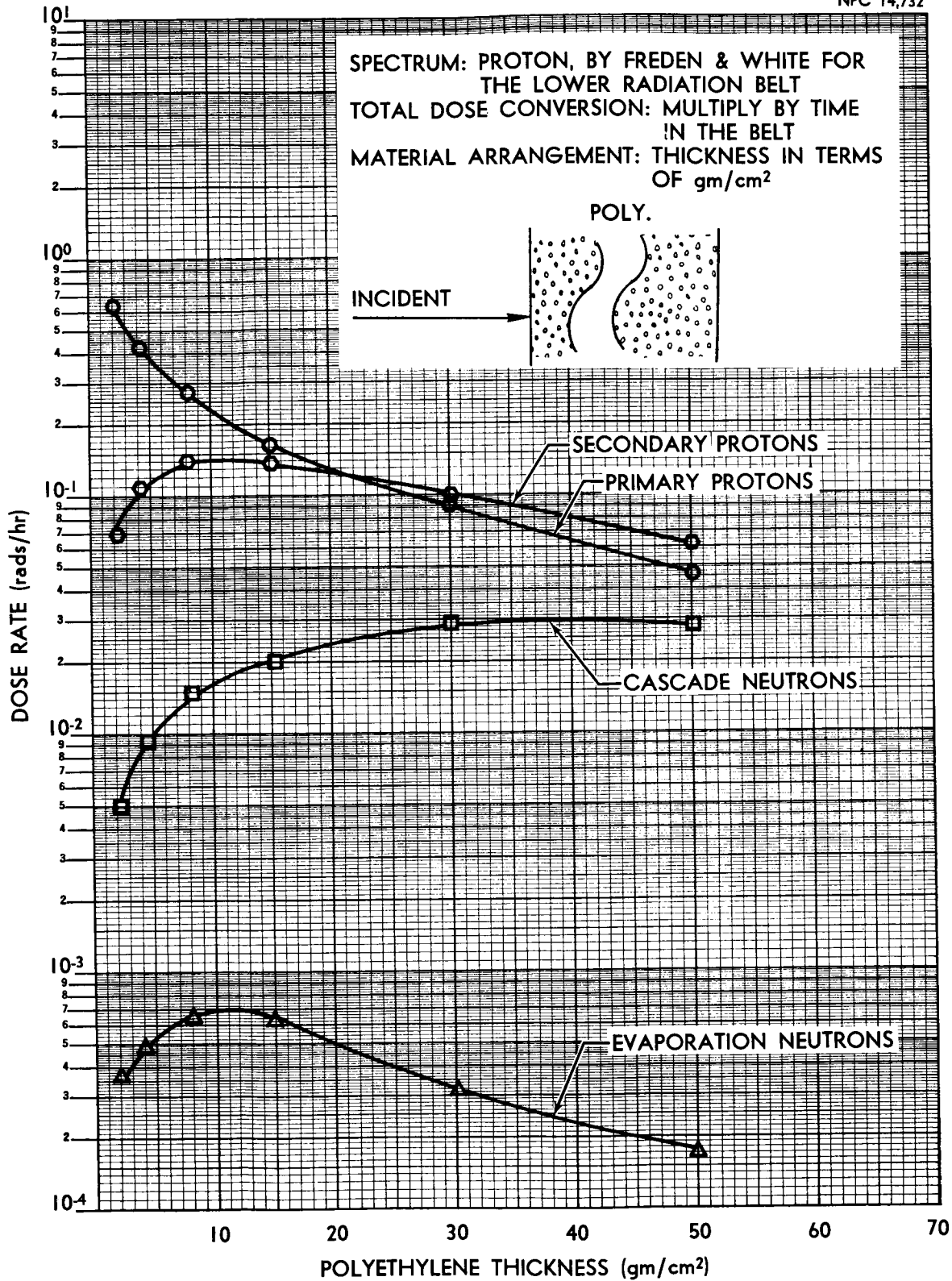
FIGURE 5.8. SINGLE-COMPONENT SHIELD (POLYETHYLENE) DOSE RATE AS A FUNCTION OF POLYETHYLENE THICKNESS, FREDEN & WHITE SPECTRUM
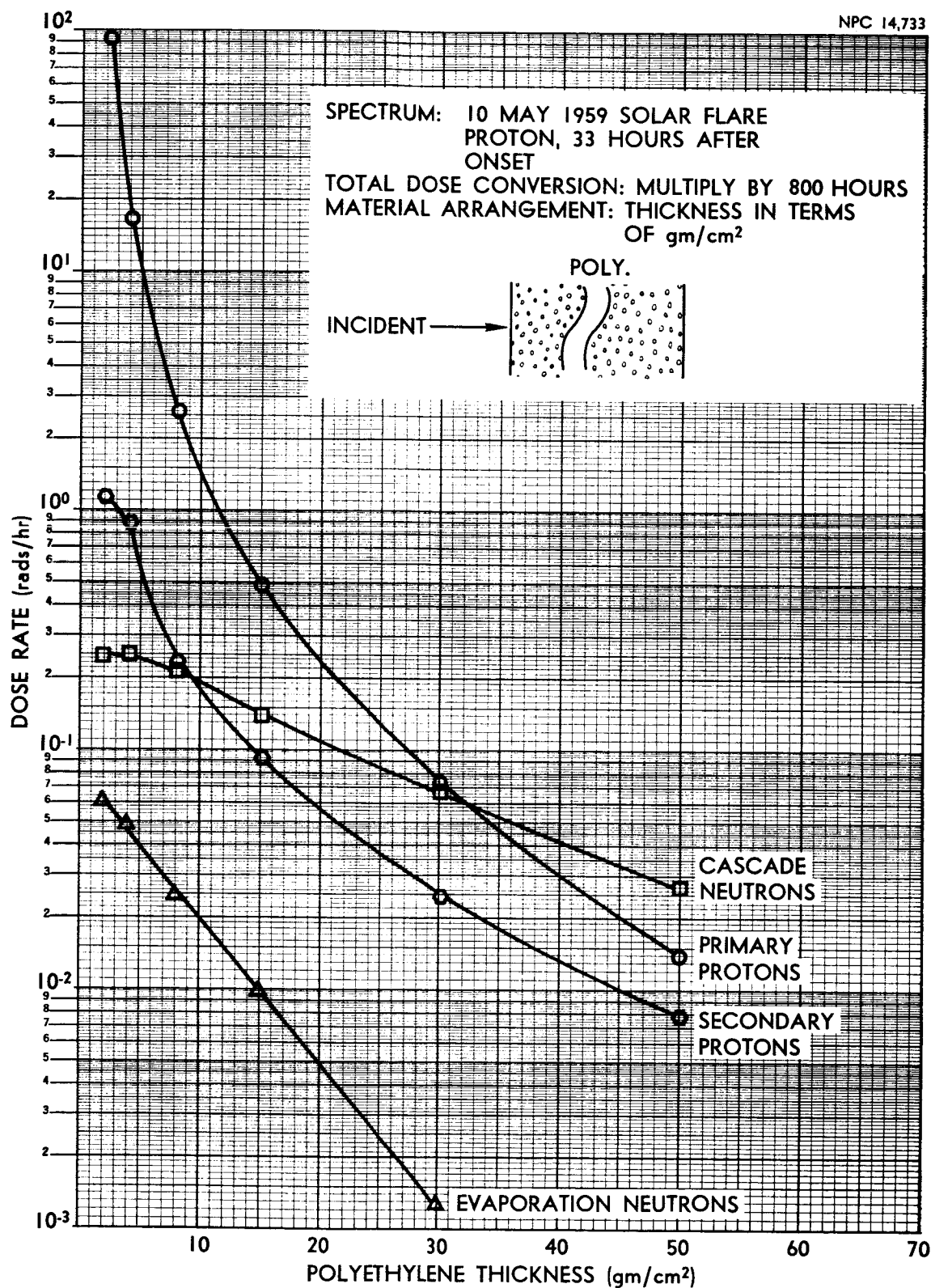
FIGURE 5.9. SINGLE-COMPONENT SHIELD (POLYETHYLENE) DOSE RATE
AS A FUNCTION OF POLYETHYLENE THICKNESS,
10 MAY 1959 SPECTRUM

173
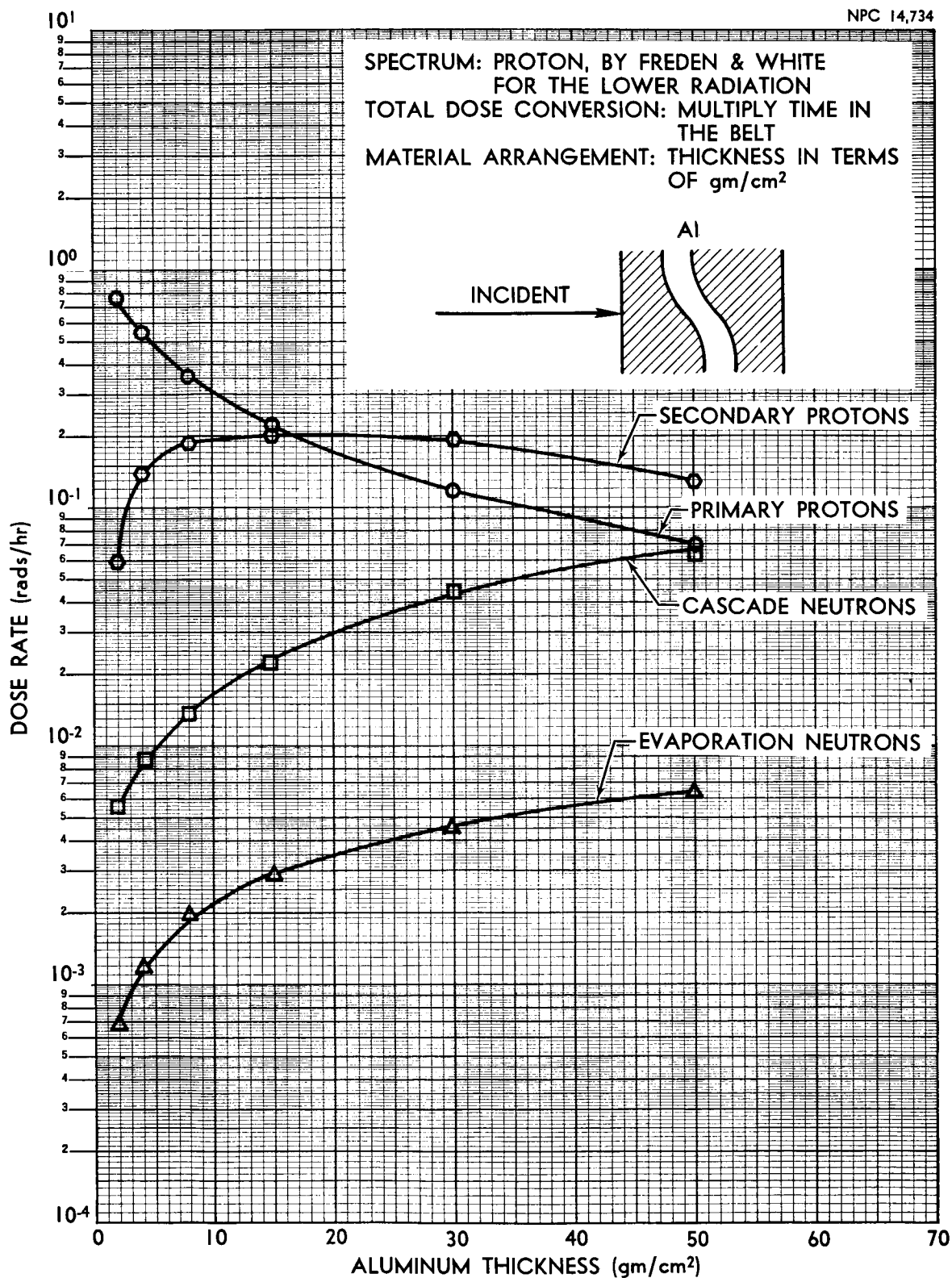
FIGURE 5.10. SINGLE-COMPONENT SHIELD (ALUMINUM) DOSE RATE AS A FUNCTION OF ALUMINUM THICKNESS, FREDEN & WHITE SPECTRUM

174
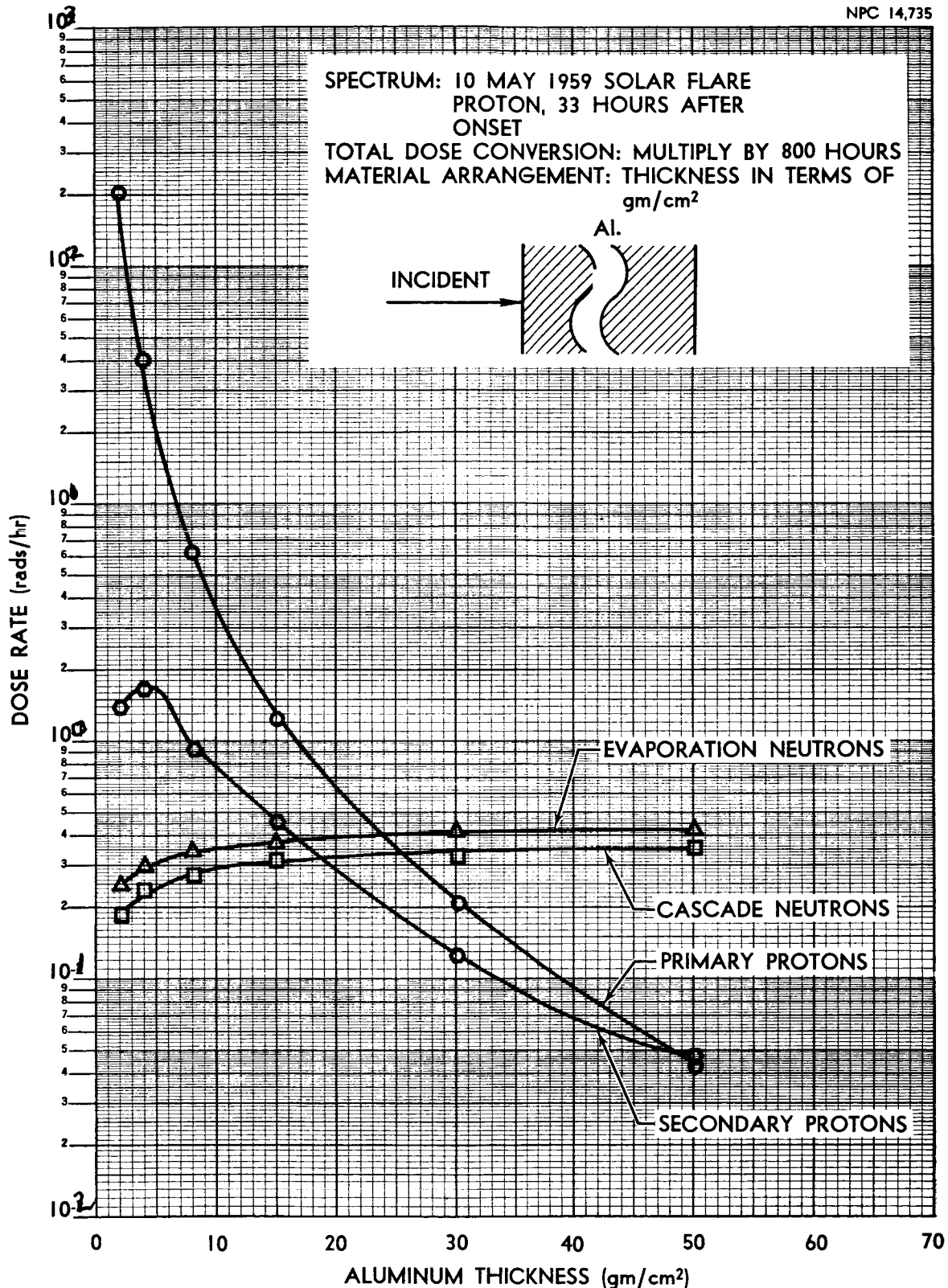
FIGURE 5.11. SINGLE-COMPONENT SHIELD (ALUMINUM) DOSE RATE AS A FUNCTION OF ALUMINUM THICKNESS, 10 MAY 1959 SPECTRUM

175
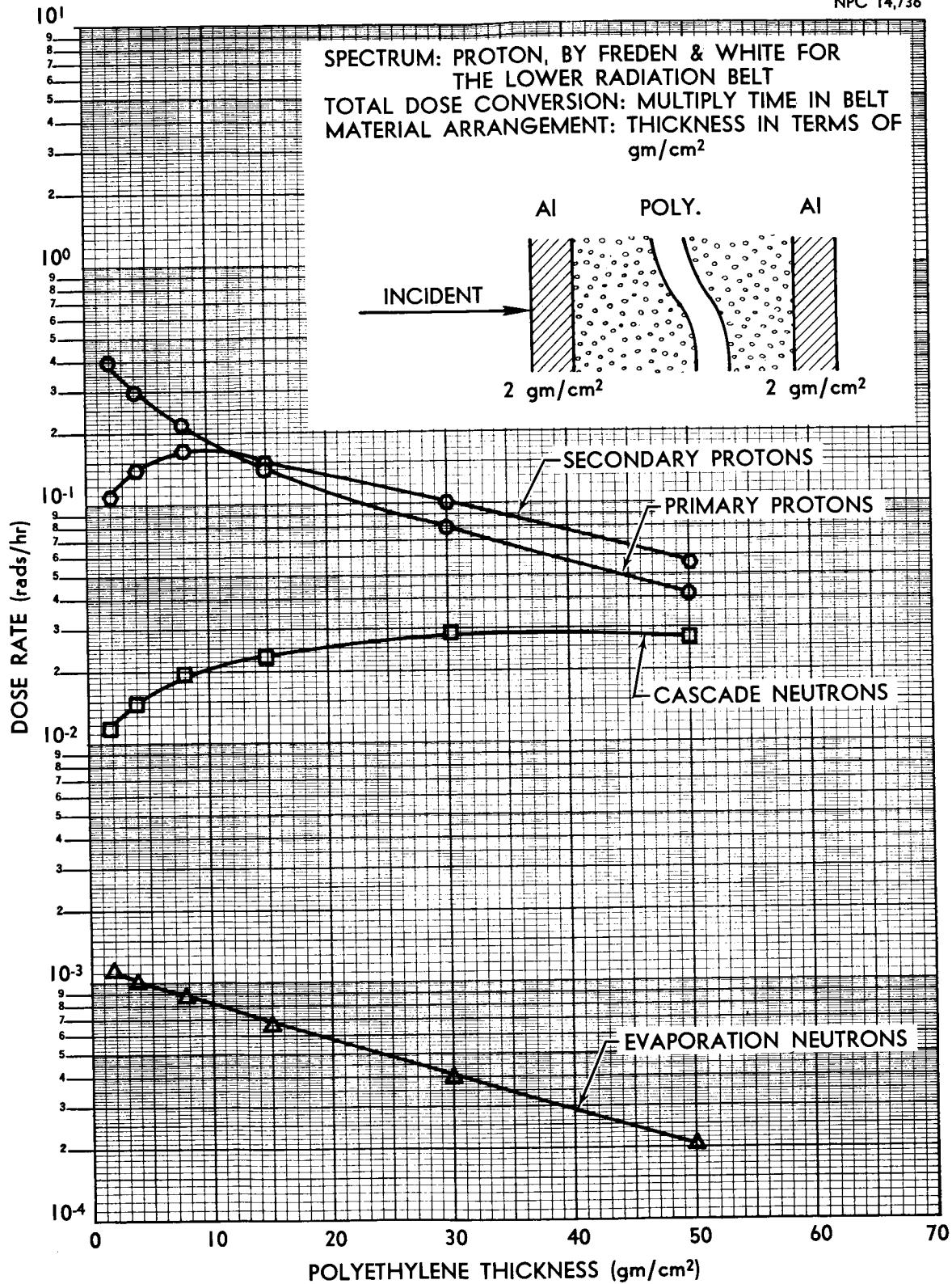
FIGURE 5.12. COMPOSITE-SHIELD (ALUMINUM-POLYETHYLENE-ALUMINUM) DOSE RATE AS A FUNCTION OF POLYETHYLENE THICKNESS, FREDEN & WHITE SPECTRUM

176
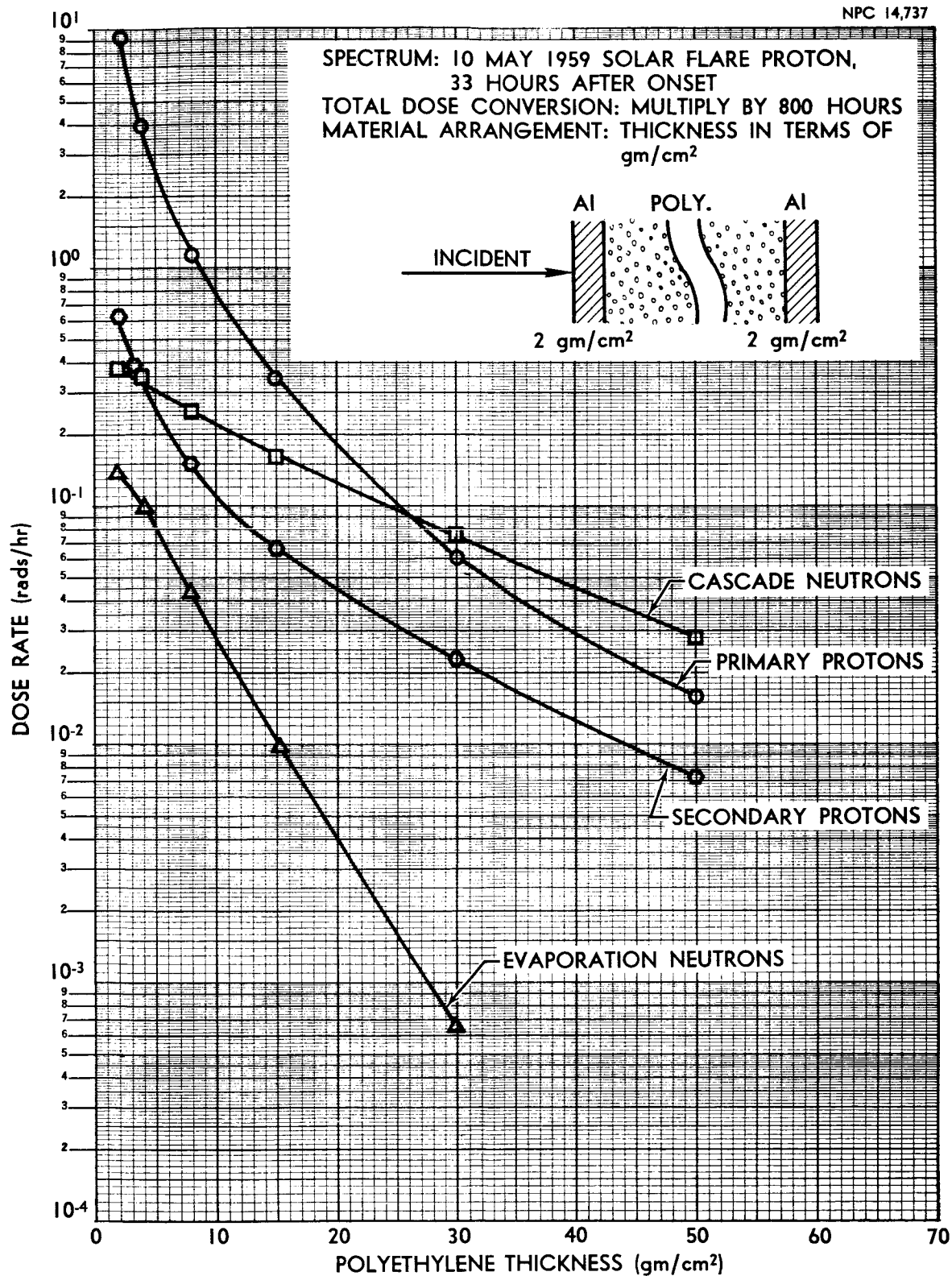
FIGURE 5.13. **COMPOSITE-SHIELD (ALUMINUM-POLYETHYLENE-ALUMINUM GEOMETRY A) DOSE RATE AS A FUNCTION OF POLYETHYLENE THICKNESS, 10 MAY 1959 SPECTRUM**
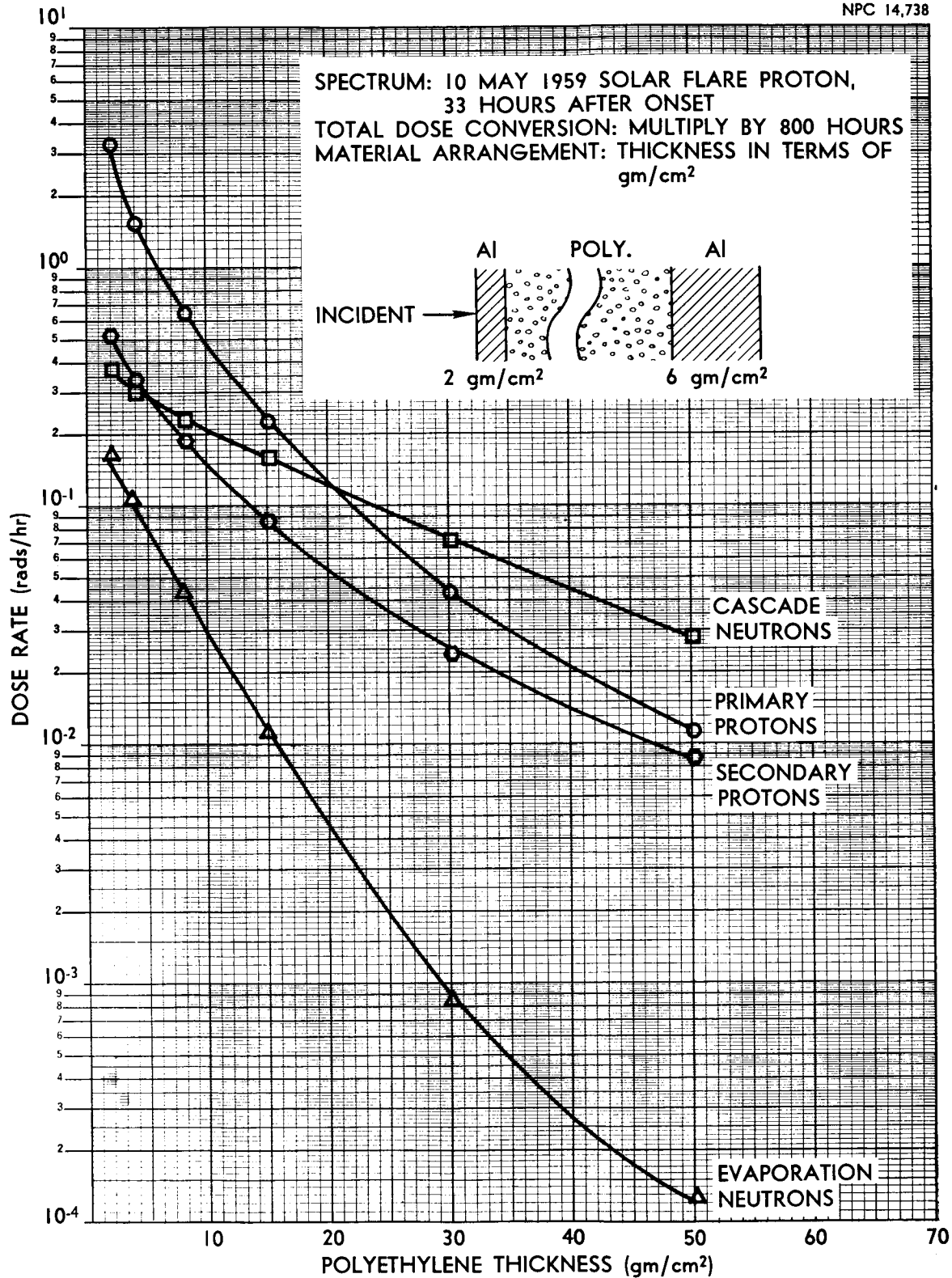
FIGURE 5.14. COMPOSITE-SHIELD (ALUMINUM-POLYETHYLENE-ALUMINUM GEOMETRY B) DOSE RATE AS A FUNCTION OF POLYETHYLENE THICKNESS, 10 MAY 1959 SPECTRUM

178
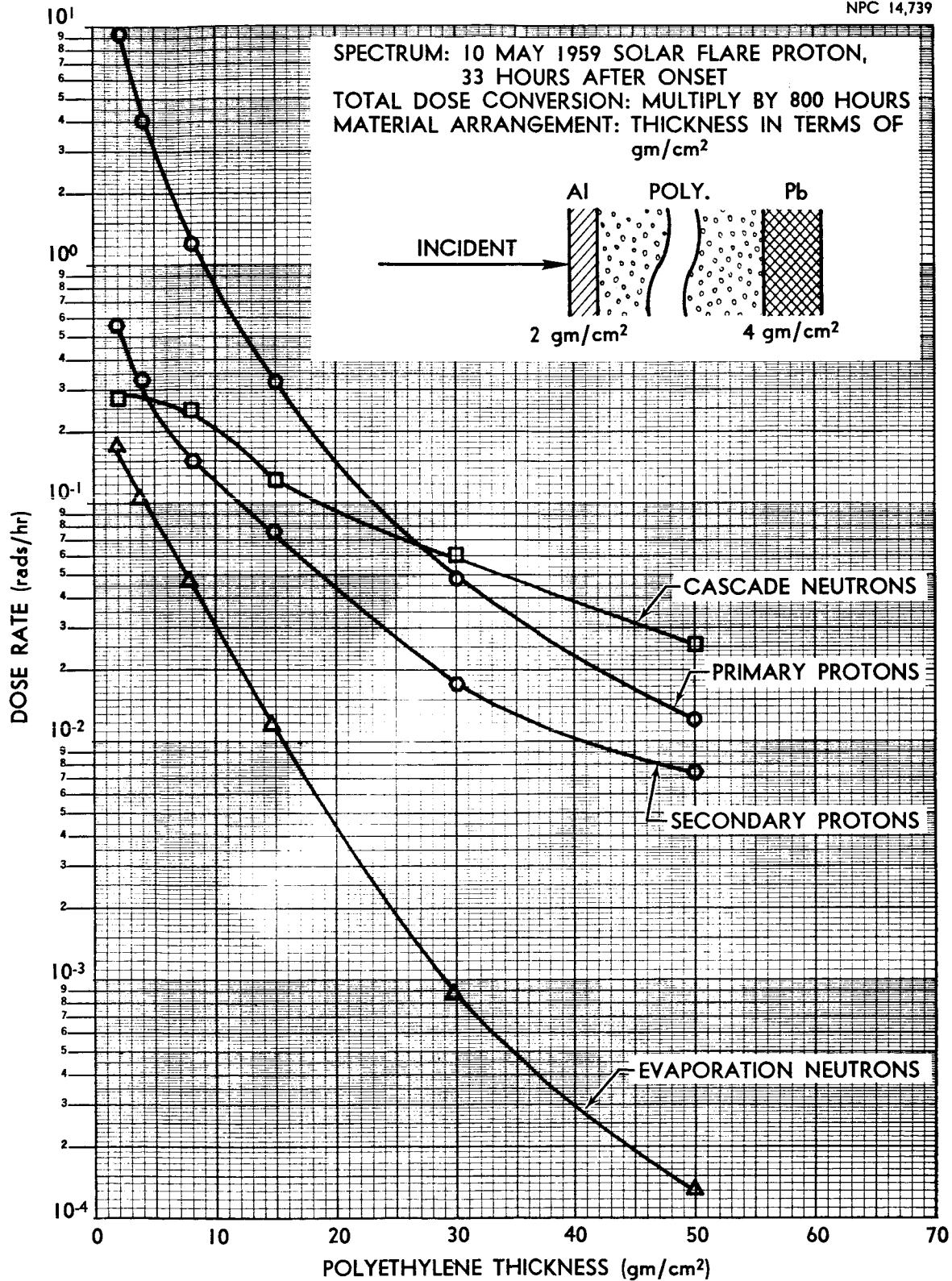
FIGURE 5.15. COMPOSITE-SHIELD (ALUMINUM-POLYETHYLENE-LEAD) DOSE
RATE AS A FUNCTION OF POLYETHYLENE THICKNESS,
10 MAY 1959 SPECTRUM

179

VI. CONCLUSIONS AND RECOMMENDATIONS

6.1 Study of the Secondary Component

The primary conclusion which must be drawn from the data presented in Section V is that the secondary component of the radiation must be considered in any shielding calculation for extraterrestrial radiation. The models used for calculation of the secondary dose were selected with the expressed intention of evaluating the relative importance of the secondary in comparison to the primary component.

On the basis of the data obtained on the relative importance of the secondaries, it would appear that not only material selection, but also composite-shield material arrangement may be extremely important in the selection of an optimum shield. This "first generation" evaluation of the importance of secondaries points out the need for further study of the angular and energy dependence of these components.

6.2 Depth-Dose Patterns in Target

It has been customary in the case of fission-neutron sources to speak of the whole-body dose received by a human target. In the energy region up to 10 Bev for extraterrestrial radiation, it would seem inappropriate to continue to calculate the whole-body dose, but rather to look for the maximum dose in the body. Studies of H. J. Schaeffer (Ref. 28) and R. D. Evans (Ref. 94) indicate that for the spectra encountered in space (decreasing intensity with energy) the maximum dose due to the

primary component will always occur at the surface of the target. With more shielding in front of the target, the less peaked the dose is at the target surface (Fig. 3.2); thus, the rate of energy loss across the body target does not change a great deal. Only for thin shields (less than about 20 gm/cm^2 of polyethylene) would the dose change more than about a factor of 2 across the short dimensions of the human torso, even for a soft spectrum such as that of 10 May 1959. For the present, it would appear that surface-dose calculations are adequate, since the concept of an unacceptably high skin dose but acceptable total body dose is nebulous.

6.3   Improvements

As previously described (Sec. V), the selection of a "typical" flare spectrum and its time-integrated intensity is at present, and, it would seem for the immediate future, rather uncertain. Future studies should be performed on a parametric basis, i.e., unit intensity for single incident energies. With data reported in this form, one can construct at some later time his own dose values on the basis of spectral data available at that time.

Before sufficient accuracy can be obtained to analyze the dose received by a human target shielded by a space-vehicle shield, it will be necessary to consider, at least in some approximate fashion, the angular distribution of the secondaries on the inner face of the shield. With the development of some approximate scheme as the goal, the use of Monte Carlo techniques or the Carlson S_n (Ref. 95) method for solution of the transport

182

equation is necessary. These methods may lead to approximations which could be used in conjunction with the scalar dose (non-angular dependent) values calculated by a code like PAP to give sufficient accuracy for design purposes. Other results from the use of these more elegant models for calculating the dose due to secondaries would provide a check of the models presently used in PAP and point out necessary modifications for improvement.

APPENDIX A

RANGE-ENERGY RELATIONS FOR PROTONS

The primary mechanisms for energy loss for fast protons
($E > 1$ Mev) and heavier ionized particles as they pass through
material is by excitation and ionization of particles in their
vicinity. The theory of such energy loss per unit path length
for charged particles is based on a quantum mechanical formula-
tion which considers wave scattering by the field of the atomic
electrons in the material. The energy of a proton must be
sufficiently high so that capture of electrons from the material
does not occur in order for the following formulation to be
correct.

For the above conditions, the average energy loss per
centimeter of path for a relativistic particle (Ref. 96) is

$$S(E) = -dE/dx = \frac{4\pi e^4 z^2 NB}{mv^2} \tag{A.1}$$

with

$$B = Z \left[\log \frac{2mv^2}{I} - \log(1-\beta^2) - \beta^2 \right] , \quad \beta = v/c .$$

Here, v is the velocity and Ze the charge of the incident
particle, N the number of atoms/cubic centimeter of material,
Z the atomic number of the material nuclei in question, and I
the average excitation potential of the atom. The term $-dE/dx$
is generally called the "stopping power" for the material and B
the "stopping number". No nuclear collisions (called hard colli-
sions) are assumed to occur in this formulation for energy loss.

The range of a heavy particle (protons in this study) of energy E is found by integrating numerically the stopping-power relation

$$R(E) = - \int_E^{E_0} dE/(dE/dx) + R(E_0),\qquad (A.2)$$

where $R(E_0)$ is the range of a proton with energy E_0 below which Equation A.1 is not applicable, i.e., experimental data are used in the range where a proton can pick up an electron.

Curves from Reference 97 for the range of a proton as a function of energy are shown in Figure A.1. In the evaluation of the range in molecular shields, such as polyethylene, it is assumed that the stopping powers for the constituent atoms combine independently of each other and that

$$S_{Molecular}(E) = \sum_i A_i S_i(E),\qquad (A.3)$$

where A_i is the fraction of the molecular weight for atoms of type i, and $S_i(E)$ is the corresponding stopping power. The range is then evaluated by use of Equation A.2.

An example of demonstrating the calculation of the exit energy E of an incident proton of energy E_0 for an aluminum-polyethylene-lead composite shield is shown in Figure A.2.

A more complete discussion of this subject can be found in References 94 and 95. The latter reference includes numerous approximations which can be used that eliminate the use of tables if only a rough approximation is necessary.
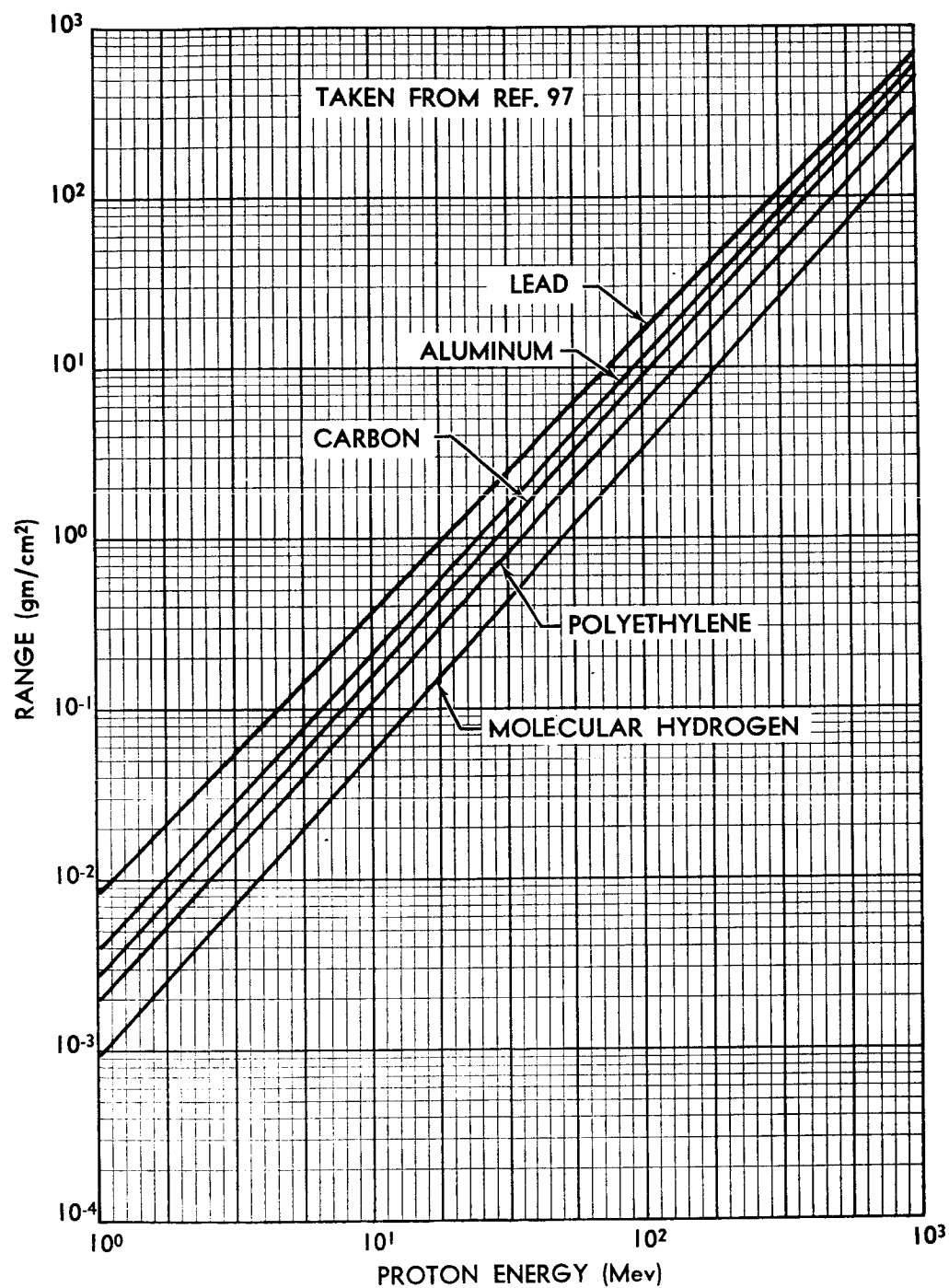
FIGURE A-1. PROTON RANGE-ENERGY CURVES
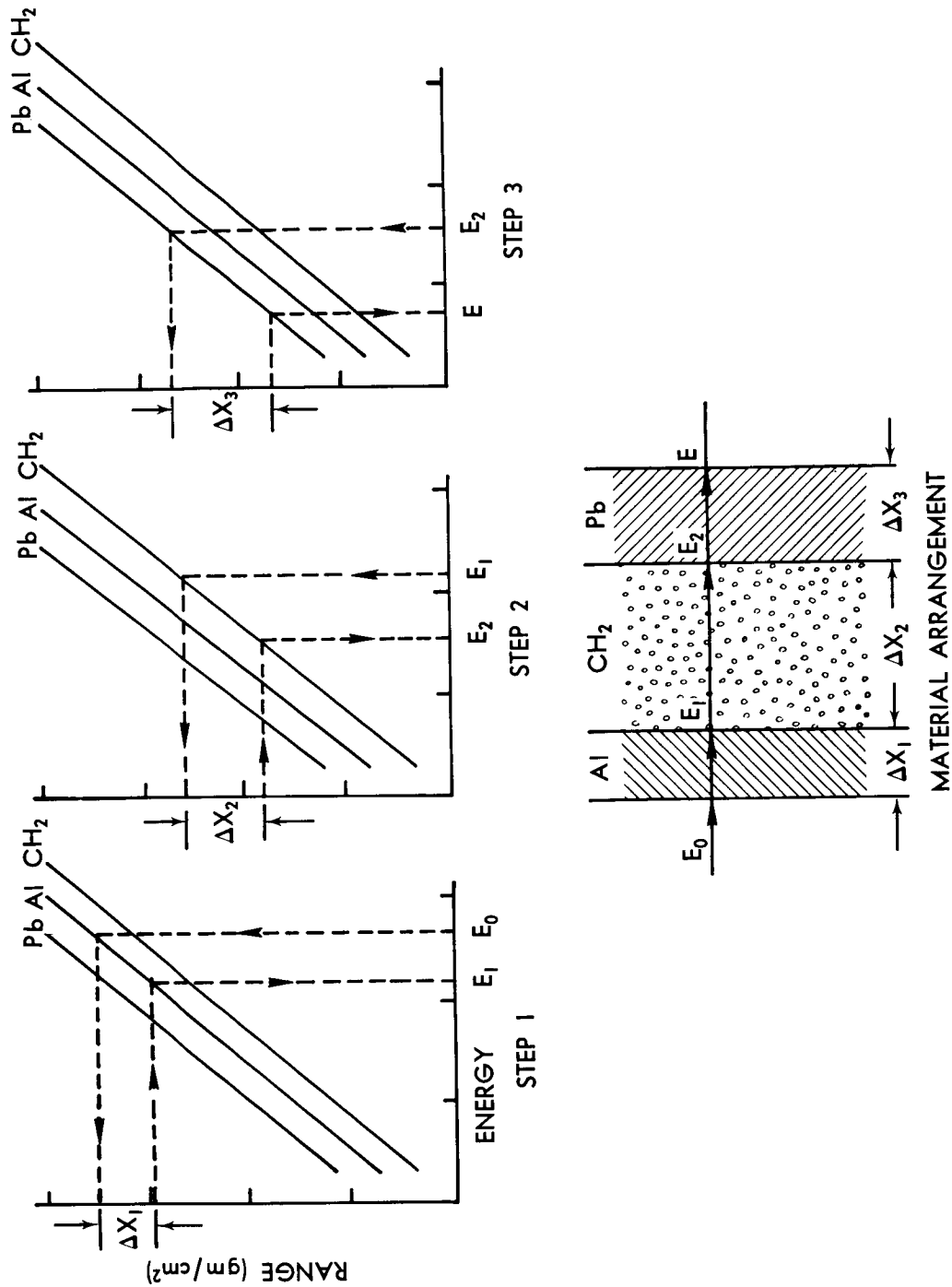
FIGURE A-2. EXAMPLE: DETERMINATION OF EXIT ENERGY E FOR PROTON OF ENERGY E_0 INCIDENT ON A COMPOSITE SHIELD

188

APPENDIX B

PROTON ATTENUATION PROCEDURE (PAP)

The non-analytic solutions of the equations presented in Section III for the calculation of the dose due to primaries and secondaries are outlined in this section. Because of the complex nature of the equations, a computer program (PAP) was written for solutions of the model equations.

For ease of computation, all the model equations developed in Section III are in terms of either the energy incident or the energy at the point of birth of the secondaries. Although the form of the equations is much more tractable than if they were expressed in terms of energies at the target, the dose must still be determined on the basis of the energies at the target. It was emphasized in Section 5.3.1 that the integrand in the primary-proton equation for dose was rapidly varying. In order to find the total area under such an integrand (Fig. 5.3) by numerical integration, it is necessary to choose judiciously the energies at which the integrand will be evaluated. The same problem is encountered in the integration over secondary-proton energies. The selection of these energies is based on picking a particular exit energy for which $S_p(E_R)$, where E_R is the proton energy at the target, is, for example, a factor of 10 below its maximum near $E_R = 0$. This energy is taken as the exit energy, and the corresponding incident energy is determined on the basis of the materials and arrangements making up the shield. In the same operation, the energy which a secondary proton must have at its

189

birth is determined for each source location in order for it to exit with the preselected energy. On the basis of this single energy for the incident spectrum and each of the secondary source locations, and the minimum energy to get from a point in the slab to the target, the whole range of energies for representing the various integrands is chosen. The solution of the secondary-neutron model equation is complicated only by the large energy range of the primary spectrum. It is necessary to consider the interval from $E*(x)$, the minimum incident energy to get to a secondary-source location, to E_{max}. Incident energies are chosen on the basis of the steepness of the incident spectrum.

A brief flow chart for the PAP program is shown in Figure B-1, and the basic operating information is listed below:

1. Number of incident energies used to represent primary and secondary spectra................... 20

2. Number of slabs allowed to make up composite shield.. 15

3. Number of secondary sources allowed (any placement).. 80

4. Optional incident-spectrum representation

   a. Analytic

   b. Discrete point-by-point input as a function of energy (maximum number of points 80)

5. Optional secondary-particle-spectra representation

   a. Average energy

   b. Analytic

       (1) $K \tan \pi/2 \ 1-E/E'(x)$ secondary protons
       (2) $K \tan \pi/2 \ 1-E/E'(x)$ cascade protons
       (3) Evaporation neutron model as described in Reference 31.

   c. Double interpolation on primary and secondary energies for input data, if available.
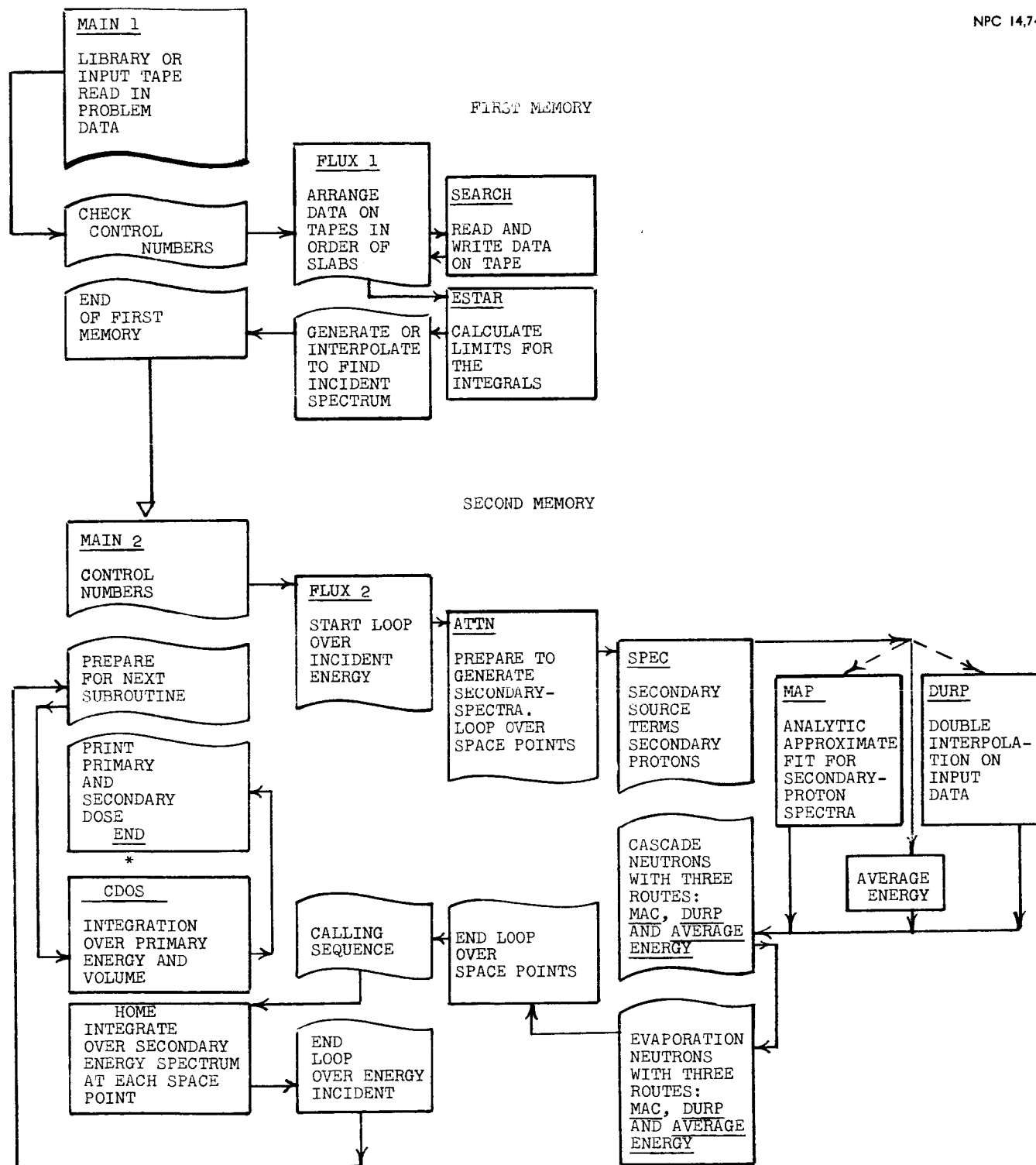
FIGURE B-1. FLOW CHART OF PAP

REFERENCES

1. Keller, J. W., A Study of Shielding Requirements for Manned Space Missions. Convair-Fort Worth Report FZK-124 (10 October 1960). (U)

2. Singer, S. F., "On the Nature and Origin of the Earth's Radiation Belts", Space Research, H. Kahlman, Editor, North-Holland Publishing Co., Amsterdam (1960), pp. 797-820.

3. "Preliminary Results from Explorer XII." NASA News Release No. 62-14, Washington, D. C. (19 January 1962).

4. O'Brien, B. J., Van Allen, J. A., Laughlin, C. D., and Frank, L. A., "Absolute Electron Intensities in the Heart of the Earth's Outer Radiation Zone," J. Geophys. Res. 67, (1962), 397-403.

5. Freden, S. C. and White, R. S., "Particle Fluxes in the Inner Radiation Belt," J. Geophys. Res. 65, (1960), 1377-1383.

6. Naugle, J. E. and Kniffen, D. A., "The Flux and Energy Spectra of the Protons in the Inner Van Allen Belt," Phys. Rev. Letters 7, (1961), 3-6.

7. Hoffman, R. A., Arnoldy, R. L., and Winckler, J. R., "Observations of the Van Allen Radiation Regions During August and September 1959," J. Geophys. Res. 67, (1962), 1-12.

8. Freden, S. C. and White, R. S., "Protons in the Earth's Magnetic Field," Phys. Rev. Letters 3, (1959), 9.

9. Armstrong, A. H. and Heckman, H. A., "Flux and Spectrum of Charged Particles in the Lower Van Allen Belt," Bull. Amer. Phys. Soc. 6, (1961), 361.

10. Holly, F. E., Allen, L., Jr., and Johnson, R. G., "Radiation Measurements to 1500 Kilometers Altitude at Equatorial Latitudes," J. Geophys. Res. 66, (1960), 1377-1383.

11. Van Allen, J. A., "Geomagnetically Trapped Corpuscular Radiation," Science in Space, L. V. Berkner, Editor, McGraw-Hill, New York, (1961), pp. 275-295.

12. Cladis, J. B., Chase, L. F., Imhof, W. L., and Knecht, D. J., "Energy Spectrum and Angular Distributions of Electrons Trapped in the Geomagnetic Field," J. Geophys. Res. 66, (1961), 2297-2312.

13. Freeman, J. W., "Detection of An Intense Flux of Low-Energy Protons or Ions Trapped in the Inner Radiation Zone," J. Geophys. Res. 67, (1962), 921-928.

14. Flugge, S., Ed., Handbuch der Physik, Vol. LII, Astrophysics III: The Solar System, Springer-Verlag, Berlin (1959), p. 80.

15. Winckler, J. R., "Primary Cosmic Rays," Radiation Research 14, (1961), 521-539.

16. Chubb, T. A. Friedman, H., Kreplin, R. W., "Measurements Made of High-Energy X-rays Accompanying Three Class 2+ Solar Flares," J. Geophys. Res. 65, (1960), 1831-1832.

17. Winckler, J. R., May, T. C., Mosley, A. J., "Observations of a Solar Bremsstrahlung Burst of 1926 UT, August 11, 1960," J. Geophys. Res. 66, (1961), 316-320.

18. Bhavsar, P. D., "Scintillation Counter Observation of Auroral X-rays During the Geomagnetic Storm of 12 May 1959," J. Geophys. Res. 66, (1961), 679-692.

19. Biswas, S., Fichtel, C. E., and Guss, D. E., "Solar Protons, Alpha Particles, and Heavy Nuclei from November 12, 1960 Flare," AGU Meeting, UCLA, 27-29 December, 1961.

20. McCracken, J. G., "The Cosmic-Ray Flare Effect," J. Geophys. Res. 67, (1962), 423-458.

21. Gold, T., "Plasma and Magnetic Fields in the Solar System," J. Geophys. Res. 64, (1959), 1665-1674.

22. Parker, E. N., "Sudden Expansion of the Corona Following a Large Solar Flare and the Attendant Magnetic Field and Cosmic-Ray Effects," Astrophys. J., 133, (1961), 1014-1033.

23. Van Allen, J. E., and Whelpley, W. A., "Injun I Observations During Latter September-Early October 1961," Amer. Geophys. U. Meeting, Los Angeles, 27 December 1961.

24. Flugge, S., Ed., Handbuch der Physik, Vol. XLVI, Cosmic Rays 1, Springer-Verlag, Berlin (1961).

25. Vernov, S. N., Chudakov, A. E., Vakulov, P. K., and Logachev, Y. I., "Study of Terrestrial Corpuscular Radiation and Cosmic Rays During the Flight of a Cosmic Rocket," Soviet Physics Doklady, 4, (1959), 338-342.

26. Tolan, J. H., Ed., Shielding Problems in Manned Space Vehicles. Lockheed Nuclear Products, Marietta, Georgia, Report No. NR-140 (September 1961). (U)

27. Schaefer, H. J., Radiation Tolerance Criteria in Space Operations. U. S. Naval School of Aviation Medicine, Pensacola, Florida, Report No. 20 (September 1961). (U)

28. Schaefer, H. J., Dosimetry of Proton Radiation in Space, U. S. Naval School of Aviation Medicine, Pensacola, Florida, Report No. 19 (June 1961). (U)

29. Permissible Dose from External Sources of Ionizing Radiation. National Bureau of Standards Handbook No. 59 (September 1954).

30. Gibson, W. A., Private Communication based on ORNL Internal Memorandum: Energy Removed from Primary Proton and Neutron Beams by Tissue. Oak Ridge National Laboratory Report CF 61-6-48 (1961). (U)

31. Blatt, J. M., and Weisskopf, V. F., Theoretical Nuclear Physics. John Wiley and Sons, Inc., New York (1952).

32. Foelsche, T., Protection Against Solar Flare Protons. Paper presented at the Seventh Annual Meeting of the American Astronautical Society, Dallas, Texas (16 January 1961).

33. Hughes, D. J., and Harvey, J. A., Neutron Cross Sections. Brookhaven National Laboratory Report BNL 325 (1958). (U)

34. Bowen, P. H., et al., "Neutron Total Cross Section in the Energy Range 15 to 120 Mev." Nuclear Physics 22, (1961), 640.

35. Hess, W. N., "Summary of High-Energy Nucleon-Nucleon Cross-Section Data," Rev. Mod. Phys. 30, (1958), 368.

36. Hildebrand, R. H., and Leith, C. E., "Total Cross Sections of Nuclei for 42-Mev Neutrons," Phys. Rev. 80, (1950), 842

37. Hodgson, P. E., "Optical Model Analysis of the Scattering of 96 Mev Neutrons by Nuclei," Nuclear Physics 21, (1960), 21.

38. Ashmore, R. G. J., et al., "Nuclear Total Cross Sections for 350-Mev Neutrons," Proc. Phys. Soc. (A) 70, (1957), 745.

39. DeJuren, J., "Nuclear Cross Sections for 270-Mev Neutrons," Phys. Rev. 80, (1950), 27.

40. Fox, R., et al., "Total Cross Sections of Nuclei for 280-Mev Neutrons," Phys. Rev. 80, (1950), 23.

41. Nedzel, V. A., "Total Cross Sections for 400-Mev Neutrons," Phys. Rev. 90, (1953), 169.

42. Nedzel, V. A., "Total Cross Sections for 410-Mev Neutrons," Phys. Rev. 94, (1954), 174.

43. Booth, N. E., et al., "Nuclear Cross Sections for 765-Mev Neutrons," Proc. Phys. Soc. 71, (1958), 293.

44. Taylor, A. E., and Wood, E., "Proton Scattering from Light Elements at 142 Mev," Nuc. Phys. 25, (1961), 642.

45. DeCarvalho, H. G., "Total Cross Sections of 208-Mev and 315-Mev Protons for Light Elements," Phys. Rev. 96, (1954), 398.

46. Flügge, S., Ed., Handbuch der Physik, Vol. XL; Nuclear Reactions, Springer-Verlag, Berlin (1957).

47. Richardson, R. E., "Nuclear Elastic Scattering of High-Energy Protons," Phys. Rev. 86, (1952), 29.

48. Marshall, J., et al., "Total Cross Sections of 408-Mev Protons for Hydrogen and Light Elements," Phys. Rev. 91, (1953), 767.

49. Chen, F. F., et al., "Attenuation Cross Sections for 860-Mev Protons," Phys. Rev. 99, (1955), 857.

50. Booth, N. E., et al., "Nuclear Cross Sections for 900-Mev Protons," Proc. Phys. Soc. (A) 70, (1957), 209.

51. Voss, R. G. P., and Wilson, R., "Neutron Inelastic Cross Sections Between 55 and 140 Mev," Proc. Roy. Soc. (London) (A) 236, (1956), 41.

52. Hadley, J. H., and York, H., "Protons and Deuterons Ejected from Nuclei by 90-Mev Neutrons," Phys. Rev. 80, (1950), 345.

53. Ashmore, A., et al., "The Elastic Scattering of 350-Mev Neutrons by Complex Nuclei," Proc. Phys. Soc. 71, (1958), 558.

54. Ball, W. P., Nuclear Scattering of 300-Mev Neutrons. Thesis, UCRL-1938 (1952). (U)

55. Coor, T., Hill, D. A., Hornyak, W. F., Smith, L. W., and Snow, C., Phys. Rev., 98, (1955), 1369.

56. Barrett, P. H., "Nuclear Absorption Cross Sections for 3.6-Bev Neutrons," Phys. Rev. 114, (1959), 1374.

57. Burge, E. J., "The Total Proton Reaction Cross Section of Carbon from 10-63 Mev by a New Method," Nuclear Phys. 13, (1959), 511.

58. Johansson, A., et al., "Total Nuclear Reaction Cross Sections for 180-Mev Protons," Arkiv Fysik 19, (1961), 527.

59. Gooding, T. J., "Proton Total Reaction Cross Sections at 34 Mev," Nuclear Phys. 12, (1959), 241.

60. Meyer, V., et al., "Total Reaction Cross Sections of Several Nuclei for 61-Mev Protons," Phys. Rev. 117, (1960), 1334.

61. Millburn, G. P., et al., "Nuclear Radii from Inelastic Cross Section Measurements," Phys. Rev. 95, (1954), 1268.

62. Booth, N. E. et al., "Nuclear Cross Sections for 900-Mev Protons," Proc. Phys. Soc. (A) 70, (1957), 209.

63. Crandall, W. E., et al., "$C^{12}(x,xn)C^{11}$ and $Al^{27}(x,x2pn)Na^{24}$ Cross Sections at High Energies," Phys. Rev. 101, (1956), 329.

64. Cummings, J. B., et al., "$C^{12}(p,pn)C^{11}$ Cross Section at 2 and 3 Bev," Phys. Rev. 111, (1958), 1386.

65. Benioff, P. A., "Nuclear Reactions of Low-Z Elements with 5.7-Bev Protons," Phys. Rev. 119, (1960), 316.

66. Baker, E., et al., "Formation of Be^7 in Interactions of Various Nuclei with High-Energy Protons," Physics Rev. 112, (1958), 1319.

67. Lefort, M., et al., "Reactions Nucléaires De Spallation Induites Sur Le Thorium Par Des Protons De 150 Et 82 Mev," Nuclear Physics 25, (1961), 220.

68. Fernbach, S., et al., "The Scattering of High-Energy Neutrons by Nuclei." Phys Rev. 75, (1949), 1352.

69. Goldberger, M. L., "The Interaction of High-Energy Neutrons and Heavy Nuclei," Physics Rev. 74, (1948), 1269.

70. Strauch, K., and Titus, F., "Direct Excitation of Nuclear Energy States in Carbon by 96-Mev Protons," Phys. Rev. 103, (1956), 200.

71. Johansson, A., et al., "The Elastic Scattering of 180-Mev Protons from Nuclei," Arkiv För Fysik 19, (1961), 541.

72. Maris, Th. A. J., and Tyrén, H., "Some Remarks Concerning Measurements on Inelastic Scattering of 155-185 Mev Protons on Carbon, Oxygen, and Calcium," Nuclear Physics 4, (1957), 662.

197

73. Harding, R. S., "Asymmetry Measurements in the Scattering of 155-Mev Neutrons by Carbon, Aluminum, Copper, Cadmium, and Lead," Phys. Rev. 111, (1958), 1164.

74. Hecht, D. J., Angular Distribution of Charged Particles from 31-Mev Protons on Carbon. UCRL-2969(21 April 1955). (U)

75. Bostick, H. A., Spectrum and Yield of Neutrons from 31.5-Mev Proton Bombardment of Selected Isotopes of Cobalt and Nickel. UCRL-8528 (10 October 1958). (U)

76. Adelson, N. E., Energy Spectra and Angular Dependence of Nucleons from the 31.5 Mev Proton Bombardment of Beryllium-9, Nitrogen-14, and Aluminum-27. UCRL-8568 (11 December 1958). (U)

77. Gross, Edward, The Absolute Yield of Low-Energy Neutrons from 190-Mev Proton Bombardment of Gold, Silver, Nickel, Aluminum, and Carbon. UCRL-3330 (29 February 1956). (U)

78. Hofmann, J. A., and Strauch, K., "On the Interaction of 95-Mev Protons with D, Li, Be, C, Al, Cu, and Pb." Phys. Rev. 90, (1953), 449.

79. Metropolis, N., et al., "Monte Carlo Calculations on Intra-nuclear Cascades, II. High-Energy Studies and Pion Processes," Phys. Rev. 110, (1958), 204.

80. Metropolis, N., et al., "Monte Carlo Calculation on Intra-nuclear Cascades. I. Low-Energies Studies," Phys. Rev. 110, (1958), 885.

81. Bailey, L. E., Angle and Energy Distributions of Charged Particles from the High-Energy Nuclear Bombardment of Various Elements. UCRL-334 (1 March 1956). (U)

82. Kellogg, D. A., "Cross Sections for Products of 90-Mev Neutrons on Carbon," Phys. Rev. 90, (1953), 224.

83. Dostrovsky, I., et al., "Monte Carlo Calculation of High-Energy Nuclear Interactions. I. Systematics of Nuclear Evaporation," Phys. Rev. 111, (1958), 1969.

84. Graves, E. R., and Davis, R. W., "Cross Sections for Non-Elastic Interaction of 14-Mev Neutrons with Various Elements," Phys. Rev. 97, (1955), 1205.

85. Gol'Danskii, V. I., et al., "Emission of Secondary Neutrons from Nuclei Bombarded by High-Energy Neutrons," Phys. Rev. 109, (1958), 1762.

86. Niemann, F. L., et al., "Energy Spectrum of Charged Pions from 2.2-Bev Protons on Be," Phys. Rev. 108, (1957), 1331.

87. Weisskopf, V., "Statistics and Nuclear Reactions," Phys. Rev. 52, (1937), 295.

88. Shal'Nov, M. I., "Tissue Doses of Fast and Ultra-Fast Neutrons," Sov. J. At. En. 4, (1958), 735.

89. Krumkein, A. O., Summary of NDA Unclassified Results of Moments Calculations for the Penetration of Neutrons Through Various Materials. Nuclear Development Corp. Report No. 92-2 (Rev.) (30 August 1957). (U)

90. Winckler, J. R., and Bhavsar, P. D., "Low-Energy Solar Cosmic Rays and the Geomagnetic Storm of 12 May 1959," J. Geophys. Res. 65, (1960), 2637-2655.

91. Ney, E. P., Winckler, J. R., and Frier, P. S., "Protons from the Sun on 12 May 1959," Phys. Rev. Letters 3, (1959), 183-185.

92. Winckler, J. R., Bhavsar, P. D., and Peterson, L., "The Time Variations of Solar Cosmic Rays During July 1959 at Minneapolis," J. Geophys. Res. 66, (1961), 995-1022.

93. Charakhch'yan, V. F., et al., Energy Spectrum and Time Dependence of the Intensity of Solar Cosmic-Ray Protons. JETP Translation 14, (1962), 530.

94. Evans, R. D., Principles for the Calculation of Radiation Dose Rates in Space Vehicles, Arthur D. Little Report No. 63270-05-01 (July 1961). (U)

95. Edmonson, N., and Bostick, L. M., Angular Segmentation Method. GD/FW Report FZK-9-172 (NARF-61-43T, 1961). (U)

96. Segre, E., Experimental Nuclear Physics, Vol. I. John Wiley and Sons, New York (1953).

97. Rich, M., and Madey, R., Range-Energy Tables. University of California Radiation Laboratory Report UCRL-2301 (1954). (U)

98. Evans, R. D., The Atomic Nucleus. McGraw-Hill, New York (1955).

DISTRIBUTION

FZK-144   8 June 1962

Addressee	No. of Copies
NASA, George C. Marshall Space Flight Center Huntsville, Alabama	50
NASA Headquarters 1520 H Street, NW Washington 25, D.C.	5
NASA Langley Field, Virginia	2
NASA Goddard Space Flight Center Greenbelt, Maryland	8
NASA Lewis Research Center Cleveland 35, Ohio	5
NASA Manned Space Craft Center Houston, Texas	2
Air Force Systems Command Wright-Patterson, AFB, Ohio	5
USAF Aerospace Medical Center Brooks AFB, Texas	2
Air Force Special Weapons Center Kirtland AFB, New Mexico	1
Air Force Cambridge Research Center Bedford, Mass.	2
U. S. Naval School of Aviation Medicine Pensacola, Florida	1
U. S. Naval Research Laboratory Washington 25, D. C.	1
U. S. Naval Radiological Defense Laboratory San Francisco 24, California	1

DISTRIBUTION (Cont'd)

Addressee	No. of Copies
U. S. Atomic Energy Commission Washington 25, D. C.	2
National Bureau of Standards Boulder, Colorado	1
National Naval Medical Center Washington, D. C.	1
National Institute of Health Bethesda, Maryland	1
Office of Surgeon General Hq. USAF Washington 25, D. C.	1
Space Science Board National Academy of Sciences Washington, D. C.	1
Aerospace Corporation Los Angeles 45, California	2
Los Alamos Scientific Laboratory Los Alamos, New Mexico	2
Oak Ridge National Laboratory Oak Ridge, Tennessee	2
Space Technology Laboratories, Inc. Los Angeles, California	2
Brookhaven National Laboratory Upton, New York	1
Lockheed Aircraft Corporation Missiles and Space Division Palo Alto, California	1
Lockheed Nuclear Products Marietta, Georgia	1
University of Minnesota Minneapolis, Minnesota	1

DISTRIBUTION (Cont'd)

Addressee	No. of Copies
State University of Iowa Iowa City, Iowa	1
University of California Berkeley, California	1
Louisiana State University Baton Rouge, Louisiana	1
University of Maryland College Park, Maryland	1
Institute of Geophysics UCLA Los Angeles 24, California	1
The Rand Corporation Santa Monica, California	1
University of Chicago Chicago, Illinois	1
Battelle Memorial Institute Columbus, Ohio	1
General Dynamics/Astronautics San Diego, California	3
The Boeing Company Seattle, Washington	1
North American Aviation, Inc. Space and Information Systems Division Downey, California	1
The Martin Company Denver, Colorado	1
Republic Aviation Company Farmingdale, New York	1
Avco&Everett Research Laboratory Everett 49, Massachusetts	1

Addressee	No. of Copies
McDonnell Aircraft Corporation St. Louis 66, Missouri	1
General Electric Company Missiles and Space Vehicle Department Philadelphia, Pennsylvania	1

GENERAL DYNAMICS/Fort Worth

15 August 1962

To: All Distribution

From: P. H. Billman

Subject: Errata in FZK-144, dated 8 June 1962

Please change your copy of FZK-144 as follows:

1.   Page 60.   Equation 3.8 should read

$$2\pi \int_{-1}^{1} d\mu \int_{0}^{E''} dE \, f_{sp}(E'',E;\mu',\mu) = 1 \qquad (3.8)$$

and   Equation 3.9 should read

$$2\pi \int_{\mu_0}^{1} d\mu' \int_{0}^{E''} dE \, f_{sp}(E'',E;\mu',1) \approx 1 \qquad (3.9)$$

2.   Page 61.   The paragraph beginning, "For Equation 3.10,···"
should have the following sentence added at the end:

The function $g(E'',E)$ in Equation 3.12 is normalized so that

$$\int_{E^{\ddagger}}^{E''} g(E'',E)dE = 1/2\pi$$

where $E^{\ddagger}$ is some lower limit arbitrarily selected for this
component.

3. Page 69. The next-to-the-last paragraph of Section 3.2.2.3 should have the following sentence added at the end:

The normalization of the function $f_{en}(E'',E)$ appearing in Equation 3.24 is

$$\int_0^{E_{ex}} dE\, f_{en}(E'',E) = 1/2\pi$$

4. Page 74. In Figure 4.1, the 23 February 1956 curve is to be multiplied by 4π to give its correct magnitude.

5. Page 163. The last sentence in Section 5.3 is to be footnoted as follows:

The assumed secondary-energy spectra $g(E'',E)$ and $f_{en}(E'',E)$ were put into the code with an incorrect normalization. Thus, it is necessary to divide all secondary-dose components by a factor of 2π (Figs. 5.7 through 5.15). The primary components are correct.

Paul H. Billman, Jr.